RAMAN SPECTROSCOPY OF NANOGRAPHITES

Luiz Gustavo de Oliveira Lopes Cançado

Setembro de 2006

RAMAN SPECTROSCOPY of NANOGRAPHITES

LUIZ GUSTAVO DE OLIVEIRA LOPES CANÇADO

Orientador: Prof. Marcos Assunção Pimenta

co-Orientador: Prof. Ado Jório Vasconcelos

Tese apresentada à UNIVERSIDADE FEDERAL DE MINAS GERAIS, como requisito parcial para a obtenção do grau de DOUTOR EM FÍSICA.

Setembro de 2006

BANCA EXAMINADORA

Prof. Marcos Assunção Pimenta

Prof. Ado Jório Vasconcelos

Prof. José Francisco Sampaio

Prof. Roberto Nogueira

Prof. Ricardo Vagner (suplente)

Universidade Federal de Minas Gerais.

Prof. Mildred Dresselhaus

Massachussets Institute of Technology.

Prof. Riichiro Saito

Tohoku University.

Contents

Aos meus pais Mário e Dulce.

Agradecimentos

Ao Marquim, meu mestre e amigo, por acreditar em mim desde o início e me ensinar a ter uma visão voltada para aspectos relevantes na ciência que nos levam a crescer e somar.

Ao Ado, que sempre foi para mim uma referência de caráter e profissionalismo, pelo muitíssimo que me ensinou sobre física e vida.

À minha esposa Lu; meu amor e meu descanso.

Aos meus irmãos Dani, Titi e Lilica pela diversão nos momentos fáceis e apoio nos difíceis, que felizmente foram raros.

Aos tios David e Simone, Silvio e Lúcia, e também aos primos Fael e Thi, pela presença constante e sempre repleta de amizade e carinho.

Ao meu amigão Kneicker, pela compania incondicional durante a confecção da tese.

Ao Bernardo pelas medidas de microscopia nos trabalhos envolvendo fitas de nanografite e bordas de HOPG.

À Sica pela colaboração durante as medidas de espalhamento Raman nas bordas de HOPG.

Ao Enoki-sensei, pelo apoio pessoal e científico durante meu período de trabalho em seu laboratório.

Ao Takai-san, pela amizade e dedicação com as quais me ensinou inúmeros aspectos da física experimental. Em especial, agradeço por ter me orientado nos trabalhos the STM e na síntese de nanografites.

Ao Fukui-sensei pelas discussões e apoio técnico nos trabalhos envolvendo STM.

Aos colegas do laboratório Raman; Cris, Maurício, Paulo, Indhira, Ana Paula, Dani,

Pedro I, Pedro II e Chubaka pela ótima convivência e inúmeros galhos quebrados.

Aos colegas do Enoki-Fukui Lab.; Daikou-san, Ishikawa-san, Aoki-san, Yokota-san, Fijita-san, Kinoshita-san, Eto-san, Sakai-san, Kudo-san, Aimatsu-san, Takahara-san, Kobayashi-san, Miazaki-san, Kuroiwa-san, Ota-sa, Katsuyama-san, Suzuki-san, Chen-san, Kurouchi-san, Naya-san e Tanaka-san pela gentileza e atenção dedicados a mim.

Aos professores Endo-sensei e Kim-sensei, e aos colegas da universidade de Nagano pelo apoio na síntese das amostras de nanografite.

Ao Saito-sensei por financiar minhas visitas à Tohoku University em Sendai, e pelas discussões sobre espalhamento Raman e teoria de grupos no grafite.

Ao professor Rogério Paniago pelas medidas de difração de raios x no LNLS.

À Lets, pelo apoio nas medidas de diffração de raios x no LNLS e pela roça mais marivilhosa de todas as roças.

Ao Mário pelas várias discussões sobre fônons, elétrons, e cerveja, além da força durante a preparação da aprensentação.

Ao Dr. Gilberto Medeiros pelas medidas de STM nas fitas de nanografite.

Ao Nivaldo e ao Alexandre pelas medidas de difração de raios x.

À Professora Paola Cório pelas medidas de FT-Raman.

Aos Professores do Departamento por tentarem me ensinar Física.

Aos Professores do Colegiado de Pós Graduação, por confiarem no meu potencial ao me conceder a bolsa, e pela ótima convivência e respeito durante o período no qual eu fui representante dos alunos. Um agrdecimento especial aos Professores Luiz Paulo, Beth, Paulo Sérgio, Dickman e Ricardo pela luta pelo Colegiado e o corpo discente.

Aos funcionários do departamento de Física, pessoal das secretarias e bibliotecárias. Em especial, Idalina, Fernanda, Marluce e Shirley.

Aos amigos da física nos ótimos momentos de descontração, cerveja e samba.

Aos Professores Sampaio, Bob, Millie, e Saito-sensei por fazerem parte da banca exami-

nadora, e por terem contribuído de forma relevante para a versão final da tese.

Ao Instituto do Milênio, que financiou minhas visitas à USP e ao LNLS.

Ao CNPq, que financiou meu doutorado no Brasil e meu estágio de doutorado no exterior.

Ao Povo Brasileiro por financiar o CNPq.

Resumo

Este trabalho apresenta a aplicação da espectroscopia Raman no estudo e caracterização de nanografites. Mostramos aqui o primeiro experimento onde fitas de nanografite foram detectadas sobre um substrato de grafite pirolítico altamente orientado através de espectroscopia Raman. Encontramos uma maneira de diferenciar os sinais Raman provenientes da fita e do substrato, sendo o sinal obtido da fita de mesma ordem de magnitude daquele obtido do substrato, apesar de a quantidade de átomos de carbono iluminados pelo laser ser muito menor ($\sim 1\,/\,1000$). Os resultados mostram que estas estruturas apresentam singularidades de van Hove na densidade de estados eletrônicos devido ao confinamento quântico proveniente de sua estrutura 1D. Em outro experimento, utilizamos o espalhamento micro-Raman para determinar o arranjo cristalino dos átomos de carbono nas proximidades de uma borda de grafite. A borda de um plano semi-infinito pode ser considerada como um defeito uni-dimensional, acarretando em um processo não usual de espalhamento Raman induzido por defeito, que é seletivo à estrutura da borda. Neste caso, o espalhamento Raman pode ser utilizado para definir a orientação dos hexágonos de carbono em relação às bordas do plano de grafite, em configurações chamadas de *armchair* (cadeira de braço) e zigzag. Estes foram os primeiros experimentos nos quais foi detectada a anisotropia na absorsoção óptica no grafite, confirmando as previsões teóricas. Apresentamos também um estudo sistemático da razão entre as intensidades integradas da banda induzida pela desordem D e da banda permitida em primeira ordem G (I_D/I_G), em amostras de nanografite com diferentes tamanhos de cristalitos, no qual as amostras foram excitadas com linhas de laser de diferentes energias (comprimentos de onda). Os tamanhos de cristalito L_a das amostras foram obtidos através de difração de raios x utilizando radiação síncrotron e também por observação direta através de imagens de microscopia de varredura por tunelamento de elétrons. Baseando-se na comparação entre os resultados obtidos, estabelecemos uma equação que permite medir o tamanho do cristalito L_a através de espalhamento Raman utilizando qualquer energia de laser na faixa do visível. Além disso, medimos as intensidades absolutas de espalhamento Raman para as principais bandas presentes nos espectros Raman de nanografites, obtendo a dependência da intensidade absoluta de cada banda com a energia do laser e o tamanho de cristalito.

Abstract

This work presents the application of the Raman spectroscopy to the study and characterization of nanographite systems. We report the first detection of nanographite ribbons on a highly oriented pyrolytic graphite substrate by Raman spectroscopy. We found a way to differentiate the Raman signal of the ribbon from that of the substrate, the Raman signal of the ribbon having the same order of magnitude as the one from the substrate, despite the much smaller number of illuminated carbon atoms ($\sim 1\,/\,1000$). The results indicate that these structures present van Hove singularities in the electronic density of states due to quantum confinement into their 1D structure. In another experiment, we use micro-Raman scattering to determine the arrangement of carbon atoms in a graphite edge. The edge of a semi-infinite plane can be considered as a one-dimensional defect, leading to unusual defect-induced Raman scattering that turns out to be structurally selective. In this case, Raman scattering can be used to define the orientation of the carbon hexagons with respect to the edge of a graphite plane, in the so called armchair and zigzag arrangements. These two experiments involve the first detection of the anisotropy in the optical absorption of graphite, giving strong support to previous theoretical predictions. We also present a systematic study of the ratio between the integrated intensities of the disorder-induced D band and the first-order allowed G band (I_D/I_G) in the Raman spectra of nanographite samples with different in-plane crystallite sizes (L_a) and using different excitation laser energies (wavelengths). The crystallite size L_a of the nanographite samples were obtained both by X-ray diffraction using synchrotron radiation and directly from scanning tunneling microscopy images. A general equation for the determination of L_a using any laser energy in the visible range is obtained. Moreover, we performed measurements of the absolute intensities of individual features in the Raman spectra of nanographites, showing the dependence of these features on the excitation laser energy and crystallite size.

Chapter 1

Introduction

The crystalline graphite is formed by a stacking of sheets which are composed of a hexagonal array of strongly bonded carbon atoms. The sheets are weakly connected to each other by van der Waals interactions. Due to this special geometry, the crystalline graphite has a strong anisotropy [1]. The physical properties within the sheets differ drastically from those in the perpendicular direction (along the c axis). The π electrons delocalized across the basal planes are the precursors of electrical conductivity. Therefore, graphite is a much better electrical conductor along the basal planes than along the c axis. Similar characteristics are found for elastic and thermal properties, since acoustic phonons propagate very quickly along the planes, but are slower to travel from one plane to another. Moreover, crystalline graphite exhibits the largest diamagnetic susceptibility of any solid at room temperature, being more diamagnetic along the c axis than in the basal plane.

Since the atoms are strongly bonded within the sheets, but the force between two layers is weak, the layers can slip easily over each other. Therefore, graphite is used as a dry lubricant, pencil, or standard material for scanning probe microscopy, since its cleavage is easy and atomically perfect. However, when a large number of structural defects are introduced, graphite can become a very hard material. In its synthetic forms, pyrolytic graphite and carbon fibers are extremely strong and heat-resistant (to 3000°C) materials, being applied in ultra-resistant materials for jets and missiles, high temperature reactors, firestops, electric motor brushes, electrodes in arc discharge machines, reinforced plastics, etc. In the biomedical area, because blood clots do not form easily on graphite, blood-contacting prosthesis are made by graphitic materials in order to reduce the risk of thrombosis. For example, pyrolytic graphite is used in the fabrication of artificial hearts

and prosthetic heart valves.

Due to this wide range of applications in industry, graphite has been largely studied by researchers in the material science area during the last sixty years. Moreover, it became especially important in the last decade, when its basic properties where extensively investigated for understanding the physics behind new graphitic systems, such as carbon nanotubes and fullerenes [2, 3]. Moreover, with the report of new experiments detecting a quantum Hall effect [4], and the massless and relativistic properties of the conductive electrons in a single graphene layer [5, 6], graphite itself became a strong candidate to be applied in the development of the nano-electronic technology.

Raman spectroscopy is used currently and for the last decades to investigate and characterize graphite samples. The intensity of the features present in the Raman spectrum of nanographite systems are known to be strongly dependent on the structural (defect-related) properties. The ratio between the D ($\sim 1350\,\mathrm{cm}^{-1}$) and G ($\sim 1580\,\mathrm{cm}^{-1}$) band intensities is used to evaluate the crystallite size L_a of nano-structured carbon systems, or the degree of disorder in disordered carbon [7, 8]. Raman spectroscopy is also used to measure the order occurring along the c axis, since the second order of the D band, the G' band ($\sim 2700\,\mathrm{cm}^{-1}$) is very sensitive to the degree of graphitization of the samples [9, 10]. These properties makes Raman spectroscopy one of the main tools for the structural characterization of nano-graphitic systems, where the crystalline edges act as defects. Despite the large amount of works concerning the topic, Raman spectroscopy in graphite is such a rich subject that it remains as a fashionable theme in the material science area. Within the new context, where nano-graphite devices started to be made [4, 5, 6], Raman spectroscopy will surely play an important role in their structural investigation. Moreover, the application of Raman spectroscopy in this area should advance with the development of new techniques, such as tip enhanced Raman near-field spectroscopy, which can analyze the spacial extent of structural properties of graphitic materials on a nanometric scale [11].

This thesis presents a study of our advances in the Raman spectroscopy of nanographites. In Chapter 2, the symmetry of phonons and π electrons in graphite is presented. Chapter 3 presents the basis for the theory of Raman scattering in crystals, treating the macroscopic and microscopic approaches separately, and emphasizing the origin of selection rules and resonance effects. Chapter 4 shows a detailed explanation of the spectrometer setup used

in this work, followed by an analysis of the main parts, with special considerations for the measurement process. We devote Chapter 5 for a summary of the history of the Raman spectroscopy in graphite, followed by an overview of the double-resonance Raman scattering process.

In Chapter 6, we show the experimental observation of the Raman spectra of nanographite ribbons on a highly oriented pyrolytic graphite (HOPG) substrate. The Raman peaks of the nanographite ribbon and the HOPG are split due to different thermal expansions of the ribbon and the substrate. The Raman signal from a nanographite ribbon is as intense as that of the HOPG substrate and the ribbon spectrum has a strong dependence on the light polarization. In order to explain these results, we present a model that takes into account the quantum confinement of the electrons in the 1D structure of nanographite ribbons and the anisotropy in the light absorption in 2D graphite.

Chapter 7 contains a detailed study of graphite edges with different atomic structures, combining the use of Raman spectroscopy and scanning probe microscopy. This one-dimensional defect selects the direction of the electron and phonon associated with the disorder-induced Raman process, causing a dependence of the Raman D band intensity on the atomic structure of the edge (strong for armchair and weak for zigzag edge). This work represents an effort to improve the understanding of the influence of the defect structure on the Raman spectra of graphite-like systems, which may be very useful to characterize defects in nanographite-based devices, and also shows evidence for the anisotropy in the optical absorption in graphite.

In Chapter 8, a systematic study of the Raman spectra obtained from nanographite samples with different crystallite sizes L_a, and also different crystallite thicknesses L_c, are presented. By comparing the changes in the Raman data with the structural information obtained by X-ray diffraction and STM, we determine a set of equations which allows us to quantify the parameters L_a and L_c of nanographites by Raman spectroscopy. The study takes into account the influence of the excitation laser energy on the Raman response to the structural changes of the samples, and the relations proposed are valid for experiments using any excitation laser line in the visible range.

In Chapter 9, we report a study of Raman scattering in nanographite samples with different graphitization degrees. It will be shown that the changing in the G' band from a one-peak to a two-peak profile allow us to distinguish the relative scattering intensities

from the 3D and 2D graphitic phases coexisting in the same sample, giving the information about their relative volumes. The comparison between the Raman scattering and X-Ray diffraction data shows that the out-of plane lattice parameter c, and also the crystallite thickness L_c, can be determined from the ratio between the G' band scattering intensities obtained from the 2D and 3D graphite phases.

In Chapter 10, an experimental study of the absolute Raman cross section of the main features in the Raman spectrum of nanographite samples with different crystallite sizes L_a, and using different values of excitation laser energies (in the visible range) is presented. The Raman data obtained reveal the dependence of the absolute intensities β_D and β_G on the crystallite size and excitation laser energy E_l for nanographites, showing that the dependence of the ratio I_D/I_G on E_l reported in Chapter 8 is caused by a deviation of the D band intensity from the ω^4-dependence predicted by the Raman scattering theory. An analysis of the dependence on the full width at half maximum (Γ) of the D, G, D', and G' bands on the crystallite size L_a of nanographites is performed, showing that the phonon lifetime is proportional to the crystallite size.

It will be great if our work encourages students and researchers to join the investigation of Raman spectrum of nanographites, hoping that this manuscript can be useful for their purposes.

This work originated the following publications:

1. Anisotropy of the Raman spectra of nanographite ribbons
L. G. Cançado, M. A. Pimenta, B. R. A. Neves, G. Medeiros-Ribeiro, T. Enoki, Y. Kobayashi, K. Takai, K. Fukui, M. S. Dresselhaus, R. Saito, and A. Jorio, Physical Review Letters **93**, 047403 (2004).

2. Influence of the atomic structure on the Raman spectra of graphite edges
L. G. Cançado, M. A. Pimenta, B. R. A. Neves, M S. S. Dantas, and A. Jorio, Physical Review Letters **93**, 247401 (2004).

3. General equation for the determination of the crystallite size La of nanographite by Raman spectroscopy
L. G. Cançado, K. Takai, T. Enoki, M. Endo, Y. A. Kim, H. Mizusaki, A. Jorio, L. N. Coelho, R. Magalhães-Paniago, and M. A.Pimenta, Applied Physics Letters **88**, 163106 (2006).

4. Measuring the absolute Raman cross section of nanographites as a function of laser energy and crystallite size
L. G. Cançado, A. Jorio, and M. A. Pimenta, Physical Review B **76**, 064304 (2007).

5. Measuring the degree of stacking order in graphite by Raman spectroscopy
L.G. Cançado, K. Takai, and T. Enoki, M. Endo, Y. A. Kim, H. Mizusaki, A. Jorio, N. L. Speziali, and M. A. Pimenta, Carbon **46**, 272 (2008).

This work received the following prizes:

1. Prêmio Capes de Teses 2007, from the Brazilian Department of Education: Best Brazilian Phd Thesis on Physics of the year.

2. Prm̂io Prof. Jos Leite Lopes 2007 (honorable mention), from the Brazilian Physics Society : Best Brazilian Phd Thesis on Physics of the year.

3. Prêmio UFMG de Teses 2007, from the Federal University of Minas Gerais: Best Phd Thesis on Physics of the year.

4. Grande Prêmio UFMG de Teses 2007 (honorable mention), from the Federal University of Minas Gerais: Best Phd Thesis on Hard Sciences of the year.

Chapter 2

Symmetry of Phonons and π Electrons in Graphite

In this Chapter, the symmetry properties of phonons and π electrons in graphite will be presented. The two- and three-dimensional graphite lattices are treated separately in sections 2.1 and 2.2, respectively. This Chapter will be an important reference throughout the text, since it presents crucial information necessary for the analysis of selection rules in the Raman scattering process in graphite.

2.1 2D Graphite

2.1.1 Symmetry of the 2D Graphite lattice

The two-dimensional (2D) graphite is a graphene sheet composed of a hexagonal array of strongly bonded carbon atoms by covalent forces between σ electrons [1]. It belongs the symmorphic space group D_{6h}^1 according to Schoenflies notation, or $P6/mmm$ in the Hermann-Mauguin notation [12].

Figure 2.1(a) shows the 2D graphite lattice, where $\vec{a}_1$ and $\vec{a}_2$ are the primitive vectors. In the cartesian system, the primitive vectors are written as [12]:

$$\vec{a}_1 = \frac{a}{2}\left(\sqrt{3}\,\hat{x} + \hat{y}\right) \text{ , and} \tag{2.1}$$

$$\vec{a}_2 = \frac{a}{2}\left(-\sqrt{3}\,\hat{x} + \hat{y}\right) \text{ ,} \tag{2.2}$$

where a is the lattice parameter. Although the lattice parameter of the 2D graphite lattice has not been measured yet, its value has been considered the same as the in plane lattice parameter of the 3D graphite lattice, which is $a = 2.46\,\text{Å}$ [1].

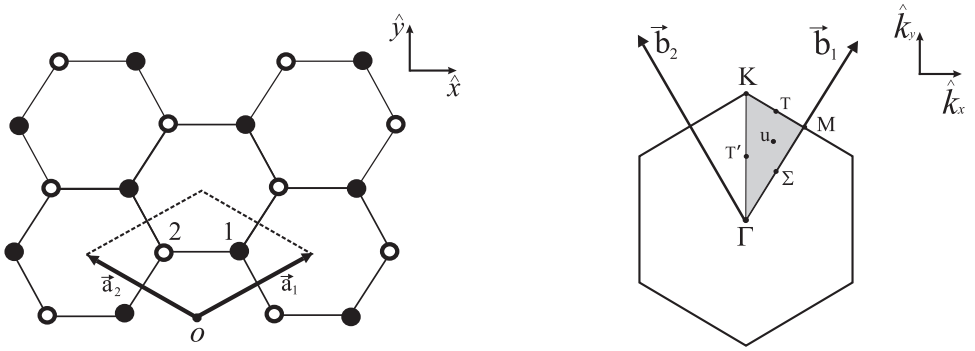

(a) **(b)**

Figure 2.1: **(a)**: 2D graphite lattice. **(b)**: First Brillouin zone of the 2D graphite lattice.

The solid lines in Figure 2.1(a) connect the two distinct groups of equivalent atoms (solid and open circles respectively), and the dashed lines delimit the unit cell which is formed by two inequivalent carbon atoms, denoted **1** and **2**. In the cartesian system, the coordinates of the atoms **1** and **2**, respectively, are [12]:

$$\vec{w}_1 = \frac{a}{2\sqrt{3}}\,\hat{x} + \frac{a}{2}\,\hat{y}\ , \text{ and} \tag{2.3}$$

$$\vec{w}_2 = -\frac{a}{2\sqrt{3}}\,\hat{x} + \frac{a}{2}\,\hat{y}\ , \tag{2.4}$$

where the origin of the vectors $\vec{w}_1$ and $\vec{w}_2$ is centered at the O point in Figure 2.1(a).

Figure 2.1(b) shows the first Brillouin zone of the 2D graphite. The symbols indicate the symmetry lines and points. The primitive vectors of the reciprocal lattice, $\vec{b}_1$ and $\vec{b}_2$, can be obtained evaluating the relation:

$$\vec{a}_i.\vec{b}_j = 2\pi\delta_{ij}\ , \tag{2.5}$$

where $i, j = 1, 2$ label the primitive vectors of the direct and reciprocal lattices, respectively, and δ_{ij} is a Kronecker delta. Therefore, by applying equation 2.5 for the primitive vectors given in equations 2.1 and 2.2 we obtain:

$$\vec{b}_1 = \frac{2\pi}{a}\left(\frac{\sqrt{3}}{3}\,\hat{k}_x + \hat{k}_y\right) \text{ , and} \tag{2.6}$$

$$\vec{b}_2 = \frac{2\pi}{a}\left(-\frac{\sqrt{3}}{3}\,\hat{k}_x + \hat{k}_y\right) \text{ .} \tag{2.7}$$

Table 2.1 shows the coordinates of inequivalent points inside of the first Brillouin zone of 2D graphite.

Table 2.1: Coordinates of inequivalent points inside of the first Brillouin zone of 2D graphite.

Point	Coordinate
Γ	$(0, 0, 0)$
Σ	$\left(\frac{h}{a}, 0, 0\right) \quad ; \quad 0 < h < \frac{2\pi}{\sqrt{3}}$
M	$\left(\frac{2\pi}{\sqrt{3}a}, 0, 0\right)$
T'	$\left(\frac{2\pi}{\sqrt{3}a}, \frac{m}{a}, 0\right) \quad ; \quad 0 < m < \frac{2\pi}{3}$
K	$\left(0, \frac{4\pi}{3a}, 0\right)$
T	$\left(0, \frac{v}{a}, 0\right) \quad ; \quad 0 < v < \frac{4\pi}{3}$
u	$\left(\frac{h}{a}, \frac{m}{a}, 0\right)$

2.1.2 Phonons in 2D graphite

In this section, the symmetry properties of the lattice vibrations for all points in the first Brillouin zone of 2D graphite will be presented. The procedures necessary to obtain the results presented in this section are detailed in Appendix A, where the group theory for 2D graphite is developed.

As discussed before, there are two atoms in the 2D graphite unit cell [see Figure 2.1(a)]. Therefore, the phonon dispersion diagram for 2D graphite is composed of three acoustic branches and three optic branches. The lattice vibration representation at the Γ point can be decomposed in the irreducible representations of the $P6/mmm$ group as follows (see Table A.3 in Appendix A):

$$\Gamma^{LV} = \Gamma_4^+ \oplus \Gamma_6^+ \oplus \Gamma_2^- \oplus \Gamma_5^- \text{ .} \tag{2.8}$$

These irreducible representations can be separated in two distinct groups. The lattice vibration representation of the acoustic modes

$$\Gamma^{LV}_{\text{acoustic}} = \Gamma^{-}_{2} \oplus \Gamma^{-}_{5} \ , \tag{2.9}$$

and the lattice vibration representation of the optic modes

$$\Gamma^{LV}_{\text{optic}} = \Gamma^{+}_{4} \oplus \Gamma^{+}_{6} \ . \tag{2.10}$$

Among the two irreducible representations of the optic modes, one is Raman active (Γ^{+}_{6}), and one is silent (Γ^{+}_{4}). The information above is depicted in Table 2.2.

Figure 2.2 shows the phonon dispersion curves for the high symmetry points and lines in the first Brillouin zone of 2D graphite, obtained by ab initio calculations [13]. Table 2.2 shows the symmetry assignment of the normal modes at the Γ point for each branch of the phonon dispersion curve depicted in Figure 2.2. The last two columns of Table 2.2 show the phonon eigenvectors associated with each normal mode of vibration at the Γ point.

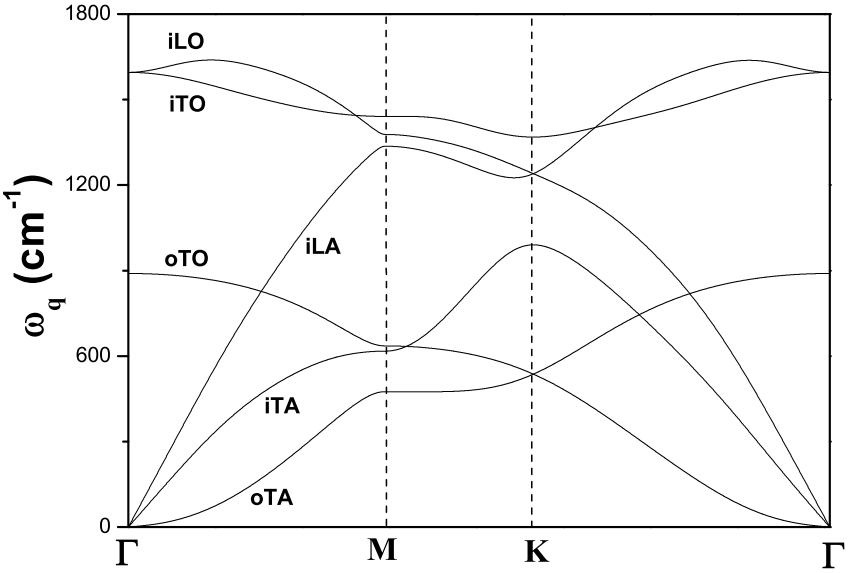

Figure 2.2: Phonon dispersion curves of 2D graphite for the high symmetry points and lines in the first Brillouin zone (data provided by Ge. G. Samsomidze).

Table 2.3 shows the irreducible representations associated with the lattice vibrations for all

Table 2.2: Lattice vibrations at Γ point.

Mode	Mode	ω_Γ (cm^{-1})	Branch	Type	Direction	Basis Function	Optical Status	**1**	**2**
$\Gamma_5^{-(x)}$	$E_{1u}^{(x)}$	0	iLA	acoustic	in plane (x)	x		$(1,0,0)$	$(1,0,0)$
$\Gamma_5^{-(y)}$	$E_{1u}^{(y)}$	0	iTA	acoustic	in plane (y)	y		$(0,1,0)$	$(0,1,0)$
Γ_2^-	A_{2u}	0	oTA	acoustic	out of plane	z		$(0,0,1)$	$(0,0,1)$
$\Gamma_6^{+(x)}$	$E_{2g}^{(x)}$	1580	iLO	optic	in plane (x)	(x^2-y^2, xy)	Raman	$(1,0,0)$	$(-1,0,0)$
$\Gamma_6^{+(y)}$	$E_{2g}^{(y)}$	1580	iTO	optic	in plane (y)	(x^2-y^2, xy)	Raman	$(0,1,0)$	$(0,-1,0)$
Γ_4^+	B_{2g}	890	oTO	optic	out of plane		silent	$(0,0,1)$	$(0,0,-1)$

points in the first Brillouin zone of 2D graphite (see Tables A.3 to A.8, and also the details to obtain the lattice vibration representations for points inside the first Brillouin zone in Appendix A.) Table 2.4 shows the correlation between the irreducible representations of the phonon branches along all points and lines in the first Brillouin zone of 2D graphite. Such correlation was made by following the compatibility relations obtained from Tables A.3 to A.8 in Appendix A.

Table 2.3: Irreducible representations associated with the lattice vibrations for all points in the first Brillouin zone of 2D graphite.

point	Γ^{LV}
Γ	$\Gamma_4^+ \oplus \Gamma_6^+ \oplus \Gamma_2^- \oplus \Gamma_5^-$
K	$K_1 \oplus K_2 \oplus K_3 \oplus K_6$
M	$M_1^+ \oplus M_2^+ \oplus M_3^+ \oplus M_2^- \oplus M_3^- \oplus M_4^-$
Σ	$2\Sigma_1 \oplus 2\Sigma_3 \oplus 2\Sigma_4$
T (**T**′)	$2T_1 \oplus T_2 \oplus 2T_3 \oplus T_4$
u	$4u^+ \oplus 2u^-$

2.1.3 π electrons in 2D graphite

In the ground state, the carbon atom presents the electronic configuration $1s^2 2s^2 2p^2$. The most internal electrons 1s are the core electrons, with energy $-270\,eV$. The four electrons remaining are the valence electrons. The energies of the 2s and 2p levels are $-13\,eV$ and $-5\,eV$, respectively, relative to the Fermi level.

Table 2.4: Symmetry of the phonon branches along all points and lines in the first Brillouin zone of 2D graphite.

Branch	Γ	Σ	**M**	**T′**	**K**	**T**	**u**
iLA	Γ_5^+	Σ_1	M_3^-	T_1'	K_3	T_1	u^+
iTA	Γ_5^+	Σ_3	M_4^-	T_3'	K_2	T_3	u^+
oTA	Γ_2^-	Σ_4	M_2^-	T_4'	K_6	T_4	u^-
iLO	Γ_6	Σ_3	M_2^+	T_3'	K_3	T_3	u^+
iTO	Γ_6	Σ_1	M_1^+	T_1'	K_1	T_1	u^+
oTO	Γ_4^+	Σ_4	M_3^+	T_2'	K_6	T_2	u^-

The natural carbon solid can be found in nature in two basic allotropic forms: graphite and diamond. The bonds between the atoms are different for these two forms. In diamond, the atomic bonds are provided by the hybridization sp^3 of the atomic orbitals (four bonds forming an angle of 109.5° with each other). In graphite, the hybridization sp^2 of the atomic orbitals form a sheet of carbon atoms bonded by covalent forces forming an angle of 120° with each other.

The 2s electrons have a wave function with spherical symmetry ψ_{2s}. The 2p electrons have the eigenfunctions $\psi_{2p}^{(x)}$, $\psi_{2p}^{(y)}$ and $\psi_{2p}^{(z)}$. In the sp^2 hybridization, the eigenfunctions ψ_{2s}, $\psi_{2p}^{(x)}$, and $\psi_{2p}^{(y)}$ are hybridized and form three bonds with the neighboring atoms by the σ orbitals (see Figure 2.3). The fourth wavefunction $\psi_{2p}^{(z)}$ will generate the π non-hybrid orbitals [14].

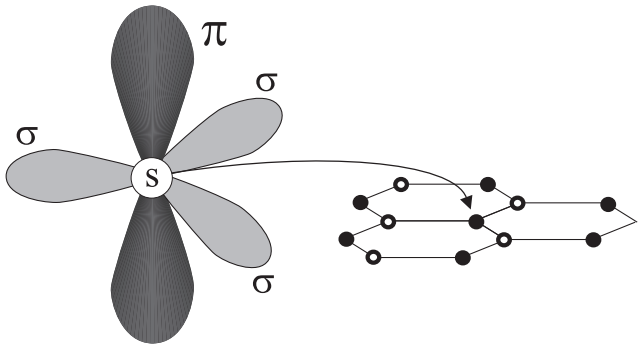

Figure 2.3: Electronic orbitals in 2D graphite.

Since there are two atoms in the 2D graphite unit cell, the band diagram for π electrons is composed of the valence and conduction bands, π and π^*, respectively. An analytical

expression for the dispersion curves of π electrons in 2D graphite can be obtained by the first neighbor tight-binding method, and the result is [2]:

$$E(\vec{k}) = \frac{\pm\gamma_0 W(\vec{k})}{1 \mp s W(\vec{k})} \ , \tag{2.11}$$

where,

$$W(\vec{k}) = \sqrt{1 + 4\cos\left(\frac{\sqrt{3}}{2}k_x a\right)\cos\left(\frac{1}{2}k_y a\right) + 4\cos^2\left(\frac{1}{2}k_y a\right)} \ . \tag{2.12}$$

The tight-binding parameters γ_0 and s are the transfer and overlap integrals, respectively. Their values can be obtained by first principles calculations, and the results are $\gamma_0 = 3.033\,\text{eV}$, and $s = 0.129$ [2].

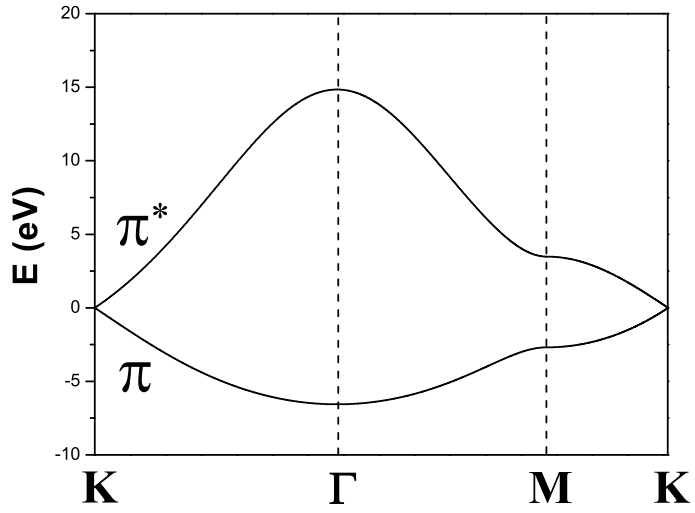

Figure 2.4: π electron dispersion curves for the high symmetry points and lines of the first Brillouin zone of 2D graphite, obtained by evaluating equation 2.11.

Figure 2.4 shows the π electron dispersion curves for the high symmetry points and lines in the first Brillouin zone of 2D graphite, obtained by evaluating equation 2.11. The upper curve refers to the energy dispersion of the conduction electrons (π^*), and the lower curve refers to the energy dispersion of the valence electrons (π). We can observe in Figure 2.4 that the dispersion curves touch each other only at the **K** (and **K′**) point. There are two π electrons per unit cell, and these two electrons fulfill the valence band. The density of states at the Fermi level is null (at $\text{T} = 0\,\text{K}$), and the π^* band is empty. This configuration gives to 2D graphite a zero gap semiconductor character [2].

For points sufficiently near the **K** point, the $W(\vec{k})$ has a linear dependence in k, where k is measured from the **K** point, which can be written as [2]:

$$W(k) = \frac{\sqrt{3}}{2}\, ka + ... \quad ; \quad ka \ll 1 \ . \tag{2.13}$$

By inserting the expansion 2.13 in equation 2.11, and taking the parameter $s = 0$, we obtain:

$$E(k) = \pm \frac{\sqrt{3}}{2}\, \gamma_0 a\, k \ . \tag{2.14}$$

An alternative way of writing equation 2.14 is obtained by defining the Fermi velocity as $v_F = \sqrt{3}\gamma_0 a/2\hbar$, where $\hbar$ is given in eV·s units ($\hbar = 6.58 \times 10^{-16}$ eV·s). Then we have:

$$E(k) = \pm \hbar\, v_F\, k \ , \tag{2.15}$$

with $v_F \sim 9.8 \times 10^{15}$ Å/s. Equation 2.14 is very useful for the study of optical phenomena in graphite, since the optical transitions occur near the **K** point.

Table 2.5 shows the π electrons irreducible representations for all points in the first Brillouin zone of 2D graphite. Table 2.6 shows the symmetry of the π electron bands inside the first Brillouin zone of 2D graphite. The assignment at the Γ point was made according to reference [15]. The symmetries of the other points and lines were determined by following the compatibility relations obtained from Tables A.3 to A.8 (Appendix A).

Table 2.5: π electrons irreducible representations for all points in the first Brillouin zone of 2D graphite.

point	Γ^{π}
Γ	$\Gamma_4^+ \oplus \Gamma_2^-$
K	K_6
M	$M_3^+ \oplus M_2^-$
Σ	$2\Sigma_4$
T (**T**′)	$T_2 \oplus T_4$
u	$2u^-$

Table 2.6: Symmetry of the π electron bands inside the first Brillouin zone of 2D graphite.

Band	Γ	Σ	**M**	**T′**	**K**	**T**	**u**
π^*	Γ_4^+	Σ_4	M_3^+	T_2'	K_6	T_2	u^-
π	Γ_2^-	Σ_4	M_2^-	T_4'	K_6	T_4	u^-

2.2 3D Graphite

2.2.1 Symmetry of the 3D Graphite lattice

The three-dimensional (3D) crystalline graphite (or bulk graphite) is formed by a stacking of graphene sheets. The sheets are weakly bonded to each other by van der Waals interactions [1]. The stacking is called by $ABABAB...$, where A and B refer to two families of planes shifted to each other [see Figure 2.5(a)]. The 3D graphite belongs the space group number D_{6h}^4 in accordance with the Schoenflies notation, or $P6_3/mmc$ in the Hermann-Mauguin notation [12].

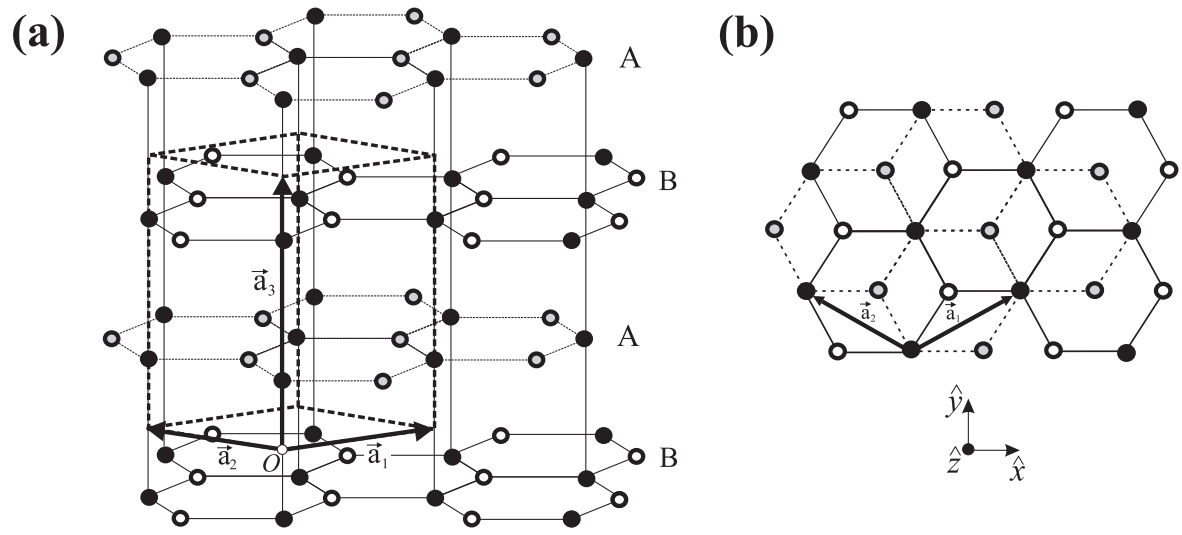

Figure 2.5: **(a)**: 3D graphite lattice. **(b)**: Top view of the 3D graphite lattice.

Figure 2.5(a) shows the 3D graphite lattice, where $\vec{a}_1$, $\vec{a}_2$, and $\vec{a}_3$ are the primitive vectors. The vectors $\vec{a}_1$ and $\vec{a}_2$ are equivalent in modulus, the lattice parameter measuring $a = 2.46$ Å [1]. The $\vec{a}_3$ vector has modulus $c = 6.71$ Å [1]. In the cartesian system [Figure

2.5(a)], the primitive vectors are written as [12]:

$$\vec{a}_1 = \frac{a}{2}\left(\sqrt{3}\,\hat{x} + \hat{y}\right) \ , \tag{2.16}$$

$$\vec{a}_2 = \frac{a}{2}\left(-\sqrt{3}\,\hat{x} + \hat{y}\right) \ , \tag{2.17}$$

$$\vec{a}_3 = c\,\hat{z} \ . \tag{2.18}$$

Figure 2.5(b) shows the top view of the 3D graphite lattice. The solid lines connect two inequivalent groups of atoms (solid and open circles, respectively) belonging to the A planes. The dashed lines connect two inequivalent groups of atoms (dark and gray circles respectively) belonging to the B planes.

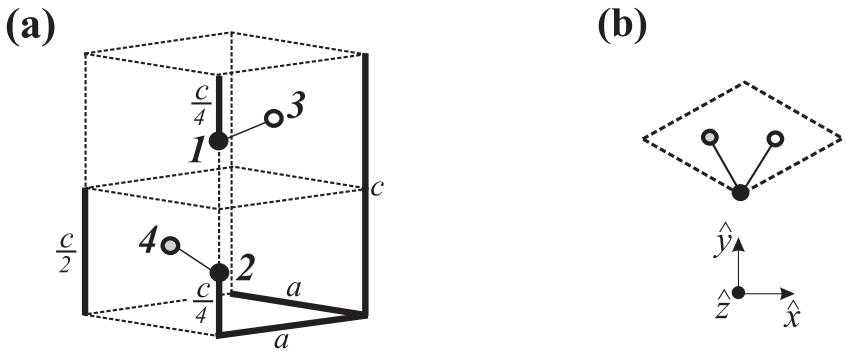

Figure 2.6: **(a)**: Unit cell of the 3D graphite lattice, which is formed by four inequivalent carbon atoms denoted by **1**, **2**, **3**, and **4** respectively. **(b)**: Top view of the unit cell of the 3D graphite lattice.

Figure 2.6(a) shows the unit cell of the 3D graphite lattice, which is formed by four inequivalent carbon atoms denoted as **1**, **2**, **3**, and **4**, respectively. Observe that atoms **1** and **3** correspond to the dark and white atoms forming the A planes in Figure 2.5, respectively, and atoms **2** and **4** correspond to the dark and gray atoms forming the B plane in Figure 2.5, respectively. In the cartesian system, the coordinates of the **1**, **2**, **3**, and **4** atoms are written, respectively, as [12]:

$$\vec{w}_1 = \frac{3c}{4}\,\hat{z} \ , \tag{2.19}$$

$$\vec{w}_2 = \frac{c}{4}\,\hat{z} \ , \tag{2.20}$$

$$\vec{w}_3 = \frac{a}{2\sqrt{3}}\,\hat{x} + \frac{a}{2}\,\hat{y} + \frac{3c}{4}\,\hat{z} \ , \tag{2.21}$$

$$\vec{w}_4 = -\frac{a}{2\sqrt{3}}\,\hat{x} + \frac{a}{2}\,\hat{y} + \frac{c}{4}\,\hat{z} \ , \tag{2.22}$$

where the origin of the vectors $\vec{w}_1$, $\vec{w}_2$, $\vec{w}_3$, and $\vec{w}_4$ is centered at the O point in Figure 2.5(a). Figure 2.6(b) shows the top view of the unit cell of the 3D graphite lattice, for reference.

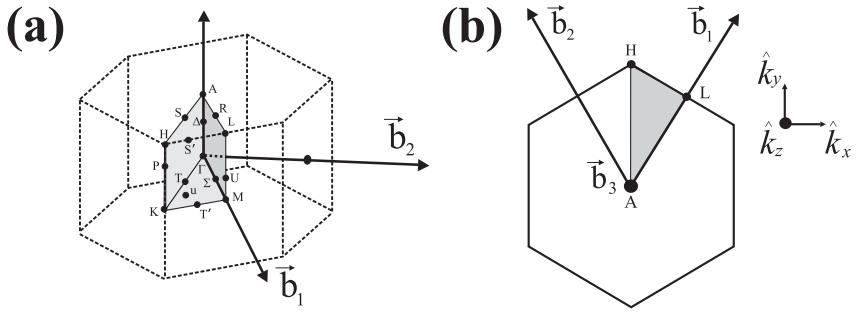

Figure 2.7: **(a)**: First Brillouin zone of the 3D graphite lattice. **(b)**: Top view of the first Brillouin zone of the 3D graphite, with the reciprocal vectors.

Figure 2.7(a) shows the first Brillouin zone of the 3D graphite lattice. The symbols indicate all the symmetry planes, lines and points. The primitive vectors of the reciprocal lattice $\vec{b}_1$, $\vec{b}_2$, and $\vec{b}_3$ can be obtained by evaluating equation 2.5, and using the relations 2.16, 2.17, and 2.18. The results are:

$$\vec{b}_1 = \frac{2\pi}{a}\left(\frac{\sqrt{3}}{3}\,\hat{k}_x + \hat{k}_y\right) \ , \tag{2.23}$$

$$\vec{b}_2 = \frac{2\pi}{a}\left(-\frac{\sqrt{3}}{3}\,\hat{k}_x + \hat{k}_y\right) \ , \tag{2.24}$$

$$\vec{b}_3 = \frac{2\pi}{c}\,\hat{k}_z \ . \tag{2.25}$$

Figure 2.7(b) shows the top view of the first Brillouin zone of the 3D graphite, with the respective reciprocal vectors, for reference. Table 2.7 shows the coordinates of inequivalent points inside the first Brillouin zone of 3D graphite.

2.2.2 Phonons in 3D graphite

We will present here the symmetry of the lattice vibrations for the points belonging to the central horizontal plane (ΓKM) in the first Brillouin zone of 3D graphite. As shown in Figure 2.6, there are four atoms in the 3D graphite unit cell. Therefore, the phonon dispersion diagram for 3D graphite is composed of three acoustic branches and nine optic

Table 2.7: Coordinates of inequivalent points inside the first Brillouin zone of 3D graphite.

Point	Coordinate	Point	Coordinate
Γ	$(\,0\,,\,0\,,\,0\,)$	S'	$\left(\,\frac{2\pi}{\sqrt{3}a}\,,\,\frac{m}{a}\,,\,\frac{\pi}{c}\,\right)$
Σ	$\left(\,\frac{h}{a}\,,\,0\,,\,0\,\right) \quad ; \quad 0 < h < \frac{2\pi}{\sqrt{3}}$	H	$\left(\,0\,,\,\frac{4\pi}{3a}\,,\,\frac{\pi}{c}\,\right)$
M	$\left(\,\frac{2\pi}{\sqrt{3}a}\,,\,0\,,\,0\,\right)$	S	$\left(\,0\,,\,\frac{v}{a}\,,\,\frac{\pi}{c}\,\right)$
T'	$\left(\,\frac{2\pi}{\sqrt{3}a}\,,\,\frac{m}{a}\,,\,0\,\right) \quad ; \quad 0 < m < \frac{2\pi}{3}$	Δ	$\left(\,0\,,\,0\,,\,\frac{2p}{c}\,\right) \quad ; \quad 0 < p < \frac{\pi}{2}$
K	$\left(\,0\,,\,\frac{4\pi}{3a}\,,\,0\,\right)$	U	$\left(\,\frac{2\pi}{\sqrt{3}a}\,,\,0\,,\,\frac{2p}{c}\,\right)$
T	$\left(\,0\,,\,\frac{v}{a}\,,0\,\right) \quad ; \quad 0 < v < \frac{4\pi}{3}$	P	$\left(\,0\,,\,\frac{4\pi}{3a}\,,\,\frac{2p}{c}\,\right)$
A	$\left(\,0\,,\,0\,,\,\frac{\pi}{c}\,\right)$	u	$\left(\,\frac{h}{a}\,,\,\frac{m}{a}\,,\,0\,\right)$
R	$\left(\,\frac{h}{a}\hat{}\,,\,0\,,\,\frac{\pi}{c}\,\right)$	u'	$\left(\,\frac{h}{a}\,,\,\frac{m}{a}\,,\,\frac{\pi}{c}\,\right)$
L	$\left(\,\frac{2\pi}{\sqrt{3}a}\,,\,0\,,\,\frac{\pi}{c}\,\right)$	g	$\left(\,\frac{h}{a}\,,\,\frac{m}{a}\,,\,\frac{2p}{c}\,\right)$

branches. The lattice vibration (LV) representation at the Γ point can be decomposed in the irreducible representations of the $P6_3/mmc$ group, as follows (see Table A.13 in Appendix A:

$$\Gamma^{LV} = 2\Gamma_4^+ \oplus 2\Gamma_6^+ \oplus 2\Gamma_2^- \oplus 2\Gamma_5^- \ . \tag{2.26}$$

The lattice vibration representations of the acoustic modes are

$$\Gamma^{LV}_{\text{acoustic}} = \Gamma_2^- \oplus \Gamma_5^- \ , \tag{2.27}$$

and the lattice vibration representations of the optic modes are

$$\Gamma^{LV}_{\text{optic}} = 2\Gamma_4^+ \oplus 2\Gamma_6^+ \oplus \Gamma_2^- \oplus \Gamma_5^- \ . \tag{2.28}$$

Two of the four irreducible representations of the optic modes are Raman active ($2\Gamma_6^+$), two are infrared active (Γ_2^- and Γ_5^-), and two are silent ($2\Gamma_4^+$) (see Table 2.8).

Figure 2.8 shows the phonon dispersion curves for the high symmetry points and lines belonging to the central horizontal plane in the first Brillouin zone of 3D graphite, obtained by ab-initio calculations [16]. Table 2.8 presents the symmetry of the normal modes at the Γ point for each branch of the phonon dispersion curve depicted in Figure 2.8. The assignment is based on reference [17].

The last four columns of Table 2.8 show the phonons eigenvectors associated with each normal mode of vibration at the Γ point (see also Appendix A). Figure 2.9 shows the

normal modes of vibrations (phonon eigenvectors) at the Γ point listed in Table 2.8, for the four atoms inside of the unit cell of 3D graphite.

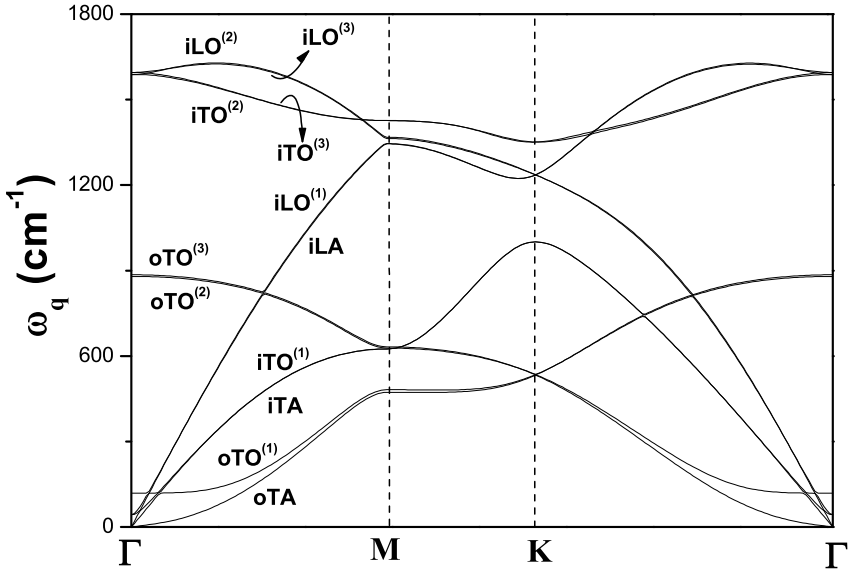

Figure 2.8: Phonon dispersion curves of 3D graphite for the points belonging to the central horizontal plane in the first Brillouin zone, obtained by ab-initio calculations in reference [16].

Table 2.8: Lattice vibrations at the Γ point.

Mode	Mode	ω_Γ (cm^{-1})	Branch	Type	Direction	Basis Function	Optical Status	**1**	**2**	**3**	**4**
$\Gamma_{5_1}^{-(x)}$	$E_{1u_1}^{(x)}$	0	iLA	acoustic	in plane (x)	x		$(1,0,0)$	$(1,0,0)$	$(1,0,0)$	$(1,0,0)$
$\Gamma_{5_1}^{-(y)}$	$E_{1u_1}^{(y)}$	0	iTA	acoustic	in plane (y)	y		$(0,1,0)$	$(0,1,0)$	$(0,1,0)$	$(0,1,0)$
$\Gamma_{2_1}^{-}$	A_{2u_1}	0	oTA	acoustic	out of plane	z		$(0,0,1)$	$(0,0,1)$	$(0,0,1)$	$(0,0,1)$
$\Gamma_{6_1}^{+(x)}$	$E_{2g_1}^{(x)}$	42	iLO$^{(1)}$	optic	in plane (x)	(x^2-y^2, xy)	Raman	$(1,0,0)$	$(-1,0,0)$	$(1,0,0)$	$(-1,0,0)$
$\Gamma_{6_1}^{+(y)}$	$E_{2g_1}^{(y)}$	42	iTO$^{(1)}$	optic	in plane (y)	(x^2-y^2, xy)	Raman	$(0,1,0)$	$(0,-1,0)$	$(0,1,0)$	$(0,-1,0)$
$\Gamma_{4_1}^{+}$	B_{2g_2}	118	oTO$^{(1)}$	optic	out of plane		silent	$(0,0,1)$	$(0,0,-1)$	$(0,0,-1)$	$(0,0,1)$
$\Gamma_{2_2}^{-}$	A_{2u_2}	879	oTO$^{(2)}$	optic	out of plane	z	infrared	$(0,0,1)$	$(0,0,1)$	$(0,0,-1)$	$(0,0,-1)$
$\Gamma_{4_2}^{+}$	B_{2g_1}	885	oTO$^{(3)}$	optic	out of plane		silent	$(0,0,1)$	$(0,0,-1)$	$(0,0,1)$	$(0,0,-1)$
$\Gamma_{6_2}^{+(x)}$	$E_{2g_2}^{(x)}$	1588	iLO$^{(2)}$	optic	in plane (x)	(x^2-y^2, xy)	Raman	$(1,0,0)$	$(-1,0,0)$	$(-1,0,0)$	$(1,0,0)$
$\Gamma_{6_2}^{+(y)}$	$E_{2g_2}^{(y)}$	1588	iTO$^{(2)}$	optic	in plane (y)	(x^2-y^2, xy)	Raman	$(0,1,0)$	$(0,-1,0)$	$(0,-1,0)$	$(0,1,0)$
$\Gamma_{5_2}^{-(x)}$	$E_{1u_2}^{(x)}$	1595	iLO$^{(3)}$	optic	in plane (x)	x	infrared	$(1,0,0)$	$(1,0,0)$	$(-1,0,0)$	$(-1,0,0)$
$\Gamma_{5_2}^{-(y)}$	$E_{1u_2}^{(y)}$	1595	iTO$^{(3)}$	optic	in plane (y)	y	infrared	$(0,1,0)$	$(0,1,0)$	$(0,-1,0)$	$(0,-1,0)$

Table 2.9 shows the lattice vibration irreducible representations for all points belonging to the central horizontal plane of the first Brillouin zone of 3D graphite (see also Tables

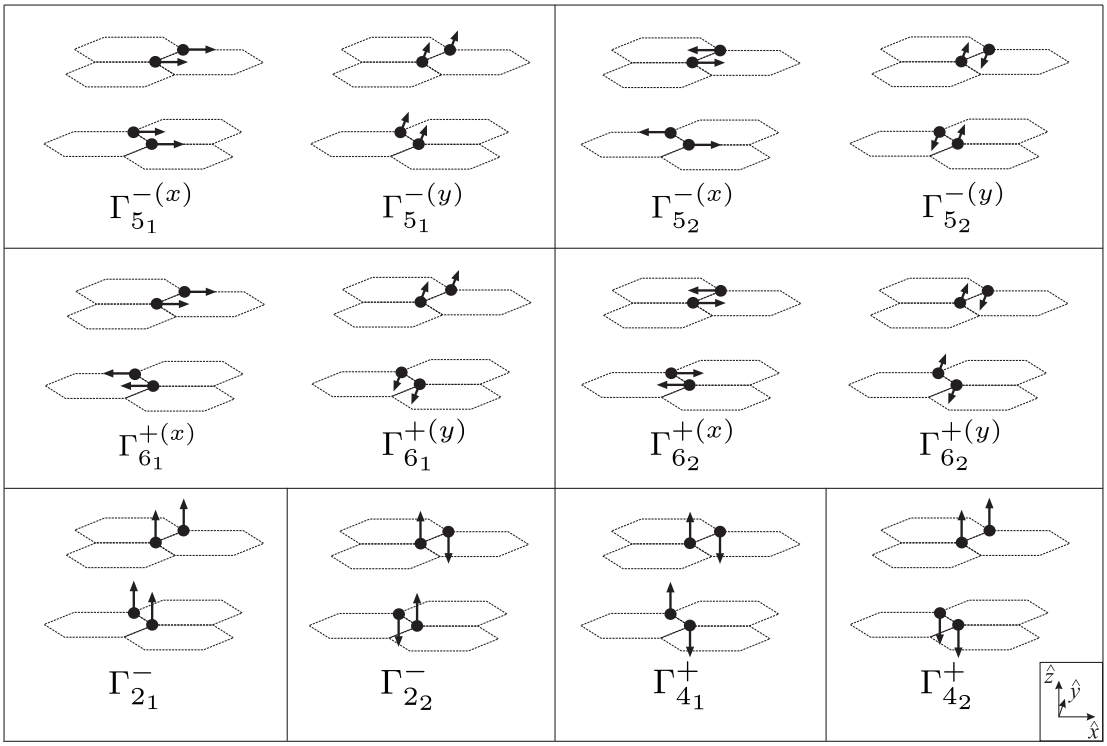

Figure 2.9: Normal mode vibrations (phonon eigenvectors) at the Γ point for the four atoms inside of the unit cell of 3D graphite listed in Table 2.8.

A.13 to A.18 in Appendix A.) Table 2.10 shows the symmetry of the phonon branches along all points and lines belonging to the ΓKM plane in the first Brillouin zone of 3D graphite. This table was made by following the compatibility relations obtained from Tables A.13 to A.18 in Appendix A.

Table 2.9: Lattice vibration irreducible representations for all points and lines belonging to the ΓKM plane in the first Brillouin zone of 3D graphite.

point	Γ^{LV}
Γ	$2\Gamma_4^+ \oplus 2\Gamma_6^+ \oplus 2\Gamma_2^- \oplus 2\Gamma_5^-$
K	$K_1 \oplus K_2 \oplus 3K_3 \oplus K_4 \oplus K_5 \oplus K_6$
M	$2M_1^+ \oplus 2M_2^+ \oplus 2M_3^+ \oplus 2M_2^- \oplus 2M_3^- \oplus 2M_4^-$
Σ	$4\Sigma_1 \oplus 4\Sigma_3 \oplus 4\Sigma_4$
T (**T**′)	$4T_1 \oplus 2T_2 \oplus 4T_3 \oplus 2T_4$
u	$8u^+ \oplus 4u^-$

Table 2.10: Symmetry of the phonon branches along all points and lines belonging to the ΓKM plane in the first Brillouin zone of 3D graphite.

Branch	Γ	Σ	**M**	**T′**	**K**	**T**	**u**
iLA	$\Gamma_{5_1}^+$	Σ_1	M_3^-	T_1'	K_{3_2}	T_1	u^+
iTA	$\Gamma_{5_1}^+$	Σ_3	M_4^-	T_3'	K_{3_1}	T_3	u^+
oTA	Γ_2^-	Σ_4	M_2^-	T_4'	K_5	T_4	u^-
iLO$^{(1)}$	$\Gamma_{6_1}^+$	Σ_3	M_2^+	T_3'	K_{3_2}	T_3	u^+
iTO$^{(1)}$	$\Gamma_{6_1}^+$	Σ_1	M_1^+	T_1'	K_{3_1}	T_1	u^+
oTO$^{(1)}$	Γ_4^+	Σ_4	M_3^+	T_2'	K_6	T_2	u^-
oTO$^{(2)}$	Γ_2^-	Σ_4	M_2^-	T_4'	K_6	T_4	u^-
oTO$^{(3)}$	Γ_4^+	Σ_4	M_3^+	T_2'	K_4	T_2	u^-
iLO$^{(2)}$	$\Gamma_{6_2}^+$	Σ_3	M_2^+	T_3'	K_{3_2}	T_3	u^+
iTO$^{(2)}$	$\Gamma_{6_2}^+$	Σ_1	M_1^+	T_1'	K_1	T_1	u^+
iLO$^{(3)}$	$\Gamma_{5_2}^-$	Σ_1	M_3^-	T_1'	K_{3_2}	T_1	u^+
iTO$^{(3)}$	$\Gamma_{5_2}^-$	Σ_3	M_4^-	T_3'	K_2	T_3	u^+

2.2.3 π electrons in 3D graphite

The band diagram for π electrons is composed of four branches: two valence branches (π_A and π_B), and two conduction branches (π_A^* and π_B^*). Figure 2.10 shows the π electron dispersion curves for the high symmetry points and lines belonging to the ΓKM plane in the first Brillouin zone of 3D graphite, obtained by the Fourier expansion model [18].

Table 2.11 shows the π electrons irreducible representations for all points belonging to the ΓKM plane in the first Brillouin zone of 3D graphite (see also Tables A.13 to A.18 in Appendix A). Table 2.12 shows the symmetries of the π electrons along all points and lines belonging to the ΓKM plane. The assignments at the Γ point was made according to reference [15]. The correlation was made by following the compatibility relations obtained from Tables A.13 to A.18 in Appendix A.

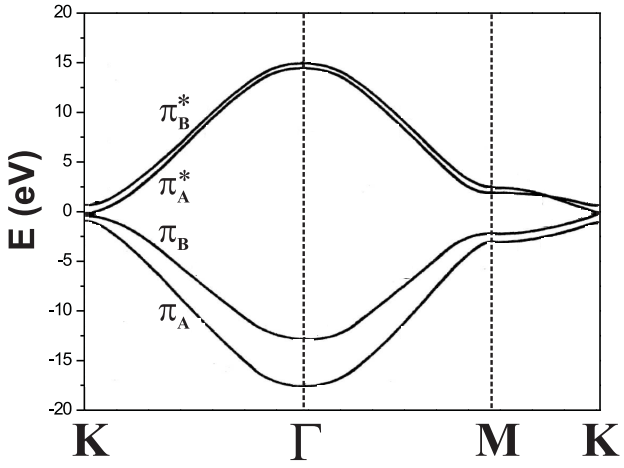

Figure 2.10: the π electron dispersion curves for the high symmetry points and lines belonging to the ΓKM plane in the first Brillouin zone of 3D graphite, obtained by the Fourier expansion model [18].

Table 2.11: π electron irreducible representations for all points belonging to the central horizontal plane in the first Brillouin zone of 3D graphite.

point	Γ^π
Γ	$2\Gamma_4^+ \oplus 2\Gamma_2^-$
K	$K_4 \oplus K_5 \oplus K_6$
M	$2M_3^+ \oplus 2M_2^-$
Σ	$4\Sigma_4$
T (**T**′)	$2T_2 \oplus 2T_4$
u	$4u^-$

Table 2.12: Correlation of the π electron symmetries along all points and lines belonging to the ΓKM plane in the first Brillouin zone of 3D graphite.

Band	Γ	Σ	**M**	**T**′	**K**	**T**	**u**
$\pi^*_{(B)}$	Γ_2^-	Σ_4	M_2^-	T_4'	K_5	T_4	u^-
$\pi^*_{(A)}$	Γ_4^+	Σ_4	M_3^+	T_2'	K_6	T_2	u^-
$\pi_{(B)}$	Γ_2^-	Σ_4	M_2^-	T_4'	K_6	T_4	u^-
$\pi_{(A)}$	Γ_4^+	Σ_4	M_3^+	T_2'	K_4	T_2	u^-

Chapter 3

Raman Scattering theory

In this chapter we will show the basic concepts of the Raman scattering theory for crystals. The chapter is divided into two parts, in which we show separately both the macroscopic and the microscopic approaches. Although these two parts deal with the same phenomena, they allow us to make different analysis in the Raman spectrum of solids, being complementary to each other in many points, such as intensity analysis and selection rules.

3.1 Macroscopic theory of Raman scattering

The macroscopic theory of the Raman scattering is based on the analysis of the influence of the susceptibilities derivatives of the crystal on the electric field of the scattered light. Therefore, in this section we will study the Raman scattering theory using an electromagnetism approach.

3.1.1 The Stokes and anti-Stokes components of the scattered light

We start our analysis by considering a light scattering experiment in which the incident light is provided by a monochromatic source (such as lasers) with a well defined frequency ω_I and wavevector $\vec{k}_I$. The incident macroscopic electric field at a position $\vec{r}$ and instant of time t is written as [19]:

$$\vec{E}_I(\vec{r},t) = \left[\vec{E}_I\, e^{i(\vec{k}_I\cdot\vec{r}-\omega_I t)} + \vec{E}_I^{\,*}\, e^{-i(\vec{k}_I\cdot\vec{r}-\omega_I t)}\right] \tag{3.1}$$

The excitation of the medium responsible for the light scattering is characterized by a space- and time-dependent amplitude of a vibrational displacement, given as [19]:

$$X(\vec{r},t) = \sum_{\vec{q}} \left[X(\vec{q},t) e^{i\vec{q}\cdot\vec{r}} + X^*(\vec{q},t) e^{-i\vec{q}\cdot\vec{r}} \right] \tag{3.2}$$

The Fourier amplitudes $X(\vec{q},t)$ are random quantities, whose magnitudes fluctuate on a time scale characteristic of the thermal excitation process. The occurrence of a specific value of magnitude is governed by some statistic probability distribution. Writing the amplitudes $X(\vec{q},t)$ in terms of their Fourier transforms in respect to the time [19]:

$$X(\vec{q},t) = \int X(\vec{q},\omega_q) e^{-i\omega_q t} d\omega_q \ . \tag{3.3}$$

The average in frequency of the amplitudes $X(\vec{q},\omega_q)$ over the probability distribution is defined as:

$$\langle X^*(\vec{q},\omega_q)\, X(\vec{q},\omega_q') \rangle \ . \tag{3.4}$$

The amplitudes inside the brackets in equation 3.4 are independent random variables, whose phases take all values between 0 and 2π. Their product, therefore, has a zero average except in the case $\omega' = \omega$ [19]:

$$\langle X^*(\vec{q},\omega_q)\, X(\vec{q},\omega_q') \rangle = \langle X^*(\vec{q})\, X(\vec{q}) \rangle_{\omega_q}\ \delta(\omega_q - \omega_q') \ , \tag{3.5}$$

where $\delta(\omega_q - \omega_q')$ is a Dirac delta function, and $\langle X^*(\vec{q})\, X(\vec{q}) \rangle_{\omega_q}$ is the power spectrum of the fluctuations. Equation 3.5 indicates that we can now consider only one Fourier component in the sum given in equation 3.3 and, consequently, equation 3.2 can be rewritten as:

$$X(\vec{r},t) = \sum_{\vec{q}} \left[X(\vec{q},\omega_q) e^{i(\vec{q}\cdot\vec{r} - \omega_q t)} + X^*(\vec{q},\omega_q) e^{-i(\vec{q}\cdot\vec{r} - \omega_q t)} \right] \ . \tag{3.6}$$

The polarization induced by the incident electric field (equation 3.1) in the absence of any excitations of the scattering medium is given as [19]:

$$\vec{P}(\vec{r},t) = \epsilon_0 \overleftrightarrow{\chi}\ (\omega_I) \vec{E}_I(\vec{r},t) \ , \tag{3.7}$$

where $\overleftrightarrow{\chi}\ (\omega_I)$ is the first order susceptibility tensor of the scattering medium at the frequency ω_I. The effect of the excitations is to modulate the wavefunctions and energy levels of the medium. The changes in these quantities are linear in $X(\vec{r},t)$ to the first order perturbation theory, and their effect is represented macroscopically by an additional contribution to the susceptibility. Since the amplitudes $X(\vec{q},\omega_q)$ are very small if compared with the lattice parameters, the susceptibility can be expanded in a Taylor series

as:

$$\overleftrightarrow{\chi} = \overleftrightarrow{\chi}_0 + \left(\frac{\partial \overleftrightarrow{\chi}}{\partial X(\vec{q}, \omega_q)} \right)_{X(\vec{q},\omega_q)=0} X(\vec{r}, t) + \mathcal{O}^2 \ , \tag{3.8}$$

or, reducing the notation:

$$\overleftrightarrow{\chi} = \overleftrightarrow{\chi}_0 + \overleftrightarrow{\chi}' \ X(\vec{r}, t) \ , \tag{3.9}$$

where $\overleftrightarrow{\chi}'$ is the second order susceptibility or susceptibility derivative. Now, we can group equations 3.7 and 3.9, in order to obtain the polarization induced by the incident electric field, taking into account the excitations created in the medium:

$$\vec{P}(\vec{r}, t) = \epsilon_0 \left[\overleftrightarrow{\chi}_0 \ \vec{E}_I(\vec{r}, t) + \overleftrightarrow{\chi}' \ X(\vec{r}, t) \vec{E}_I(\vec{r}, t) \right] \ . \tag{3.10}$$

Using equations 3.1 and 3.2, equation 3.10 becomes [19]:

$$\begin{aligned} \vec{P}(\vec{r}, t) = \ & \epsilon_0 \ \overleftrightarrow{\chi}_0 \left[\vec{E}_I \, e^{i(\vec{k}_I \cdot \vec{r} - \omega_I t)} + \vec{E}_I^* \, e^{-i(\vec{k}_I \cdot \vec{r} - \omega_I t)} \right] + \\ & + \epsilon_0 \ \overleftrightarrow{\chi}' \left[X(\vec{q}, \omega_q) \vec{E}_I \, e^{i[(\vec{k}_I + \vec{q}) \cdot \vec{r} - (\omega_I + \omega_q) t]} + X^*(\vec{q}, \omega_q) \vec{E}_I^* \, e^{-i[(\vec{k}_I + \vec{q}) \cdot \vec{r} - (\omega_I + \omega_q) t]} \right] + \\ & + \epsilon_0 \ \overleftrightarrow{\chi}' \left[X^*(\vec{q}, \omega_q) \vec{E}_I \, e^{i[(\vec{k}_I - \vec{q}) \cdot \vec{r} - (\omega_I - \omega_q) t]} + X(\vec{q}, \omega_q) \vec{E}_I^* \, e^{-i[(\vec{k}_I - \vec{q}) \cdot \vec{r} - (\omega_I - \omega_q) t]} \right] \ . \end{aligned} \tag{3.11}$$

Next, we define the terms in equation 3.11 as following:

$$\vec{P}_0(\vec{r}, t) = \epsilon_0 \ \overleftrightarrow{\chi}_0 \left[\vec{E}_I \, e^{i(\vec{k}_I \cdot \vec{r} - \omega_I t)} + \vec{E}_I^* \, e^{-i(\vec{k}_I \cdot \vec{r} - \omega_I t)} \right] \ , \tag{3.12}$$

$$\vec{K}_{AS} = \vec{k}_I + \vec{q} \ , \tag{3.13}$$

$$\omega_{AS} = \omega_I + \omega_q \tag{3.14}$$

$$\vec{P}_{AS}(\vec{K}_{AS}, \omega_{AS}) = \epsilon_0 \ \overleftrightarrow{\chi}' \ X(\vec{q}, \omega_q) \vec{E}_I \ , \tag{3.15}$$

$$\vec{K}_S = \vec{k}_I - \vec{q} \ , \tag{3.16}$$

$$\omega_S = \omega_I - \omega_q \ , \tag{3.17}$$

$$\vec{P}_S(\vec{K}_S, \omega_S) = \epsilon_0 \ \overleftrightarrow{\chi}' \ X^*(\vec{q}, \omega_q) \vec{E}_I \ , \tag{3.18}$$

and equation 3.11 can now be rewritten as:

$$\begin{aligned} \vec{P}(\vec{r}, t) = \ & \vec{P}_0(\vec{r}, t) \\ & + \left[\vec{P}_{AS}(\vec{K}_{AS}, \omega_{AS}) \, e^{i(\vec{K}_{AS} \cdot \vec{r} - \omega_{AS} t)} + \vec{P}_{AS}^*(\vec{K}_{AS}, \omega_{AS}) \, e^{-i(\vec{K}_{AS} \cdot \vec{r} - \omega_{AS} t)} \right] \\ & + \left[\vec{P}_S(\vec{K}_S, \omega_S) \, e^{i(\vec{K}_S \cdot \vec{r} - \omega_S t)} + \vec{P}_S^*(\vec{K}_S, \omega_S) \, e^{-i(\vec{K}_S \cdot \vec{r} - \omega_S t)} \right] \ . \end{aligned} \tag{3.19}$$

The first term on the right-hand side of equation 3.19 gives rise to the elastic scattering, where the scattered and incident light have the same frequency ω_I, and no excitations are induced in the medium. The second term on the right-hand side of equation 3.19 is the anti-Stokes component of the inelastic scattering, where the frequency of the scattered light is larger than the incident light by an amount of ω_q. The third term on the right-hand side of equation 3.19 refers to the Stokes component of the inelastic scattering, where the frequency of the scattered light is lower than the incident light by an amount of ω_q. In fact, equations 3.13 and 3.14 determine the momentum and energy conservation conditions for the anti-Stokes component of the inelastic scattering, while equations 3.16 and 3.17 determine the momentum and energy conservation conditions for the Stokes component of the inelastic scattering (see Figure 3.1).

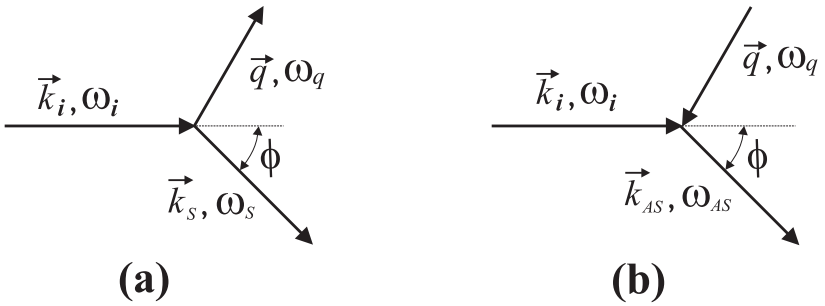

Figure 3.1: Geometry of the wavevectors involved in the Stokes (a) and anti-Stokes (b) inelastic scattering processes, imposed by the momentum conservation conditions given in equations 3.13 and 3.16, respectively.

3.1.2 The cross section

In a Raman experiment, the detection of the Stokes component of the spectrum determines the spectral differential cross section:

$$\frac{d^2\sigma}{d\Omega d\omega_S} \ . \tag{3.20}$$

The spectral differential cross section has the dimensions of area divided by solid angle Ω and frequency ω_S, and it is defined as the rate of the removal of energy from the incident beam as a result of its scattering in a volume v into a solid-angle element $d\Omega$, with a scattered frequency between ω_S and $\omega_S + d\omega_S$ [19]. The cross sectional area of the scattered beam is $A = v/L$, where v is the part of the sample which contributes to the detected scattered light. The rate of energy flow in the scattered beam is $A\overline{I}_S$, where

$\overline{I}_S$ is the cycle-averaged intensity of the incident beam. Each quantum of the scattered light $\hbar\omega_S$ is the result of a process in which the incident beam loses a larger quantum $\hbar\omega_I$. The rate in which the incident beam loses energy is, therefore, larger than the rate in which the scattered beam gains energy by a factor ω_I/ω_S. Then, in accordance with the definition of the spectral differential cross section, we have [19]:

$$\frac{d^2\sigma}{d\Omega d\omega_S} = \frac{v}{L}\frac{\omega_I}{\omega_S}\frac{d^2\overline{I}_S}{d\Omega d\omega_S}\frac{1}{\overline{I}_I} \quad , \tag{3.21}$$

where $\overline{I}_I$ is the cycle-averaged intensity of the incident beam, given as [19]:

$$\overline{I}_I = 2\epsilon_0 c\eta_I \left|\vec{E}_I\right|^2 \quad , \tag{3.22}$$

where η_I is the refractive index of the scattering medium at frequency ω_I. Appendix B gives a detailed description of the procedures necessary to obtain the intensity of the scattered beam, which can be written as:

$$\overline{I}_S = \frac{L}{8\pi^2\epsilon_0 c^3}\int\int \eta_S\omega_S^4\langle\hat{\varepsilon}_S\cdot\vec{P}_S^*(\vec{k}_S)\;\hat{\varepsilon}_S\cdot\vec{P}_S(\vec{k}_S)\rangle_{\omega_S}\,d\omega_S\,d\Omega \quad , \tag{3.23}$$

where η_S is the refractive index of the scattering medium at frequency ω_S, and $\hat{\varepsilon}_S$ is a unit vector parallel to the electric field vector $\vec{E}_S$ of the scattered beam. The insertion of equations 3.22 and 3.23 in equation 3.21 gives [19]:

$$\frac{d^2\sigma}{d\Omega d\omega_S} = \frac{\omega_I\omega_S^3 vV\eta_S\langle\hat{\varepsilon}_S\cdot\vec{P}_S^*(\vec{k}_S)\;\hat{\varepsilon}_S\cdot\vec{P}_S(\vec{k}_S)\rangle_{\omega_S}}{(4\pi\epsilon_0)^2 c^4\eta_I\left|\vec{E}_I\right|^2} \tag{3.24}$$

The most important parts of the differential spectral cross section given in equation 3.24 are the frequency factor $\omega_I\omega_S^3$ and the power spectrum of the polarization fluctuations $\langle\hat{\varepsilon}_S\cdot\vec{P}_S^*(\vec{k}_S)\;\hat{\varepsilon}_S\cdot\vec{P}_S(\vec{k}_S)\rangle_{\omega_S}$, since these quantities determine the strength and shape of the scattered spectrum [19].

Equation 3.18 relating the polarization and excitation amplitudes enables the power spectrum of the polarization fluctuations to be written as:

$$\langle\hat{\varepsilon}_S\cdot\vec{P}_S^*(\vec{k}_S)\;\hat{\varepsilon}_S\cdot\vec{P}_S(\vec{k}_S)\rangle_{\omega_S} = \left|\epsilon_0\,\hat{\varepsilon}_S\cdot\overleftrightarrow{\chi}'\;\vec{E}_I\right|^2\langle X^*(\vec{q})\,X(\vec{q})\rangle_{\omega_q}\;. \tag{3.25}$$

Defining $\vec{E}_i = \hat{\varepsilon}_I|\vec{E}_I|$, where $\hat{\varepsilon}_I$ is a unit vector along the direction of the incident electric field, and introducing equation 3.25 inside 3.24, we have a more explicit shape for the spectral differential cross section:

$$\frac{d^2\sigma}{d\Omega d\omega_S} = \frac{\omega_I\omega_S^3 vV\eta_S\left|\hat{\varepsilon}_S\cdot\overleftrightarrow{\chi}'\;\hat{\varepsilon}_I\right|^2}{\epsilon_0\,(4\pi)^2 c^4\eta_I}\,\langle X^*(\vec{q})\,X(\vec{q})\rangle_{\omega_q}\;. \tag{3.26}$$

The power spectrum of the fluctuations $\langle X^*(\vec{q})\, X(\vec{q})\rangle_{\omega_q}$ is a very important quantity in the light scattering since, as shown in equation 3.26, the cross section for scattering associated with a specific excitation is proportional to its power spectrum [19]. In the semi-classical approach, the power spectrum of the fluctuations for the Stokes component of the scattered light is proportional to the amount $\{n(\omega_q) + 1\}$, where $n(\omega_q)$ is the Bose-Eistein thermal factor given as [19]:

$$n(\omega_q) = \frac{1}{e^{\hbar\omega_q/k_BT} - 1} \ , \tag{3.27}$$

where k_B is the Boltzmann's constant, and T is the sample temperature.

As a final comment, there are two different volumes in the spectral differential cross section 3.26. v is the volume of the sample illuminated by the incident laser beam, while V is the volume of the whole sample. In fact, the volume V is canceled by a factor $1/V$ implicit in the power spectrum $\langle X^*(\vec{q})\, X(\vec{q})\rangle_{\omega_q}$, and it is just an arbitrary normalization volume. The cross section is thus proportional only to the volume v [19].

3.1.3 Selection rules for one-phonon Raman processes

Energy conservation

As we have shown in section 3.1.1, in a Stokes Raman process, the frequency of the scattered light is down-shifted from the frequency of the incident light by an amount equal to the frequency of the excitation (phonon) created in the sample (see equation 3.17). This is a consequence of the energy conservation. In quantum terms, the scattered photon has an associated energy $\hbar\omega_S$ lower than the incident photon energy $\hbar\omega_I$ by an amount which is the energy $\hbar\omega_q$ of the phonon created in the scattering process:

$$\hbar\omega_q = \hbar\omega_I - \hbar\omega_S \ . \tag{3.28}$$

On the other hand, in an anti-Stokes process, the scattered photon has an associated energy $\hbar\omega_S$ higher than the incident photon energy $\hbar\omega_I$ by an amount which is the energy $\hbar\omega_q$ of the phonon annihilated in the scattering process:

$$\hbar\omega_q = \hbar\omega_{AS} - \hbar\omega_I \ . \tag{3.29}$$

Momentum conservation

Equations 3.16 and 3.13 determine the relations between the wavevectors involved in the light scattering experiment. In order to obtain the relations between the momenta of the photons and phonons involved in the scattering process, we can just multiply the wavevectors by $\hbar$ and then equations 3.16 and 3.13 become, respectively:

$$\hbar\vec{k}_S = \hbar\vec{k}_I - \hbar\vec{q}\,, \tag{3.30}$$

$$\hbar\vec{k}_{AS} = \hbar\vec{k}_I + \hbar\vec{q}\,. \tag{3.31}$$

As pointed in section 3.1.1, equations 3.30 and 3.31 determine the selection rules associated with the momentum conservation in the Stokes and anti-Stokes one-phonon Raman processes, respectively. In fact, these relations strongly restrict the wavevectors of phonons involved in the scattering process, making them to be very close to the center of the first Brillouin zone, that is, $q \sim 0$.

To understand this restriction, let us analyze the geometry imposed in figure 3.1(a), where the magnitude of the wavevectors in the Stokes scattering follows the relation [19]:

$$q^2 = k_I^2 + k_S^2 - 2k_I k_S\, cos\phi\ . \tag{3.32}$$

The photon wavevectors are related to their frequencies by:

$$k_I = \frac{\eta_I \omega_I}{c}\ , \tag{3.33}$$

$$k_S = \frac{\eta_S \omega_S}{c}\ . \tag{3.34}$$

The insertion of the relations 3.33 and 3.34 in Equation 3.32 gives:

$$q^2 = \left(\frac{\eta_I \omega_I}{c}\right)^2 + \left(\frac{\eta_S \omega_S}{c}\right)^2 - 2\frac{\eta_S \eta_I \omega_S \omega_I}{c^2}\, cos\phi\ . \tag{3.35}$$

Next, we use the relation $\omega_S = \omega_I - \omega_q$ in order to eliminate the ω_S term in Equation 3.35, which becomes:

$$q^2 = \left(\frac{\eta_I \omega_I}{c}\right)^2 + \left[\frac{\eta_S(\omega_I - \omega_q)}{c}\right]^2 - 2\frac{\eta_S \eta_I (\omega_I - \omega_q)\omega_I}{c^2}\, cos\phi\ . \tag{3.36}$$

The first order phonon spectrum of crystals usually lies in the wavenumber range $0 < \vartheta_q < 3000\,\mathrm{cm}^{-1}$. Raman experiments are usually performed using incident light in the visible range, that is, $15000\,\mathrm{cm}^{-1} < \vartheta_I < 22000\,\mathrm{cm}^{-1}$. Then, taking the average values $\vartheta_q = 1500\,\mathrm{cm}^{-1}$, and $\vartheta_I = 19000\,\mathrm{cm}^{-1}$, and using the relation $\omega = 2\pi c\vartheta$, where $c = 3 \times 10^{10}\,\mathrm{cm/s}$,

we have the usual frequencies $\omega_q \sim 3\times10^{14}\,\mathrm{rad/s}$, and $\omega_I \sim 3.5\times10^{15}\,\mathrm{rad/s}$, for the phonon and incident photon, respectively. Substituting these values in equation 3.36, and taking the values $\eta_S = \eta_I = 1.5$, and $\phi = \pi/2$, we find the wavevector of the phonon to be $q \sim 2.5 \times 10^5\,\mathrm{cm}^{-1}$.

By comparison, the maximum wavevector in the first Brillouin zone is of the order π/d, where d is the lattice constant. This maximum is typically about $3 \times 10^8\,\mathrm{cm}^{-1}$, which is three orders of magnitude larger than the typical wavevector of the phonons analyzed in Raman scattering experiments. Therefore, the momentum conservation for one phonon Raman processes gives rise to the selection rule $q \sim 0$.

The Raman tensor

The spatial symmetry of the scattering medium is formally determined by its symmetry group, the group of all spatial transformations that leave the medium invariant. A crystal lattice is characterized by a space group that contains translations, reflections and rotations. There are 32 crystal point groups, which carry the symmetry properties of the space groups that remain after the removal of the translations.

The symmetry properties of the scattering cross section (see equation 3.26) are determined by the symmetry properties of the susceptibility derivative $\overleftrightarrow{\chi}'$, also called the Raman tensor, for the excitation concerned. The selections rules rise from the term

$$\left|\hat{\varepsilon}_S \cdot \overleftrightarrow{\chi}' \, \hat{\varepsilon}_I\right|^2 , \tag{3.37}$$

which determines if the incident and scattered light, with their respective polarization directions relative to the crystal symmetry axes, can excite a specific vibrational mode. The Raman tensor was established by Poulet and Mathieu [20] for the 32 crystal point groups. The complete list for the Raman tensor can also be found in references [19] and [21].

3.1.4 Two-phonon Raman scattering

The two-phonon Raman processes can occur in three distinct cases: both phonons are created (giving a Stokes component in the scattered light), both phonons are annihilated (giving an anti-Stokes component in the scattered light), and one phonon is created and other annihilated (giving a Stokes or anti-Stokes component in the scattered light). Most

strong scattering processes at low temperature arise from the two-phonon process where both phonons are created. We will focus our analysis on this case, where the two phonons have wavevectors $\vec{q}$ and $\vec{q}\,'$, belonging to branches σ and σ', respectively (branches σ and σ' are not necessarily different). The energy and momentum conservation give, respectively [19]:

$$\omega_{\sigma\,\vec{q}} + \omega_{\sigma'\,\vec{q}\,'} = \omega_I - \omega_S \ , \tag{3.38}$$

$$\vec{q} + \vec{q}\,' = \vec{k}_I - \vec{k}\omega_S \ . \tag{3.39}$$

Since the branches indices and wavevectors can take all values consistent with the restrictions imposed by equations 3.38 and 3.39, the phonon wavevectors are not necessarily close to the center of the Brillouin zone ($q \sim 0$). In fact, since the phonon wavevectors are up to three orders of magnitude larger than the light vavevectors over the major part of the Brillouin zone, equation 3.39 can be rewritten as:

$$\vec{q} \sim -\vec{q}\,' \ , \tag{3.40}$$

and the energy conservation condition can be replaced by:

$$\omega_{\sigma\,\vec{q}} + \omega_{\sigma'\,\vec{q}} = \omega_I - \omega_S \ . \tag{3.41}$$

Since the scattering frequency shift ($\omega = \omega_I - \omega_S$) is controlled by the number of pairs of phonons which obey relation 3.40, and with frequencies whose the sum is equal to ω, the two phonon Raman spectrum is a continuum, once the combined density of states of pairs of phonons is a continuous function of frequencies for crystals.

Strong two-phonon Raman bands are usually associated with singularities in the phonon density of states occurring in the vibrational spectrum inside the first Brillouin zone. Otherwise, because the two-phonon Raman scattering is a fourth-order quantum process, two-phonon Raman bands are usually observed as very weak features in the Raman spectra of solids, if compared with one-phonon allowed bands, which are product of a third-order quantum process. However, if resonance conditions are satisfied during the scattered process, the two-phonon Raman bands can be as strong as the one-phonon Raman bands even for phonon wavevectors outside the critical points. This is the case of the G' band in the Raman spectrum of graphite, which is associated with double- and triple-resonance processes. The mechanism behind the G' band will be treated in detail in Chapter 5.

The van Hove singularities in the single-phonon density of states occur at critical points, where $\vec{\nabla}_{\vec{q}}\,\omega_{\sigma\,\vec{q}} = 0$. On the other hand, the singularities for the combined density of states

occurs at any frequency where [19]:

$$\vec{\nabla}_{\vec{q}}\,(\omega_{\sigma\,\vec{q}} + \omega_{\sigma'\,\vec{q}}) = 0\ . \tag{3.42}$$

Such singularities occur whenever both branches σ and σ' have critical points at the wavevector $\vec{q}$, but there are additional singularities corresponding to pairs of branches that have equal and opposite slopes occurring at the same wavevector $\vec{q}$.

The macroscopic approach for the differential spectral cross section for two-phonon Raman scattering involves the third-order susceptibility derivative [19]:

$$\overleftrightarrow{\chi}'' = \frac{\partial^2 \overleftrightarrow{\chi}}{\partial X_{\sigma,\,\vec{q}}\,\partial X_{\sigma',-\vec{q}}}\ . \tag{3.43}$$

The selection rules associated with the spacial symmetry properties of the two-phonon Raman scattering are determined by the sum:

$$\sum_{\sigma,\sigma'}\sum_{\vec{q}}\left|\hat{\varepsilon}_S\cdot\overleftrightarrow{\chi}''\,\hat{\varepsilon}_I\right|^2\ , \tag{3.44}$$

which is proportional to the differential spectral cross section.

3.2 Microscopic theory of Raman scattering

The microscopic theory of Raman scattering is based on the development of the perturbation theory associated with the interaction Hamiltonians giving rise to the scattering process. In this section, we will study the Raman scattering theory using a quantum mechanical approach. This method allows us to understand, in a more detailed way, the symmetries associated with the scattering process, making the group theory a useful tool to analyze the selection rules imposed for the Raman cross section. It also clarifies the mechanism behind the resonance phenomena, which is a special feature in the inelastic scattering.

3.2.1 The cross section

The cross section σ has dimensions of area, and is defined as the ratio between the rate $\hbar\omega_I/\tau$ at which the energy of the photon beam is removed (by creating the phonons in a Stokes process) during the time interval τ in which the scattering occurs, to the rate $\overline{I}_I$

at which the energy in the incident photon beam crosses an unit of area perpendicular to its propagation direction [19]:

$$\sigma = \frac{\hbar\omega_I}{\tau \overline{I}_I} \ . \tag{3.45}$$

Let us now analyze the rate $\overline{I}_I$. Firstly, we define the scattering length L as the depth measured from the crystal surface where the scattering process occurs (see Figure 3.2). Taking A as the area of the crystal surface illuminated by the sample (dashed area in Figure 3.2), the scattering volume v is given as:

$$v = A.L \ . \tag{3.46}$$

When the sample is illuminated, the volume v is fulfilled with n_I photons with frequency ω_I. The photons travel inside the material medium with a velocity γ_I given as:

$$\gamma_I = \frac{c}{\eta_I} \ , \tag{3.47}$$

where η_I is the refractive index of the sample material. The time interval δt necessary for all the n_I photons to fulfill the volume v is given by the ratio:

$$\delta t = \frac{L}{\gamma_I} \ . \tag{3.48}$$

The rate in which the total energy carried by the n_I photons ($\hbar\omega_I n_I$) crosses a unit of area perpendicular to the propagation direction is:

$$\overline{I}_I = \frac{\hbar\omega_I n_I}{A\delta t} \ . \tag{3.49}$$

Using equations 3.46, 3.47, and 3.48, equation 3.49 becomes:

$$\overline{I}_I = \frac{\hbar\omega_I n_I c}{\eta_I v} \ . \tag{3.50}$$

Finally, combining equations 3.45 and 3.50, we have a more explicit expression for the cross section [22]:

$$\sigma = \frac{\eta_I v}{\tau n_I c} \ . \tag{3.51}$$

3.2.2 Differential cross section

The cross section determines the total scattering (associated with a particular excited state) in all directions, and its experimental evaluation requires measurements of the scattered intensity (number of photons in the time interval Δt) at a large number of

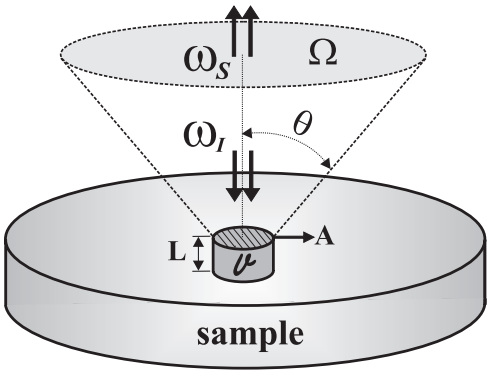

Figure 3.2: Raman back scattering geometry.

scattering angles, or by using integrators cavities. Let us look, for example, at Figure 3.2 which shows a back scattering experiment where the scattered light will be collected in the solid angle $\Delta\Omega$. This means that such experiment measures the cross section only partially, since the collection solid angle $\Delta\Omega$ is limited by the objective lens area. However, the light scattered is not isotropic in all directions, and then, it becomes necessary to define the differential cross section, which is the derivative of the cross section σ on the solid angle Ω:

$$\beta = \frac{d\sigma}{d\Omega} \ . \tag{3.52}$$

The total cross section is then obtained by integrating the differential cross section in all space:

$$\sigma = \int_{all\ space} \frac{d\sigma}{d\Omega} d\Omega \ . \tag{3.53}$$

The differential cross section has the dimension of area/solid angle.

3.2.3 Spectral differential cross section

From the measurement of the Raman spectrum for a fixed scattering angle we can also introduce a function denominated by spectral differential cross section:

$$\beta'(\nu_s, \Omega) = \frac{d^2\sigma}{d\Omega d\omega_S} \ . \tag{3.54}$$

The differential cross section is, in fact, the raw data (spectral curve) obtained in the Raman experiment. The differential cross section β is then obtained by integrating the spectral differential cross section:

$$\beta = \int \frac{d^2\sigma}{d\Omega d\omega_S} d\omega_S \ , \tag{3.55}$$

where the range of integration is usually restricted to include just a single peak in the scattered spectrum.

The spectral differential cross section has the dimension of area/(solid angle·frequency).

3.2.4 The transition rate

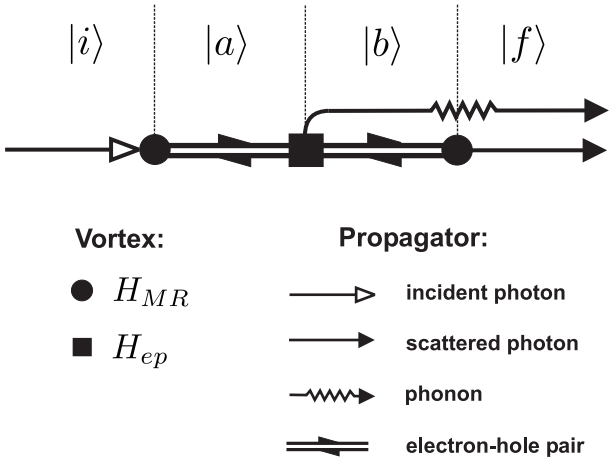

Figure 3.3: The Feynman diagram associated with a one-phonon Stokes process, where one phonon is created from the electron-phonon interaction Hamiltonian.

Figure 3.3 shows the Feynman diagram associated with a one-phonon Stokes process. The process starts with the system in an initial state $|\,i\rangle$, where the material system (sample) is in the ground state, and there is an incident photon with energy $\hbar\omega_I$. Next, the sample absorbs the incident photon, creating the electron-hole pair. After that, a phonon with energy $\hbar\omega_q$ is created. Finally, the electron recombines with the hole, creating a photon with energy $\hbar\omega_S = \hbar\omega_I - \hbar\omega_q$.

The one-phonon Raman process depicted in Figure 3.3 is, in fact, a third-order perturbative quantum process. The Hamiltonian of the whole system is composed of the sum of four parts:

$$H = H_M + H_R + H_{MR} + H_{ep} \ , \tag{3.56}$$

where H_M is the material system Hamiltonian, H_R is the radiation field Hamiltonian, H_{MR} is the material-radiation interaction Hamiltonian, and H_{ep} is the electron-phonon interaction Hamiltonian. In the quantum theory of light scattering in solids, the Hamil-

tonian H is written as the sum of two parts [21]:

$$H = H_0 + H_1 \ , \tag{3.57}$$

where $H_0 = H_M + H_R$, and $H_1 = H_{MR} + H_{ep}$. The H_1 part is then treated as a perturbation of the system, and the quantum states $|\, x\rangle$, where $x = i, a, b, f$, are treated as eigenstates of H_0 associated with their respective eigenvalues $\hbar\omega_x$.

In the process shown in Figure 3.3, the system passes through four eigenstates of H_0: the initial state $|i\rangle$, two intermediate states $|a\rangle$ and $|b\rangle$, and the final state $|f\rangle$. These eigenstates are determined by four elements of the system: the number of incident photons inside the volume v (n_I), the number of scattered photons inside the volume v (n_S), the number of phonons satisfying the energy and momentum conservation conditions (n_q), and the state function of the electron designated as ϕ^x. In this notation, the eigenstates of the Hamiltonian H_0 are written in the form $|\, x\rangle = |n_I, n_S, n_q, \phi^x\rangle$, and we have:

$$\begin{aligned} |\, i\,\rangle &= |n_I, n_S, n_q, \phi^i\rangle \ , \\ |\, a\,\rangle &= |n_I - 1, n_S, n_q, \phi^a\rangle \ , \\ |\, b\,\rangle &= |n_I - 1, n_S, n_q + 1, \phi^b\rangle \ , \\ |\, f\,\rangle &= |n_I - 1, n_S + 1, n_q + 1, \phi^i\rangle \ . \end{aligned} \tag{3.58}$$

The transition rate obtained from the third-order perturbation calculation for the process depicted in Figure 3.3 is given as [22]:

$$\frac{1}{\tau} = \frac{2\pi}{\hbar^{\,2}} \sum_f \left| \sum_{a,b} \frac{\langle f|H_{MR}|b\rangle\langle b|H_{ep}|a\rangle\langle a|H_{MR}|i\rangle}{(E_i - E_a)(E_i - E_b)} \right|^2 \delta(E_i - E_f) \ , \tag{3.59}$$

where E_i, E_a and E_b are the eigenvalues of H_0 associated with the eigenstates $|i\rangle$, $|a\rangle$, and $|b\rangle$, respectively. The substitution of equation 3.59 in equation 3.51 gives the explicit expression for the Raman cross section for a one-phonon Raman process [22]:

$$\sigma = \left(\frac{\hbar\omega_I}{\overline{I}_0}\right) \frac{2\pi}{\hbar^{\,2}} \sum_f \left| \sum_{a,b} \frac{\langle f|H_{MR}|b\rangle\langle b|H_{ep}|a\rangle\langle a|H_{MR}|i\rangle}{(E_i - E_a)(E_i - E_b)} \right|^2 \delta(E_i - E_f) \ . \tag{3.60}$$

Equation 3.60 is not strictly complete, because we should, in fact, take into account all the possible orders of the events included in the Feynman diagram depicted in Figure 3.3. The number of possible permutations is given as $n!$, where n is the order of the process. Since the one-phonon Raman scattering is a third-order ($n = 3$) process, we have six ($3! = 6$) possible orders, as depicted in Figure 3.4 [23]. Then, according to the sequence

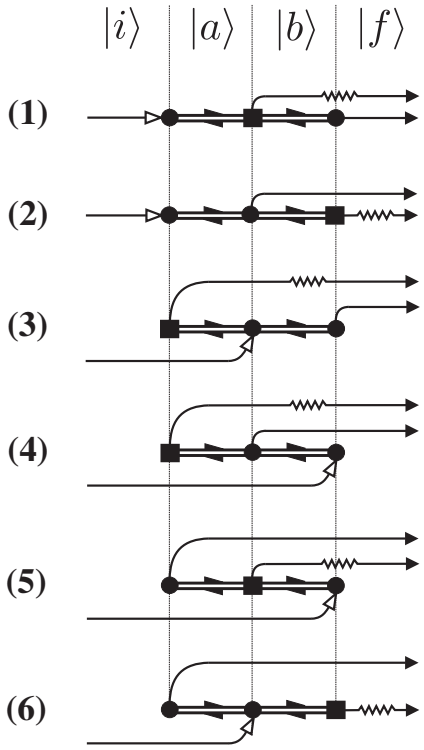

Figure 3.4: The Feynman diagrams associated with the six possible orders for the one-phonon Stokes Raman scattering [23].

depicted in Figure 3.4, the complete expression for the Raman cross section related with one-phonon Raman scattering is given as [23]:

$$\sigma = \left(\frac{\hbar\omega_I}{\overline{I}_0}\right)\frac{2\pi}{\hbar^2}\sum_f\left|\sum_{a,b}\left\{\frac{\langle f|H_{MR}(\omega_S)|b\rangle\langle b|H_{ep}|a\rangle\langle a|H_{MR}(\omega_I)|\,i\rangle}{[\hbar\omega_I-\hbar\omega_{eh}][\hbar\omega_I-(\hbar\omega_{eh}+\hbar\omega_q)]}+\right.\right. \tag{3.61}$$

$$+\frac{\langle f|H_{ep}|b\rangle\langle b|H_{MR}(\omega_S)|a\rangle\langle a|H_{MR}(\omega_I)|\,i\rangle}{[\hbar\omega_I-\hbar\omega_{eh}][\hbar\omega_I-(\hbar\omega_S+\hbar\omega_{eh})]}+$$

$$+\frac{\langle f|H_{MR}(\omega_S)|b\rangle\langle b|H_{MR}(\omega_I)|a\rangle\langle a|H_{ep}|\,i\rangle}{[\hbar\omega_I-(\hbar\omega_q+\hbar\omega_{eh}+\hbar\omega_I)][\hbar\omega_I-(\hbar\omega_q+\hbar\omega_{eh})]}+$$

$$+\frac{\langle f|H_{MR}(\omega_I)|b\rangle\langle b|H_{MR}(\omega_S)|a\rangle\langle a|H_{ep}|\,i\rangle}{[\hbar\omega_I-(\hbar\omega_q+\hbar\omega_{eh}+\hbar\omega_I)][\hbar\omega_I-(\hbar\omega_q+\hbar\omega_{eh}+\hbar\omega_I+\hbar\omega_S)]}+$$

$$+\frac{\langle f|H_{MR}(\omega_I)|b\rangle\langle b|H_{ep}|a\rangle\langle a|H_{MR}(\omega_S)|\,i\rangle}{[\hbar\omega_I-(\hbar\omega_{eh}+\hbar\omega_S)][\hbar\omega_I-(\hbar\omega_S+\hbar\omega_q+\hbar\omega_{eh})]}+$$

$$\left.\left.+\frac{\langle f|H_{ep}|b\rangle\langle b|H_{MR}(\omega_I)|a\rangle\langle a|H_{MR}(\omega_S)|\,i\rangle}{[\hbar\omega_I-(\hbar\omega_S+\hbar\omega_{eh}+\hbar\omega_I)][\hbar\omega_I-(\hbar\omega_S+\hbar\omega_{eh})]}\right\}\right|^2\delta[\hbar\omega_I-(\hbar\omega_q+\hbar\omega_S)]\ ,$$

where the energy eigenvalues were evaluated by taking the sum of the energies of the propagators present in each eigenstate of H_0 in Figure 3.4, being $\hbar\omega_{eh}$ is the energy

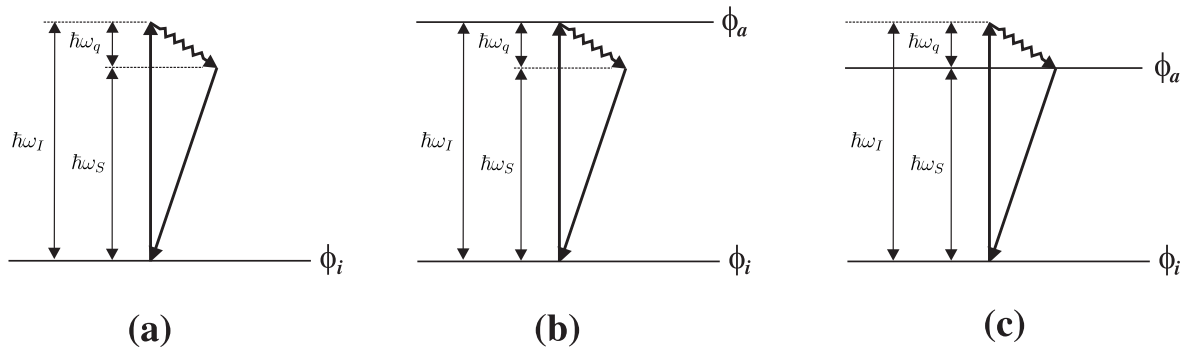

Figure 3.5: Three distinct energy configurations for the one-phonon Raman scattering. In process **(a)**, no real transitions are made during the scattering process. In process **(b)**, the incident photon has the same energy as the electronic transition $\phi^i \rightarrow \phi^a$. In process **(c)**, the scattered photon has the same energy as the electronic transition $\phi^i \rightarrow \phi^a$.

necessary for creating the electron-hole pair. Observe that for all processes depicted in Figure 3.4, the final energy eigenvalue E_f is equal to the sum $\hbar\omega_S + \hbar\omega_q$. Therefore, due to the Dirac delta function properties, the sum has a considerable value only if the energy conservation condition is satisfied in the scattering process.

If one or more terms in the denominators become zero in equation 3.61, the cross section diverges, giving rise to strong Raman features in the spectrum. This phenomena is called resonant Raman scattering. Figure 3.5 shows three distinct energy configurations for the one-phonon Raman scattering (Stokes). In process (a), no real transitions are made during the scattering process, and no resonance occurs. In process (b), the incident photon has the same energy as the electronic transition $\phi^i \rightarrow \phi^a$. In this case, $\hbar\omega_I = \hbar\omega_{eh}$, and the first term in the denominator of the first and second lines in equation 3.61 is null, and processes (1) and (2) shown in Figure 3.4 are resonant processes for the configuration shown in Figure 3.5(b). In process (c) depicted in Figure 3.5, the scattered photon has the same energy as the electronic transition $\phi^i \rightarrow \phi^a$, and we have $\hbar\omega_I = \hbar\omega_{eh} + \hbar\omega_q$. In this case, the second term in the denominator for the first and third lines in equation 3.61 is zero. Then, processes (1) and (3) in Figure 3.4 are resonant for the configuration shown in Figure 3.5(c).

Since the electron dispersion energy in graphite is linear and symmetric with respect to the Fermi level, the optical absorption or emission can always be resonant for excitation light in the visible range. Therefore, the Raman scattering of graphite always involves resonance processes. We will see in section 5.2 that the mechanism giving rise to the D

band in the Raman spectrum of nanographite involves also double-resonance conditions. Moreover, a point that was not considered here is the possibility of scattering of holes by phonons. This subject will be treated in section 5.3, when we discuss the G' band in graphite, and we will see that the scattering involving holes can cause unusual triple-resonance conditions in the Raman cross section.

The results depicted here can be generalized for scattering processes of higher orders, specially the fourth-order, which can involve the scattering of electrons (or holes) by two phonons, or one phonon and one defect, as we will see along the text. In order to treat fourth-order Raman process, we should develop the fourth-order perturbation, and the resultant cross section is given as [22]:

$$\sigma = \left(\frac{\hbar\omega_I}{\overline{I}_0}\right)\frac{2\pi}{\hbar^2}\sum_f \left|\sum_{a,b,c}\frac{\langle f|H_1|c\rangle\langle c|H_1|b\rangle\langle b|H_1|a\rangle\langle a|H_1|i\rangle}{(E_i-E_a)(E_i-E_b)(E_i-E_c)}\right|^2 \delta(E_i-E_f)\ . \tag{3.62}$$

3.2.5 Selection rules

The quantum-mechanical approach for the selection rules associated with the Raman scattering processes is based on the symmetry properties of the matrix elements. In this section we will give the basis for the understanding of how to use group theoretical methods to analyze the selection rules involving the Raman scattering cross section.

A Raman scattering process starts with a well defined initial state $|\,i\rangle = |n_I, n_S, n_q, \phi^i\rangle$, where the electron state function ϕ^i is an eigenfunction of the electron in the valence band at a given wavevector k_0, that is, $\phi^i = \phi^v(k_0)$. Although the initial and final eigenstates of H_0 are not the same ($|\,i\rangle \neq |f\rangle = |\,n_I - 1, n_S + 1, 1, \phi^i\rangle$), the energy conservation condition requires that the electron will get back to the initial electronic state after the scattering process has finished, that is, $\phi^f = \phi^i = \phi^v(k_0)$.

The irreducible representation associated with the symmetry of the intermediate state $|\,a\rangle$ must be contained in the direct product between the irreducible representation associated with the symmetry of the initial state $|\,i\rangle$ and the irreducible representation associated with the symmetry of the material-radiation Hamiltonian H_{MR}, that is:

$$\Gamma^a \supset \Gamma^I_{MR} \otimes \Gamma^i\ . \tag{3.63}$$

Equation 3.63 shows clearly that the symmetry of an allowed intermediate state $|\,a\rangle$ is

imposed by the material-radiation Hamiltonian H_{MR} and the initial state $|\,i\rangle$ symmetries. When the sum $\sum_a$ is evaluated over all eigestates of H_0, the matrix element $\langle a|H^I_{MR}|i\rangle$ will be zero for those eigenstates belonging to irreducible representations that are not contained in the product $\Gamma^I_{MR} \otimes \Gamma^i$. Following the analysis, we have for the intermediate state $|\,b\rangle$:

$$\Gamma^b \supset \Gamma_{ep} \otimes \Gamma^a \supset \Gamma_{ep} \otimes \Gamma^I_{MR} \otimes \Gamma^i \ . \tag{3.64}$$

Finally, the symmetry of the final state $|f\rangle$ is imposed by the relation:

$$\Gamma^f \supset \Gamma^S_{MR} \otimes \Gamma^b \supset \Gamma^S_{MR} \otimes \Gamma_{ep} \otimes \Gamma^I_{MR} \otimes \Gamma^i \ . \tag{3.65}$$

The initial and final eigenstates of H_0 carry the symmetry of the electronic state function $\phi^v(k_0)$. Therefore they belong to the same irreducible representation $\Gamma^{\phi^v(k_0)}$, and equation 3.65 becomes:

$$\Gamma^{\phi^v(k_0)} \supset \Gamma^S_{MR} \otimes \Gamma_{ep} \otimes \Gamma^I_{MR} \otimes \Gamma^{\phi^v(k_0)} \ . \tag{3.66}$$

Equation 3.66 implies that, in order to observe a Raman active mode, the product of the irreducible representations which transform like the interaction Hamiltonians must contain the totally symmetric representation, that is:

$$\Gamma^I_{MR} \otimes \Gamma_{ep} \otimes \Gamma^S_{MR} \subset \Gamma_1 \ . \tag{3.67}$$

This is the selection rule imposed on the Raman scattering process depicted in Figure 3.3. We have seen that the symmetry of the final eigenstate $|f\rangle$ is imposed by the symmetry of the initial state (in order to keep the energy conservation condition), and the path followed by the system must follow the condition 3.67, which determines the allowed symmetries for the interaction Hamiltonians.

Let us understand now how to manage, in a practical sense, the selection rule given in equation 3.67. The material-radiation interaction Hamiltonian transforms like the linear coordinate along the direction of the incident and scattered light polarization, that is, $\Gamma^I_{MR} = \Gamma^m$, and $\Gamma^S_{MR} = \Gamma^n$, where the superscripts m and n refer to the cartesian coordinates x, y, z (notice that n does not necessarily differ from m). In this case, from the orthogonality relations between the irreducible representations, equation 3.67 is satisfied if:

$$\Gamma^I_{MR} \otimes \Gamma_{ep} \otimes \Gamma^S_{MR} = \Gamma^m \otimes \Gamma^{m \cdot n} \otimes \Gamma^n \subset \Gamma_1 \ . \tag{3.68}$$

Equation 3.68 implies that the irreducible representation associated with the Raman active phonons should transform as quadratic basis functions.

In the case of two-phonon Raman scattering, the process involves one more electron-phonon interaction Hamiltonian. The phonons either can have the same symmetry or not. The selection rule is almost the same as for the one-phonon process, given in equation 3.67, differing only by the insertion of one more irreducible representation associated with the electron-phonon interaction Hamiltonian which connects the intermediate states $|b\rangle$ and $|c\rangle$ in equation 3.62. However, as pointed in section 3.1.4, since the two-phonon Raman scattering is a fourth-order quantum process, even bands which are allowed by symmetry are not necessarily observed in the Raman spectrum, unless they are close to a maximum in the phonon DOS, or some resonance condition is satisfied.

Chapter 4

Raman instrumentation

In this chapter, the basis of the Raman instrumentation used in this work will be presented. We will start with a general explanation about the spectrometer setup, followed by an analysis of the main parts, with special considerations about the measurement process.

4.1 The Spectrometer general configuration

The Raman spectrometer used in this thesis is a micro-Raman Dilor XY system. It has two operation options, the single- and triple-monochromator modes, respectively. The works developed in this thesis were made using the triple-monochromator mode, and we will focus on it. Figure 4.1 shows the spectrometer schema in the triple-monochromator mode. In the next sections, we will give a detailed description of the main parts of the spectrometer system depicted in Figure 4.1.

4.2 The laser sources

Our laboratory is equipped with the following laser sources:

Innova 70C Ion Laser from Coherent: This is an Argon-Krypton laser, with the following emission lines: 647.1 nm, 568.2 nm, 528.7 nm, 520 nm, 514.5 nm, 501.7 nm, 496.5 nm, 488.0 nm, 476.5 nm, 472.7 nm, 465.8 nm, and 457.9 nm.

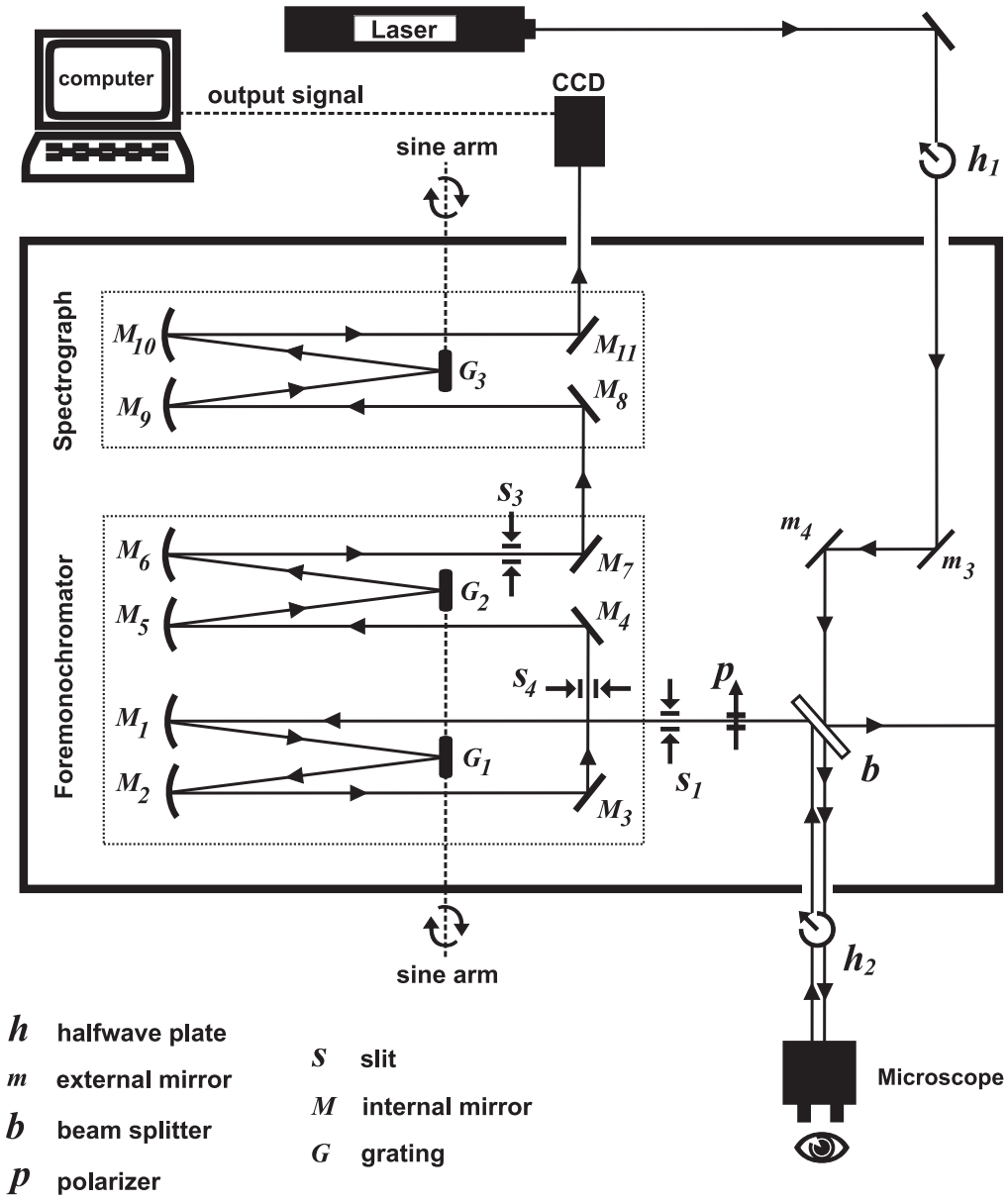

Figure 4.1: Dilor XY spectrometer schema in the triple-monochromator mode.

899-01 Dye Ring Laser from Coherent: This is a tuneable dye laser, with continuous light emission in the range from 380 nm to 880 nm, depending on the dye.

Innova 90C Ion laser from Coherent: This is an Argon laser, with the following lines: 528.7 nm, 514.5 nm, 501.7 nm, 496.5 nm, 488.0 nm, 476.5 nm, 472.7 nm, 465.8 nm, 457.9 nm, and 454.5 nm. It is usually used as a pump for the dye laser, operating in the multiline mode, in which the output power emission can reaches values up to 7 W.

4.3 Illumination of the sample and collection of the scattered light

The sample illumination and the light collection in a back scattering micro-Raman experiment are performed using an objective lens coupled to a microscope system. The Dilor XY spectrometer is equipped with a confocal microscope Olympus BH-2 and a set of four objective lenses (10×, 50×, 80×, and 100×). Figure 4.2 shows the collection optics schema.

In order to determine the main geometrical characteristics of the light collection, one should know the numerical aperture ($N.A.$) of the objective lens. This information is usually provided by the manufactor as a printed value in the objective's body. The second column of Table 4.1 gives the numerical aperture values for the four lenses used in our spectrometer setup.

The half angle of collection θ (see Figure 4.2), can be obtained from the numerical aperture ($N.A.$) as [24]:

$$\theta = sin^{-1} \frac{N.A.}{\eta_0} \ , \tag{4.1}$$

where η_0 is the refractive index of the medium adjacent to the collection optics, usually air ($\eta_0 \sim 1$). The solid angle of collection (Ω) can be obtained from the half angle of collection (θ), evaluating the following expression [24]:

$$\Omega = 2\pi(1 - cos\,\theta) \ . \tag{4.2}$$

The calculated values of θ and Ω are depicted in Table 4.1 for the four objective lenses (10×, 50×, 80×, and 100×).

In the sample illumination geometry, the size and divergence of the laser beam is often

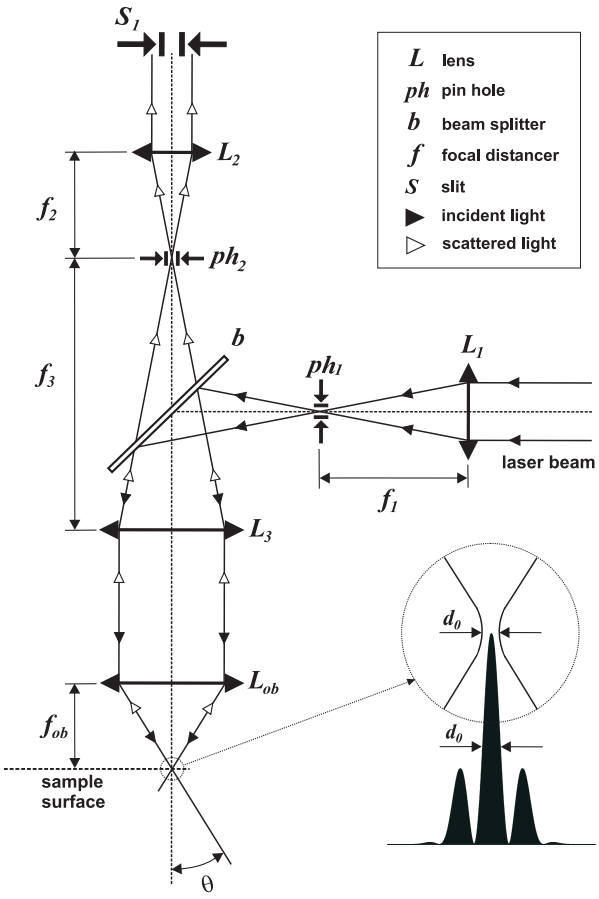

Figure 4.2: Collection optics schema.

Objective	$N.A.$	$\theta(^0)$	Ω(sr)	$\frac{4\pi}{\Omega}$
10×	0.25	14.5	0.20	62.8
50×	0.55	33.4	1.04	12.1
80×	0.75	48.60	2.13	5.9
100×	0.95	71.80	4.32	2.9

Table 4.1: Numerical aperture for the collection optics $N.A.$ (provided by the manufactor) and calculated values of θ, Ω (evaluated using equations 4.1, and 4.2, respectively), and the ratio $4\pi/\Omega$ for the four lenses (10×, 50×, 80×, and 100×).

λ_{laser} (nm)	d_0 (μm)	A_0 (μm^2)	λ_{laser} (nm)	d_0 (μm)	A_0 (μm^2)	λ_{laser} (nm)	d_0 (μm)	A_0 (μm^2)	λ_{laser} (nm)	d_0 (μm)	A_0 (μm^2)
10×			**50×**			**80×**			**100×**		
647	2.46	4.75	647	0.98	0.76	647	0.57	0.26	647	0.20	0.037
568	2.16	3.66	568	0.83	0.59	568	0.50	0.20	568	0.18	0.026
514.5	1.96	3.00	514.5	0.78	0.48	514.5	0.45	0.16	514.5	0.17	0.021
488	1.85	2.70	488	0.74	0.43	488	0.43	0.15	488	0.16	0.019
457.9	1.74	2.38	457.9	0.70	0.38	457.9	0.40	0.13	457.9	0.15	0.017

Table 4.2: Calculated values of d_0 and A_0 for the 10×, 50×, 80×, and 100× objective lenses. We present the result for the five main incident laser wavelengths in the visible range (λ_{laser} = 647, 568, 514.5, 488, and 457.9 nm).

limited mostly by diffraction. The cross-sectional profile of the laser beam intensity has a Gaussian shape (see inset to Figure 4.2). When focused, the minimum diameter d_0 of the laser beam at the sample surface is given as the half-height width of the first maximum diffraction peak, and it is related with the numerical aperture ($N.A.$) as [24]:

$$d_0 = \lambda_{laser} \sqrt{\frac{1}{N.A.^2} - 1} \ , \tag{4.3}$$

where λ_{laser} is the wavelength of the excitation laser line. The area of the laser spot in the sample surface is:

$$A_0 = \frac{\pi d_0^2}{4} = \frac{\pi \lambda_{laser}^2}{4} \left(\frac{1}{N.A.^2} - 1 \right) \ , \tag{4.4}$$

where we have considered $\eta_0 = 1$.

Table 4.2 shows the calculated values of d_0 and A_0 for the four objectives lenses (10×, 50×, 80×, and 100×) respectively, considering the five most used incident laser wavelengths in the visible range (λ_{laser} = 647, 568, 514.5, 488, and 457.9 nm).

4.4 Measurement of the incident light intensity

In order to compare the Raman cross section measured using many excitation laser lines of different wavelengths, the experimental conditions should be similar for all excitation laser lines. This means that the superficial power density in the area of the sample surface covered by the incident laser beam should be the same for all excitation laser lines. Since

λ_{laser} (nm)	P_0 (mW)	P_0 (mW)	P_0 (mW)	P_0 (mW)
objective	**10**×	**50**×	**80**×	**100**×
647	29.6	4.8	1.6	0.21
568	22.9	3.7	1.3	0.16
514.5	18.8	3	1	0.13
488	16.9	2.7	0.9	0.12
457.9	14.9	2.4	0.8	0.10

Table 4.3: Values of P_0 for a fixed incident light intensity $I_0 = 6.25\times10^8$ mW/cm^2, for the five main laser lines ($\lambda_{laser} = 647$, 568, 514.5, 488, and 457.9 nm), for the four objective lenses.

the laser spot area depends on the laser wavelength, the laser power measured in the power meter (in mW units) should be adjusted in order to obtain the same superficial power density (in mW / cm^2), that is, the same intensity of the incident laser beam I_0, in experiments using different laser lines (wavelengths), or objective lenses.

Let us start by defining the incident light intensity I_0 as:

$$I_0 = \frac{P_0}{A_0} \ , \tag{4.5}$$

where P_0 is the measured power of the incident laser beam, and A_0 is the laser spot area. Using equation 4.4, we can put explicitly in Equation 4.5 the dependence of the laser spot area A_0 on λ_{laser}, and on the objective lens numerical aperture $N.A.$ used in the experiment:

$$I_0 = \frac{4P_0}{\pi\lambda_{laser}^2}\left(\frac{N.A.^2}{1-N.A.^2}\right) \ . \tag{4.6}$$

Table 4.3 shows the values of P_0 for a fixed intensity $I_0 = 6.25\times10^8$ mW/cm^2, for the five main laser lines ($\lambda_{laser} = 647$, 568, 514.5, 488, and 457.9 nm), using the 10×, 50×, 80×, and 100× objective lenses. In fact, 6.25×10^8 mW/cm^2 is the value of I_0 referring to $P_0 \sim 1$ mW, for a laser beam with wavelength $\lambda = 514.5$ nm, using a 80× objective lens. This is a usual incident light intensity used in Raman experiments, since it is small enough to avoid damage to the samples due to heating. Therefore, we have chosen it as a good practical reference.

4.5 The fore-monochromator

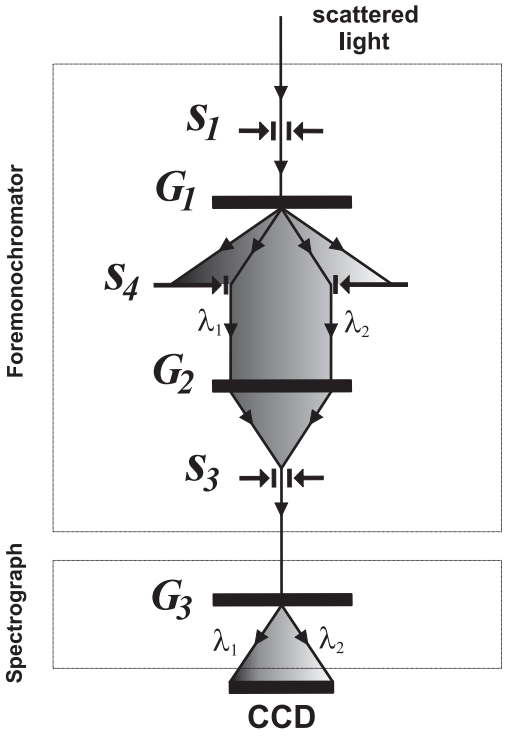

Figure 4.3: Fore-monochromator schema.

In a typical Raman experiment in our laboratory, we use a double fore-monochomator which can work in a subtractive or additive configuration. Figure 4.3 shows schematically how the fore-monochromator works in the subtractive configuration, which is the one used in this work. As depicted in the picture, the scattered light beam passes through the slit S_1 and reaches the grating G_1. This grating disperses the light beam by diffraction in such a way that only the desired range of wavelengths (from λ_1 to λ_2, as depicted in Figure 4.3) will pass trough the slit S_4. In this case, the main role of the slit S_4 is to avoid the Rayleigh line. The range of wavelengths from λ_1 to λ_2 depends on the position of the grating relative to the scattered light beam. The selection is made by rotating the grating using a sine arm. Back to Figure 4.3, the grating G_2 focuses the light beam in the slit S_3 before it goes to the spectrograph. Finally, the signal is sent to the CCD detector through the spectrograph.

4.6 Scattered light detection

A Charge Coupled Device (CCD) is essentially a large area of silicon photodiodes constructed in such way that the area is divided into a two dimensional matrix of pixels. It works by the photoelectric process, that is, it responds to the illumination from photons by releasing electrons. The Dilor XY spectrometer setup in our laboratory is equipped with a CCD2000 from Spectrum One.

When illuminated by opening the shutter, each pixel in the CCD integrates a charge arising from the photoelectric effect. The charges of adjacent pixels are kept separated by a grid of electrodes that confine the charges by an electrostatic force. At the end of the signal integration time Δt, the shutter is closed. Then the electrode grid voltages are manipulated by control signals from the Detector Interface Unit. This will sequentially move the charges column by column to the edge of the chip into a read out register. The signal of the CCD is than processed, amplified and converted to digital datapoints by electronics in the Interface Detector Unit. The data is passed from the detector Interface Unit to the memory of the computer. This allows the software running in the host PC to access it rapidly for further processing and display.

An Analog to Digital Converter (ADC) converts a sample of an analog voltage or current signal to a digital value. The value may then be communicated, stored and manipulated mathematically. The value of each conversion is displayed as a datapoint. In fact, the CCD2000 setup is formed by 1024 columns of 256 pixels, that is, is a net of 1024×256 pixels. Therefore, the CCD2000 receives from the spectrograph one image which is projected along 1024 columns of pixels, and the spectrum obtained is formed by a set of 1024 datapoints, each one giving the number of counts coming from a specific column of pixels.

The vertical axes of the displayed spectrum is then scaled by counts. In our system, each count refers from 1 to 16 photoelectrons. Let us consider the real number as the average value, that is, 8 photoelectrons are converted into a count unit. The quantum efficiency of the CCD2000 is about 50%. This means that for each couple of photons releasing the CCD2000, one photoelectron is created. Therefore, each count in a specific data point gives the information provided by about sixteen photons released the column of pixels during the integration time Δt:

$$1\,\text{Count} \sim 16\,\text{photons}\ . \tag{4.7}$$

This information, although interesting, is far to be exact and, therefore, is not useful for a intensity calibration process. The CCD efficiency surely caries a dependence on the wavelength λ of the scattered light which is not considered in relation 4.7 which is just an average value. The procedures necessary for the intensity calibration process involve the comparison of the power emission spectrum of a standard light source with the spectrum measured by using the spectrometer system. This process is reported in Appendix D, where the spectrometer intensity calibration is performed in order to measure the absolute Raman cross section of nanographite systems, which is the theme of Chapter 10.

4.7 The spectrograph

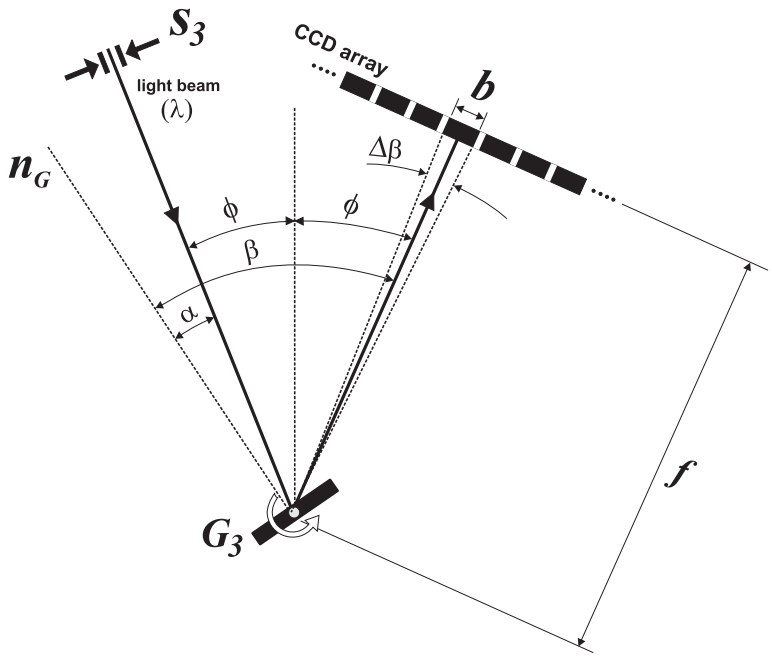

Figure 4.4: Spectrograph schema.

The spectrograph is formed by a diffraction grating used to send photons with different wavelengths to reach different columns of pixels in the CCD. Figure 4.4 shows the spectrograph schema. The scattered light with wavelength λ passes through the slit S_3 at an angle $\alpha(\lambda)$, and is diffracted at an angle $\beta(\lambda)$. The angles $\alpha(\lambda)$ and $\beta(\lambda)$ are measured from the grating normal n_G. The diffracted light beam with wavelength λ will reach a column of pixels localized at an angle 2ϕ formed by the incident and diffracted beams.

The angle ϕ is related to $\alpha(\lambda)$ and $\beta(\lambda)$ as:

$$\phi = \frac{\beta(\lambda) - \alpha(\lambda)}{2} \ . \tag{4.8}$$

Observe that the angle ϕ does not depend on λ, since it is determined by the positions of the silt S_3 and of the column of pixels, which are fixed parameters in the spectrometer setup (see Figure 4.4).

The first maximum of interference for the diffracted light with wavelength λ occurs for the values of $\alpha(\lambda)$ and $\beta(\lambda)$ which satisfy the relation [25]:

$$\lambda = a[sin\,\alpha(\lambda) + sin\,\beta(\lambda)] \tag{4.9}$$

where a is the groove spacing in the diffraction grating. Since the Dilor XY system is equipped with a 1800 grating (1800 lines per millimeter), we have $a \sim 555.6\,\text{nm}$. In order to keep the relation 4.9 for different values of λ, the spectrograph changes the relative position of the grating normal n_G with the incident and diffracted light beams, changing the angles $\alpha(\lambda)$ and $\beta(\lambda)$.

Now we will analyze the spectral range covered by a specific column of pixels. In fact, the pixels have a finite size $b \sim 26\,\mu\text{m}$ (see Figure 4.4), and each column of pixels will cover a spectral range $\Delta\lambda(\lambda)$, located in an angle interval $\Delta\beta(\lambda)$. By differentiating equation 4.9, and using equation 4.8, we have:

$$\Delta\lambda(\lambda) = a\ \Delta\beta\{cos[\beta(\lambda) - 2\phi] + cos\,\beta(\lambda)\} \ . \tag{4.10}$$

Since $\Delta\beta$ is very small, we can write:

$$\Delta\beta \sim \frac{b}{f} \tag{4.11}$$

where f is the distance from the grating to the CCD, *i. e.*, the spectrometer focal distance (see Figure 4.4). In the Dilor XY setup, $f = 60\,\text{cm}$. Finally, combining equations 4.10 and 4.11, we have:

$$\Delta\lambda(\lambda) = \frac{ab}{f}\{cos[\beta(\lambda) - 2\phi] + cos\,\beta(\lambda)\} \tag{4.12}$$

Figure D.2 shows the measurement of the wavelength range $\Delta\lambda(\lambda)$ covered by the central column of pixels *vs* the absolute wavelength λ. Observe that $\Delta\lambda$ becomes smaller by increasing the absolute wavelength of the light beam reaching the CCD. Therefore, for a given spectrograph's position, the software associates a specific column of pixels in the CCD to the correct spectral range $\Delta\lambda(\lambda)$ which that column is covering.

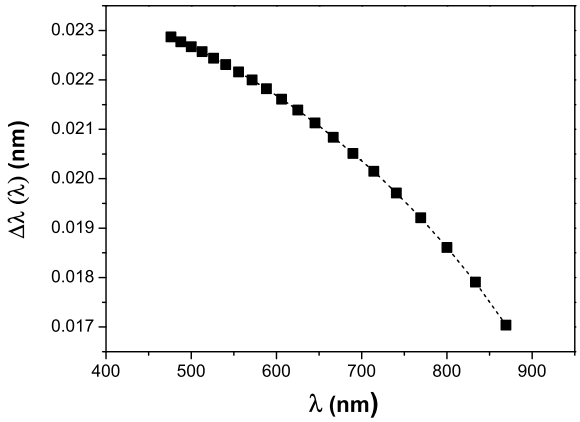

Figure 4.5: The measurement of the frequency range $\Delta\lambda$ covered by the central column of pixels *vs* the absolute wavelength λ.

4.8 Linearity of the measured Raman intensity on the integration time Δt

Figure 4.6 shows a test of the linearity of the measured Raman intensity on the integration time. The vertical scale refers to the integrated area (in count units) of the G band (centered at $\sim$1580 cm^{-1}), present in the Raman spectra of highly oriented pyrolytic graphite (see Chapter 5). The graphic confirms that, in the measured range (from 10 to 240 s), the Raman intensity is linear with the integration time Δt.

4.9 Linearity of the measured Raman intensity on the incident light intensity I_0

Figure 4.7 shows a test of the linearity of the measured Raman intensity on the incident light intensity. The vertical scale refers to the integrated area (in count units) of the first order Raman band of silicon (centered at $\sim 520\text{cm}^{-1}$), obtained by using the 514.5 nm laser line, and the 80× objective lens, *vs* the incident light intensity I_0, in photon/s·cm^2 units (bottom scale). The top scale shows the laser power at the sample surface in mW units, obtained for reference from equation 4.6. The graphic confirms that, in the measured range (from 1.5×10^7 to 5×10^9mW/cm^2), the Raman intensity is linear with the incident light intensity I_0.

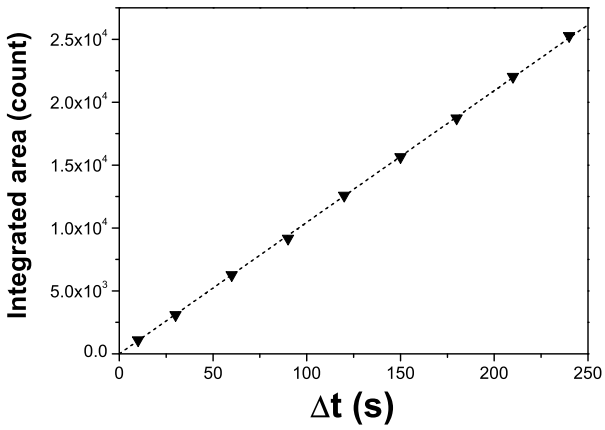

Figure 4.6: Integrated area (in count units) of the G band (centered at $\sim$1580 cm^{-1}), present in the Raman spectra of highly oriented pyrolytic graphite *vs.* the integration time Δt.

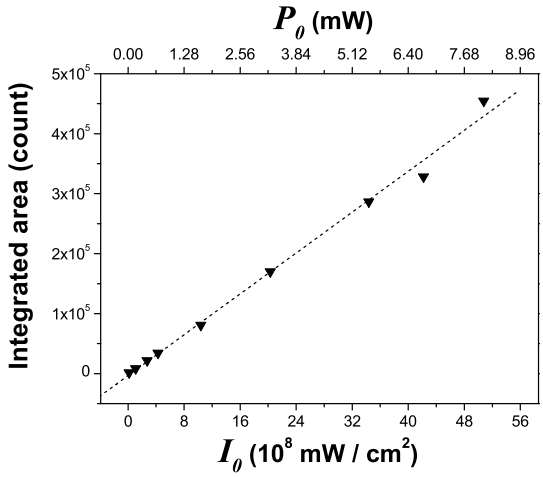

Figure 4.7: Integrated area (in count units) of the first order Raman band of silicon (centered at $\sim$520cm^{-1}) *vs.* the incident light intensity I_0. The top scale shows the laser power at the sample surface in mW units, obtained for reference from equation 4.6.

4.10 Measuring polarization effects

For experiments involving the dependence on the light (incident or scattered) polarization direction, we use a set of two halfwave plates, h_1 and h_2, and a polarizer p (see Figure 4.1). These are optional parts in the spectrometer setup, and for experiments where polarization effects will not be considered they are removed.

The laser sources in our lab always emit light polarized in the vertical direction that we call V. The halfwave plate h_1 can rotate the incident light polarization by any angle. With the halfwave plate h_2 inserted at the microscope entrance, the incident and scattered light polarizations are rotated by the angles θ and $-\theta$, respectively. Therefore, we can rotate the polarization of the incident light on the sample by θ, and keep the same polarization condition for the scattered light. This is an important point, because the spectrometer detection system has a large dependence on the relative polarization direction of the scattered light.

In the VV configuration, the scattered light will be analyzed at the same polarization direction as the incident light. For experiments using the VV configuration, the polarizer p should be put in the vertical position. By rotating the halfwave plate h_2 by an angle θ, we rotate the polarization direction of the incident light by θ, and we then analyze the scattered light at θ also. Therefore, we can make the VV experiment at any angle θ, that is, we can make a (θ, θ) experiment without worrying about the polarization dependence of the spectrometer response.

For the HV (or VH) configuration, we should insert the halfwave plate h_1 at the entrance of the spectrometer (see Figure 4.1) in order to rotate the polarization of the incident light by 90°. By keeping the polarizer P in the vertical direction, the scattered light will be analyzed in a direction perpendicular to the polarization direction of the incident light. Moreover, by rotating the halfwave plate h_2 by an angle θ, we rotate the polarization direction of the incident light by θ, and we analyze the scattered light at θ+90°. Therefore, we can make the HV experiment at any $(\theta, \theta + 90°)$ configuration.

Chapter 5

Raman spectrum of graphite

The Raman spectrum of graphite is known to be very sensitive to structural changes, making the Raman spectroscopy as a widely used tool for the characterization of graphitic materials in the past four decades. Moreover, the physics behind the Raman spectrum of graphite has intrigued many research groups. This chapter will start with a summary of the history of the Raman spectroscopy in graphite, followed by an overview of the double-resonance model, which successfully explains many features in the Raman spectra of graphite. Finally, we will show that by considering the scattering of holes by phonons, triple-resonance Raman processes are also predicted for the G' band scattering.

5.1 The historical survey

In 1969, Tuinstra and Koenig showed that the one-phonon Raman spectrum of crystalline graphite presents a single strong peak centered at $1580\,\mathrm{cm}^{-1}$, named the G band [7, 8]. The upper spectrum in Figure 5.1 is a Raman spectrum obtained from a highly oriented pyrolytic graphite (HOPG) sample, where the presence of the G band can be observed. Tuinstra and Koenig proposed that the G band originates from the doubly degenerate vibrational mode Γ_6^+ (E_{2g}) that occurs at the crossing of the iLO and iTO phonon branches at the Γ point in the first Brillouin zone of graphite (see Figure 2.2 and Table 2.4).

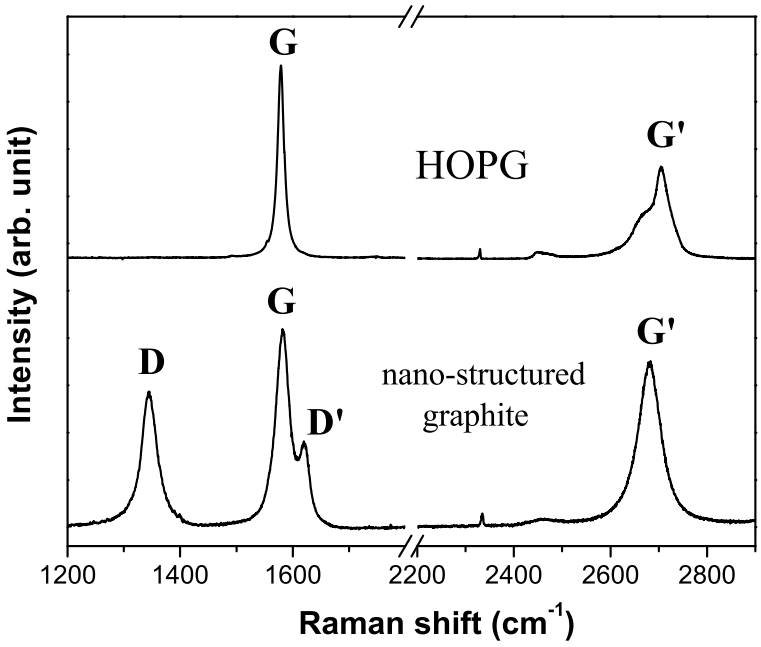

Figure 5.1: **Upper spectrum:** Raman spectrum obtained from a highly oriented pyrolytic graphite (HOPG) sample, in which the presence of the one- and two-phonon allowed G and G' bands, respectively, is observed. **Bottom spectrum:** Raman spectrum of a nano-structured graphite film with crystallite size $L_a = 35\,\text{nm}$, in which the disorder-induced D and D' bands are observed, in addition to the allowed G and G' bands. Both spectra (upper and bottom) were obtained using the Dilor XY spectrometer with an excitation laser energy $E_l = 2.18\,\text{eV}$.

In the Raman spectra obtained from samples with small crystallite size L_a ($< 0.5\,\mu\text{m}$), Tuinstra and Koenig observed the presence of an additional peak centered at $1350\,\text{cm}^{-1}$ (see bottom spectrum in Figure 5.1). Later on, this feature was named as D band, making an analogy with the fact that it is a disorder-induced band. Tuinstra and Koenig proposed that this band was caused by a totally symmetric vibration mode occurring at the K point in the first Brillouin zone of graphite, which "achieves Raman activity at the borders of the crystallite areas due to a loss of translational symmetry" [7, 8].

In order to illustrate the explanation given by Tuinstra and Koenig about the origin of the D band, Figures 5.2(a) and 5.2(b) show two confocal Raman images of a HOPG crystallite deposited on a glass substrate. Figure 5.2(a) shows a Raman image of the crystallite, plotting the spacial dependence of the G band intensity. In Figure 5.2(b),

the intensity for the disorder-induced D band is shown. Figure 5.2(c) shows two Raman spectra, one at the interior of the crystallite, and the other at the edge [regions 1 and 2 (white circles) in Figure 5.2(c), respectively]. It is clear from Figures 5.2(a - c) that the G band intensity is uniform in the whole graphite surface, while the D band intensity is localized at the edges of the crystallite. The edges in the surface of HOPG samples can work as defects involved in the Raman scattering process giving rise to the D band, as we have shown in 2004 [26]. We will show in Chapter 7 that the D band spectrum measured from HOPG edges allows the characterization of the crystallographic orientation of atoms near the borders, thus making Raman spectroscopy a tool for structural analysis [26].

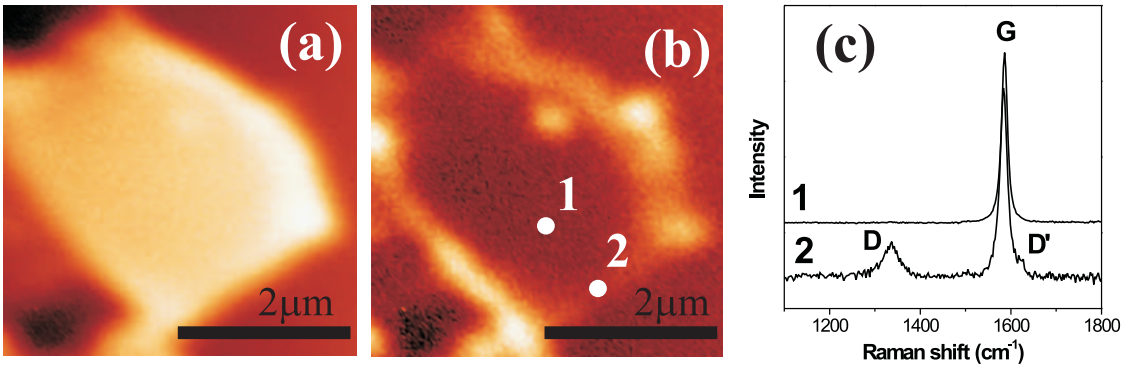

Figure 5.2: G band (a) and D band (b) confocal (600 nm resolution) Raman images of an HOPG crystallite deposited on a glass substrate [27]. In (c) the Raman spectra obtained in regions 1 and 2 (white circles) depicted in panel (b) are shown. The excitation comes from a HeNe ($\lambda = 633$ nm) laser. This experiment was performed by Prof. Ado Jorio at Tuebingen University with the help of Prof. Achim Hitschuh and Ms. Huihong Qian (see reference [28] for experimental setup description).

Based on the assumption that the D band is a border band, Tuinstra and Koenig proposed that its intensity should be proportional to the amount of crystallite boundary in the sample. Supporting this idea, they showed that the ratio between the intensities of the D and G bands (I_D/I_G) is linearly proportional to the inverse of the crystallite size L_a [7, 8]. Figure 5.3(a) shows the Raman spectra obtained from nano-structured graphite films with different crystallite sizes L_a. We observe that the relative intensity between the D and G bands strongly depends on the crystallite size L_a. In 1982, Mernagh *et al.* showed that the ratio I_D/I_G depends strongly on the excitation laser energy used in the Raman experiment [29]. Figure 5.3(b) shows the Raman spectra taken from the disordered carbon sample

with $L_a = 35\,\text{nm}$, obtained using five different excitation laser energies whose respective values are depicted in the right side of the graphic. The dependence of the ratio I_D/I_G on the laser energy is clear in Figure 5.3(b). Chapter 8 reports a work where we have obtained a general equation for the determination of the crystallite size L_a by Raman spectroscopy, taking into account the excitation laser energy used in the experiment [30].

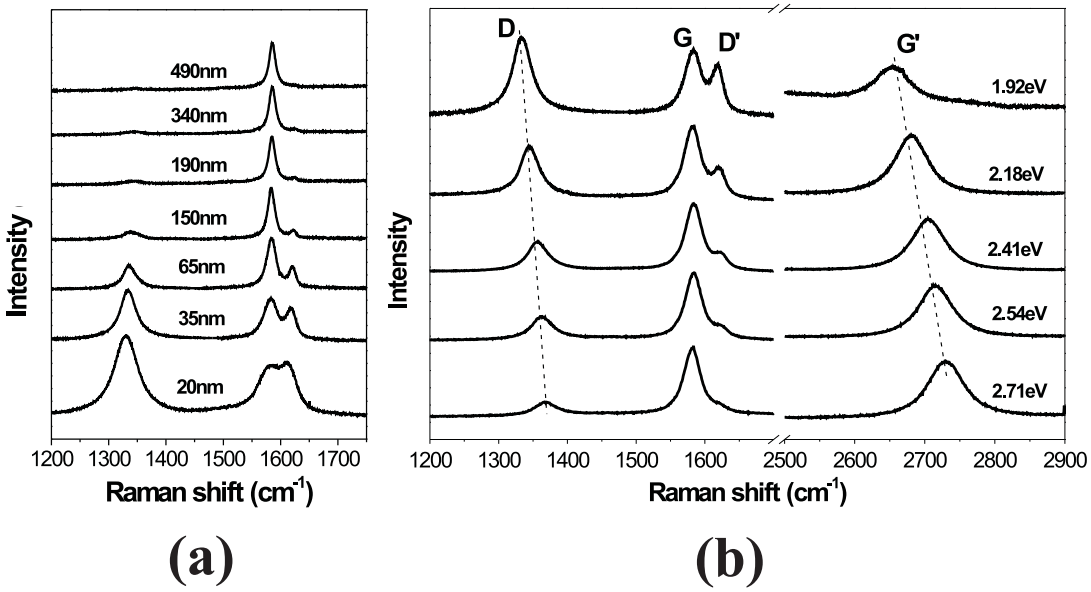

Figure 5.3: (a) Raman spectra obtained from nano-structured graphite films with different crystallite sizes with values shown in the graphic. All spectra were obtained using $E_l = 1.92\,\text{eV}$. (b) Raman spectra taken from the nano-structured graphite film with $L_a = 65\,\text{nm}$, obtained using five different excitation laser energies (1.92, 2.18, 2.41, 2.54, and 2.71 eV, respectively). The dashed lines show the dispersive character of the D and G' bands. All the spectra in parts (a) and (b) were obtained in the Dilor XY spectrometer.

Another Raman feature centered at $1620\,\text{cm}^{-1}$ can be observed in Figures 5.1 and 5.3. This band is called by D' band, and was reported in 1977 by Tsu *et al.* [31]. The D' band is another disorder-induced band, and its relative intensity compared to the G band intensity also depends on L_a and E_l, as can be observed in Figures 5.3(a) and 5.3(b), respectively.

The second-order Raman spectrum of graphite is marked by the presence of a strong feature centered at $2700\,\text{cm}^{-1}$. This feature is called by G' band, and was reported by Nemanich and Solin [32, 33] [see Figures 5.1 and 5.3(b)]. Although the G' band is the two-phonon band associated with the D band, it is not a disorder-induced band, since

the momentum conservation condition in two-phonon Raman processes does not require that the associated phonon wavevectors must be close to the Brillouin zone center (see discussion in section 3.1.4). Therefore, as depicted in figure 5.1, the G' can be observed in both single crystal and disordered graphite.

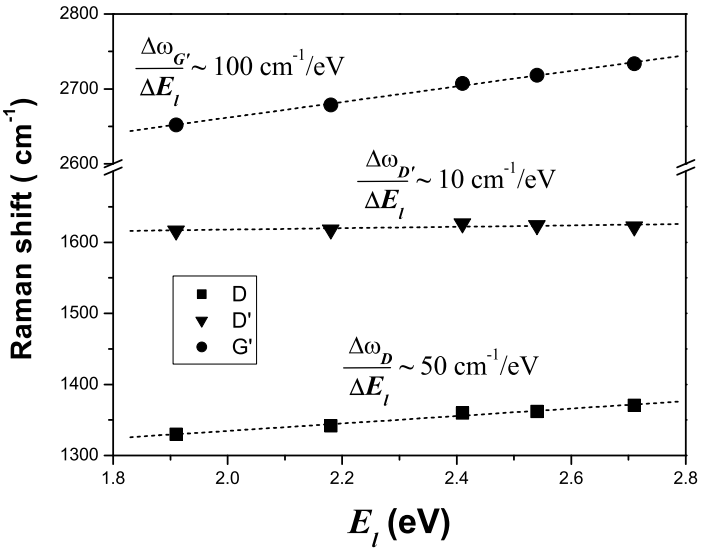

Figure 5.4: Plot of the frequencies (wavenumbers) of the D, D', and G' bands *vs* the excitation laser energy (E_l) for the spectra depicted in Figure 5.3(b).

In 1981, Vidano *et al.* showed that the D and G' bands have a dispersive behavior, since their frequencies change with the incident laser energy [34]. The slope of the dispersion is about 50 and 100 cm^{-1}/eV for the D and G' bands, respectively [observe the dashed lines in Figure 5.3(b) showing the dispersive character of the D and G' bands]. The D' band is also dispersive, although its dispersion has a lower value (~ 10 cm^{-1}/eV). Figure 5.4 shows a plot of the frequencies (wavenumbers) of the D, D', and G' bands *vs* the excitation laser energy (E_l) for the spectra depicted in Figure 5.3(b).

Baranov *et al.* (1987) [35], Pócsik *et al.* (1998) [36], and Matthews *et al.* (1999) [37] proposed that the dispersive behavior of the D band comes from the fact that the wavevector q of the phonon involved in the scattering process couples to the electron wavevector k_0 near the K point in the Brillouin zone, following the relation $q \sim k_0$ (or $q \sim 2k_0$ as proposed by Baranov *et al.*). As the optical transitions are resonant in different electron wavevectors k_0 for different excitation laser energies, the phonon wavevector q should also

be different. Despite the fact that this model qualitatively explains the dispersive behaviour of the D band, these works do not explain the physical process coupling $q \sim k_0$. This point was clarified in the double-resonance model, as discussed in the next section.

5.2 The double-resonance model

Although Baranov *et al.* have mentioned the double-resonance model for the D band [35], it was Thomsen and Reich in 2000 who explained that the momentum conservation can be satisfied in the coupling $q \sim 2k_0$ if the electron is elastically back-scattered by a defect with momentum $d \sim 2k_0$ [38]. Figure 5.5 shows the double-resonance model proposed by Thomsen and Reich [38]. Parts (a), (b), and (c) refer to intermediate states occurring during the scattering process. The left side of Figures 5.5(a), 5.5(b), and 5.5(c) show the first Brillouin zone of graphene, while the right side shows the plot of the π electrons dispersion curve along the direction $\overline{KMK'}$, obtained from the tight-binding method (see section 1) [2]. The small dark and white circles refer to the electron and hole, respectively. The process starts in Figure 5.5(a) with the graphene system absorbing an incident photon with energy $E_I = \hbar\omega_I$ from the incident laser beam, creating an electron-hole pair. Since the valence and conduction bands (π and π^*, respectively) touch each other at the K (K') point in the electron dispersion curve of graphene, the resonant optical transitions occur between the π and π^* bands near the K (K') point.

In order to keep the momentum conservation, the sum of the electron and hole momenta should be equal to the incident photon momentum, *i. e.*, $\vec{q}_e + \vec{q}_h = \vec{q}_i$. However, since the incident photon momentum is much smaller than the electron momentum near the K point ($|\vec{q}_i| \sim |\vec{q}_e|^{-3}$), the electron and hole momenta are equal in modulus, and opposite in direction, *i. e.*, $\vec{q}_h \sim -\vec{q}_e$ (vertical transition). Therefore, as depicted in Figure 5.5(a), the electron and hole wavevectors are $\vec{q}_0$ and $-\vec{q}_0$, respectively. In the graphics depicted on the right side of Figure 5.5, the top scale refers to the component of the electron wavevector $\vec{q}_e$ along the line $\overline{KMK'}$, and the bottom scale refers to the component of the hole wavevector $\vec{q}_h$ along the line $\overline{KMK'}$. Observe that the bottom scale (referring to the hole) is inverted in order to clarify the momentum conservation during the scattering process.

Due to the linearity of the energy dispersion of the π electrons around the K (K') point,

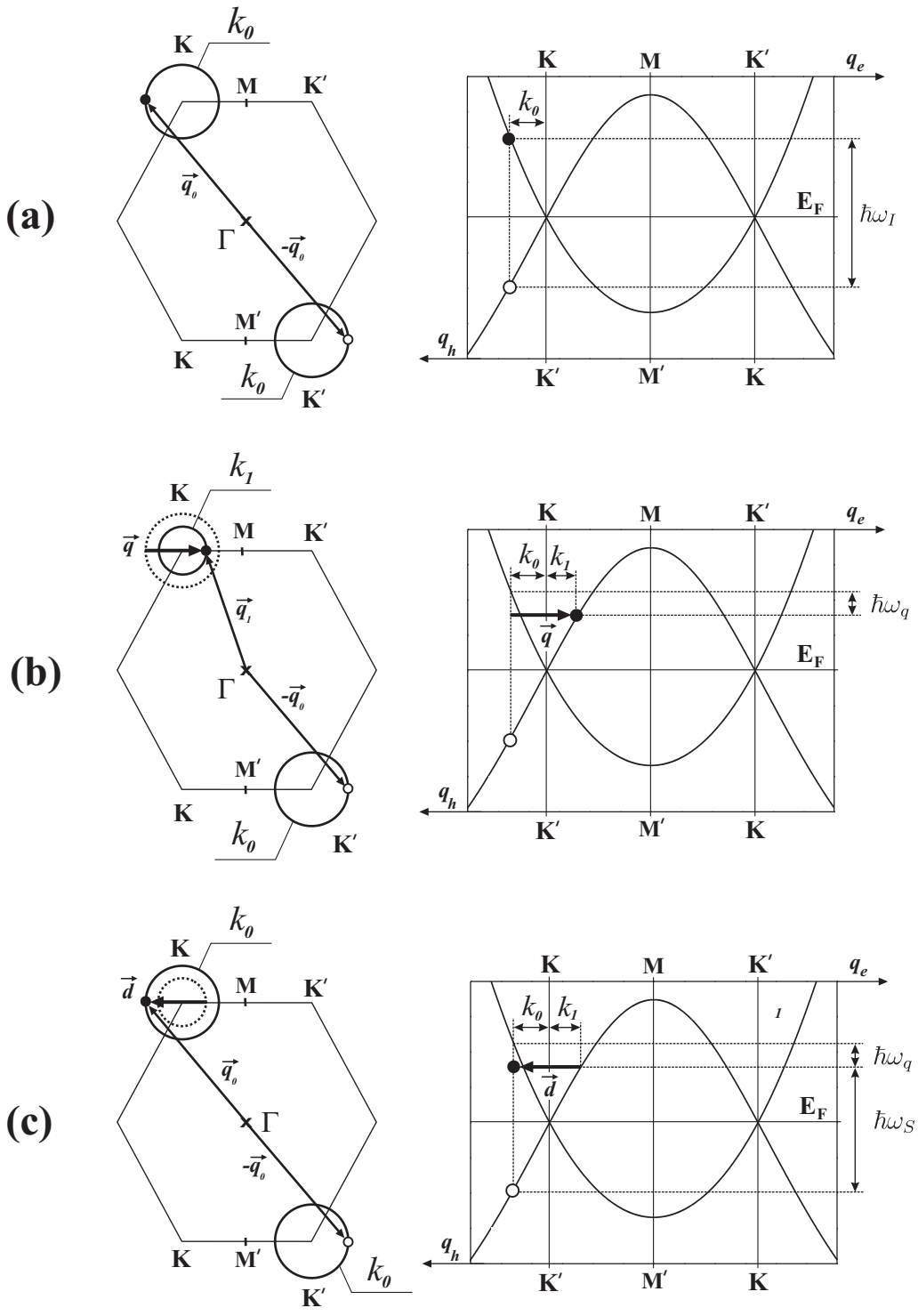

Figure 5.5: The double-resonance intravalley model proposed by Thomsen and Reich [38] for the D band which is, in fact, one of the possible processes giving rise to the D' band. Parts (a), (b), and (c) refer to intermediate states occurring during the scattering process. The left side of parts (a), (b), and (c) show the first Brillouin zone of graphene, while the right side shows the plot of the π electrons dispersion curve along the direction $\overline{KMK'}$, obtained from the tight binding method (see section 1) [2]. The small dark and white circles refer to the electron and hole, respectively. Left panels do not show energy information.

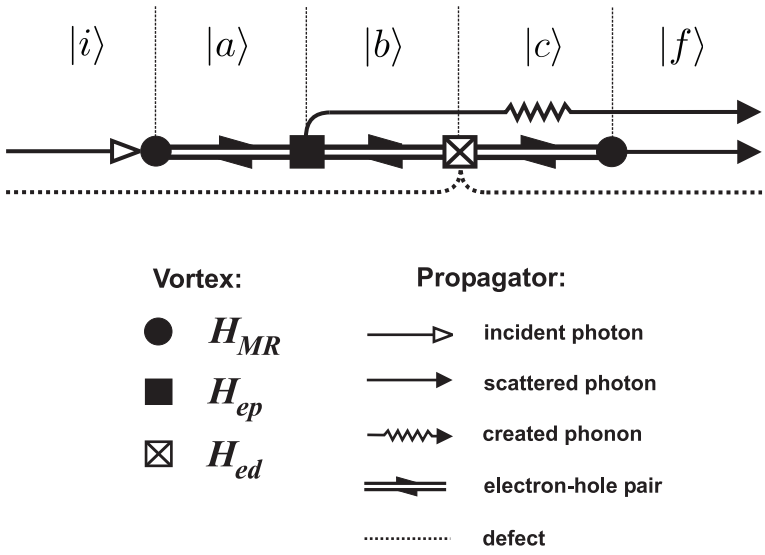

Figure 5.6: The Feynman diagram related to the the one-phonon Raman process depicted in Figures 5.5 and 5.8.

the electron and the hole energies after the absorption of the incident photon are $\epsilon^c(\vec{q}_0) = \hbar\omega_I/2$ and $\epsilon^v(-\vec{q}_0) = -\hbar\omega_I/2$, respectively (we are considering here that the energy is zero at the Fermi level). The collection of all electrons and holes able to take part in this process form two circles [left side of Figure 5.5(a)] centered at the K and K' points[1], respectively, with the same radius given by $k_0 = \hbar\omega_I/2A$, where $A = \sqrt{3}\gamma_0 a/2$ is the slope of the π and π^* bands near the K and K' points (see equation 2.14) [40, 41].

Figure 5.5(b) shows the configuration of the system after the electron has been scattered by a phonon with wavevector $\vec{q}$, and energy $\hbar\omega_q$, to a point belonging to another circle centered at the K point, in a intravalley process. The electron wavevector is now $\vec{q}_1 = \vec{q} + \vec{q}_0$, and the radius of the circle is given by $k_1 = k_0 - \hbar\omega_q/A$.

Figure 5.5(c) shows the configuration of the system after the electron is elastically scattered by a defect with wavevector $\vec{d} = -\vec{q}$, to a point belonging the circle of radius k_0, in another intravalley process. The process finishes when the electron recombines with the hole, and the graphene system emits a photon with energy $\hbar\omega_S = \hbar\omega_I - \hbar\omega_q$.

Figure 5.6 shows the Feynman diagram associated with the process depicted in Figure 5.5. The process starts with the system in an initial state $|\,i\rangle$, where the material system (graphite sheet) is in the ground state, and there is an incident photon with energy $\hbar\omega_I$

[1]We are disregarding the trigonal warping effect, which is important when moving away from K (K') [39].

and a defect. Next, the graphite sheet absorbs the incident photon, creating the electron-hole pair. In this stage, the system is in the first intermediate state $|a\rangle$. Next, a phonon with energy $\hbar\omega_q$ is created, and the system goes to the intermediate state $|b\rangle$. After that, the electron is elastically scattered by the defect, and the system goes to the intermediate state $|c\rangle$. Finally, the electron recombines with the hole, creating a photon with energy $\hbar\omega_S = \hbar\omega_I - \hbar\omega_q$. The system is then in the final state $|f\rangle$. Observe that the configuration of the system depicted in parts (a), (b), and (c) of Figure 5.5 refer to the intermediate states $|a\rangle$, $|b\rangle$, and $|c\rangle$ in Figure 5.6, respectively.

The one-phonon Raman process depicted in Figures 5.5 and 5.6 is, in fact, a fourth-order time dependent perturbative quantum process, and the Raman cross section associated with this process is given by equation 3.62, reproduced here in the form:

$$\sigma = \left(\frac{\hbar\omega_I}{\overline{I}_0}\right)\frac{2\pi}{\hbar^2}\sum_f \left|\sum_{a,b,c}\frac{\langle f|H_{MR}|c\rangle\langle c|H_{ed}|b\rangle\langle b|H_{ep}|a\rangle\langle a|H_{MR}|i\rangle}{(E_i-E_a)(E_i-E_b)(E_i-E_c)}\right|^2 \delta(E_i-E_f)\ . \quad (5.1)$$

The eigenstates of H_0 in equation 5.1 can be written as:

$$\begin{aligned} |\,i\,\rangle &= |n_I, n_S, n_q, \phi^i\rangle\ , \\ |\,a\,\rangle &= |n_I-1, n_S, n_q, \phi^a\rangle\ , \\ |\,b\,\rangle &= |n_I-1, n_S, n_q+1, \phi^b\rangle\ , \\ |\,c\,\rangle &= |n_I-1, n_S+1, n_q+1, \phi^f\rangle\ . \end{aligned} \quad (5.2)$$

In order to understand why the Raman process depicted in Figures 5.5 and 5.6 is a double-resonance process, the three terms in the denominator of Equation 5.1 should be calculated, and the result for two of them should be zero. The eigenvalues E_i, E_a, E_b, and E_c can be evaluated by taking the sum of the energies of the propagators present in each eigenstate of H_0 (see details in section 3.2.4) in Figure 5.6, and the results are given, respectively, as:

$$E_i = E_{photon} = \hbar\omega_I\ , \quad (5.3)$$

$$E_a = E_{eh} = \varepsilon^c(\vec{q}_0) - \varepsilon^v(\vec{q}_0) = \frac{\hbar\omega_I}{2} - \left(-\frac{\hbar\omega_I}{2}\right) = \hbar\omega_I\ , \quad (5.4)$$

$$E_b = E_{eh}+E_{phonon} = \varepsilon^c(\vec{q}_1)-\varepsilon^v(\vec{q}_0)+\hbar\omega_q = \left(\frac{\hbar\omega_I}{2}-\hbar\omega_q\right)-\left(-\frac{\hbar\omega_I}{2}\right)+\hbar\omega_q = \hbar\omega_I\ , \quad (5.5)$$

$$E_c = E_{eh}+E_{phonon} = \varepsilon^c(\vec{q}_0)-\varepsilon^v(\vec{q}_0)+\hbar\omega_q = \left(\frac{\hbar\omega_I}{2}\right)-\left(-\frac{\hbar\omega_I}{2}\right)+\hbar\omega_q = \hbar\omega_I+\hbar\omega_q\ . \quad (5.6)$$

It can be seen from Equations 5.3 to 5.6 that the terms $(E_i - E_a)$ and $(E_i - E_b)$ in the denominator of Equation 5.1 are null, since the eigenvalues E_i, E_a, and E_b are equal to

the incident photon energy $\hbar\omega_I$.[2] Therefore, the process depicted in Figures 5.5 and 5.6 is, in fact, a double-resonance process, and the Raman cross section diverges. As pointed out in section 3.2.4, in a complete analysis the sum inside the square modulus in Equation 5.1 should take into account all different timing orders in the Raman process. However, this sum is composed by twenty-four terms in a fourth-order Raman process, and its evaluation does not give any additional important information.

Let us now understand how the double-resonance process proposed in references [35] and [38] explains the dispersive behavior of the D band. Figure 5.7 shows in a schematic way two distinct double-resonance processes involving incident photons with different frequencies. Let us suppose that one of them belongs to the red range of frequency in the visible spectrum, and the other belongs to the blue range. Since the energy of the "blue" photon is larger than the energy of the "red" photon ($\hbar\omega_B > \hbar\omega_R$), the resonant optical transitions for these two photons will occur for different wavevectors $k_B = \hbar\omega_B/2A$ and $k_R = \hbar\omega_R/2A$. The modulus of the phonon wavevector associated with the two processes are given by:

$$q_B = k_B + \left(k_B - \frac{\hbar\omega_{q_B}}{A}\right) = \frac{\hbar\omega_B - \hbar\omega_{q_B}}{A} \ , \tag{5.7}$$

$$q_R = k_R + \left(k_R - \frac{\hbar\omega_{q_R}}{A}\right) = \frac{\hbar\omega_R - \hbar\omega_{q_R}}{A} \ . \tag{5.8}$$

As pointed in section 3.1.3, the phonon energy is usually 10 times smaller then the incident photon energy, that is $\hbar\omega_q \sim \hbar\omega_I/10$. Therefore, equations 5.7 and 5.8 can be rewritten, respectivaly, as:

$$q_B \sim \frac{\hbar\omega_B}{A} \ , \tag{5.9}$$

$$q_R \sim \frac{\hbar\omega_R}{A} \ . \tag{5.10}$$

Therefore, the wavevector of the phonons involved in both processes depicted in Figure 5.7 are different, being $q_B > q_R$, since the modulus of the phonon wavevector are linearly proportional to the incident photon energy, as imposed by equations 5.9 and 5.10. In this case, the experimental value of the D band dispersion ($\partial\omega_D/\partial E_l \sim 50\,\mathrm{cm}^{-1}/\mathrm{eV}$) would be associated to the slope $\partial\omega_q/\partial q$ of a specific branch in the phonon dispersion curve of

[2] Observe that we have disregarded in equations 5.3 to 5.6 energy related to the defect. In fact, strictly speaking, since we considered the defect as an entity not belonging the perfect graphite lattice, it should be added to all eigenvalues of H_0, once the associated propagator is present in all eigenstates of H_0 (see Figure 5.6). However, we consider the defect energy having a constant value all over the process and, since we are interested in the difference between the eigenvalues, its inclusion can be neglected.

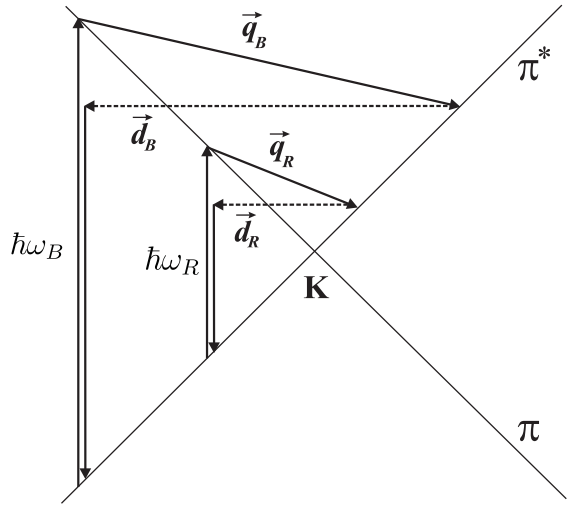

Figure 5.7: Two distinct double-resonance intravalley processes involving incident photons with different energies where $\hbar\omega_B > \hbar\omega_R$. The phonon wavevectors in both processes are different, being $q_B > q_R$. The modulus of the phonon wavevector is linearly proportional to the incident photon energy, as imposed by equations 5.9 and 5.10.

graphite. The relation between $\partial\omega_q/\partial q$ and $\partial\omega_D/\partial E_l$ can be obtained as:

$$q \sim \frac{E_l}{A} \quad \longrightarrow \quad \frac{\partial\omega_q}{\partial q} \sim A\,\frac{\partial\omega_D}{\partial E_l} \sim 320\,\mathrm{cm}^{-1}/\mathrm{\AA}^{-1}\ . \tag{5.11}$$

At this point, the double-resonance model proposed in reference [38] needs to be generalized, because the wavevectors of the phonons involved in the double-resonance process depicted in Figure 5.5 are close to the Γ point in the first Brillouin zone of graphite, where no phonon branch with such a dispersion ($\partial\omega_q/\partial q \sim 320\,\mathrm{cm}^{-1}/\mathrm{\AA}^{-1}$) can be observed in the range of frequency compatible with the D band frequency (Raman shift).

In 2000, Saito *et al.* published a work explaining that the double-resonance process giving rise to the D band is an intervalley process, where the electron (or hole) is scattered by the phonon (or defect) from a point belonging to a circle centered at the K point to another circle centered at an inequivalent K' point [40]. Figure 5.8 shows the intervalley process proposed by Saito *et al.* giving rise to the D band in the Raman spectrum of graphite.

Figure 5.9(a) shows in the top part the double-resonance mechanism depicted in Figure 5.8, where a phonon with wavevector $\vec{q}_{inter}$ connects two points belonging to the circles with radii k_0 and k_1 centered at K and K', respectively. If the vector $\vec{q}_{inter}$ is measured from the Γ point in the Brillouin zone, its end is close to the K'' point in Figure 5.9(a), which is equivalent to the K point by symmetry. Therefore, Saito *et al.* have shown that the assignment of the D band experimental data in the phonon dispersion curve of

graphite should be made in the neighborhood of the K point [40]. Figure 5.9(a) also shows in the bottom part an intravalley process, where the end of the wavevector of the phonon involved in the double-resonance process ($\vec{q}_{intra}$) is close to the Γ point. Saito *et al.* explained that the mechanism associated with the D' band is a double-resonance intravalley process, such as that depicted in Figures 5.5 and 5.7, and successfully assigned the D' band data to the iLO phonon branch near the Γ point in the first Brillouin zone of graphene (see Figure 2.2 for reference). Moreover, Saito *et al.* applied the double-resonance model to identify many weak Raman features in graphite materials, giving strong support to the double-resonance model and showing that it is possible to obtain experimental information about the phonon dispersion relation of graphite near the Γ and K points with light scattering [40].

Saito *et al.* also explained that the set of all possible phonon wavevectors connecting any points in the circles around K and K' in the double-resonance mechanism giving rise to the D band (measured from the Γ point) have ends in the area between the two circles around K'' [see Figure 5.9(b)]. The radii of the inner and outer circle around K'' correspond, respectivelt, to the modulus of the difference and the sum of the radii of the two circles around K and K'. There is a high density of phonon wavevectors $\vec{q}$ satisfying the double-resonance mechanism when the ends of the wavevectors measured from the Γ point are in the inner and outer circles around K'' [40, 41]. The phonons associated with the singularities in the density of $\vec{q}$ vectors are expected to make a significant contribution to the double-resonance Raman spectra. The D and G' bands are associated with the phonons with ends at the outer circle around K''. On other hand, the D' band is associated with the phonons with ends at the outer circle around Γ, since it comes from an intravalley scattering.

In 1998, Tan *et al.* presented experimental data showing that the Raman spectra of graphite have an anomalous behavior, where there is a shift in the D band frequency in the Stokes and anti Stokes spectra, and that the frequency of the overtone G' band is not twice the D band frequency [42]. In 2002, we showed that there are four possible double-resonance mechanisms associated with either the Stokes or the anti-Stokes processes (see Figure 5.10) [41]. We explained that considering these four processes, the D band is composed of two peaks, D_1 and D_2 in the Stokes spectrum, and D_2 and D_3 in the anti-Stokes spectrum. On the other hand, the G' band is composed of a single peak, centered at $2\omega_{D_1}$ in the Stokes spectrum and at $2\omega_{D_3}$ in the anti-Stokes spectrum [41].

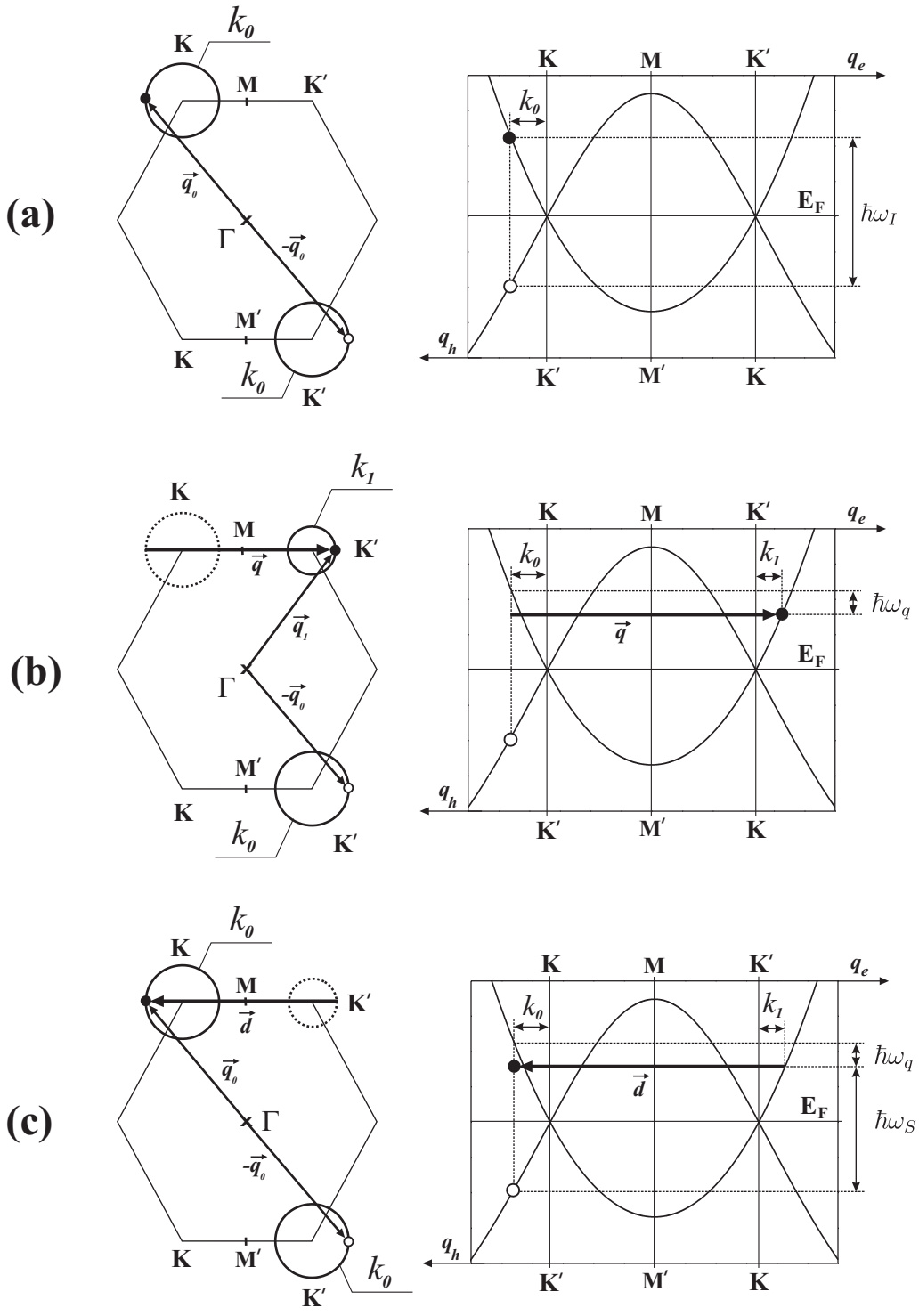

Figure 5.8: A double-resonance intervalley process proposed in reference [40] for the D band. Left panels do not show energy information.

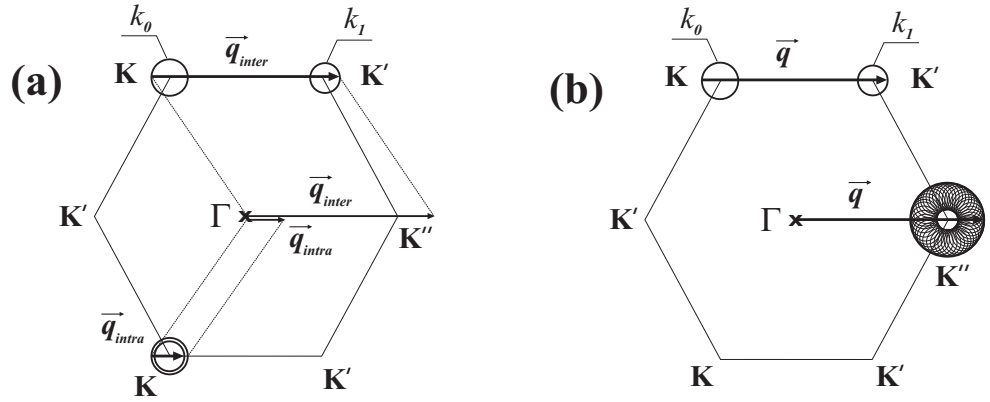

Figure 5.9: **(a):** In the top part, an intervalley process where a phonon with wavevector $\vec{q}_{inter}$ connects two points belonging to the circles with radii k_0 and k_1 around K and K', respectively. If the wavevector $\vec{q}_{inter}$ is measured from the Γ point in the Brillouin zone, its end is close to the K'' point, which is equivalent to the K point by symmetry. In the bottom part, an intravalley process where the end of the wavevector of the phonon ($\vec{q}_{intra}$) is close to the Γ point. **(b):** The set of all possible phonon wavevectors connecting any points in the circles around K and K' in the double-resonance mechanism giving rise to the D band (measured from the Γ point) have ends in the area between the two circles around K''. The radii of the inner and outer circles around K'' correspond, respectively, to the modulus of the difference and the sum of the radii of the two circles around K and K'.

We can discuss now how the definitive assignment of the D band experimental data in the phonon dispersion curve of graphite was made. The iTO phonon branch is totally symmetric in its whole extension inside the first Brillouin zone of graphene (except at the Γ point), including the K point neighborhood (see Table 2.4). As pointed out in the beginning of this chapter, Tuinstra and Koenig proposed that the D band would be generated by the totally symmetric mode, which strongly modulates the susceptibility [7, 8]. Ferrari and Roberston associated the D band with the iTO phonon branch based in these symmetry arguments [43, 44]. However, despite these evidences, the assignment of the D band was a subject of intense discussion [45], because the theoretical calculations for the iTO phonon branch in the dispersion curve of graphite around the K point usually does not fit the D band experimental dispersion data [16], and many works associated the D band experimental data to the iLO branch dispersion [36, 37, 38, 40, 46].

This discussion was finished in 2004, when Maultzsch *et al.* determined the iLO and iTO branches in the phonon dispersion curve of graphite, based in very accurate experimental data obtained from inelastic X-ray scattering [47], and showed that the experimental value of the D band dispersion matches the iTO phonon branch determined experimentally by

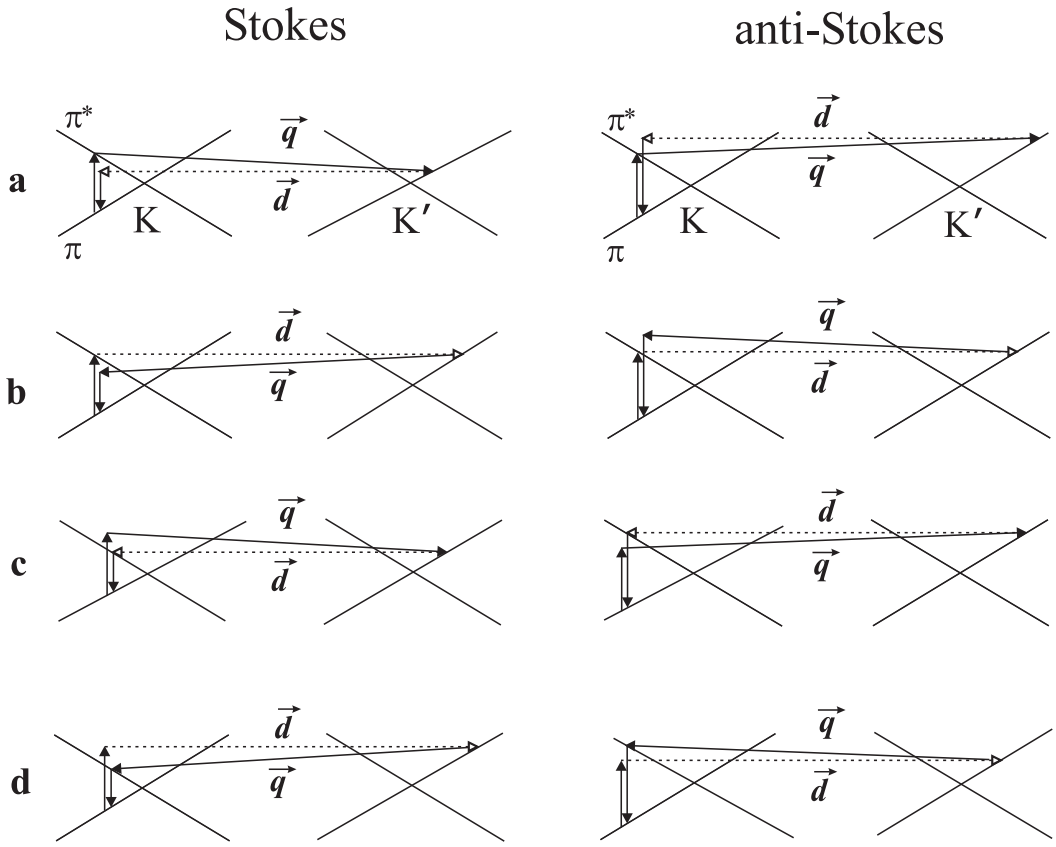

Figure 5.10: **Right side:** Four possible double-resonance mechanisms giving rise to the D band associated with the Stokes processes. The process **a** is the same as that depicted in Figure 5.8, where the incident photon is in resonance with the $\pi - \pi^*$ transition, and the inelastic scattering of the electron occurs before the elastic back-scattering. In the process **b**, the scattering from a point around K to a point around K' is elastic and occurs before the inelastic back-scattering, associated with the emission of the phonon. In processes **c** and **d**, the incident photon is not in resonance with the $\pi - \pi^*$ transition, and the resonance occurs only for the scattered photon in the electron-hole recombination. In this case, the electron-hole pair must have a different momentum compared to processes **a** and **b**. In process **c**, the inelastic scattering of the electron occurs before the elastic back-scattering, whereas in process **d** the elastic scattering occurs before the inelastic scattering process. **Left side:** Four possible double-resonance mechanisms associated with the anti-Stokes scattering, which are equivalent to the Stokes processes **a**, **b**, **c** and **d** in the right side. The only difference in this case is that the inelastic scattering, connecting points around the K and K' points, is due to the absorption of a phonon with wavevector $\vec{q}$.

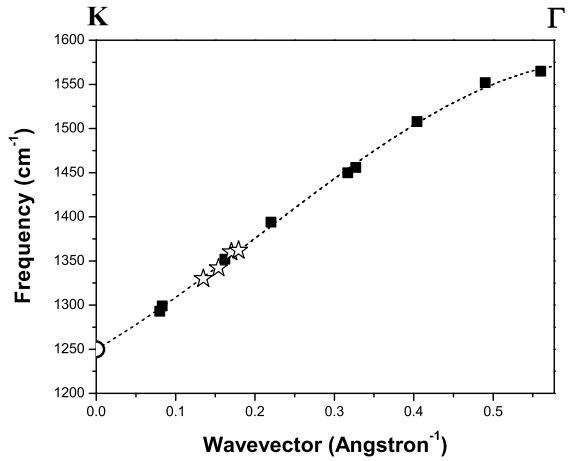

Figure 5.11: plot of the D band experimental data (Raman shift) on the iTO phonon branch. The D band data (open stars) were obtained from the spectra depicted in Figure 5.3. The solid squares are the inelastic X-ray scattering data obtained by Maultzsch *et al.* (taken from reference [50]). The open circle is the value of the frequency of the iTO phonon branch at the K point calculated by Piscanec *et al.* taking into account the Khon anomaly effect [49].

the inelastic X-ray scattering [48]. Moreover, Maultzsch *et al.* pointed out that, since the scattering of electrons by phonons in the double-resonance process connects two points belonging to the same electron band, the phonon involved must be fully symmetric and, therefore, it should belong to the iTO branch [48]. Also in 2004, Piscanec *et al.* [49] showed that the overbending of the iTO phonon branch near the K point observed in phonon dispersion curves calculated by first principles is associated with Khon anomaly effect [49]. The calculations made by the authors taking in account the Khon anomaly effect successfully explained the experimental data obtained by Maultzsch *et al.* (2004).

Figure 5.11 shows the plot of our D band experimental data (Raman shift) on the iTO phonon branch obtained by Maultzsch *et al.*. The D band data (open starts) were obtained from the spectra depicted in Figure 5.3. The solid squares are the inelastic X-ray scattering data obtained by Maultzsch *et al.* (taken from reference [50]). The open circle is the value of the frequency of the iTO phonon branch at the K point calculated by Piscanec *et al.* taking into account the Khon anomaly effect [49].

5.3 The triple-resonance condition in the G' band scattering

Despite the wide acceptance of the double-resonance model, the discussion has been restricted to the scattering of electrons by phonons (or defects, in the case of the D and D' bands scattering). No emphasis has been given to the scattering of holes, although it is also a possible Raman process. We will show now that by considering the scattering of holes in the Raman process giving rise to the G' band, the occurrence of the triple-resonance is also possible. The prediction of a triple-resonance condition among all processes giving rise to the G' band is confirmed by the fact that this two-phonon band is usually as strong as the allowed one-phonon G band in the Raman spectrum of graphite (see Figure 5.1).

Figure 5.12 shows a two-phonon Stokes Raman scattering giving rise to the G' band. The process starts with the graphene system absorbing an incident photon with energy $\hbar\omega_I$ creating the electron-hole pair, where the electron and hole wavevectors are $\vec{q}_0$ and $-\vec{q}_0$, respectively, belonging to two circles of radii $k_0 = \hbar\omega_I/2\,A$. In Figure 5.12(b), the electron is scattered by a phonon with wavevector $\vec{q}$, and energy $\hbar\omega_q$, to a point belonging to a circle centered at an adjacent K' point. The electron wavevector is now $\vec{q}_1 = \vec{q} + \vec{q}_0$, and the radius of the circle centered at the K' point is given by $k_1 = k_0 - \hbar\omega_p/A$. In the double-resonance models for the G' band considering only the scattering of electrons by phonons, the next step would be the electron being scattered back to the circle with radius k_0 by a phonon with wavevector $-\vec{q}$. However, Figure 5.12(c) shows a different situation in which the hole is scattered by another phonon with wavevector $-\vec{q}$, and energy $\hbar\omega_q$, to a point belonging to a circle centered at an adjacent K point, in an intervalley process. The hole wavevector is now $-\vec{q}_1 = -\vec{q} - \vec{q}_0$, and the radius of the circle centered at the K' point is also given by $k_1 = k_0 - \hbar\omega_p/A$. The process finishes when the electron recombines with the hole, and the graphene system emits a photon with energy $\hbar\omega_S = \hbar\omega_I - 2\hbar\omega_q$.

Figure 5.13 shows the Feynman diagram associated with the process depicted in Figure 5.12. The Raman cross section in this case can be written as:

$$\sigma = \left(\frac{\hbar\omega_I}{I_0}\right)\frac{2\pi}{\hbar^2}\sum_f \left|\sum_{a,b,c}\frac{\langle f|H_{MR}|c\rangle\langle c|H_{hp}|b\rangle\langle b|H_{ep}|a\rangle\langle a|H_{MR}|i\rangle}{(E_i - E_a)(E_i - E_b)(E_i - E_c)}\right|^2 \delta(E_i - E_f)\ , \quad (5.12)$$

where H_{hp} is the hole-phonon interaction hamiltonian. Based on Figure 5.13, we can

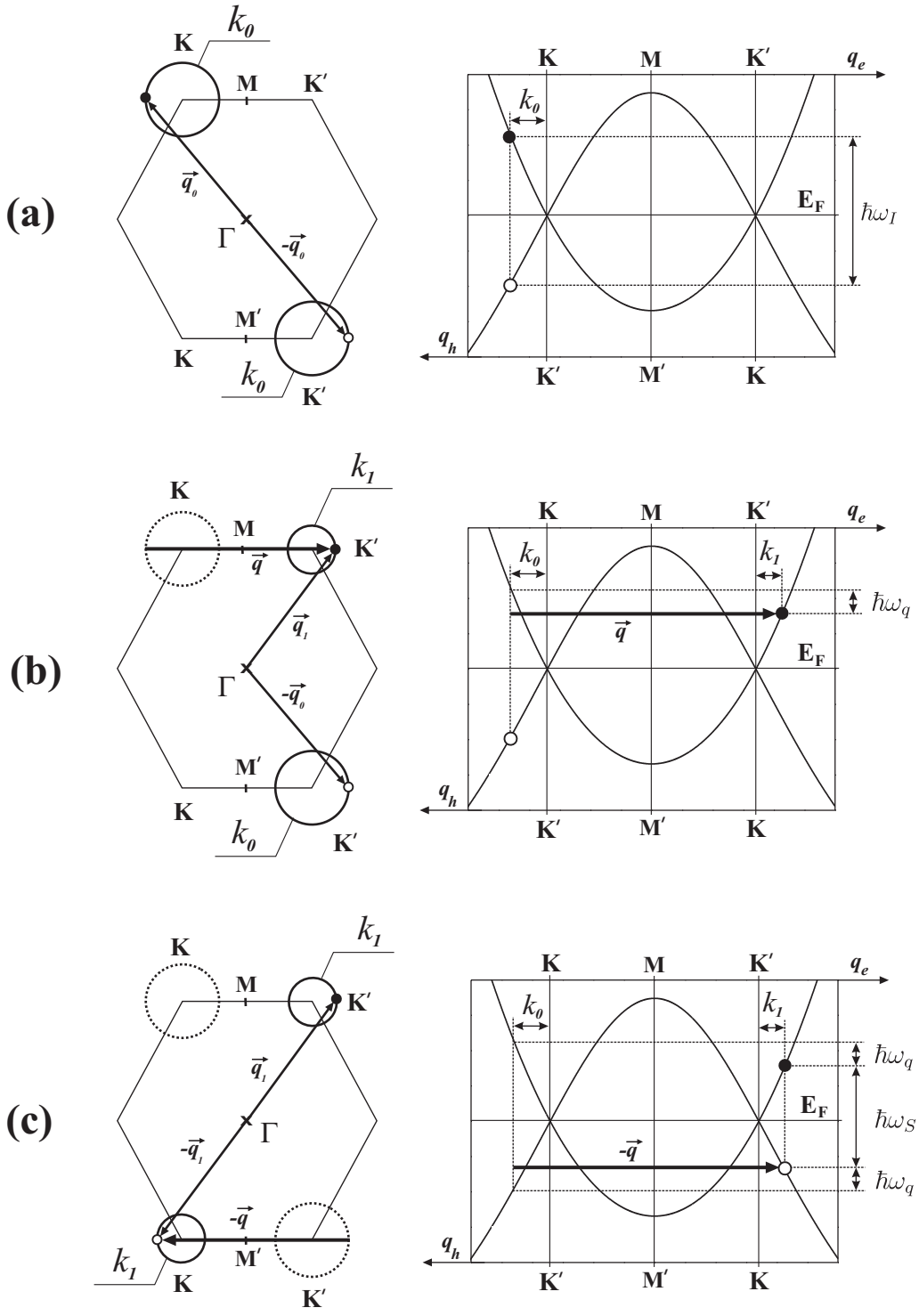

Figure 5.12: A triple-resonance intervalley process giving rise to the G' band. Left panels do not show energy information.

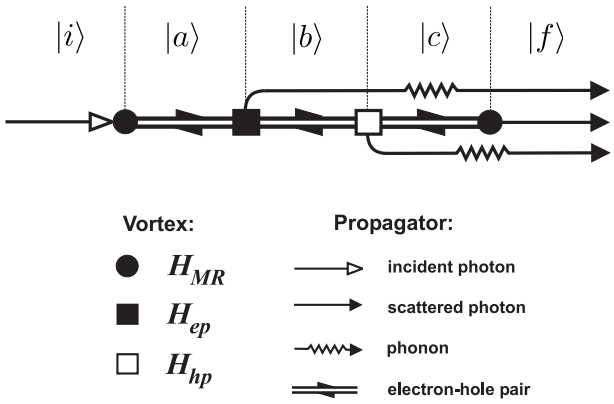

Figure 5.13: The Feynman diagram related to the the two-phonon triple-resonance Raman process depicted in Figure 5.12.

calculate the eigenvalues E_i, E_a, E_b, E_c as:

$$E_i = E_{photon} = \hbar\omega_I \ , \tag{5.13}$$

$$E_a = E_{eh} = \varepsilon^c(\vec{q}_0) - \varepsilon^v(\vec{q}_0) = \frac{\hbar\omega_I}{2} - \left(-\frac{\hbar\omega_I}{2}\right) = \hbar\omega_I \ , \tag{5.14}$$

$$E_b = E_{eh} + E_{phonon} = \varepsilon^c(\vec{q}_1) - \varepsilon^v(\vec{q}_0) + \hbar\omega_q = \left(\frac{\hbar\omega_I}{2} - \hbar\omega_q\right) - \left(-\frac{\hbar\omega_I}{2}\right) + \hbar\omega_q = \hbar\omega_I \ , \tag{5.15}$$

$$E_c = E_{eh}+2E_{phonon} = \varepsilon^c(\vec{q}_1)-\varepsilon^v(\vec{q}_1)+2\hbar\omega_q = \left(\frac{\hbar\omega_I}{2} - \hbar\omega_q\right)-\left(-\frac{\hbar\omega_I}{2} + \hbar\omega_q\right)+2\hbar\omega_q = \hbar\omega_I \ . \tag{5.16}$$

It can be seen from Equations 5.13 to 5.16 that the three terms in the denominator of Equation 5.12 are null, since the eigenvalues E_i, E_a, E_b, E_c are all equal to the incident photon energy $\hbar\omega_I$. Therefore, the process depicted in Figures 5.12 and 5.13 is, in fact, a triple-resonance process.

The G' band is a special case of two-phonon Raman scattering, since it is not associated with any maximum in the phonon density of states, and its intensity is comparable with the allowed one-phonon G band, as can be seen in Figure 5.1.

Finally, it is worth to noticing that the π electron dispersion energy near to the K and K' points in the first Brillouin zone of graphene, which are linear and symmetric with respect to the Fermi level, makes possible the occurrence of triple-resonance processes, a very unusual case in the optical spectroscopy of crystals.

Chapter 6

Raman Spectra of Nanographite Ribbons

Graphite-related materials have been the object of many studies[1] in the last decades including, and in particular, carbon nanotubes that can be obtained by rolling up a graphene sheet into a tube of nanometric diameter [2]. This large interest in carbon nanotubes is due to the fact that they are quasi-one dimensional (1D) systems and have many properties related to quantum confinement [2]. Another form of a 1D carbon system is a strip of a graphene sheet, which is called a nanographite ribbon in the literature [51, 52]. Previous works have shown the existence of 1D graphite nanostructures in polyperinaphthalene (PPN) [53, 54] and in fibers obtained from carbon nanotubes subjected to high temperature and pressure [55]. The synthesis of nanographite ribbons grown from a SiC arc-discharge has been reported, including the observation of a ribbon bifurcated along the c-axis, forming a nano Y-junction [56]. This is a promising structure in the field of nano-electronic devices because of its interesting transport properties [57].

In this Chapter, a Raman study of nanographite ribbons on an HOPG substrate is reported. We found a way to differentiate the Raman signal of the ribbon from that of the substrate, the Raman signal of the ribbon having the same order of magnitude as that of the substrate, despite the much smaller number of illuminated carbon atoms ($\sim 10^{-3}$). The Raman peak of the nanographite ribbons also exhibits an intensity dependence on the light polarization direction relative to the nanographite ribbon axis. These results are explained by the quantum confinement of the electrons in the 1D band structure of the nanographite ribbons, combined with the anisotropy of the light absorption in 2D graphite.

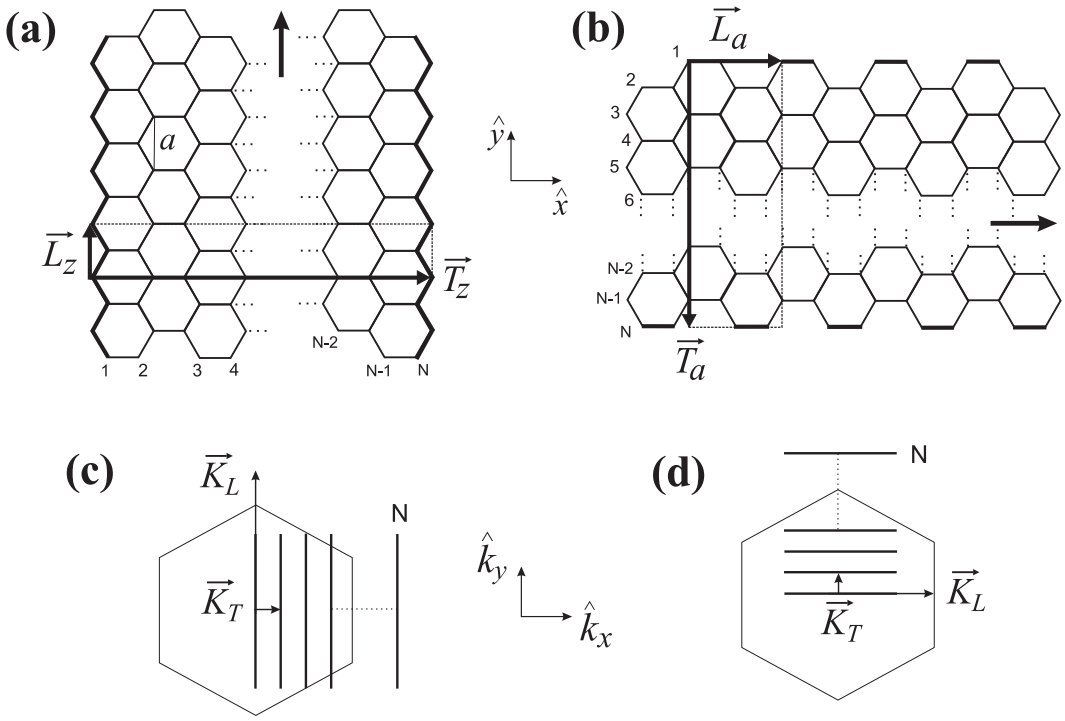

Figure 6.1: General structure of a zigzag [part (a)] and an armchair [part (b)] nanographite ribbon with N dimer lines. Parts (c) and (d) show the Brillouin zone of zigzag and armchair nanographite ribbons (cutting lines), respectively, inside the first Brillouin zone of 2D graphite.

6.1 Electronic properties of nanographite ribbons

There are two basic types of nanographite ribbons: zigzag and armchair, defined according to the form of the edge. Figures 6.1(a) and 6.1(b) show the general structure of zigzag and armchair nanographite ribbons, respectively. The longitudinal ($\vec{L}$) and transversal ($\vec{T}$) vectors define the unit cells in real space. In both cases, the unit cell has 2N atoms, where N is the number of dimer lines.

The Brillouin zone of the nanographite ribbon can be obtained by the zone folding technique [51, 52]. Due to the translational symmetry of the vector $\vec{L}$, we have a continuum of wave vectors along the direction of $\vec{K}_L$ for a ribbon of infinite length. On the other hand, because of the finite size of nanographite ribbon in the transversal direction, we have N possible discrete k values separated by $|\vec{K}_T|$. Figures 6.1(c) and 6.1(d) show the Brillouin zone (cutting lines) of zigzag and armchair nanographite ribbons respectively, inside the first Brillouin zone of 2D graphite. Table 6.1 shows the vectors $\vec{L}$, $\vec{T}$, $\vec{K}_L$, and $\vec{K}_T$ for zigzag and armchair ribbons with N dimer lines.

Table 6.1: Vectors $\vec{L}$, $\vec{T}$, $\vec{K}_L$, and $\vec{K}_T$ for zigzag and armchair ribbons with N dimer lines.

	$\vec{L}$	$\vec{T}$	$\vec{K}_L$	$\vec{K}_T$
zigzag	$a\,\hat{y}$	$\frac{a}{\sqrt{3}}\left[\frac{3(N-1)}{2}\right]\hat{x}\ ,\ (N\ odd)$ $\frac{a}{\sqrt{3}}\left[\frac{3N}{2}-1\right]\hat{x}\ ,\ (N\ even)$	$\frac{2\pi}{a}\,\hat{k}_y$	$\frac{2\pi}{\frac{a}{\sqrt{3}}\left[\frac{3(N-1)}{2}\right]}\hat{k}_x\ ,\ (N\ odd)$ $\frac{2\pi}{\frac{a}{\sqrt{3}}\left[\frac{3N}{2}-1\right]}\hat{k}_x\ ,\ (N\ even)$
armchair	$a\sqrt{3}\,\hat{x}$	$\frac{a(N-1)}{2}\,\hat{y}$	$\frac{2\pi}{\sqrt{3}a}\,\hat{k}_x$	$\frac{4\pi}{a(N-1)}\,\hat{k}_y$

The electronic structure of nanographite ribbons is formed by 1D sub-bands due to the quantization of k space in the transversal ribbon direction. These 1D sub-bands are obtained by the projection of the dispersion curves of 2D graphite along the cutting lines [51, 52, 58]. The electronic density of states (DOS) exhibits one-dimensional van Hove singularities [51, 52, 59, 60, 61].

An armchair nanographite ribbon can be either metallic[1] semiconductor, depending on their width. They are metallic if N =3M − 1, where M is an integer number, and semiconductor otherwise. The metallic types exhibit linear energy bands next to the Fermi level, like in a graphite bulk. On the other hand, semiconductors poss an energy gap that decreases as the ribbon width increases. Figures 6.2(a), 6.2(b), and 6.2(c) show the calculated band structure for armchair ribbons with N = 4, N = 5, and N = 6, respectively. Observe that the armchair ribbon with N = 5 is metallic.

The zigzag nanographite ribbons are always metallic. They present a flat band at the Fermi level associated with states localized in the vicinity of the edge (called edge states). Therefore, there is a sharp peak in the electronic DOS of zigzag nanographite ribbons at the Fermi level associated with these flat bands. The origin of the edge states in zigzag edges is discussed in detail in Appendix C. Figures 6.3(a), 6.3(b), and 6.3(c) show the

[1]We are calling here as metallic those nanographite ribbons for which the valence and conduction bands touch each other at the Fermi level. Using the same arguments as those presented in section , we can conclude that they are, in fact, zero gap semiconductors.

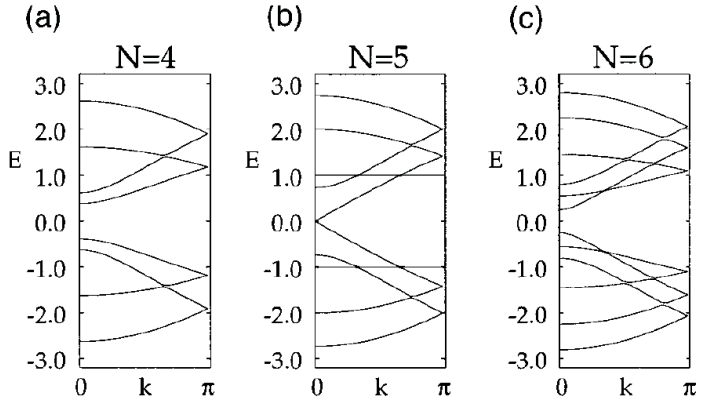

Figure 6.2: Calculated band structures for armchair ribbons with N = 4 (a), N = 5 (b), and N = 6 (c). The horizontal scales are given in $1/a\sqrt{3}$ units. The vertical scale refers to the energy value in eV units divided by $\gamma_0 = 3.033\,\text{eV}$. Taken from reference [52].

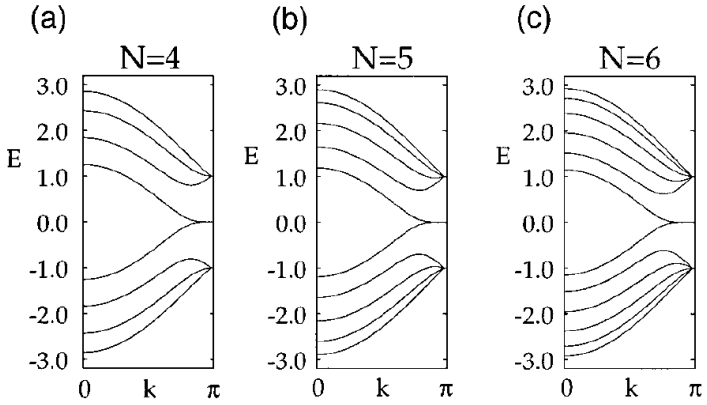

Figure 6.3: Calculated band structures for zigzag ribbons with N = 4 (a), N = 5 (b), and N = 6 (c). The horizontal scales are given in $1/a$ units. The vertical scale refers to the energy value in eV units divided by $\gamma_0 = 3.033\,\text{eV}$. Taken from reference [52].

calculated band structure for zigzag ribbons with N = 4, N = 5, and N = 6, respectively.

6.2 Production and identification of nanographite ribbons

The sample used in the experiment was prepared by the electrophoretic deposition (EPD) of diamond nano-particles on a highly oriented pyrolytic graphite (HOPG) substrate [62]. At a heat-treatment temperature (HTT) of 1600° C, the diamond nano-particles are graphitized, forming nano-graphite sheets [63].

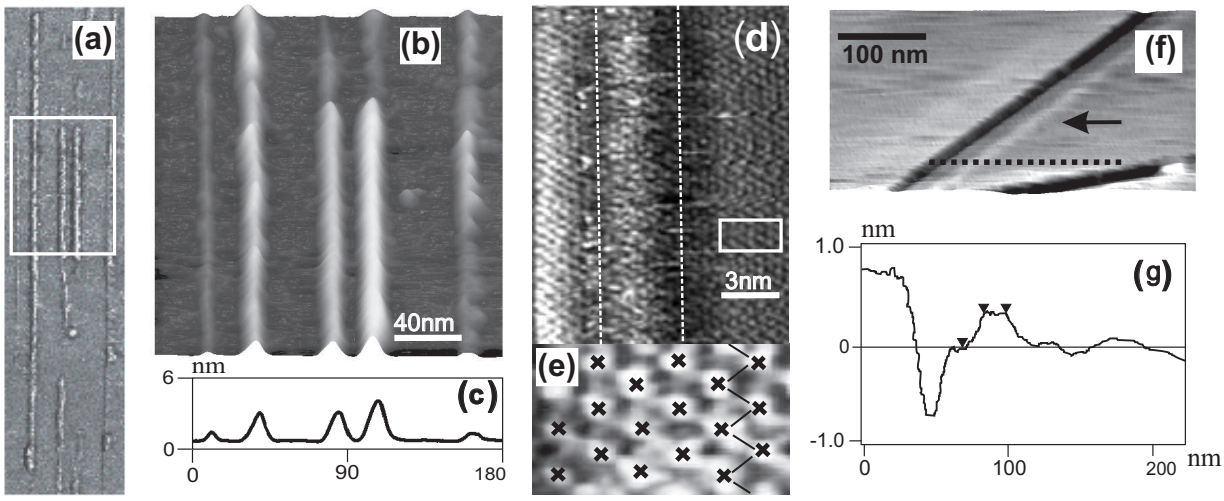

Figure 6.4: **(a):** AFM image of many ribbons parallel to each other. **(b):** Zoom image taken from the white square in part (a). **(c):** The averaged height profile obtained along the ribbons of part (b). **(d):** STM image with atomic resolution of a nanographite ribbon with a width of approximately 3nm. **(e):** Zoom image of the substrate taken from the white square in part(d). **(f):** AFM image of a nanographite ribbon near a step. The arrow indicates the position of the ribbon for reference. **(g):** The height profile obtained through the dotted line on part (f). The sample was produced by Dr. Y. Kobayashi at the Enoki-Fukui Laboratoty, Tokyo Institute of Technology (Japan). STM measurements were performed at the Laboratório Nacional de Luz Síncrontron (Campinas-Brazil) with the help of Dr. Gilberto Medeiros.

Atomic Force Microscopy (AFM) images of the sample were acquired using a Nanoscope IV MultiMode microscope from Veeco Instruments, operating in the intermittent contact (tapping) mode, at room temperature, using standard Si cantilevers. Figure 6.4(a) shows an AFM image, where many ribbons parallel to each other are observed. Figure 6.4(b) shows the zoom image taken from the white square in part (a). The average width of the ribbons is 8 nm and the length can be as large as 1 μm. Figure 6.4(c) shows the averaged height profile obtained along the ribbons of part (b). Figure 6.4(d) shows an STM image with atomic resolution of a nanographite ribbon with a width of approximately 3nm. Figure 6.4(e) shows a zoom image of the substrate taken from the white square in part(d). Figure 6.4(e) shows an AFM image where the presence of a ribbon near a step of the HOPG substrate is evident. The ribbon is larger than 500 nm in length. The height profile [Figure 6.4(g)] shows a height of 0.35 nm, which corresponds exactly to the interlayer distance of bulk graphite, indicating that the ribbon has only one layer of atoms.

6.3 The Raman spectra of nanographite ribbons

Back-scattering micro Raman spectra were taken at room temperature using the DILOR XY triple-monochromator. The laser energy, spot area and power density on the sample were 2.41 eV, $10^{-8}\,\mathrm{cm}^2$ and $3\times 10^5\,\mathrm{W/cm}^2$, respectively. A half-wave plate was coupled with the microscope in order to rotate the polarization of the incident and the scattered light, allowing measurements of the angular dependence of the polarized Raman spectra (see the spectrometer setup schema in Figure 4.1). The spectra were taken in the region of the sample where the ribbons depicted in Figure 6.4(a) were observed.

Figure 6.5(a) shows the Raman spectra obtained with different polarization directions for the incident light. The propagation of the incident light is perpendicular to the graphite plane and θ is the angle between the longitudinal direction of the ribbon and the light polarization ($\vec{P}$) [see inset to Figure 6.5(a)]. The information about the ribbon direction was obtained by AFM [Figure 6.4(a)]. Note that the Raman band is composed of two peaks, centered at $1568\,\mathrm{cm}^{-1}$ and $1579\,\mathrm{cm}^{-1}$, that will be called the G_1 and G_2 peaks, respectively. By increasing the angle θ, the intensity of the G_1 peak decreases gradually, while the intensity of the G_2 peak remains constant. Figure 6.5(b) shows the angular dependence of the G_1 peak intensity fitted by a $\cos^2\theta$ curve. Figure 6.5(c) shows the dependence of the G_1 and G_2 peak frequencies on the laser power used in the experiment, as discussed below. The angular dependence of the Raman spectra shown in Figures 6.5(a) and 6.5(b) can be explained by considering the selection rules for light absorption in graphite and the quantum confinement in 1D nanographite ribbon. The Raman efficiency is related to the absorption coefficient since the one-phonon Raman scattering is a third-order process which involves the absorption of an incident photon, the creation (or annihilation) of a phonon, and the emission of a scattered photon. According to theoretical calculations for 2D graphite, the probability of light absorption $W(\vec{k})$ per unit time is associated with the polarization vector of incident light $\vec{P} = (p_x, p_y)$ and with the wavevector $\vec{k} = (k_x, k_y)$ of the electron by [64, 65]:

$$W(\vec{k}) \;\propto\; \frac{\left|\vec{P}\times\vec{k}\right|^2}{k^2}\;, \tag{6.1}$$

where $\vec{k}$ is measured from the K point situated at the corner of the first Brillouin zone. As previously shown, for points k near the K point, the energy dispersion of π electrons

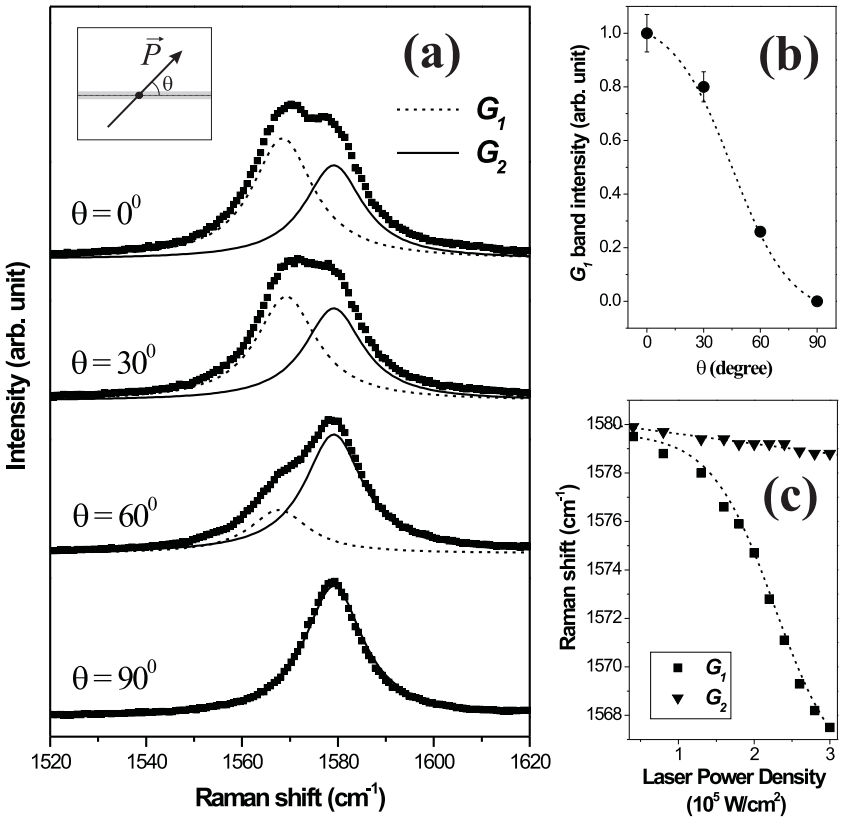

Figure 6.5: **(a):** Raman spectra obtained for light incident with different polarization angles (θ) with respect to the ribbon direction. The inset shows a schematic figure of the sample showing the direction between the ribbon axis and the light polarization vector ($\vec{P}$) for reference. **(b):** Intensity of the G_1 peak versus θ. The dotted line is a $\cos^2\theta$ theoretical curve. The error bars are associated with baseline corrections. **(c):** Raman frequencies of the G_2 (triangles) and G_1 (squares) peaks as a function of the laser power density.

is symmetric around K and is linearly proportional to k, that is,

$$E(k) = \pm A\,k\ , \tag{6.2}$$

where $A = \sqrt{3}\gamma_0 a/2$ is the slope of the π and π^* bands near the K and K' points (see equation 2.14) [40, 41]. In the light absorption process with a fixed laser energy (E_l), the energy separation between the valence and conduction bands is $E_l = 2|E(k)|$. Therefore, the wavevector of electrons involved in the light absorption process forms a circle around the K point with radius $k_{abs} = E_l/2A$. We are disregarding here the trigonal warping effect [2], considering that optical transitions occur sufficiently near to the K point.

Equation 6.1 shows that the light absorption has a maximum for electrons with a $\vec{k}$ vector perpendicular to the polarization of the incident light ($\vec{P}$) and is zero for electrons with $\vec{k}$ parallel to $\vec{P}$. This fact is not measurable in 2D crystalline graphite because the density of electrons involved in the absorption process is isotropic in the graphene plane, and no changes in the Raman intensity can be observed by rotating the incident light polarization [64, 65]. Therefore, based on the fact that the observed G_2 peak frequency is not affected in the angular dependence depicted in Figure 6.5(a), it can be concluded that G_2 is associated with the Γ_6^+ (E_{2g}) vibrational mode of the HOPG substrate (G band) [7, 8].

The situation is different for nanographite ribbons because, in this case, the k dependence on the light absorption process is very important. Figure 6.6(a) shows the network of a zigzag nanographite ribbon with N = 8, where N is the number of dimer lines. As pointed out in section 6.1, the unit cell has 2N atoms, and is defined by the longitudinal ($\vec{L}$) and transverse ($\vec{T}$) vectors. The Brillouin zone, depicted in Figure 6.6(b), is formed by N cutting lines parallel to the direction of the $\vec{K}_L$ vector and separated by $|\vec{K}_T|$ [51, 52]. The optical absorption process in nanographite ribbons is associated with electronic transitions between the valence (π) and conduction (π^*) 1D sub-bands [66, 67]. The quantum confinement of the electrons in a 1D structure restricts the wave vector ($\vec{k}$) of the electrons involved in the absorption process that are associated with transitions between van Hove singularities in the valence and conduction bands. The optical transition energies between van Hove singularities are different for nanographite ribbons with different widths or crystalline directions of the $\vec{L}$ vector [see Figure 6.6(a)]. By scanning the sample, the Raman signal from a particular nanographite ribbon is obtained when the light spot reaches a ribbon that is in resonance with $E_l = 2.41$ eV. The observation of Raman signal from a nanographite ribbon with an intensity similar to the Raman signal from the HOPG substrate is possible when considering the quantum confinement of the electronic states in the ribbon. Note that the number of C atoms from the HOPG substrate under the laser spot is at least 100 times larger than the number of C atoms from the ribbon.

A van Hove singularity in the electronic DOS occurs when a cutting line is tangential to the circle of radius k_{abs}. This condition is obtained for electrons with a wavevector along the $\vec{K}_T$ direction. When the photon energy of the incident laser is resonant with an allowed transition between singularities in the 1D density of electronic states, the Raman scattering cross section diverges, and the intensity of the Raman peak is enhanced. This

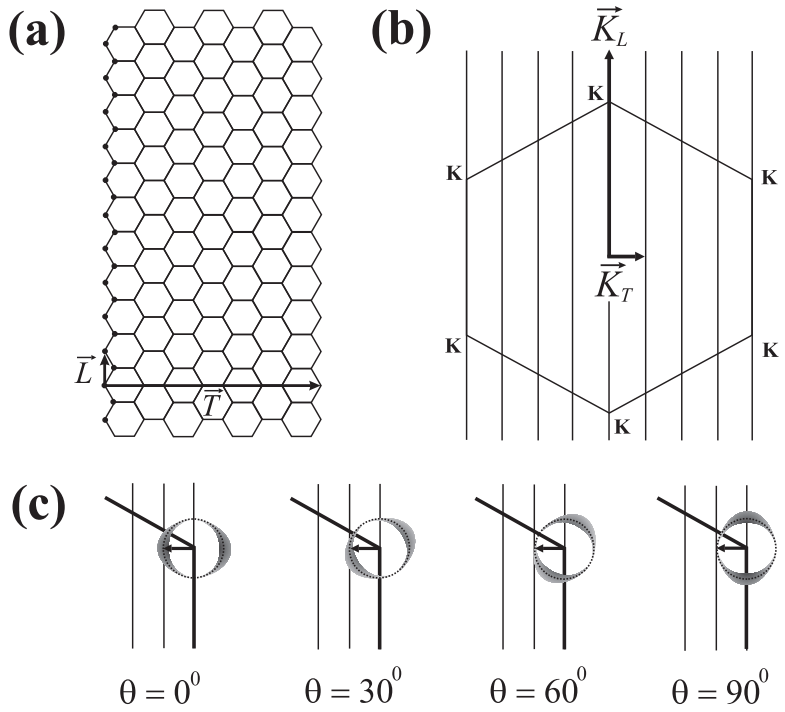

Figure 6.6: **(a):** A zigzag nanographite ribbon network with N = 8. $\vec{L}$ and $\vec{T}$ are the longitudinal and transverse vectors that define the unit cell. **(b):** The reciprocal lattice of the zigzag nanographite ribbon shown in part (a). $\vec{K}_L$ and $\vec{K}_T$ represent reciprocal lattice vectors. **(c):** The k dependence for the probability of absorption [W($\vec{k}$)] near to a K point, for the four different values of θ. The dark region gives a large absorption coefficient. The arrow indicates the K_T vector, that coincides with a maximum in the optical absorption for $\theta = 0°$, and with a node in the optical absorption for $\theta = 90°$ [64, 65].

resonant mechanism selects the $\vec{k}$ vector of electrons and only those along the $\vec{K}_T$ direction are involved in the absorption process, that is, $\vec{k} \parallel \vec{K}_T$.

According to Equation 6.1, the light absorption probability is proportional to the square of the projection of the polarization vector ($\vec{P}$) in the direction perpendicular to the vector $\vec{K}_T$, that is the longitudinal ribbon direction. Figure 6.6(c) shows that the vector $\vec{K}_T$ coincides with a maximum in the optical absorption for $\theta = 0°$, and with a node in the optical absorption for $\theta = 90°$. As θ is the angle between $\vec{P}$ and the longitudinal ribbon direction, we expect that $W(\vec{k}) \propto \cos^2\theta$. Since the Raman intensity is proportional to the number of absorbed photons, it must be also proportional to $\cos^2\theta$. As shown in Figures 6.5(a) and 6.5(b), the intensity of the G_1 peak has a maximum value for the incident light polarized parallel to the longitudinal ribbon direction ($\theta = 0°$), decreases according to $\cos^2\theta$, and is null when $\vec{P}$ is perpendicular to the longitudinal ribbon direction

($\theta = 90°$). The experimental results shown in Figures 6.5(a) and 6.5(b) are in excellent agreement with theoretical predictions and allow us to conclude that the G_1 peak is indeed associated with the Γ_6^+ (E_{2g}) vibrational mode of the nanographite ribbon. It is important to emphasize that the analysis above is valid not only for zigzag type ribbons, but also for ribbons with any type of edge form.

Finally, it is worth analyzing the frequency shift of the two peaks, G_1 and G_2, depicted on Figure 6.5(c). In fact, this shift is due to a thermal effect. Using a low laser power density, one just observes a single peak for the G band at $1580\,cm^{-1}$. The G band splits into two peaks when the laser power is increased. The frequencies of these two peaks decrease with increasing the laser power, owing to the increase in the local temperature. However, the G_1 frequency decreases nonlinearly, whereas the G_2 frequency only exhibits a small laser power dependence. This is expected, since the Raman frequency of nanosized graphite systems exhibit a stronger thermal dependence compared to bulk graphite [68, 69, 70]. The high thermal conduction coefficient in the graphene plane avoids the excessive heating with an increase of the laser power density, keeping the lattice parameters almost constant. However, in finite size systems, the heat dissipation is less efficient, and therefore the force constants are more affected, providing a strong dependence of the Raman frequency on laser power density, as shown in Figure 6.5(c). It is interesting to emphasize that this thermal effect makes it possible to observe a Raman signal from a nanographite ribbon sitting on a graphite bulk substrate.

6.4 Conclusion

In summary, this Chapter presents a Raman study of nanographite ribbons which shows evidence for the anisotropic character of light-scattering in this system. The results give experimental evidence for the predicted existence of a node in the optical absorption in graphite and the presence of van Hove singularities in the DOS of the nanographite ribbons. A more complete characterization of the DOS profile could be performed using a tunable laser. This is a challenging experiment that requires a tunable laser system with high laser power to separate the Raman signal from nanographite ribbons and the HOPG substrate.

Chapter 7

Influence of the Atomic Structure on the Raman spectra of Graphite Edges

In this Chapter, we present combined micro-Raman spectroscopy and scanning probe microscopy experiments, showing that micro-Raman spectroscopy can be used to give information about the local arrangement of carbon atoms in a graphite edge. Specifically, the intensity of a disorder-induced Raman peak is used to define the orientation of the carbon hexagons with respect to the graphite edge, in the so-called armchair or zigzag arrangements, as well as to define the local degree of order for the atomic structure at the edge. The physics leading to this structurally selective effect is explained on the basis of the well-established double-resonance effect [38, 40] that is here applied to a semi-infinite crystal limited by a one-dimensional defect. The work developed in this Chapter represents an effort to improve the understanding of the influence of the defect structure on the Raman spectra of graphite-like systems, which may be very useful to characterize defects in nanographite-based devices.

7.1 Raman spectra of graphite edges

Figure 7.1 shows three Raman spectra obtained at different locations of a highly oriented pyrolytic graphite (HOPG). The inset to Figure 7.1 shows an optical image of the sample, obtained by a CCD camera coupled to the microscope of the micro-Raman system. Locations **1** and **2** are at HOPG edges, while location **3** is on the flat HOPG surface.

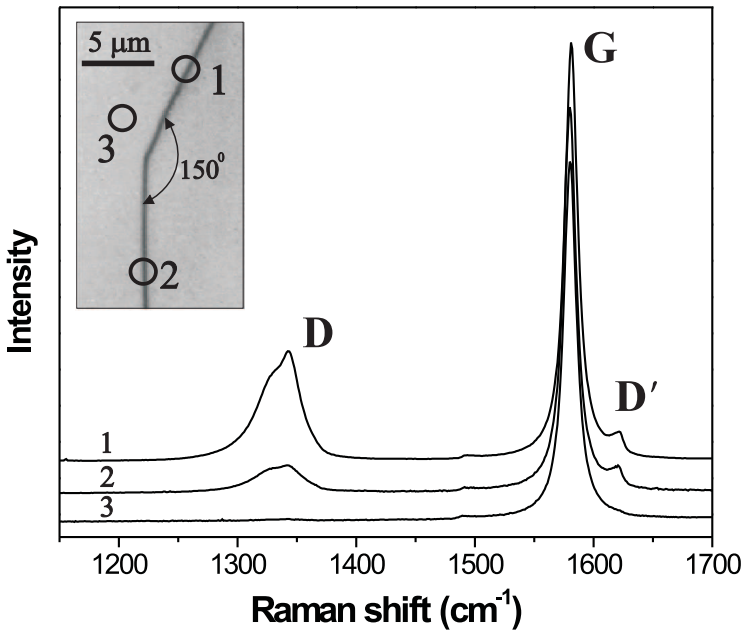

Figure 7.1: Raman spectra obtained in three different regions of the HOPG sample. The spectra were taken at room temperature using a Spectronics monochromator system. The laser power density on the sample was $3\times10^5\,\mathrm{W/cm^2}$ and the laser energy was 1.96 eV. The inset shows an optical image of the step and the regions where spectra **1**, **2** and **3** were taken (open circles).

The light propagation is perpendicular to the HOPG basal plane. The polarization of the incident light is parallel to the edge direction in spectra **1** and **2**. The G band is present in the three spectra with the same intensity (there is no normalization in Figure 7.1).

As explained in Chapter 5, the disorder-induced D and D' bands are observed in defective graphite structures. The mechanism giving rise to these bands, the double-resonance process, involves a resonant optical absorption or emission, and another resonance for an electron or hole scattering by a defect or a phonon in the interior of the Brillouin zone. For the observation of the D and D' bands, therefore, the existence of a defect with a specific wavevector is necessary to satisfy the momentum conservation. In fact, the disorder-induced D and D' bands are observed in spectra **1** and **2**, but not in spectrum **3**. Spectrum **3** was taken in a flat region of the HOPG sample with a perfect crystalline order [see Figure 7.1]. The edge, on other hand, behaves as a defect necessary for momentum conservation in the double-resonance Raman process. However, the most striking result

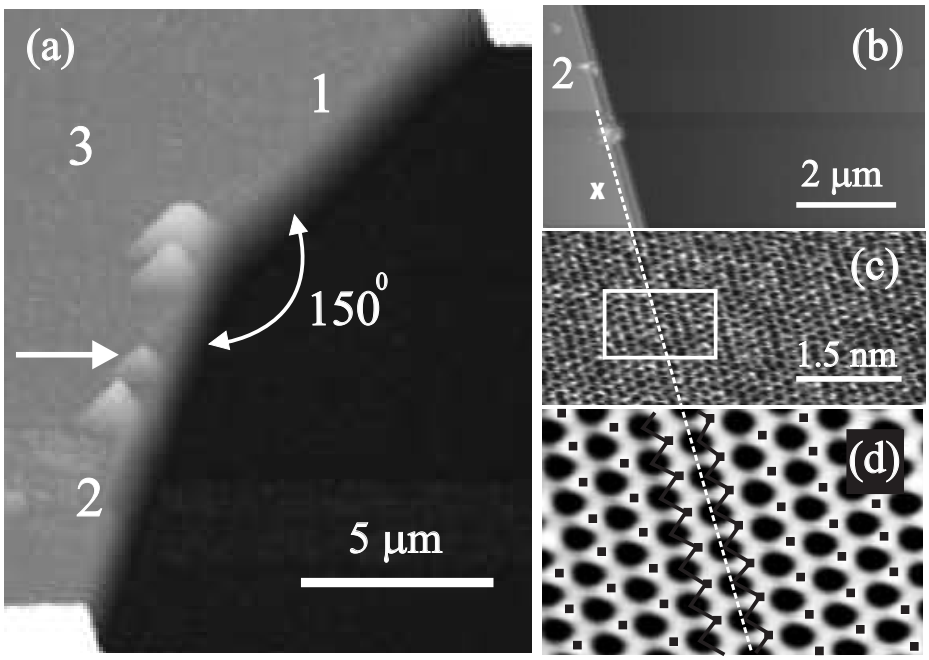

Figure 7.2: **(a):** AFM image of the step on the HOPG substrate where Raman spectra shown in Figure 7.1 were taken. **(b):** AFM image of edge **2**. **(c):** Atomic resolution STM image of the region marked by the white **X** in part (b). The STM measurements were performed under ambient conditions in the constant-height mode. **(d):** FFT filtered image from the region marked by a white square in part (c).

shown in Figure 7.1 is the fact that the D band is about four times less intense in spectrum **2** compared to spectrum **1**, whereas the D' band intensity remains almost constant in both spectra. The different intensities observed for the D band in spectra **1** and **2**, but not for the D' band, indicate an intrinsic structural property of the scattering process in graphite edges.

7.2 Structural characterization of the edges

In order to structurally characterize the sample, scanning probe microscopy measurements were performed using a Nanoscope IV MultiMode microscope from Veeco Instruments. Atomic force microscopy (AFM) data were obtained in the intermittent contact mode, at room temperature, using standard Si cantilevers. Figure 7.2(a) shows an AFM image of the step on the HOPG substrate where the Raman measurements in Figure 7.1 were performed. This structure is a common defect in HOPG surfaces and it is easily formed during the cleavage of graphite planes [71]. The step is composed of two edges, forming

an angle of 150°. The step height is about 230 nm, which corresponds to ∼700 graphene sheets. The spikes along the edges [see white arrow in Figure 7.2(a)] are probably caused by agglomeration of dust deposited on the HOPG surface due to laser heating. Figure 7.2(b) shows another AFM image of the edge **2** and scanning tunneling microscopy (STM) measurements were performed in the region marked by the white **X** in Figure 7.2(b). The raw STM data [Figure 7.2(c)] exhibit atomic spacing resolution, allowing a structural analysis of the edges. Figure 7.2(d) shows a FFT-filtered zoom image of the region marked by a white square in Figure 7.2(c). There are two inequivalent atoms in the graphite unit cell, **A** and **B**, and STM measurements performed in the basal plane of graphite are normally able to distinguish one of them (**B** atoms) [72], which correspond to the dark regions in Figure 7.2(d). The positions of **A** atoms are also indicated by small black squares in Figure 7.2(d). A zigzag line connects **A** and **B** neighbor atoms and, following the white dashed line in Figure 7.2, it can be concluded that edge **2** has a zigzag structure. Therefore, edge **1** must have an armchair structure since, as shown in Figures 7.1 and 7.2(a), edges **1** and **2** form an angle of 150° to each other [see Figure 7.3(b)].

7.3 Influence of the atomic structure in the Raman spectra of the edges

Knowing the edge structures, the Raman scattering events shown in Figure 7.1 can be discussed. Figure 7.3(a) shows one possible inter-valley double resonance process that gives rise to the D band in the Stokes spectra, where an electron of wavevector $\vec{k}_0$ (measured from the K point) absorbs a photon of energy E_l, and is inelastically scattered by a phonon of wavevector $\vec{q}$ and energy E_q to a point belonging to a circle around the K' point, with radius $|\vec{k}_1|$. After that, the electron is scattered back to $\vec{k}_0$ by a defect with wavevector $\vec{d} = -\vec{q}$. Finally, the electron-hole recombination occurs at $\vec{k}_0$, giving rise to the scattered photon with energy $E_l - E_q$. The double resonance process that gives rise the D' band is an intra-valley process [not shown in Figure 7.3(a)], since it connects two points belonging to the same circle around the K point (or the K' point) [40].

The most common case of disorder-induced bands in the Raman spectra of graphite-related materials occurs in samples formed by aggregates of small crystallites. In this case, the crystallite borders form defects in the real space. Since the crystallites have different sizes and their boundaries are randomly oriented, the defect wavevectors exhibit

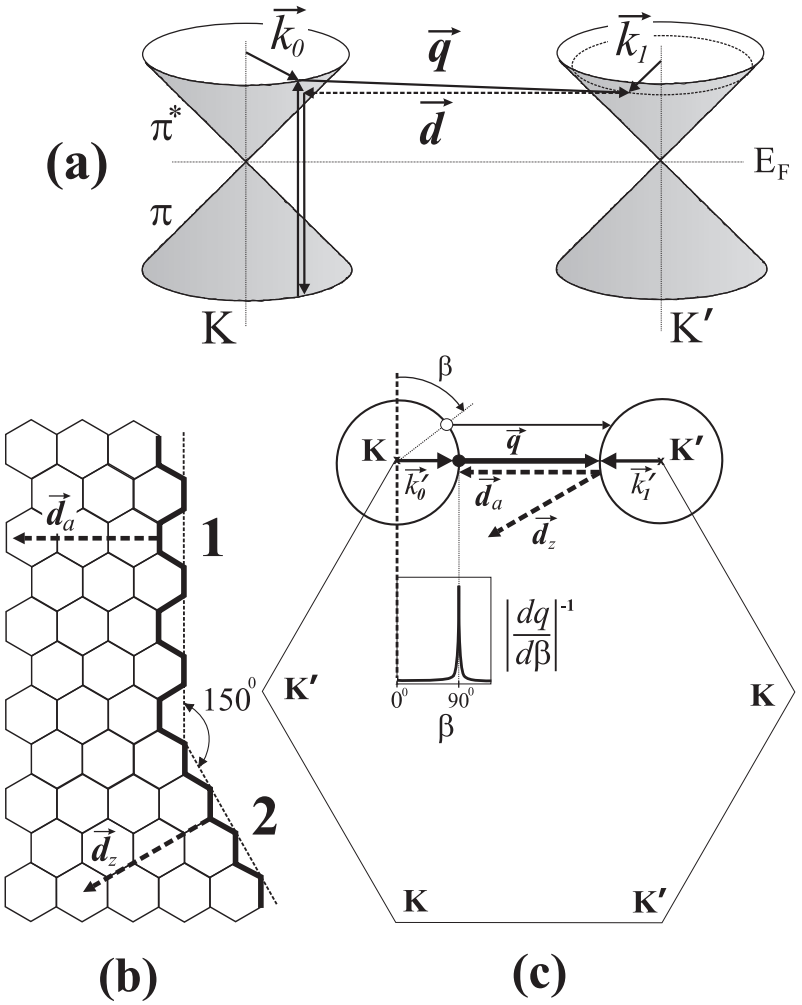

Figure 7.3: **(a):** Representation of a double resonance Raman process that gives rise to the D band in the Stokes spectra of disordered graphite materials [40, 41]. **(b):** Schematic illustration of the atomic structure of the step shown in Figures 7.1 and 7.2. **(c):** First Brillouin zone of 2D graphite, showing the double resonance mechanism for an armchair graphite edge and the density of phonons (inset) associated with this process.

all possible directions and values. Therefore, the existence of a defect with momentum exactly opposite to the phonon momentum is always possible, giving rise to double-resonance processes connecting any pair of points in the circles around the K and K' points. In this case, the intensity of the D band is isotropic and does not depend on the light polarization direction. However, in the case of edges, the D band intensity is anisotropic because the double-resonance process cannot occur for any pair of points. Since, in real space, the edge defect is well localized in the direction perpendicular to the edge, it is completely delocalized in this direction in reciprocal space and, therefore, the wavevector of such defect assumes all possible values perpendicular to the step edge. Consequently,

the defect associated with a step edge has a one-dimensional character and it is only able to transfer momentum in the direction perpendicular to the edge.

Figure 7.3(b) shows the structure of the two kinds of edges shown in Figures 7.1 and 7.2(a). The bold lines show the edge structures, armchair for edge **1** and zigzag for edge **2**. The wavevectors of the defects associated with these edges are represented by $\vec{d_a}$ for armchair and $\vec{d_z}$ for the zigzag edge. Figure 7.3(c) shows the first Brillouin zone of 2D graphite oriented according to the lattice in the real space shown in Figure 7.3(b). Note that only the armchair $\vec{d_a}$ vector is able to connect points belonging to circles centered at two inequivalent K and K' points. Considering the laser energy used in this work (2.54 eV), the radii of the circles around K' and K points are not large enough to allow the connection of any $\vec{k}_1$ and $\vec{k}_0$ states by a zigzag d_z vector. As a result, the inter-valley double-resonance process associated with this defect cannot occur for a perfect zigzag edge. The mechanism depicted in Figure 7.3(c) can thus explain the results shown in Figure 7.1. The D band is much less intense in the spectra obtained in edge **2**, which has a zigzag structure.

It is also important to note the observation of a weak D band in spectrum **2**, where it should be absent. This weak D band can be described to imperfections in the atomic structure of the edge, allowing the scattering of the electron by phonons and defects with wavevectors not perpendicular to the edge. Similar measurements performed on different closely related armchair and zigzag graphite edges (similar to Figure 7.2) show different D band intensity ratios, indicating different degrees of order for the local atomic arrangement at the different edges.

On the other hand, the D' band, around 1620 cm^{-1}, is given by an intra-valley process, which connects points belonging to the same circle around the K (or K') point. In this case, momentum conservation can be satisfied by both $\vec{d_a}$ and $\vec{d_z}$ vectors and, therefore, the observation of the D' band must be independent on the edge structure. This conclusion is confirmed by the experimental result shown in Figure 7.1, where the D' band has the same intensity in both spectra **1** and **2**, with armchair and zigzag structures, respectively. The different intensity behavior for the D and D' bands shown in Figure 7.1 can be, therefore, understood in terms of the one-dimensional character of the defect and the atomic structure of the edge for inter-valley and intra-valley double resonance processes.

The inter-valley double-resonance mechanism in armchair edges can now be discussed in

detail to fully characterize the one-dimensional character of the defect. The arrow starting from the open dot in Figure 7.3(c) represents a possible phonon that can be associated with the D band in an armchair edge, since its wavevector has the same direction as $\vec{d}_a$. In principle all phonons with wavevectors in this direction, connecting circles centered at K and K', satisfy the double resonance condition. An important point to be analyzed is the density of such phonons, which is given by the relation $|dq/d\beta|^{-1} \propto |sec\,\beta|$, where β is an arbitrary angle measured from the armchair edge direction [see Figure 7.3(c)]. As shown in the inset of Figure 7.3(c), the density of phonons exhibits a singularity for $\beta = 90°$. Thus, it can be concluded that the D band is mainly associated with the phonon represented by the bold arrow starting from the black dot in Figure 7.3(c), connecting the electronic states whose wavevectors $\vec{k}'_0$ and $\vec{k}'_1$ have the same direction as $\vec{d}_a$.

7.4 Polarization effects

Figure 7.4 shows the dependence of the D band intensity on the polarization of both the incident and scattered light. The spectra were obtained at the armchair edge (edge **1**), and θ is the angle between the polarization vector of the incident light and the edge direction [see inset of Figure 7.4, where the dotted line represents the armchair edge direction]. For spectra obtained in VV (VH) configuration, the scattered light was analyzed parallel (perpendicular) to the polarization direction of the incident light (see section 4.10). As shown in Figure 7.4, the D band intensity in the VV configuration [I_D(VV)] decreases gradually with increasing value of θ (filled squares), while in the VH configuration, I_D(VH) exhibits a maximum value for $\theta = 45°$ (open squares).

In order to explain these results, it is first necessary to consider the polarization dependence of the optical transitions in graphite. Theoretical calculations predicted the anisotropy in the optical absorption (emission) coefficient of 2D graphite given by [64, 65]:

$$W_{abs,ems} \propto |\vec{P} \times \vec{k}|^2 \ , \tag{7.1}$$

where $\vec{P}$ is the polarization of the incident (scattered) light for the absorption (emission) process, and $\vec{k}$ is the wavevector of the electron measured from the K point. The thickness of the gray region around the circle shown in the inset to Figure 7.4 illustrates the anisotropy in the optical absorption relative to $\vec{P}$ (the thicker the stronger), given by equation 7.1. Note that the light absorption (emission) has a maximum for electrons with

wavevector $\vec{k}$ perpendicular to $\vec{P}$, and it is null for electrons with wavevector parallel to $\vec{P}$. For the mechanism discussed in Figure 7.3(c), the existence of a singularity in the density of phonons that participate in the one-dimensional double resonance inter-valley process restricts the wavevector $\vec{k}$ of the electron to the direction perpendicular to the armchair edge ($\vec{k} = \vec{k}'_0$). In the VV configuration, $\vec{P}$ has the same direction for the incident and scattered light, and since $\vec{k}'_0$ is perpendicular to the armchair edge direction, the coefficients of absorption W_{abs} and emission W_{ems} are both proportional to $cos^2\theta$. In VH configuration, the polarization of the incident and scattered light are perpendicular to each other and, therefore, W_{abs} and W_{ems} are proportional to $cos^2\theta$ and $sin^2\theta$, respectively. Since the Raman scattering involves absorption and emission of photons, the D band intensity depicted in Figure 7.4 is expected to be given by $I_D(VV) \propto cos^4\theta$ and $I_D(VH) \propto sin^2\theta cos^2\theta$. The fit of the experimental data according to these expressions are also shown in Figure 7.4, where solid and dashed lines are the curves obtained for I_D(VV) and I_D(VH), respectively. It is interesting to observe in Figure 7.4 that the minimum values obtained for both I_D(VV) and I_D(VH) are not zero, but correspond in fact to the D band intensity in the Raman spectrum of the zigzag edge **2** (see Figure 7.1). In this way, the angular dependence of I_D(VV) and I_D(VH) were fit considering an intensity background which is related to the double-resonance Raman process associated with imperfections in the edge structure, that also contributes to the D band intensity. As pointed out earlier, the intensity background is different for different graphite edges, giving a measure of the local order of the C atoms arrangement at the different edges. Furthermore, similar measurements on the zigzag edges show that the polarization dependence of the weak D band in spectrum **2** is anisotropic, with minimum intensity when the light polarization is perpendicular to the armchair edge.

Finally, it is worth observing that the anisotropy in the optical transitions of graphitic systems can only be detected in one-dimensional systems, where the wavevectors of the involved electrons are restricted to only one direction. For example, this anisotropy has been detected in the Raman spectra of nanotubes [73] and nanographite ribbons [74], where the electrons are confined in van Hove singularities. In the case of Raman scattering in graphite edges, no quantum confinement occurs but the one-dimensional character of the defect gives rise to a singularity in the density of phonon states associated with the D band double-resonance mechanism, restricting the wavevector of the electrons involved in this process to only one direction.

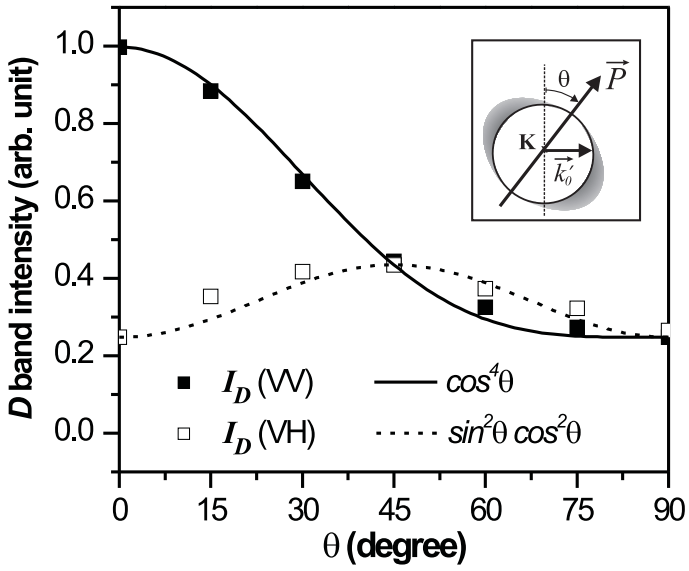

Figure 7.4: Dependence of the D band intensity on the polarization direction of incident and scattered light. The spectra were taken in region **1** (armchair edge) at room temperature using a Dilor XY triple-monochromator system. The laser power density on the sample was 3×10^5 W/cm^2 and the laser energy was 2.41 eV. The inset shows a schematic illustration of the optical anisotropy around the K point of 2D graphite, where the thickness of the gray shadow indicates the absorption strength. θ is the angle between light polarization $\vec{P}$ and the armchair edge direction.

7.5 Analysis of the spacial extension of the D band intensity near to the edge

Figure 7.5(a) shows the Raman spectra of the D and G bands obtained by scanning the armchair edge shown in Figure 7.2(a). The scan was performed in steps of 0.2 μm along a straight line (perpendicular to the edge) with a length of 2 μm [see inset to Figure 7.5(a)]. It is clear in Figure 7.5(a) that the D band intensity increases when the laser spot approaches the edge, and decreases when the laser spot moves way from the edge. On the other hand, the G band intensity does not exhibit significant changes.

Figure 7.5(b) shows the plot of the D band intensity *vs.* the laser spot position. It is clear in the graphic that the spacial dependence of the D band intensity has a Gaussian profile with a full width of half-maximum of $\sim$ 400 nm. In fact, the Gaussian profile shown

in Figure 7.5(b) is due to the laser spot intensity profile (see discussion in section 4.3), showing that the Raman process giving rise to the D band happens in a small region localized near the edges, smaller than the light wavelength in the visible range.

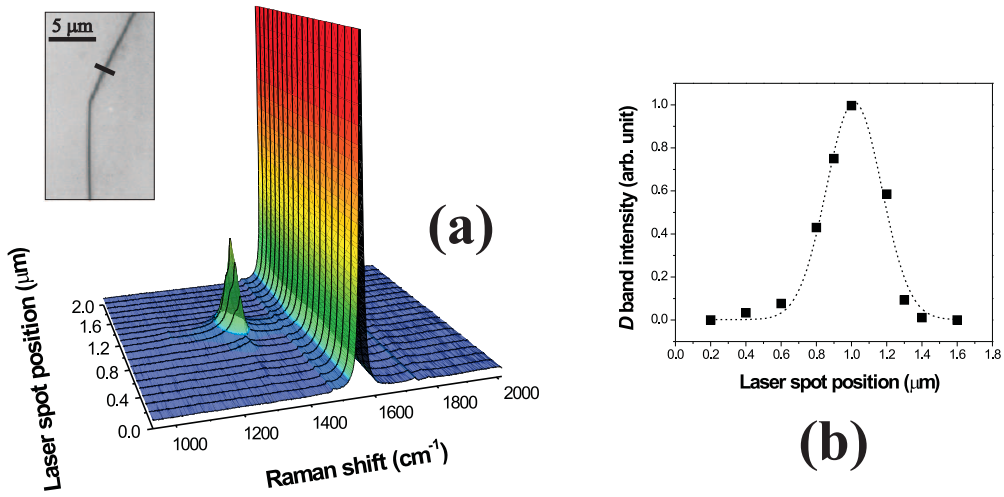

Figure 7.5: **(a):** Raman spectra of the D and G bands obtained by scanning the armchair edge shown in Figure 7.2(a). The scan was performed along a straight line of $2\,\mu$ (bold line indicated in the inset), in steps of $0.2\,\mu$m. **(b):** Plot of D band intensity $vs.$ the laser spot position.

7.6 Final remarks

In summary, this Chapter presents a detailed study of graphite edges with different atomic structures, combining the use of Raman spectroscopy and scanning probe microscopy. This one-dimensional defect selects the direction of the electron and phonon associated with the disorder-induced Raman process, and causes a dependence of the Raman D band intensity on the atomic structure of the edge (strong for armchair and weak for zigzag edge).

Chapter 8

Measuring the crystallite size of nanographites by Raman spectroscopy

8.1 Introduction

In 1969, Tuinstra and Koenig [7, 8] performed systematic Raman and X-ray diffraction studies of many graphitic samples with different in-plane crystallite sizes L_a, and concluded that the ratio of the D and G bands intensities (I_D/I_G) was inversely proportional to the crystallite sizes L_a, which were obtained from the width of the X-ray diffraction peaks. Later, Knight and White summarized the Raman spectra of various graphite systems measured using the $\lambda_l = 514.5\,\text{nm}$ ($E_l = 2.41\,\text{eV}$) laser line and derived an empirical expression which allows the determination of L_a from the (I_D/I_G) ratio [75]. Afterwards, Mernagh *et al.* [29] showed that the ratio I_D/I_G depends strongly on the excitation laser energy (E_l) used in the Raman experiment, revealing that the Knight and White empirical formula was only valid when the experiment was done using the $\lambda_l = 514.5\,\text{nm}$ ($E_l = 2.41\,\text{eV}$) laser line. Despite the fact that the empirical relation relating L_a and I_D/I_G has been widely applied to characterize the nano-graphitic structures, there is no report until now generalizing this relation for Raman experiments performed with different excitation laser energies. In this Chapter, a general formula that gives the crystallite size L_a of nano-graphitic systems for any excitation laser energy in the visible range is presented.

8.2 Experimental Details

The samples used in the experiment were prepared from diamond-like carbon (DLC) films with thicknesses of several microns, heat treated at different temperatures and, thus, giving rise to nanographites with different L_a values. The films were prepared by a pulsed laser deposition method using a highly oriented pyrolytic graphite target in vacuum conditions (5×10^{-6} Torr). The heat treatment was made using an electrical furnace setup, at heat treatment temperatures (HTT) of 1800°C, 2000°C, 2200°C, 2300°C, 2400°C, 2600°C and 2700°C. During the heat treatment process, the samples were kept inside a closed graphite tube, within an inert gas atmosphere (Argon with 99.999% of purity) flowing at 1 liter/min. Before the heat treatment, the sp^3 and sp^2 carbon phases coexist in the samples, but the sp^3 phase completely disappears for heat treatment temperatures above 1600°C [76]. Therefore, the samples used in this work correspond to aggregates of nanographite crystals.

Raman scattering experiments were performed at room temperature using the triple monochromator micro-Raman spectrometer (DILOR XY) for the following laser energies (wavelengths): Krypton 1.92 eV (647 nm) and 2.18 eV (568 nm), and Argon 2.41 eV (514.5 nm), 2.54 eV (488 nm) and 2.71 eV (457.9 nm). The laser power density was always less than 10^5 W/cm^2. The X-ray diffraction measurements were performed in the transmission ($\theta/2\theta$) geometry. The energy of the synchrotron radiation used was 10.0 keV ($\lambda = 0.120$ nm). The transmission geometry was used since the (100) direction lies on the sample surface. Scanning tunneling microscopy (STM) measurements were performed using a Nanoscope II MultiMode microscope from Digital Instruments.

8.3 Dependence of the ratio I_D/I_G on the crystallite size and excitation laser energy

Figure 8.1 shows the STM images of the samples obtained at different heat treatment temperatures. The evolution of the crystallite sizes with increasing heat treatment temperature can be clearly observed in the STM images. The grain boundaries are very clear, and the samples present good structural homogeneity. A high resolution STM analysis shows that the c axis is always perpendicular to the sample surface.

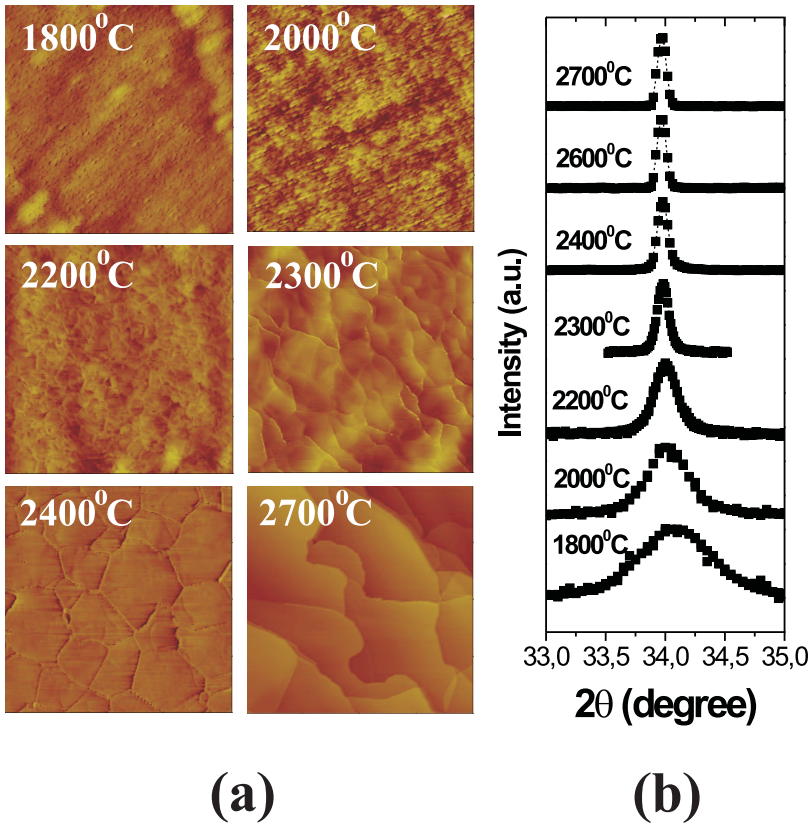

Figure 8.1: **(a):** STM images of the sample heat treated at different temperatures. All images are shown in the same scale ($1\,\mu m \times 1\,\mu m$). **(b):** X-ray diffraction profile of the (100) peak for samples heat treated at different temperatures. The X-ray diffraction measurements were performed at the Laboratório Nacional de Luz Síncrontron (Campinas-Brazil) with the help of Prof. Rogério Paniago and Ms. Letícia Coelho.

Figure 8.2 shows the evolution of the (100) X-ray diffraction peak obtained using synchrotron radiation, for the samples heat treated at different temperatures. The crystallite size L_a was obtained by evaluating the Scherer relation $L_a = 1.84\lambda/\beta cos\theta$, where λ is the synchrotron radiation wavelength (0.120 nm), θ is the position of the (100) peak, and β is the half-height width of the (100) peak of graphite in 2θ(rad) units [77]. In order to avoid the intrinsic instrumental broadening, the β parameter was corrected using the equation $\beta = \sqrt{\beta_m^2 - \beta_{Si}^2}$, where β_m is the half-height width of the measured (100) peak of the samples, and β_{Si} is the half-height width of the (220) peak of a standard silicon sample obtained experimentally.

The analysis of X-ray diffraction profiles is the usual and standard way to measure the crystallite size of nanocrystals. However, this is an indirect measurement and the results

HTT (°C)	L_a (nm) (X-ray)	L_a (nm) (STM)
2700	490	550
2600	340	300
2400	190	220
2300	150	120
2200	65	60
2000	35	40
1800	20	20

Table 8.1: L_a values of the heat treated samples obtained by X-ray diffraction analysis and from the STM images.

can be modified by different factors, such as the asymmetric profile of the peak and the low resolution of the X-ray diffraction setup. In the present case, we have used a high resolution synchrotron X-ray apparatus, and the diffraction peaks are quite symmetric. The mean crystallite sizes were also obtained directly from the STM images and are in good agreement with the L_a parameter obtained by X-ray diffraction (see Table 8.1).

Figure 8.2(a) shows the Raman spectra obtained from graphite films with different crystallite sizes L_a (different heat treatment temperatures), obtained using $E_l = 1.92\,\text{eV}$. Observe that the relative intensity between the D and G bands strongly depends on the crystallite size L_a. In fact, the ratio I_D/I_G decreases with increasing the L_a parameter, in agreement with the results reported by Tuinstra and Koenig [7, 8]. Figure 8.2(b) shows the Raman spectra of the D, G, and D' bands of the sample heat treated at 2000°C ($L_a = 35\,\text{nm}$), for five different laser energy values (1.92 eV, 2.18 eV, 2.41 eV, 2.54 eV, and 2.71 eV). Notice that the ratio (I_D/I_G) is strongly dependent on the excitation laser energy, in accordance with the results reported by Mernagh *et al.* [29]. Therefore, it is clear that the empirical formula proposed by Knight and White [75] for the determination of L_a from the I_D/I_G ratio must be generalized for other excitation laser energies. The ratio between the D' and G bands intensities also exhibits an interesting and particular laser energy dependency, which will be discussed in Chapter 10.

Figure 8.3(a) shows the plot of the integrated intensities of the D and G bands (I_D/I_G) *vs* $1/L_a$ for all samples and laser energies used in the experiment. In order to collapse the different straight lines with a single one, the experimental values I_D/I_G were multiplied by

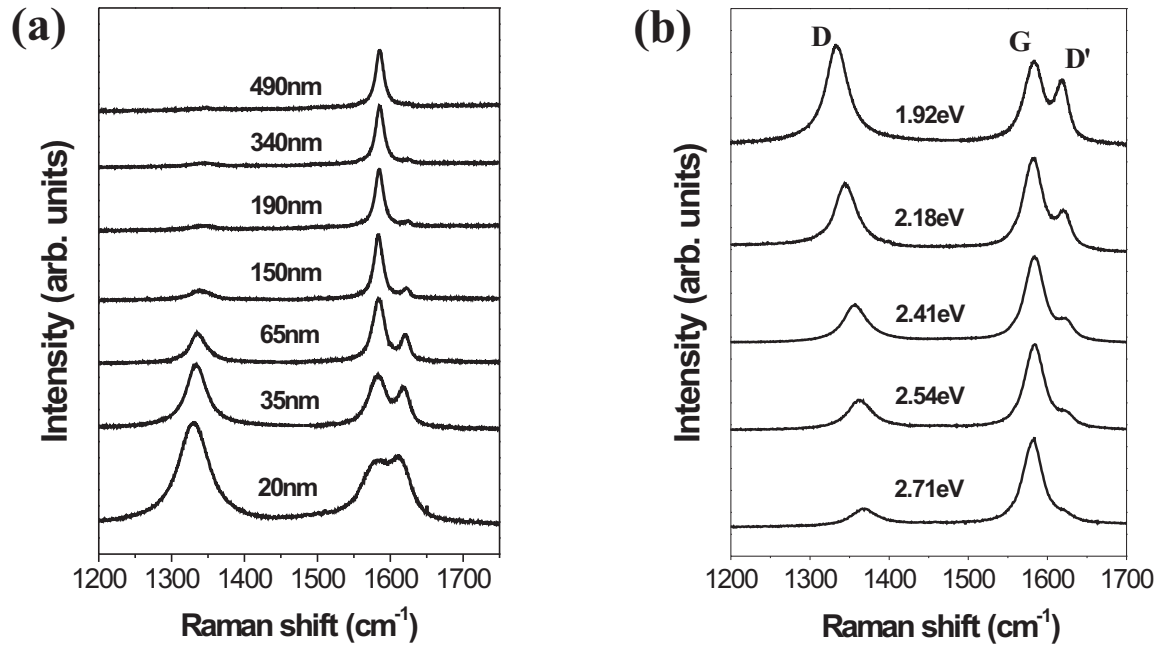

Figure 8.2: **(a):** Raman spectra obtained from graphite films with different crystallite sizes L_a (different heat treatment temperatures) for a fixed $E_l = 1.92\,\text{eV}$. Observe that the ratio I_D/I_G decreases with increasing the L_a parameter. **(b):** Raman spectra of the sample heat treated at 2000°C ($L_a = 35\,\text{nm}$), for five different laser energy values (1.92 eV, 2.18 eV, 2.41 eV, 2.54 eV, and 2.71 eV). All spectra depicted in parts (a) and (b) where normalized in a such way that the G band intensity has the same value for all of them.

different powers of E_l, and the best result was obtained when we multiplied I_D/I_G by the fourth power of the excitation laser energy (E_l^4). Figure 8.3(b) shows that all experimental points collapse in the same straight line in the $(I_D/I_G) * E_l^4$ *vs* $1/L_a$ plot. By fitting the data depicted in Figure 8.3(b), a general expression that gives the L_a crystallite size from the integrated intensity ratio I_D/I_G by using any laser line in the visible range can be obtained and is given by:

$$L_a(nm) = \frac{560}{E_l^4}\left(\frac{I_D}{I_G}\right)^{-1} , \tag{8.1}$$

where E_l is the excitation laser energy used in the Raman experiment in eV units. Considering the laser line wavelength (λ_l) in nm units, equation 8.1 can be rewritten as:

$$L_a(nm) = (2.4 \times 10^{-10})\lambda_l^4\left(\frac{I_D}{I_G}\right)^{-1} . \tag{8.2}$$

The constant of proportionality between L_a and $(I_D/I_G)^{-1}$ obtained from equations 8.1 and 8.2 by using $E_l = 2.54\,\text{eV}$ (13.5 nm) is higher than that reported by Knight and White

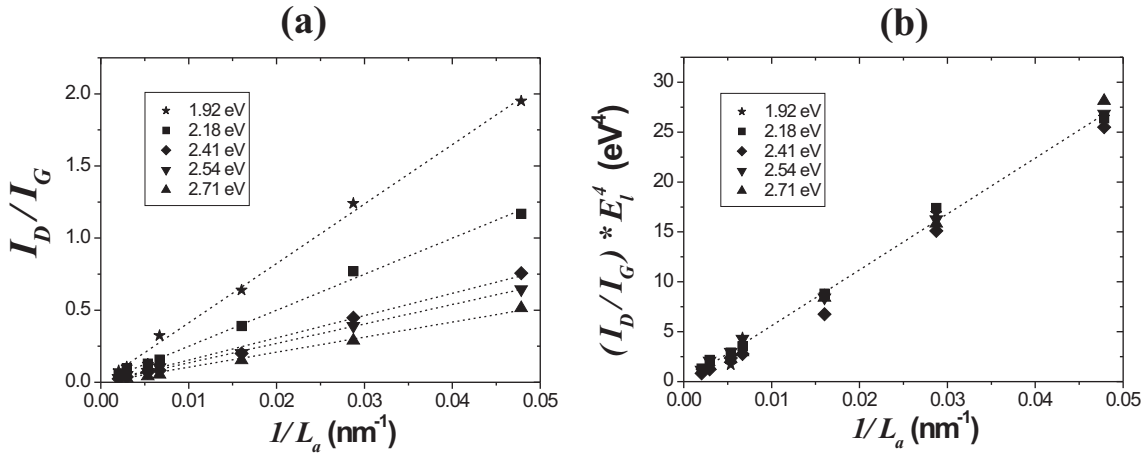

Figure 8.3: **(a):** Plot of the ratio of the integrated intensities of the D and G bands (I_D/I_G) vs $1/L_a$ for all spectra obtained with the five different excitation laser energies. **(b):** All experimental results shown in part (a) collapse in the same straight line in the $(I_D/I_G) * E_l^4$ vs $1/L_a$ plot. The values of L_a used here were those obtained from X-Ray diffraction measurements depicted in Table 8.1.

(4.4 nm) [75]. First, we have considered here the integrated intensities (areas) of the D and G bands instead of using the ratio of the peak amplitudes, as in References [7] and [8]. On the other hand, different values of the proportionality constant can be also ascribed to the instrumental width of the X-ray diffraction peaks obtained from different X-ray sources or to a broad distribution of crystallite sizes in different samples. In the present study, the width of the Raman D band is very narrow, reflecting the narrow distribution of crystallite sizes. It must be stressed that equations 8.1 and 8.2 are certainly valid in the range of laser energies used in this work (visible range).

8.4 Final remarks

In summary, a systematic analysis of the dependence of the ratio between the integrated intensities of the D and G bands (I_D/I_G) on the crystallite size and on the excitation laser energy is presented. The crystallite sizes L_a of nanographite samples were obtained by X-ray diffraction using synchrotron radiation and directly from scanning tunneling microscopy images. Resonant Raman spectroscopy was performed using five excitation laser energies in the visible range. From the analysis of the experimental results, a general formula that allows the determination of the crystallite size L_a by Raman spectroscopy

using any excitation laser energy E_l in the visible range is obtained. We also show that, for a given sample, I_D/I_G is inversely proportional to E_l^4.

Chapter 9

Measuring the degree of stacking order in graphite by Raman spectroscopy

This Chapter reports the analysis of the G' band profile in the Raman spectra of nanographites with different degrees of stacking order. Since the G' band scattering coming from the 2D and 3D phases coexisting in the same sample can be nicely distinguished, the relative volumes of 3D and 2D graphite phases present in the samples can be estimated from their Raman spectra. The comparison between Raman scattering and X-Ray diffraction data shows that Raman spectroscopy can be used as an alternative tool for measuring the degree of stacking order of graphitic systems.

9.1 Introduction

Raman spectroscopy plays an important role in the structural characterization of graphitic materials. The ratio between the intensities of the disorder-induced D band (at $\sim 1350\,\mathrm{cm}^{-1}$) and the first-order allowed G band (at $\sim 1580\,\mathrm{cm}^{-1}$) I_D/I_G is inversely proportional to the in-plane crystallite size L_a [7, 8, 75, 30]. On the other hand, the second harmonic of the D band, the G' band (at $\sim 2700\,\mathrm{cm}^{-1}$) is very sensitive to structural changes along the c axes, since its profile changes from a single peak to two peaks in the Raman spectra obtained from turbostratic to crystalline graphite [32, 33, 9]. Wilhelm *et al.* suggested that the origin of the double structure of the G' band in crystalline graphite was associated with the stacking order occurring along the c axes [10]. Recent works have reported the

evolution of the G' band in the Raman spectra obtained from one to a multilayer graphene structure [78, 79, 80]. These works show that the G' band of a monolayer graphene is composed by a single peak, whereas a two-peaks profile is observed for samples formed by a large number of graphene layers, giving the definite proof for the hypothesis of Wilhelm *et al.* [10].

This Chapter reports a study of Raman scattering in nanographite samples with different degrees of graphitization. It will be shown that the changes in the G' band from a one-peak to a two-peak profile allow us to distinguish the relative volumes of the 3D and 2D graphitic phases coexisting in the same sample. The comparison between the Raman scattering and X-Ray diffraction data shows that the out-of-plane lattice parameter c and the crystallite thickness L_c can be quantitatively determined from the ratio between the G' band scattering intensities obtained from the 2D and 3D graphite phases.

9.2 Experimental details

The samples used in the experiment are disordered graphite films heat-treated at different temperatures, giving rise to nanographites with different crystallinity degrees. The films were prepared by a pulsed laser deposition method. The heat-treatment was made using an electrical furnace setup, at heat-treatment temperatures (HTT) of 2200°C, 2300°C, 2500°C and 2700°C (see Chapter 8 for details). Previous scanning tunneling microscopy (STM) measurements of the samples show that the crystallites have planar structure and well defined boundaries (see Chapters 8 and 10). Raman scattering measurements were performed using a triple monochromator micro-Raman spectrometer (DILOR XY) using the following laser wavelengths (energies): Krypton 647 nm (1.92 eV) and 568 nm (2.18 eV), and Argon 514.5 nm (2.41 eV), 488 nm (2.54 eV) and 457.9 nm (2.71 eV).[1] X-ray diffraction measurements where performed using a Rigaku setup, in ($\theta/2\theta$) geometry, using a copper X-ray emission tube.

[1] It is important to characterize the G' band intensity behavior with different excitation laser lines, since the G' band scattering is known to exhibit a resonance behavior, as explained in Chapter 5 [41].

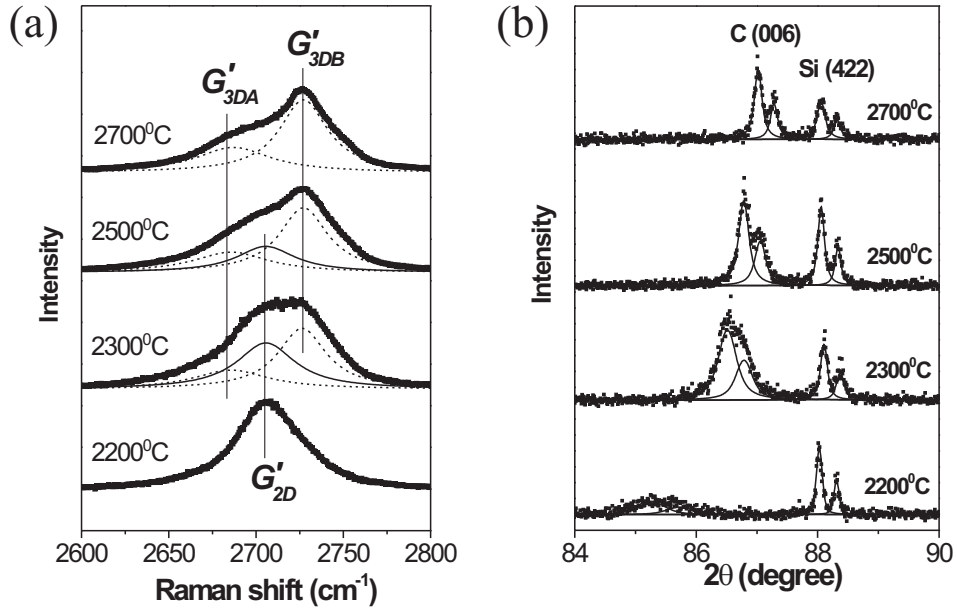

Figure 9.1: (a): G′ band Raman spectra of partially disordered graphite samples heat-treated at different temperatures, performed using the excitation laser wavelength of 514.5 nm (2.41 eV). The G′ band changes from a one-peak to a two-peak profile with increasing heat-treatment temperature. (b): X-ray diffraction profile of the (006) peak of the heat-treated samples. The heat-treatment temperature is indicated at the right side of the respective curve.

9.3 Measuring the out-of-plane parameters L_c and c by Raman spectroscopy

Figure 9.1(a) shows the G' band spectra of partially disordered graphite samples heat-treated at different temperatures, obtained using the 514.5 nm excitation laser wavelength.[2] The Raman spectrum of the sample heat-treated at 2200°C (bottom part) can be fit using only one single peak centered at 2707cm^{-1}, called here G'_{2D}. This is the typical profile of the G' band in Raman spectra of two-dimensional graphite samples [10, 78, 79, 80]. At the top, the spectrum of the sample heat-treated at 2700°C presents a two-peaks shape, which is the typical profile for the G' band in 3D graphite samples [10, 78, 79, 80]. Notice that this band can be fit using two Lorentzians (G'_{3DA} and G'_{3DB}) centered at 2687cm^{-1} and 2727cm^{-1} respectively. The Raman spectra of the samples heat-treated at intermediate temperature values (2300°C, and 2500°C) show the evolu-

[2]The other Raman features present in the one-phonon Raman spectra (D, G, and D' bands) obtained from the samples used here have been analyzed in Chapters 8 and 10.

tion of the G' band from a one-peak to a two-peak profile. Three Lorentzian peaks are needed to fit the Raman spectra of these samples. The relative intensity (integrated area) of the G'_{3DA} and G'_{3DB} peaks ($I_{G'_{3DA}}$ and $I_{G'_{3DB}}$ respectively) increases while the relative intensity of the G'_{2D} peak ($I_{G'_{2D}}$) decreases with increasing heat-treatment temperature. Furthermore, for all spectra depicted in Fig. 9.1(a), the intensity ratio of the peaks G'_{3DA} and G'_{3DB} is constant, being $I_{G'_{3DB}}/I_{G'_{3DA}} \sim 2$. The same result was obtained for the other four excitation laser wavelengths used in the experiment (not shown in Fig. 9.1(a)).

The two-peak profile of the G' band in the Raman spectrum obtained from the sample heat-treated at 2700°C is caused by a splitting in the π electrons dispersion occurring for the 3D graphite lattice [78]. For the sample heat-treated at 2200°C, the G' band is composed by a single peak, indicating that the interaction between the basal planes is weak enough so that the splitting in the π electrons dispersion energies does not occurs, being the sample composed by a turbostratic structure.

The coexistence of the doublet G'_{3DA} and G'_{3DB} with the G'_{2D} peak in the Raman spectra of the samples heat-treated at 2300°C and 2500°C indicates the simultaneous presence of the 3D and 2D graphite phases in these samples. Considering V as the volume of the sample which is illuminated by the incident laser beam, there is a fraction of V composed by only the 3D graphite phase (V_{3D}), and another one (V_{2D}) composed by the turbostratic graphite, being $V = V_{3D} + V_{2D}$. Since the Raman intensity is proportional to the volume of the sample illuminated from the incident laser beam, and the contribution to the G' band from the 3D and 2D phases coexisting in the same sample can be distinguished [83], the relative volumes $v_{3D} = V_{3D}/V$ and $v_{2D} = V_{2D}/V$ can be estimated from the ratio R given by:

$$R = \left| \frac{I_{G'_{3DB}}}{I_{G'_{3DB}} + I_{G'_{2D}}} \right| \quad , \tag{9.1}$$

being $v_{3D} = R$, and $v_{2D} = 1 - R$.

In an early work, Franklin has shown that, in a sample were the 2D and 3D graphitic phases coexist, the intermediate value of the out-of-plane lattice parameters measured from the X-Ray diffraction profiles is, in fact, an average value determined by the relative amount of the 2D and 3D phases composing the sample [84]. In this case, since the Raman spectrum of such samples can estimate the relative volumes of the 2D and 3D phases, the average value of the lattice parameter can be obtained from the ratio R.

In order to check this assumption, we performed an X-ray diffraction analysis of the samples. Figure 9.1(b) shows the X-ray diffraction profile of the (006) peak of the samples heat-treated at different temperatures. The profiles are composed of two peaks, related to the κ_{α_1} and κ_{α_2} lines from the copper X-ray tube emission. From the X-ray diffraction peaks, the interlayer spacing $[d_{(006)}]$ can be obtained as $d_{(006)} = \lambda \,/\, 2\, sin\, \theta$, where λ is the wavelength of the copper κ_{α_1} X-ray line ($\lambda = 0.154\,\mathrm{nm}$), and θ is the diffraction angle of the (006) peak [77]. To avoid the intrinsic instrumental error, the diffraction angle θ was corrected from the value of the diffraction angle of the (422) peak of the standard silicon sample (shown in Figure 9.1(b)).

Figure 9.2 shows the plot of the average out-of-plane lattice parameter $c = 6 \cdot d_{(006)}$ of the heat-treated samples obtained from the X-ray diffraction data depicted in Figure 9.1(b) *vs* the ratio R for the five excitation laser energies. It is clear in Fig. 9.2 that there is a linear dependence between the parameters R and c. The solid line in Fig. 9.2 is the linear linear fit of the data given by:

$$c\,(nm) = 0.682 - 0.11R \ . \tag{9.2}$$

Equation (9.2) provides a formula which allow us to evaluate the out-of-plane lattice parameter of partially disordered graphites from Raman scattering experiments using any excitation laser energy in the visible range. The value for the out-of-plane lattice parameter obtained for the sample heat-treated at 2700°C ($c = 0.671\,\mathrm{nm}$) is in excellent agreement with the value of c for crystalline graphite [84]. However, the value of the out-of-plane lattice parameter obtained here for the sample heat-treated at 2200°C ($c = 0.682\,\mathrm{nm}$) is lower than that established for turbostratic samples ($c = 0.688\,\mathrm{nm}$) [84]. In fact, for samples with values of c ranging around 0.688 nm, Babu and Seehra have pointed out that these systems are no longer purely graphitic [82]. Instead, these samples are formed not only by sp^2 bonds, but also by sp^3, which presence causes a considerable expansion in the interlayer distance due to lattice deformations [76]. As previously reported in Chapter 8 (see also Reference [76]), the nanographite samples used here do not contain sp^3 bounds, explaining why this relatively high value for the out-of-plane lattice parameter was not detected in our X-Ray analysis. This conclusion is also supported by the fact that the G'_{2D} peak present in the Raman spectrum of the sample heat-treated at 2200° C shown in Fig. 9.1(a) has a considerable narrow linewidth if compared with samples composed by amorphous carbon (see for example Reference [82]). This is an indication of

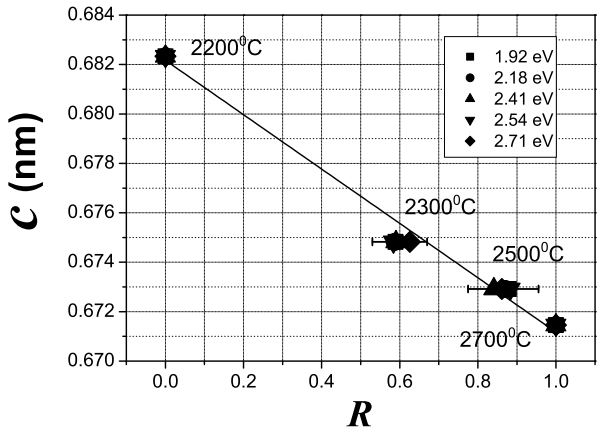

Figure 9.2: Plot of the average out-of-plane lattice parameter $c = 6 \cdot d_{(006)}$ of the heat-treated samples obtained from the X-ray diffraction data depicted in Figure 9.1(b) *vs* the ratio R for the five excitation laser energies used in the experiment. The solid line is the linear fit giving according to Equation 9.2.

a large in-plane phonon lifetime, occurring for purely graphitic samples with good in-plane crystallinity degree (see section 10.7 and Reference [81]).

Another important factor in the analysis of the stacking order of graphite is the crystallite thickness L_c. Raman spectroscopy is known to be an useful tool for measuring the in-plane crystallite size L_a in nano-sized graphite materials [7, 8, 75, 30]. We show here that the dependence of the G' band profile of graphitic samples with different degrees of stacking order shown in Figure 9.1(a) can also give a quantitative information about their average crystallite thickness L_c. Figure 9.3 shows the plot of the L_c values obtained from the X-ray data depicted in Figure 9.1(b) *vs* the ratio R taken from the Raman spectra obtained for the five different excitation laser energies. The L_c parameter was evaluated from the Scherrer equation $L_c = 0.91\lambda/(\beta \cdot \cos\theta)$, where β is the half-height width of the (006) diffraction peak in 2θ (rad) units [77]. To avoid the intrinsic instrumental broadening, the β parameter was corrected using the equation $\beta = \sqrt{\beta_m^2 - \beta_{Si}^2}$, where β_m is the half-height width of the measured (006) peak of the samples, and β_{Si} is the half-height width of the (422) peak of the standard silicon sample. The plot in Figure 9.3 shows that L_c increases with increasing R in the same way for the five excitation laser energies, indicating that the heat-treatment process performed in these samples increases the crystallite thickness L_c which can be detected by the Raman spectra. The solid line

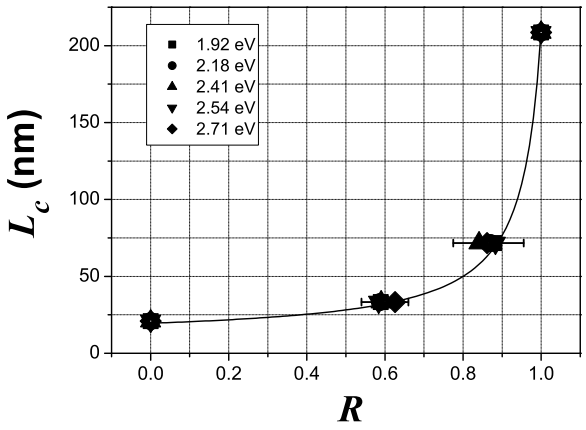

Figure 9.3: Plot of the average out-of-plane crystallite thickness L_c of the heat-treated samples obtained from the X-ray diffraction data depicted in Figure 9.1(b) *vs* the ratio R for the five excitation laser energies used in the experiment.

is a fit of the experimental data giving the empirical formula:

$$L_c\,(nm) = 10 + \frac{10}{1.05 - R}\ , \tag{9.3}$$

relating the average crystallite thickness L_c and the ratio R for any excitation laser energy in the visible range.

It should be noticed that the full width at half maximum Γ of the G'_{2D} peak depends on the average in-plane size L_a of the nanographite crystallites, as will be shown in Chapter 10. In fact, the G'_{2D} peak becomes narrower by increasing the in-plane crystallite size, as a consequence from the enlargement of the mean-free path of phonons inside of the crystallites (see section 10.7). This fact presents an extra complication for the determination of the values of Γ in the Raman spectra obtained from samples where the G' band have contributions from the 2D and 3D phases. In order to fit the experimental data depicted in Figure 9.1(a), we fixed the value of Γ for the G'_{2D} peak in the Raman spectra obtained from the samples heat-treated at 2300°C and 2500°C, using the same value ($\Gamma \sim 40\,\mathrm{cm}^{-1}$) obtained from the sample heat-treated at 2200°C. However, since the in-plane crystallite size L_a of nanographite samples increases by increasing the heat-treatment temperature, we have an estimated uncertainty of about 10% on the value of the ratio R obtained from the samples heat-treated at 2300°C and 2500°C. Therefore, the error bars depicted in Figures 9.2 and 9.3 are related with the uncertainty imposed by the determination of the full width at half maximum of the G'_{2D} peak in the Raman spectra

obtained from the samples where the 2D and 3D graphite phases coexist.

Finally, it is worth to emphasized here that although the parameters c and L_c can be obtained directly from the X-Ray diffraction, Equations (9.2) and (9.3) provide a valuable alternative way for measure them, since Raman spectroscopy is a versatile non-destructive technique for which special sample preparation procedures are not necessary, and the data acquisition time is relatively short.

9.4 Conclusion

In summary, this work shows that the analysis of the G' band profile in the Raman spectra of partially disordered graphites give the information about the relative volumes of 3D and 2D graphite phases present in the samples. Since the average value of the lattice parameter c is determined by the fraction of 3D and 2D phases coexisting in the same sample, we show that Raman spectroscopy can be used as an alternative tool for measuring the out-of-plane lattice parameter of nanographitic systems. An empirical formula relating the ratio R obtained from Raman scattering and the crystallite thickness L_c of nanographites is determined for any excitation laser energy used in the experiment.

Chapter 10

Measuring the absolute Raman cross section of nanographites as a function of laser energy and crystallite size

In this Chapter, the dependence of the differential Raman cross section β of the D, G, D', and G' bands of nanographites on the excitation laser energy and also on the crystallite size is reported. We show that β_G is proportional to the fourth power of the excitation laser energy (E_l), as predicted by the Raman scattering theory. For the bands which arise from the double-resonance mechanism (D, D', and G') the differential cross section does not depend on E_l, explaining the strong dependence of the ratio I_D/I_G on the excitation laser energy E_l used in the Raman experiment. The L_a dependence of D and D' bands differential cross sections is measured, confirming that the proportionality $I_D/I_G \propto L_a^{-1}$ originates from the strong dependence of β_D on the inverse of the crystallite size. In the G' band case, the data show that its differential cross section increases with the increasing crystallite size L_a, following an opposite behavior when compared with the disorder induced D and D' bands. An analysis on the dependence of the full width at half maximum (Γ) of the D, G, D', and G' bands on the crystallite size L_a of nanographites is performed, showing that the phonon lifetime is proportional to the crystallite size.

10.1 Introduction

Despite the large amount of experimental data available in the literature concerning to values of the the ratio I_D/I_G [29, 75, 43, 44, 85, 30], the experimental study of the absolute intensities of the D and G Raman bands of nanographite systems is still missing. In this Chapter, an experimental study of the absolute Raman cross section of the main features in the Raman spectrum of nanographite samples with different crystallite sizes L_a, and using different values of excitation laser energies (in the visible range) is presented. The samples have no stacking order and present well defined crystallite borders, being considered as prototypes of two-dimensional nanographite systems. The Raman data obtained reveal the dependence of the absolute intensities β_D and β_G on the crystallite size and excitation laser energy E_l for nanographites, showing that the dependence of the ratio I_D/I_G on E_l reported in Chapter 8 is caused by a deviation of the D band intensity from the ω^4-dependence predicted by the Raman scattering theory [21, 86, 87, 88, 89, 90, 91, 92, 93]. The absolute differential cross section for the G' band is also obtained, giving support to the analysis of the D band intensity dependence on the excitation laser energy, and indicating that such a deviation from the ω^4-dependence occurs for those bands which originate from the double-resonance process. The L_a dependence of D and D' bands differential cross sections is measured, confirming that the proportionality $I_D/I_G \propto L_a^{-1}$ originates from the strong dependence of β_D on the inverse of the crystallite size. The data allow us to establish a general equation giving the dependence of the ratio $I_{D'}/I_G$ on the excitation laser energy and crystallite size L_a. In contrast with the disorder-induced D and D' bands, the results show that the differential cross section of the G' band increases with the increasing crystallite size L_a. An analysis of the dependence on the full width at half maximum (Γ) of the D, G, D', and G' bands on the crystallite size L_a of nanographites is performed, showing that the phonon lifetime is proportional to the crystallite size.

10.2 Experimental details

The Raman spectra of nanographites were measured in a Dilor XY spectrometer setup, using five excitation laser energies, $E_l = 1.92\,\text{eV}$, $2.18\,\text{eV}$, $2.41\,\text{eV}$, $2.54\,\text{eV}$, and $2.71\,\text{eV}$. The samples were nanographite films with average in-plane crystallite sizes $L_a = 20$, 35,

and 65 nm, (for details about the synthesis of the samples and measurement of the crystallite sizes, see Chapter 8). As reported in Chapter 9, X-ray diffraction and Raman spectroscopy analysis show that these samples do not present stacking order, having a turbostratic structure. The spectrometer intensity calibration was performed using a standard LS-1-CAL-INT tungsten halogen Calibrated Light Source provided by NIST. The absolute values of the differential Raman cross section were obtained by comparison with those obtained from the Raman bands of the cyclohexane liquid (C_6H_{12}), for which the dependence of the absolute Raman cross sections are known from the literature [94]. Appendix D shows a detailed description of the procedures necessary for the spectrometer intensity calibration. The Raman spectra of the nanographite samples were obtained under the same conditions with a fixed incident laser intensity $I_0 = 6.25 \times 10^8\,\mathrm{mW/cm^2}$, and accumulation time $t = 60$ s.

10.3 Excitation laser energy dependence for the absolute Raman cross section of nanographites

Figure 10.1 shows the calibrated Raman spectra (spectral differential cross section β') of the nanographite sample with $L_a = 35$ nm, obtained using the five distinct values of E_l, after applying the procedure necessary for the intensity calibration process (for details, see Appendix D). The graphic shows an increase on the G band intensity with the excitation laser energy. For the D, D', and G' bands, the spectral differential cross section is roughly constant.

Figure 10.2(a-c) shows the differential cross section β (integrated area) for D, G and D' bands vs the excitation laser energy E_l, obtained from the samples with $L_a = 20$ nm [part (a)], $L_a = 35$ nm [part (b)], and $L_a = 65$ nm [part (c)]. It is clear in Figure 10.2 that the differential cross sections of the disorder induced D and D' bands do not depend considerably on the excitation laser energy. On the other hand, the differential cross section of the G band increases with increasing excitation laser energy. Considering that the differential Raman cross section is predicted to follows the proportionality $\beta \propto E_l^4 \left|W\right|^2$, [1] in

[1] In fact, the theory of Raman scattering predicts that the Raman cross section is proportional to the third power of the frequency of the scattered light (ω_s), times the frequency of the excitation laser beam (ω_l), that is $\beta \propto \omega_s^3 \omega_l$. However, since the frequency of the phonon is about 10 times smaller than the frequencies of the excitation laser and scattered light beams, we consider that the absolute Raman intensity is proportional to the fourth power of the excitation laser frequency (energy).

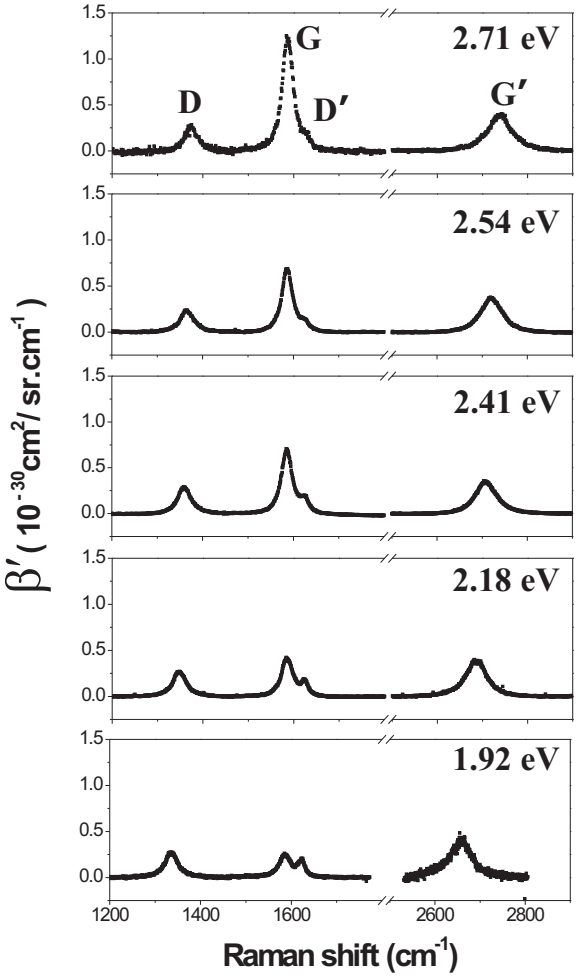

Figure 10.1: The spectral differential cross section of the D, G, D' and G' bands for the nanographite sample with $L_a = 35\,\text{nm}$, using five different values of E_l (indicated at the top of each spectrum). The same vertical scale was used for the five spectra for comparison.

the so-called ω^4-dependence, where W is the microscopic amplitude probability obtained from the time dependent perturbation theory [21, 86, 87, 88, 89, 90, 91, 92, 93], the solid curves in Figures 10.2(a-c) are the fits for the G band (β_G) data, $\beta_G \propto E_l^4$, in agreement with the theory of Raman scattering.

In contrast to the G band data, the experimental data for the D and D' bands in Figures 10.2(a-c) indicate that β_D and $\beta_{D'}$ do not follow the ω^4-dependence. In fact, deviation from the ω^4-dependence occurs for bands originated from resonance processes in which the matrix elements composing the amplitude probability W carry some dependence on E_l [95]. These results show that the dependence of the ratio I_D/I_G on the excitation

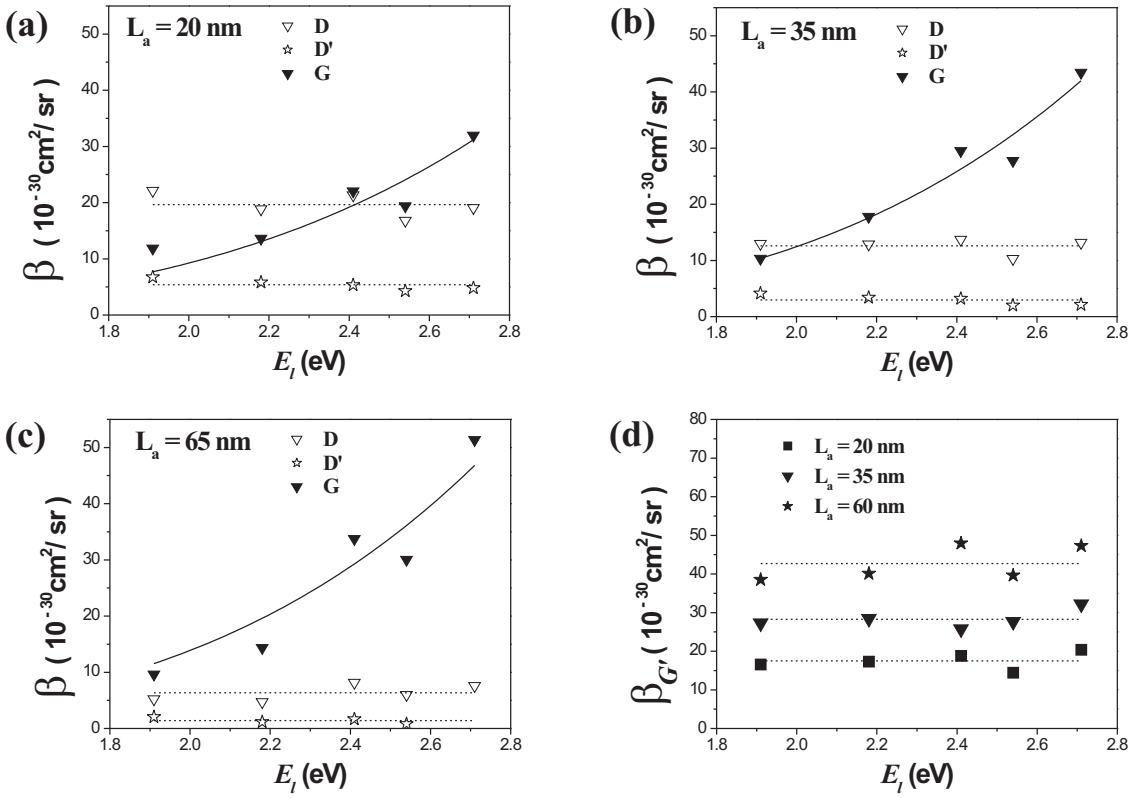

Figure 10.2: The differential cross section of the D, G and D' bands *vs* the excitation laser energy E_l, obtained from the samples with $L_a = 20\,\text{nm}$ [part (a)], $L_a = 35\,\text{nm}$ [part (b)], and $L_a = 65\,\text{nm}$ [part (c)]. (d) The differential cross section of the G' band *vs* the excitation laser energy, for the samples with crystallite sizes $L_a = 20\,\text{nm}$, 35 nm, and 65 nm.

laser energy observed by many authors [29, 30, 85] comes from the fact that the G band differential cross section is proportional to E_l^4, and the D band differential cross section does not changes with the excitation laser energy.

As explained in Chapter 5, the mechanism giving rise to the G band is quite different from that giving rise to the D and D' bands. The G band is a first-order allowed band originated from the double degenerated vibrational mode Γ_6^+ (E_{2g}) that occurs at the crossing of the iLO and iTO phonon branches at the Γ point in the 1^{st} Brillouin zone of graphite [7, 8]. The D and D' scattering are defect-induced double-resonance processes which become Raman active at the borders of the graphite crystallites due to loss of translational symmetry [7, 8, 38, 40]. Therefore the differential Raman cross section for the D and D' bands includes an additional matrix element term associated with the

electron-defect interaction Hamiltonian, absent in the G band differential cross section (see equation 5.1 in Chapter 5) [38, 40]. In order to check if the deviation from the ω^4-dependence observed for the the D and D' bands absolute intensities is associated with the electron-defect interaction matrix element, we have also measured the G' band absolute intensity. The G' band is the overtone of the D band, and it does not require a disorder-induced process to become active, since momentum conservation is guaranteed in two-phonon Raman processes. Figure 10.2(d) shows the measured values of $\beta_{G'}$ *vs* the excitation laser energy for the samples with crystallite sizes $L_a = 20\,\text{nm}$, 35 nm, and 65 nm. As depicted in Figure 10.2(d), $\beta_{G'}$ is affected by the crystallite size L_a, but it does not depend on the excitation laser energy, similarly to the case of the D and D' bands. This result indicates that the deviation of the D and D' intensities from the ω^4-dependence is not associated with the electron-defect interaction matrix elements.

These results are in agreement with the recent work where the square modulus of the transition probability $|W|^2$ is predicted to be proportional to ω_l^{-4} for the D band scattering [96]. Therefore, the square modulus of the transition probability cancels the ω^4-dependence for the D band cross section. It is also shown in this work that the dependence of the square modulus of the transition rate for the D band scattering on ω_l^{-4} comes from the electron-radiation coupling matrix element in the double-resonance process of spatially confined nanographites. Since the D' and G' bands are also generated by a double-resonance mechanism, this result should also apply, in agreement with the observations reported in this section.

10.4 Crystallite size L_a dependence for the differential cross sections of the disorder-induced D and D' bands

As shown in Chapters 5 and 7, the borders of the crystallites work as defects involved in the double-resonance process giving rise to the D and D' bands in the Raman spectra of nanographites [26]. Therefore, the D and D' bands differential cross sections are expected to be proportional to the amount of crystallite boundary in the nanographite sample, which means that they should be inversely proportional to the the crystallite size L_a. Figure 10.3(a) shows the plot of the D (filled symbols) and D' (open symbols) bands differential cross sections *vs* the inverse of the crystallite size L_a, using the five values of

E_l. The plot shows that both β_D and $\beta_{D'}$ are linearly proportional to $1/L_a$, as predicted by Tuinstra and Koenig for the D band scattering [7, 8]. The dependencies of β_D and $\beta_{D'}$ on $1/L_a$ were quantified from the linear fits depicted in Figure 10.3(a) (solid line for the D band data, and dashed line for the D' data) giving $\beta_D = 405/L_a$ and $\beta_{D'} = 115/L_a$, respectively, where β_D and $\beta_{D'}$ are given in $10^{-30}\,\mathrm{cm}^2/\mathrm{sr}$ units, and L_a is given in nm units.

Although the ratio I_D/I_G in nanographitic systems has been measured previously by many groups [29, 75, 43, 44, 85, 30], our measurement of the the D band differential cross section shows that the proportionality $I_D/I_G \propto L_a^{-1}$originates from the strong dependence of β_D on the inverse of the crystallite size.

10.5 L_a and E_l dependence of the ratios β_D/β_G and $\beta_{D'}/\beta_G$

Figure 10.4 shows the plot of the ratios β_D/β_G (solid squares) and $\beta_{D'}/\beta_G$ (empty squares) *vs* the inverse of the product $E_L^4 \cdot L_a$, for the data depicted in Figures 10.2(a)-(c). The lines (solid and dashed lines for the D and D' bands data, respectively) are linear plots

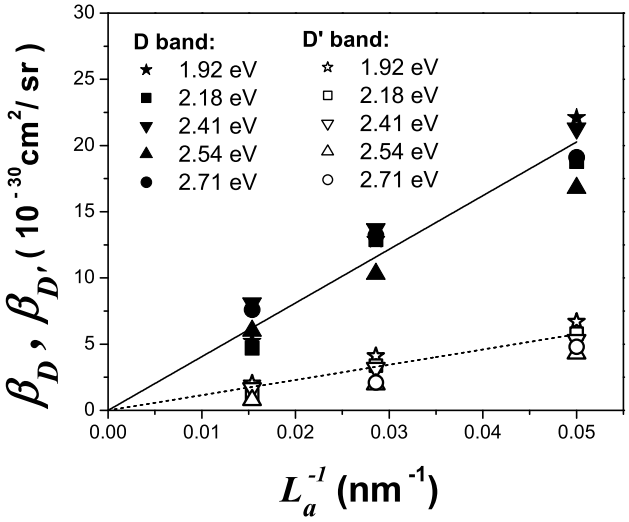

Figure 10.3: Plot of the D (filled symbols) and D' (open symbols) band differential cross sections *vs* the inverse of the crystallite size L_a, obtained using the five values of E_l.

giving the following relations:

$$\frac{\beta_D}{\beta_G} = \frac{560}{L_a \cdot E_l^4} \ , \tag{10.1}$$

and,

$$\frac{\beta_{D'}}{\beta_G} = \frac{160}{L_a \cdot E_l^4} \ , \tag{10.2}$$

where L_a and E_l are in nm and eV units, respectively. While equation (10.1) confirms our result previously reported in Chapter 5, equation (10.2) gives an expression associating the crystallite size L_a with the ratio $\beta_{D'}/\beta_G$, for experiments using any excitation laser energy in the visible range.

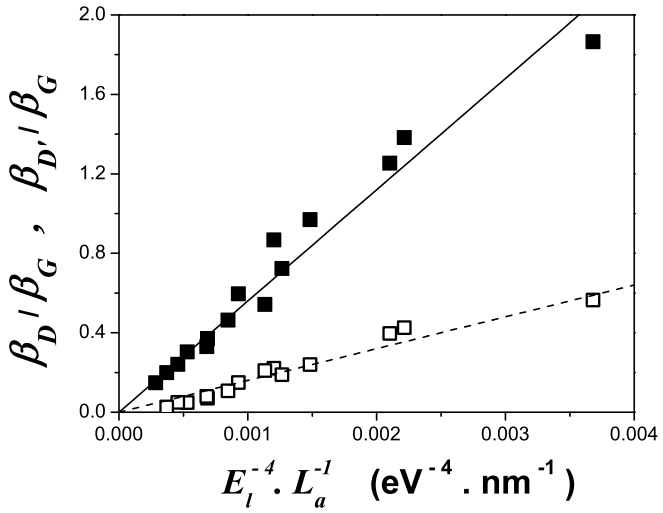

Figure 10.4: Plot of the ratios β_D/β_G (solid squares) and $\beta_{D'}/\beta_G$ (empty squares) *vs* the inverse of the product $E_L^4 \cdot L_a$, for the whole data obtained in the experiment. The lines (solid and dashed lines for the D and D' bands data, respectively) are the linear fit originating equations 10.1 and 10.2.

10.6 Crystallite size L_a dependence of the G' band differential cross section

Figure 10.5(a) shows the the plot of the differential cross section of the G' band *vs* the crystallite size L_a. As shown in Figure 10.5(a), the absolute intensity of the G' band has the opposite direction from that followed by the D and D' bands, since $\beta_{G'}$ becomes stronger with increasing L_a. These results should not be associated with the amount of

carbon material under illumination, since the sample completely fill the laser focus in all cases.

Figure 10.5(b), shows the plot of the ratio $\beta_{G'}/\beta_G$ with the inverse of the crystallite size L_a, for the data obtained using five different values of E_l. The extrapolation of the experimental data for an infinite graphene crystal [dashed lines in Figure 10.5(b)], shows that the absolute intensity of the G' band is larger than the absolute intensity of the G band, being the value of the ratio $\beta_{G'}/\beta_G$ estimated to be about 2.5 and 5 for experiments using the 2.41eV and 1.92eV excitation laser lines, respectively. These values are in good agreement with the results obtained from References [78, 79, 80] for micron-sized graphene samples, showing that the strong dependence of the G' band on the crystallite size L_a originates the relative high values of the ratio $\beta_{G'}/\beta_G$ observed in these systems.

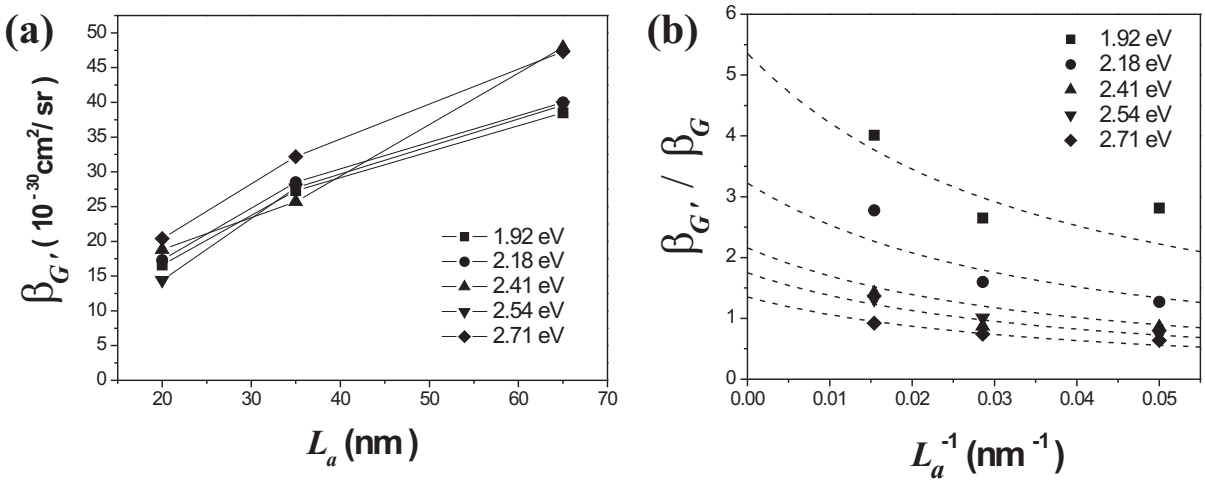

Figure 10.5: (a) The differential cross section of the G' band *vs* the crystallite size L_a. (b) The ratio $\beta_{G'}/\beta_G$ *vs* the inverse of the crystallite size L_a, for the data obtained using five different values of E_l.

10.7 Crystallite size L_a dependence of the full width at half maximum

Figure 10.6 shows the plot of the full width at half maximum (FWHM) Γ for the D, D', G, G' bands [parts (a), (b), (c), and (d), respectively] *vs* the crystallite size observed in the Raman spectra taken from the samples with L_a= 20, 35, and 65 nm, using five

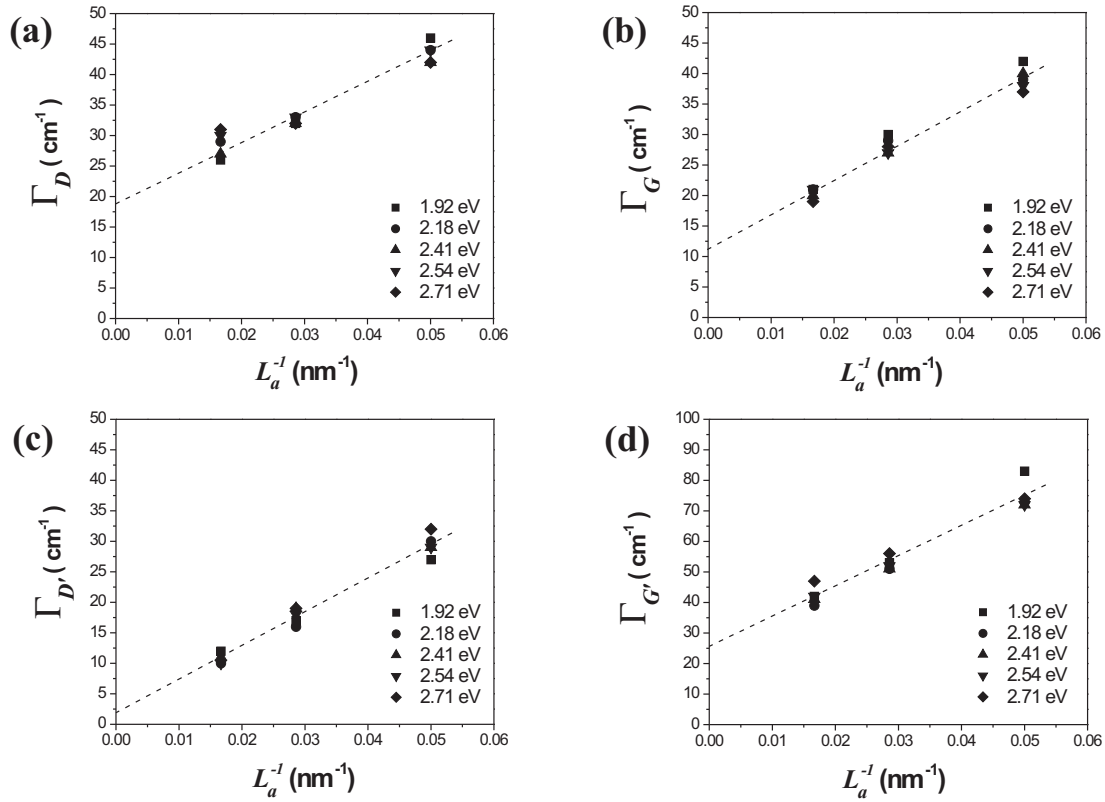

Figure 10.6: The full width at half maximum Γ for the D, D', G, G' bands [parts (a), (b), (c), and (d), respectively] *vs* the crystallite size observed in the Raman spectra taken from the samples with L_a= 20, 35, and 65 nm, using five different values for the excitation laser energy E_l.

different values for the excitation laser energy E_l. The linear fits [dashed lines in Figures 10.6(a)-(d)] show that Γ is proportional to $1/L_a$ for the D, D', G, G' bands, and does not depend siginificantly on E_l. The linear fit parameters A and B are given in Table 10.1, where the notation $\Gamma = A + BL_a^{-1}$ has been used. It is interesting to notice that the slope parameter B is similar for the the one-phonon process bands ($\sim 550\,\mathrm{cm}^{-1}\cdot\mathrm{nm}$), and approximately twice for the two phonon G' band process ($1000\,\mathrm{cm}^{-1}\cdot\mathrm{nm}$).

The proportionality between Γ and $1/L_a$ observed in Figure 10.6 can be discussed in the following terms: if the crystallite size is smaller than the phonon mean free path, the phonon lifetime τ will be proportional to the crystallite size L_a. Since the FWHM is determined by lifetime effects in Raman bands involving resonance conditions [97], we have that $\Gamma \propto 1/\tau$ and, consequently, $\Gamma \propto 1/L_a$.

Table 10.1: The linear fit parameters A and B, where the notation $\Gamma = A + BL_a^{-1}$ was used, obtained from the plot of the full width at half maximum Γ for the D, D', G, G' bands depicted in Figures 10.6(a)-(d), respectively.

	A	B
	(cm^{-1})	($\mathrm{cm}^{-1} \cdot \mathrm{nm}$)
Γ_D	19	500
Γ_G	11	560
$\Gamma_{D'}$	2	550
$\Gamma_{G'}$	26	1000

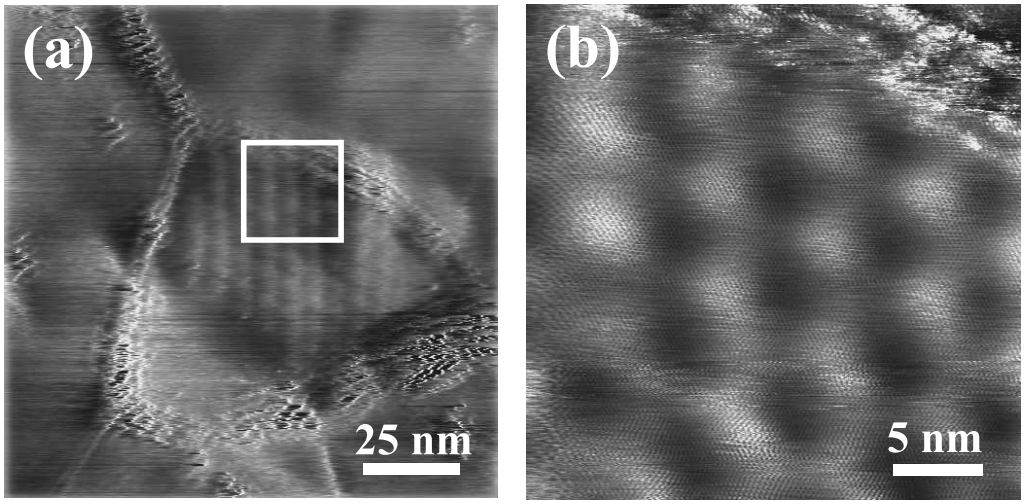

Figure 10.7: Scanning tunneling microscopy (STM) images with atomic resolution obtained from the surface of a crystallite of the sample with L_a= 65 nm. (a) A Moire pattern at the crystallite surface is observed. (b) Magnification of the region delimitated by the white square in part (a), where the carbon atom positions in the graphite lattice can be observed. The STM measurements were performed using a Nanoscope II MultiMode microscope from Digital Instruments. For more details, see Chapter 8

We must consider that the phonon lifetime can be shorter for samples with small L_a due to the presence of defects in the crystallites, increasing the probability for the phonon-defect scattering. However, it does not seem to occur in the present case. First, the relatively small linewidth of the Raman bands obtained from the samples used in this experiment, when compared with those obtained from samples with similar values of the ratio I_D/I_G reported in other works (see linewidths for spectra at Refs. [7, 8] for comparison), gives an evidence that the samples used here exhibit a low density of defects inside the crystallites. Moreover, Figure 10.7 shows two scanning tunneling microscopy (STM)

images with atomic resolution obtained from the surface of a crystallite at the sample with L_a= 65 nm. The atomic arrangement of the carbon atoms observed in these pictures indicates that the samples are actually formed by nanographitic crystallites, instead of disordered carbon. Finally, another strong evidence that the size of the crystallites actually defines the phonon lifetime is the value of the parameter A in Table 10.1. Considering that the FWHM obtained here is due to the finite size of the crystallites, the parameter A corresponds to the extrapolation for the value of the FWHM of the respective band obtained from the Raman spectrum of a sample with an infinite L_a. In fact, the values of A obtained here are very close to the FWHM values recently reported in References [78, 79, 80] for the Raman bands obtained from micron-sized graphene samples.

10.8 Final remarks

In summary, we have reported in this Chapter the dependence of the absolute differential cross section β of the D, G, D', and G' bands on the excitation laser energy (in the visible range) and also on the crystallite size. We show that β_G is proportional to the fourth power of the excitation laser energy, as predicted by the Raman scattering theory. For the bands which arise from the double-resonance mechanism (D, D', and G') the absolute differential cross section does not depend on E_l. The results show that the dependence of the ratio I_D/I_G on E_l is caused by a deviation of the D band intensity from the ω^4-dependence predicted by the Raman scattering theory. The L_a dependence of D and D' bands absolute differential cross sections is measured, confirming that the proportionality $I_D/I_G \propto L_a^{-1}$ originates from the strong dependence of β_D on the inverse of the crystallite size. The same treatment shows a strong enhancement of the absolute differential cross section of the G' band with increasing the crystallite size L_a. An analysis on the dependence of the full width at half maximum (Γ) of the D, G, D', and G' bands on L_a of nanographites is performed, showing that the phonon lifetime is proportional to the crystallite size.

Chapter 11

Conclusion

This thesis presented the study of Raman spectroscopy in nanographite systems. We reported the experimental observation of the Raman spectra of nanographite ribbons on a highly oriented pyrolitic graphite (HOPG) substrate, where the Raman signal from the ribbon is as intense as that of the HOPG substrate and has a strong dependence on the light polarization. The results give experimental evidence for the predicted existence of a node in the optical absorption in graphite and the presence of van Hove singularities in the DOS of the nanographite ribbons.

We also have shown a study of graphite edges with different atomic structures, combining the use of Raman spectroscopy and scanning probe microscopy. The one-dimensional defect selects the direction of the electron and phonon associated with the disorder-induced Raman process, and causes a dependence of the Raman D band intensity on the atomic structure of the edge. We showed that the D band is strong for armchair edges, and weak for zigzag edges. The physics leading to this structurally selective effect was explained on the basis of the well-established double-resonance effect which was applied to a semi-infinite crystal limited by a one-dimensional defect.

A systematic analysis of the dependence of the ratio between the integrated intensities of the D and G bands (I_D/I_G) on the crystallite size and on the excitation laser energy was presented. The crystallite sizes L_a of nanographite samples were obtained by X-ray diffraction using synchrotron radiation and directly from scanning tunneling microscopy images. Resonant Raman spectroscopy was performed using five excitation laser energies in the visible range. From the analysis of the experimental results, a general formula that allows the determination of the crystallite size L_a by Raman spectroscopy using any

excitation laser energy E_l in the visible range was obtained. We have also shown that, for a given sample, the ratio I_D/I_G is inversely proportional to E_l^4.

We have reported the analysis of the G' band profile in the Raman spectra of nanographites with different stacking order. Since the G' band scattering coming from the 2D and 3D phases coexisting in the same sample can be nicely distinguished, the we have shown that the relative volumes of 3D and 2D graphite phases present in the samples can be estimated from their Raman spectra. The comparison between the Raman scattering and X-Ray diffraction data shows that the out-of plane lattice parameter c, and also the crystallite thickness L_c, can be determined from the ratio between the G' band scattering intensities obtained from the 2D and 3D graphite phases.

Finally, the dependence of the absolute differential Raman cross section β of the D, G, D', and G' bands of nanographites on the excitation laser energy and also on the crystallite size was reported. We have show that β_G is proportional to the fourth power of the excitation laser energy (E_l), as predicted by the Raman scattering theory. For the bands which arise from the double-resonance mechanism (D, D', and G') the differential cross section does not depend on E_l, explaining the strong dependence of the ratio I_D/I_G on the excitation laser energy E_l used in the Raman experiment. The L_a dependence of D and D' bands differential cross sections is measured, confirming that the proportionality $I_D/I_G \propto L_a^{-1}$ is originated by the strong dependence of β_D on the inverse of the crystallite size. In the G' band case, the data show that its differential cross section increases with the increasing crystallite size L_a, following an opposite behavior when compared with the disorder induced D and D' bands. An analysis on the dependence of the full width at half maximum (Γ) of the D, G, D', and G' bands on the crystallite size L_a of nanographites is performed, showing that the phonon lifetime is proportional to the crystallite size.

Appendix A

Group theory in graphite

In this Appendix, the procedure to obtain the symmetry of phonons and electrons in graphite by group theory will be presented. The two- and three-dimensional graphite are treated separately in sections **A.1** and **A.2**, respectively.

A.1 2D graphite

A.1.1 Irreducible representations for the Γ point

As pointed out in Chapter 2, 2D graphite belongs to the space group D_{6h}^1 ($P6/mmm$) [12]. This is a symmorphic space group since there are no translations associated with any symmetry operation.

Table A.1 shows the transformation matrices for the 24 symmetry operations associated with the 2D graphite lattice. Figure A.1 shows the top view of the unit cell of the 2D graphite, with the directions of the horizontal rotation axes (C_2' and C_2'') and the directions of the vertical mirrors (σ_d and σ_v), for reference.

With the transformation matrices listed in Table A.1, we can construct all the irreducible representations for the Γ point using the orthogonality rules. The irreducible representations obtained are depicted in Table A.2.

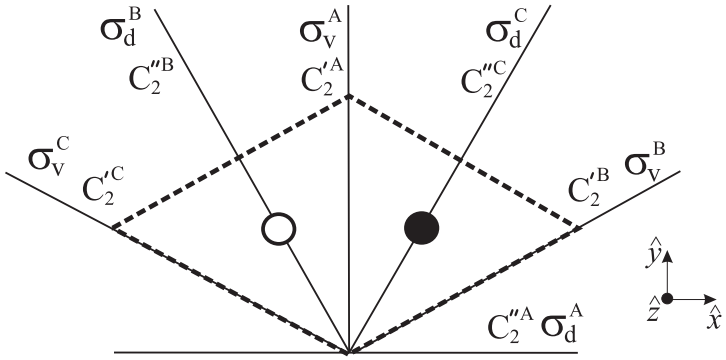

Figure A.1: Top view of the unit cell of the 2D graphite, with the directions of the horizontal rotation axes (C_2' and C_2'') and the directions of the vertical mirrors (σ_d and σ_v).

Table A.1: Transformation matrices for the 24 symmetry operations associated with the 2D graphite lattice, in the cartesian system (x, y, z).

$$E = \begin{bmatrix} 1 & 0 & 0 \\ 0 & 1 & 0 \\ 0 & 0 & 1 \end{bmatrix} \qquad C_3^+ = \begin{bmatrix} -1/2 & -\sqrt{3}/2 & 0 \\ \sqrt{3}/2 & -1/2 & 0 \\ 0 & 0 & 1 \end{bmatrix} \qquad C_3^- = \begin{bmatrix} -1/2 & \sqrt{3}/2 & 0 \\ -\sqrt{3}/2 & -1/2 & 0 \\ 0 & 0 & 1 \end{bmatrix}$$

$$C_2 = \begin{bmatrix} -1 & 0 & 0 \\ 0 & -1 & 0 \\ 0 & 0 & 1 \end{bmatrix} \qquad C_6^- = \begin{bmatrix} 1/2 & \sqrt{3}/2 & 0 \\ -\sqrt{3}/2 & 1/2 & 0 \\ 0 & 0 & 1 \end{bmatrix} \qquad C_6^+ = \begin{bmatrix} 1/2 & -\sqrt{3}/2 & 0 \\ \sqrt{3}/2 & 1/2 & 0 \\ 0 & 0 & 1 \end{bmatrix}$$

$$C_2'^A = \begin{bmatrix} -1 & 0 & 0 \\ 0 & 1 & 0 \\ 0 & 0 & -1 \end{bmatrix} \quad C_2'^B = \begin{bmatrix} 1/2 & \sqrt{3}/2 & 0 \\ \sqrt{3}/2 & -1/2 & 0 \\ 0 & 0 & -1 \end{bmatrix} \qquad C_2'^C = \begin{bmatrix} 1/2 & -\sqrt{3}/2 & 0 \\ -\sqrt{3}/2 & -1/2 & 0 \\ 0 & 0 & -1 \end{bmatrix}$$

$$C_2''^A = \begin{bmatrix} 1 & 0 & 0 \\ 0 & -1 & 0 \\ 0 & 0 & -1 \end{bmatrix} \quad C_2''^B = \begin{bmatrix} -1/2 & -\sqrt{3}/2 & 0 \\ -\sqrt{3}/2 & 1/2 & 0 \\ 0 & 0 & -1 \end{bmatrix} \quad C_2''^C = \begin{bmatrix} -1/2 & \sqrt{3}/2 & 0 \\ \sqrt{3}/2 & 1/2 & 0 \\ 0 & 0 & -1 \end{bmatrix}$$

$$i = \begin{bmatrix} -1 & 0 & 0 \\ 0 & -1 & 0 \\ 0 & 0 & -1 \end{bmatrix} \qquad S_6^+ = \begin{bmatrix} 1/2 & \sqrt{3}/2 & 0 \\ -\sqrt{3}/2 & 1/2 & 0 \\ 0 & 0 & -1 \end{bmatrix} \qquad S_6^- = \begin{bmatrix} 1/2 & -\sqrt{3}/2 & 0 \\ \sqrt{3}/2 & 1/2 & 0 \\ 0 & 0 & -1 \end{bmatrix}$$

$$\sigma_h = \begin{bmatrix} 1 & 0 & 0 \\ 0 & 1 & 0 \\ 0 & 0 & -1 \end{bmatrix} \qquad S_3^- = \begin{bmatrix} -1/2 & -\sqrt{3}/2 & 0 \\ \sqrt{3}/2 & -1/2 & 0 \\ 0 & 0 & -1 \end{bmatrix} \qquad S_3^+ = \begin{bmatrix} -1/2 & \sqrt{3}/2 & 0 \\ -\sqrt{3}/2 & -1/2 & 0 \\ 0 & 0 & -1 \end{bmatrix}$$

$$\sigma_d^A = \begin{bmatrix} 1 & 0 & 0 \\ 0 & -1 & 0 \\ 0 & 0 & 1 \end{bmatrix} \qquad \sigma_d^B = \begin{bmatrix} -1/2 & -\sqrt{3}/2 & 0 \\ -\sqrt{3}/2 & 1/2 & 0 \\ 0 & 0 & 1 \end{bmatrix} \qquad \sigma_d^C = \begin{bmatrix} -1/2 & \sqrt{3}/2 & 0 \\ \sqrt{3}/2 & 1/2 & 0 \\ 0 & 0 & 1 \end{bmatrix}$$

$$\sigma_v^A = \begin{bmatrix} -1 & 0 & 0 \\ 0 & 1 & 0 \\ 0 & 0 & 1 \end{bmatrix} \qquad \sigma_v^B = \begin{bmatrix} 1/2 & \sqrt{3}/2 & 0 \\ \sqrt{3}/2 & -1/2 & 0 \\ 0 & 0 & 1 \end{bmatrix} \qquad \sigma_v^C = \begin{bmatrix} 1/2 & -\sqrt{3}/2 & 0 \\ -\sqrt{3}/2 & -1/2 & 0 \\ 0 & 0 & 1 \end{bmatrix}$$

Table A.2: Irreducible representations for the Γ point.

	E	C_3^+	C_3^-	C_2	C_6^-	C_6^+
Γ_1^+	1	1	1	1	1	1
Γ_2^+	1	1	1	1	1	1
Γ_3^+	1	1	1	-1	-1	-1
Γ_4^+	1	1	1	-1	-1	-1
Γ_5^+	$\begin{bmatrix} 1 & 0 \\ 0 & 1 \end{bmatrix}$	$\begin{bmatrix} -1/2 & -\sqrt{3}/2 \\ \sqrt{3}/2 & -1/2 \end{bmatrix}$	$\begin{bmatrix} -1/2 & \sqrt{3}/2 \\ -\sqrt{3}/2 & -1/2 \end{bmatrix}$	$\begin{bmatrix} -1 & 0 \\ 0 & -1 \end{bmatrix}$	$\begin{bmatrix} 1/2 & \sqrt{3}/2 \\ -\sqrt{3}/2 & 1/2 \end{bmatrix}$	$\begin{bmatrix} 1/2 & -\sqrt{3}/2 \\ \sqrt{3}/2 & 1/2 \end{bmatrix}$
Γ_6^+	$\begin{bmatrix} 1 & 0 \\ 0 & 1 \end{bmatrix}$	$\begin{bmatrix} -1/2 & \sqrt{3}/4 \\ -\sqrt{3} & -1/2 \end{bmatrix}$	$\begin{bmatrix} -1/2 & -\sqrt{3}/4 \\ -\sqrt{3} & -1/2 \end{bmatrix}$	$\begin{bmatrix} 1 & 0 \\ 0 & 1 \end{bmatrix}$	$\begin{bmatrix} -1/2 & \sqrt{3}/4 \\ -\sqrt{3} & -1/2 \end{bmatrix}$	$\begin{bmatrix} -1/2 & -\sqrt{3}/4 \\ \sqrt{3} & -1/2 \end{bmatrix}$
Γ_1^-	1	1	1	1	1	1
Γ_2^-	1	1	1	1	1	1
Γ_3^-	1	1	1	-1	-1	-1
Γ_4^-	1	1	1	-1	-1	-1
Γ_5^-	$\begin{bmatrix} 1 & 0 \\ 0 & 1 \end{bmatrix}$	$\begin{bmatrix} -1/2 & -\sqrt{3}/2 \\ \sqrt{3}/2 & -1/2 \end{bmatrix}$	$\begin{bmatrix} -1/2 & \sqrt{3}/2 \\ -\sqrt{3}/2 & -1/2 \end{bmatrix}$	$\begin{bmatrix} -1 & 0 \\ 0 & -1 \end{bmatrix}$	$\begin{bmatrix} 1/2 & \sqrt{3}/2 \\ -\sqrt{3}/2 & 1/2 \end{bmatrix}$	$\begin{bmatrix} 1/2 & -\sqrt{3}/2 \\ \sqrt{3}/2 & 1/2 \end{bmatrix}$
Γ_6^-	$\begin{bmatrix} 1 & 0 \\ 0 & 1 \end{bmatrix}$	$\begin{bmatrix} -1/2 & \sqrt{3}/4 \\ -\sqrt{3} & -1/2 \end{bmatrix}$	$\begin{bmatrix} -1/2 & -\sqrt{3}/4 \\ -\sqrt{3} & -1/2 \end{bmatrix}$	$\begin{bmatrix} 1 & 0 \\ 0 & 1 \end{bmatrix}$	$\begin{bmatrix} -1/2 & \sqrt{3}/4 \\ -\sqrt{3} & -1/2 \end{bmatrix}$	$\begin{bmatrix} -1/2 & -\sqrt{3}/4 \\ \sqrt{3} & -1/2 \end{bmatrix}$

	$C_2'^A$	$C_2'^B$	$C_2'^C$	$C_2''^A$	$C_2''^B$	$C_2''^C$
Γ_1^+	1	1	1	1	1	1
Γ_2^+	-1	-1	-1	-1	-1	-1
Γ_3^+	-1	-1	-1	1	1	1
Γ_4^+	1	1	1	-1	-1	-1
Γ_5^+	$\begin{bmatrix} -1 & 0 \\ 0 & 1 \end{bmatrix}$	$\begin{bmatrix} 1/2 & \sqrt{3}/2 \\ \sqrt{3}/2 & -1/2 \end{bmatrix}$	$\begin{bmatrix} 1/2 & -\sqrt{3}/2 \\ -\sqrt{3}/2 & -1/2 \end{bmatrix}$	$\begin{bmatrix} 1 & 0 \\ 0 & -1 \end{bmatrix}$	$\begin{bmatrix} -1/2 & -\sqrt{3}/2 \\ -\sqrt{3}/2 & 1/2 \end{bmatrix}$	$\begin{bmatrix} -1/2 & \sqrt{3}/2 \\ \sqrt{3}/2 & 1/2 \end{bmatrix}$
Γ_6^+	$\begin{bmatrix} 1 & 0 \\ 0 & -1 \end{bmatrix}$	$\begin{bmatrix} -1/2 & \sqrt{3}/4 \\ \sqrt{3} & 1/2 \end{bmatrix}$	$\begin{bmatrix} -1/2 & -\sqrt{3}/4 \\ -\sqrt{3} & 1/2 \end{bmatrix}$	$\begin{bmatrix} 1 & 0 \\ 0 & -1 \end{bmatrix}$	$\begin{bmatrix} -1/2 & \sqrt{3}/4 \\ \sqrt{3} & 1/2 \end{bmatrix}$	$\begin{bmatrix} -1/2 & -\sqrt{3}/4 \\ -\sqrt{3} & 1/2 \end{bmatrix}$
Γ_1^-	1	1	1	1	1	1
Γ_2^-	-1	-1	-1	-1	-1	-1
Γ_3^-	-1	-1	-1	1	1	1
Γ_4^-	1	1	1	-1	-1	-1
Γ_5^-	$\begin{bmatrix} -1 & 0 \\ 0 & 1 \end{bmatrix}$	$\begin{bmatrix} 1/2 & \sqrt{3}/2 \\ \sqrt{3}/2 & -1/2 \end{bmatrix}$	$\begin{bmatrix} 1/2 & -\sqrt{3}/2 \\ -\sqrt{3}/2 & -1/2 \end{bmatrix}$	$\begin{bmatrix} 1 & 0 \\ 0 & -1 \end{bmatrix}$	$\begin{bmatrix} -1/2 & -\sqrt{3}/2 \\ -\sqrt{3}/2 & 1/2 \end{bmatrix}$	$\begin{bmatrix} -1/2 & \sqrt{3}/2 \\ \sqrt{3}/2 & 1/2 \end{bmatrix}$
Γ_6^-	$\begin{bmatrix} 1 & 0 \\ 0 & -1 \end{bmatrix}$	$\begin{bmatrix} -1/2 & \sqrt{3}/4 \\ \sqrt{3} & 1/2 \end{bmatrix}$	$\begin{bmatrix} -1/2 & -\sqrt{3}/4 \\ -\sqrt{3} & 1/2 \end{bmatrix}$	$\begin{bmatrix} 1 & 0 \\ 0 & -1 \end{bmatrix}$	$\begin{bmatrix} -1/2 & \sqrt{3}/4 \\ \sqrt{3} & 1/2 \end{bmatrix}$	$\begin{bmatrix} -1/2 & -\sqrt{3}/4 \\ -\sqrt{3} & 1/2 \end{bmatrix}$

	I	S_6^+	S_6^-	σ_h	S_3^-	S_3^+
Γ_1^+	1	1	1	1	1	1
Γ_2^+	1	1	1	1	1	1
Γ_3^+	1	1	1	-1	-1	-1
Γ_4^+	1	1	1	-1	-1	-1
Γ_5^+	$\begin{bmatrix} 1 & 0 \\ 0 & 1 \end{bmatrix}$	$\begin{bmatrix} -1/2 & -\sqrt{3}/2 \\ \sqrt{3}/2 & -1/2 \end{bmatrix}$	$\begin{bmatrix} -1/2 & \sqrt{3}/2 \\ -\sqrt{3}/2 & -1/2 \end{bmatrix}$	$\begin{bmatrix} -1 & 0 \\ 0 & -1 \end{bmatrix}$	$\begin{bmatrix} 1/2 & \sqrt{3}/2 \\ -\sqrt{3}/2 & 1/2 \end{bmatrix}$	$\begin{bmatrix} 1/2 & -\sqrt{3}/2 \\ \sqrt{3}/2 & 1/2 \end{bmatrix}$
Γ_6^+	$\begin{bmatrix} 1 & 0 \\ 0 & 1 \end{bmatrix}$	$\begin{bmatrix} -1/2 & \sqrt{3}/4 \\ -\sqrt{3} & -1/2 \end{bmatrix}$	$\begin{bmatrix} -1/2 & -\sqrt{3}/4 \\ \sqrt{3} & -1/2 \end{bmatrix}$	$\begin{bmatrix} 1 & 0 \\ 0 & 1 \end{bmatrix}$	$\begin{bmatrix} -1/2 & \sqrt{3}/4 \\ -\sqrt{3} & -1/2 \end{bmatrix}$	$\begin{bmatrix} -1/2 & -\sqrt{3}/4 \\ \sqrt{3} & -1/2 \end{bmatrix}$
Γ_1^-	-1	-1	-1	-1	-1	-1
Γ_2^-	-1	-1	-1	-1	-1	-1
Γ_3^-	-1	-1	-1	1	1	1
Γ_4^-	-1	-1	-1	1	1	1
Γ_5^-	$\begin{bmatrix} -1 & 0 \\ 0 & -1 \end{bmatrix}$	$\begin{bmatrix} 1/2 & \sqrt{3}/2 \\ -\sqrt{3}/2 & 1/2 \end{bmatrix}$	$\begin{bmatrix} 1/2 & -\sqrt{3}/2 \\ \sqrt{3}/2 & 1/2 \end{bmatrix}$	$\begin{bmatrix} 1 & 0 \\ 0 & 1 \end{bmatrix}$	$\begin{bmatrix} -1/2 & -\sqrt{3}/2 \\ \sqrt{3}/2 & -1/2 \end{bmatrix}$	$\begin{bmatrix} -1/2 & \sqrt{3}/2 \\ -\sqrt{3}/2 & -1/2 \end{bmatrix}$
Γ_6^-	$\begin{bmatrix} -1 & 0 \\ 0 & -1 \end{bmatrix}$	$\begin{bmatrix} 1/2 & -\sqrt{3}/4 \\ \sqrt{3} & 1/2 \end{bmatrix}$	$\begin{bmatrix} 1/2 & \sqrt{3}/4 \\ -\sqrt{3} & 1/2 \end{bmatrix}$	$\begin{bmatrix} -1 & 0 \\ 0 & -1 \end{bmatrix}$	$\begin{bmatrix} 1/2 & -\sqrt{3}/4 \\ \sqrt{3} & 1/2 \end{bmatrix}$	$\begin{bmatrix} 1/2 & \sqrt{3}/4 \\ -\sqrt{3} & 1/2 \end{bmatrix}$

	σ_d^A	σ_d^B	σ_d^C	σ_v^A	σ_v^B	σ_v^C
Γ_1^+	1	1	1	1	1	1
Γ_2^+	-1	-1	-1	-1	-1	-1
Γ_3^+	-1	-1	-1	1	1	1
Γ_4^+	1	1	1	-1	-1	-1
Γ_5^+	$\begin{bmatrix} -1 & 0 \\ 0 & 1 \end{bmatrix}$	$\begin{bmatrix} 1/2 & \sqrt{3}/2 \\ \sqrt{3}/2 & -1/2 \end{bmatrix}$	$\begin{bmatrix} 1/2 & -\sqrt{3}/2 \\ -\sqrt{3}/2 & -1/2 \end{bmatrix}$	$\begin{bmatrix} 1 & 0 \\ 0 & -1 \end{bmatrix}$	$\begin{bmatrix} -1/2 & -\sqrt{3}/2 \\ -\sqrt{3}/2 & 1/2 \end{bmatrix}$	$\begin{bmatrix} -1/2 & \sqrt{3}/2 \\ \sqrt{3}/2 & 1/2 \end{bmatrix}$
Γ_6^+	$\begin{bmatrix} 1 & 0 \\ 0 & -1 \end{bmatrix}$	$\begin{bmatrix} -1/2 & \sqrt{3}/4 \\ \sqrt{3} & 1/2 \end{bmatrix}$	$\begin{bmatrix} -1/2 & -\sqrt{3}/4 \\ \sqrt{3} & 1/2 \end{bmatrix}$	$\begin{bmatrix} 1 & 0 \\ 0 & -1 \end{bmatrix}$	$\begin{bmatrix} -1/2 & \sqrt{3}/4 \\ \sqrt{3} & 1/2 \end{bmatrix}$	$\begin{bmatrix} -1/2 & -\sqrt{3}/4 \\ -\sqrt{3} & 1/2 \end{bmatrix}$
Γ_1^-	-1	-1	-1	-1	-1	-1
Γ_2^-	1	1	1	1	1	1
Γ_3^-	1	1	1	-1	-1	-1
Γ_4^-	-1	-1	-1	1	1	1
Γ_5^-	$\begin{bmatrix} 1 & 0 \\ 0 & -1 \end{bmatrix}$	$\begin{bmatrix} -1/2 & -\sqrt{3}/2 \\ -\sqrt{3}/2 & 1/2 \end{bmatrix}$	$\begin{bmatrix} -1/2 & \sqrt{3}/2 \\ \sqrt{3}/2 & 1/2 \end{bmatrix}$	$\begin{bmatrix} -1 & 0 \\ 0 & 1 \end{bmatrix}$	$\begin{bmatrix} 1/2 & \sqrt{3}/2 \\ \sqrt{3}/2 & -1/2 \end{bmatrix}$	$\begin{bmatrix} 1/2 & -\sqrt{3}/2 \\ -\sqrt{3}/2 & -1/2 \end{bmatrix}$
Γ_6^-	$\begin{bmatrix} -1 & 0 \\ 0 & 1 \end{bmatrix}$	$\begin{bmatrix} 1/2 & -\sqrt{3}/4 \\ -\sqrt{3} & -1/2 \end{bmatrix}$	$\begin{bmatrix} 1/2 & \sqrt{3}/4 \\ -\sqrt{3} & -1/2 \end{bmatrix}$	$\begin{bmatrix} -1 & 0 \\ 0 & 1 \end{bmatrix}$	$\begin{bmatrix} 1/2 & -\sqrt{3}/4 \\ -\sqrt{3} & -1/2 \end{bmatrix}$	$\begin{bmatrix} 1/2 & \sqrt{3}/4 \\ \sqrt{3} & -1/2 \end{bmatrix}$

A.1.2 Character tables

In this section, the character tables for all points inside the first Brillouin zone of 2D graphite will be introduced. We start constructing the character table for the Γ point, which can be obtained from the irreducible representations depicted in Table A.2. For that, we can group the symmetry elements in their respective classes, and take the value of the one-dimensional representations or the value of the trace of the matrices of the two-dimensional representations for each class. The character table for the Γ point is depicted in Table A.3. Observe that the two columns at the right side of the Table A.3 give the one- and two-dimensional basis functions, respectively, for each irreducible representation.

In order to construct the character tables for the other points inside the first Brillouin zone, we should select the symmetry elements which bring the point in consideration to an equivalent one. In other words, we should select those symmetry operations which leave the star of k invariant. Then, using the character table for the Γ point (Table A.3), and the orthogonality relations, we can construct the character tables for the other points inside the Brillouin zone. Tables A.3, A.4, A.5, A.6, A.7, and A.8 show the character tables for the Γ, $\mathbf{K}$, $\mathbf{M}$, Σ, $\mathbf{T}(\mathbf{T}')$, and $\mathbf{u}$ points in the first Brillouin zone of 2D graphite, respectively.

Table A.3: Character table for the Γ point (D^1_{6h}, $P6/mmm$, No. 191).

	E	C_3^+	C_3^-	C_2	C_6^+	C_6^-	$C_2'^A$	$C_2''^A$	$C_2'^B$	$C_2''^B$	i	S_6^+	S_6^-	σ_h	S_3^+	S_3^-	σ_d^A	σ_v^A	σ_d^B	σ_v^B	σ_d^C	σ_v^C		
Γ_1^+	1	1	1	1	1	1	1	1	1	1	1	1	1	1	1	1	1	1	1	1	1		x^2+y^2 , z^2
Γ_2^+	1	1	1	1	-1	-1	1	1	1	1	1	1	1	1	1	1	-1	-1	-1	-1	-1	-1	
Γ_3^+	1	1	-1	-1	-1	1	1	1	1	1	1	1	1	1	-1	-1	-1	1	-1	1	-1	1	
Γ_4^+	1	1	-1	-1	1	-1	1	1	1	1	1	1	1	1	-1	-1	1	-1	1	-1	1	-1	
Γ_5^+	2	-1	-2	1	0	0	2	2	-1	-1	2	-1	-2	1	0	0	0	0	0	0	0	0	(xz, yz)
Γ_6^+	2	-1	2	-1	0	0	2	2	-1	-1	2	-1	2	-1	0	0	0	0	0	0	0	0	(x^2-y^2, xy)
Γ_1^-	1	1	1	1	1	1	-1	-1	-1	-1	-1	-1	-1	-1	-1	-1	-1	-1	-1	-1	-1	-1	
Γ_2^-	1	1	1	1	-1	-1	-1	-1	-1	-1	-1	-1	-1	-1	-1	-1	1	1	1	1	1	1	z
Γ_3^-	1	1	-1	-1	-1	1	-1	-1	-1	-1	-1	-1	-1	-1	1	1	1	-1	1	-1	1	-1	
Γ_4^-	1	1	-1	-1	1	-1	-1	-1	-1	-1	-1	-1	-1	-1	1	1	-1	1	-1	1	-1	1	
Γ_5^-	2	-1	-2	1	0	0	-2	-2	1	1	-2	1	2	-1	0	0	0	0	0	0	0	0	(x, y)
Γ_6^-	2	-1	2	-1	0	0	-2	-2	1	1	-2	1	-2	1	0	0	0	0	0	0	0	0	
χ^{eq}	2	2	0	0	0	0	2	2	0	0	2	0	0	2	2	2	0						Γ^{eq}	$\Gamma_1^+ \oplus \Gamma_3^-$
χ^{vector}	3	0	-1	2	-1	-1	-3	0	1	-2	1	1											$\Gamma^{a.s.}$	$\Gamma_2^- \oplus \Gamma_5^-$
χ^{LV}	6	0	0	0	0	-2	0	0	2	-4	2	0											Γ^{LV}	$\Gamma_4^+ \oplus \Gamma_6^+ \oplus \Gamma_2^- \oplus \Gamma_5^-$
χ^z	1	1	1	1	-1	-1	-1	-1	-1	-1	1	1											Γ^z	Γ_2^-
χ^π	2	2	0	0	0	-2	0	0	-2	-2	2	0											Γ^π	$\Gamma_4^+ \oplus \Gamma_2^-$

Table A.4: Character table for the **K** point (D^3_{3h}, $P\bar{6}2m$, No. 189).

	E	C_3^+	C_3^-	$C_2'^A$	$C_2'^B$	$C_2'^C$	σ_h	S_3^-	S_3^+	σ_v^A	σ_v^B	σ_v^C		
K_1	1	1	1	1	1	1	1	1	1	1	1	1		x^2+y^2 , z^2
K_2	1	1	1	-1	-1	-1	1	1	1	-1	-1	-1		
K_3	2	-1	-1	0	0	0	2	-1	-1	0	0	0	(x, y)	(x^2-y^2, xy)
K_4	1	1	1	1	1	1	-1	-1	-1	-1	-1	-1		
K_5	1	1	1	-1	-1	-1	-1	-1	-1	1	1	1	z	
K_6	2	-1	-1	0	0	0	-2	1	1	0	0	0		(xz, yz)
χ^{eq}	2	-1	-1	0	0	0	2	-1	-1	0			Γ^{eq}	K_3
χ^{vector}	3	0	0	-1	-1	-1	1	-2	-2	1			Γ^{vector}	$K_3 \oplus K_5$
χ^{LV}	6	0	0	0	0	0	2	2	2	0			Γ^{LV}	$K_1 \oplus K_2 \oplus K_3 \oplus K_6$
χ^z	1	1	1	-1	-1	-1	-1	-1	-1	1			Γ^z	K_5
χ^π	2	-1	-1	0	0	0	-2	1	1	0			Γ^π	K_6

Table A.5: Character table for the **M** point (D_{2h}^{19}, $Cmmm$, No. 65).

	E	C_2	$C_2^{'A}$	$C_2^{''A}$	i	σ_h	σ_d^A	σ_v^A		
M_1^+	1	1	1	1	1	1	1	1		x^2 , y^2 , z^2
M_2^+	1	1	-1	-1	1	1	-1	-1		xy
M_3^+	1	-1	1	-1	1	-1	1	-1		xz
M_4^+	1	-1	-1	1	1	-1	-1	1		yz
M_1^-	1	1	1	1	-1	-1	-1	-1		
M_2^-	1	1	-1	-1	-1	-1	1	1	z	
M_3^-	1	-1	1	-1	-1	1	-1	1	y	
M_4^-	1	-1	-1	1	-1	1	1	-1	x	
χ^{eq}	2	0	0	2	0	2	2	0	Γ^{eq}	$M_1^+ \oplus M_4^-$
χ^{vector}	3	-1	-1	-1	-3	1	1	1	Γ^{vector}	$M_2^- \oplus M_3^- \oplus M_4^-$
χ^{LV}	6	0	0	-2	0	2	2	0	Γ^{LV}	$M_1^+ \oplus M_2^+ \oplus M_3^+ \oplus M_2^- \oplus M_3^- \oplus M_4^-$
χ^z	1	1	-1	-1	-1	-1	1	1	Γ^z	M_2^-
χ^π	2	0	0	-2	0	-2	2	0	Γ^π	$M_3^+ \oplus M_2^-$

Table A.6: Character table for the Σ point (C_s^3, Cm, No. 8).

	E	$C_2^{''A}$	σ_h	σ_d^A		
Σ_1	1	1	1	1	x	x^2 , y^2 , z^2
Σ_2	1	1	-1	-1		zy
Σ_3	1	-1	1	-1	y	xy
Σ_4	1	-1	-1	1	z	zx
χ^{eq}	2	2	2	2	Γ^{eq}	$2\Sigma_1$
χ^{vector}	3	-1	1	1	Γ^{vector}	$\Sigma_1 \oplus \Sigma_3 \oplus \Sigma_4$
χ^{LV}	6	-2	2	2	Γ^{LV}	$2\Sigma_1 \oplus 2\Sigma_3 \oplus 2\Sigma_4$
χ^z	1	-1	-1	1	Γ^z	Σ_4
χ^π	2	-2	-2	2	Γ^π	$2\Sigma_4$

Table A.7: Character table for **T** and **T′** points (C_s^3, Cm, No. 8).

	E	$C_2'^A$	σ_h	σ_v^A		
T_1	1	1	1	1	y	x^2 , y^2 , z^2
T_2	1	1	-1	-1		xz
T_3	1	-1	1	-1	x	xy
T_4	1	-1	-1	1	z	yz
χ^{eq}	2	0	2	0	Γ^{eq}	$T_1 \oplus T_3$
χ^{vector}	3	-1	1	1	Γ^{vector}	$T_1 \oplus T_3 \oplus T_4$
χ^{LV}	6	0	2	0	Γ^{LV}	$2T_1 \oplus T_2 \oplus 2T_3 \oplus T_4$
χ^{z}	1	-1	-1	1	Γ^{z}	T_4
χ^{π}	2	0	-2	0	Γ^{π}	$T_2 \oplus T_4$

Table A.8: Character table for the **u** point (C_s^1, Pm, No. 6).

	E	σ_h		
u^+	1	1	x , y	x^2 , y^2 , z^2 , xy
u^-	1	-1	z	zy , zx
χ^{eq}	2	2	Γ^{eq}	$2u^+$
χ^{vector}	3	1	Γ^{vector}	$2u^+ \oplus u^-$
χ^{LV}	6	2	Γ^{LV}	$4u^+ \oplus 2u^-$
χ^{z}	1	-1	Γ^{z}	u^-
χ^{π}	2	-2	Γ^{π}	$2u^-$

A.1.3 The characters of the equivalence representations

In order to obtain the representations associated with phonons and electrons in a crystal, it is necessary to know the equivalence representations. Therefore, it is necessary to calculate the equivalence matrices.

We will start our analysis by introducing the matrix of the atomic sites $M_{as}^{(n)}$, with elements defined as a_{ij}, where the subscripts i and j describe the atoms and the atomic sites [**1** **2** (see Figure 2.1)], respectively. The value of the matrix element a_{ij} is one ($a_{ij} = 1$), if the atom i goes to the atomic site j, by applying the symmetry operation $\mathbf{D}^{(n)}$, and 0 otherwise. In fact, by performing the 24 symmetry operations, it can be concluded that only two cases for the matrices of the atomic sites are possible for the 2D graphite lattice. The first case occurs for those operations in which the two atoms of the unit cell remain in their original (or equivalent) sites. In this case, the atomic site matrix is a 2×2 identity matrix. In the second case, the atoms **1** and **2** change their respective sites. In this case, the matrix of the atomic site is:

$$M_{as} = \begin{pmatrix} 0 & 1 \\ 1 & 0 \end{pmatrix} . \tag{A.1}$$

Next, we define the phase factor matrix $M_{pf}^{(n)}$, which is a diagonal matrix whose elements are the exponential factors $e^{\vec{t}_i \cdot \vec{k}}$, where $\vec{k}$ is the coordinate of the point (in the reciprocal space) under consideration, and $\vec{t}_i$ is the vector which brings the i^{th} atom back to its original position after the application of the symmetry operation $\mathbf{D}^{(n)}$, that is:

$$M_{pf}^{(n)} = \begin{pmatrix} e^{\vec{t}_1 \cdot \vec{k}} & 0 \\ 0 & e^{\vec{t}_2 \cdot \vec{k}} \end{pmatrix} . \tag{A.2}$$

Finally, the equivalence matrix is defined as the product between the atomic site and phase factor matrices, that is:

$$M_{eq}^{(n)} = M_{as}^{(n)} \times M_{pf}^{(n)} . \tag{A.3}$$

In order to calculate the phase factors, we have to calculate the position of the i^{th} atom after application of the n^{th} symmetry operation ($\vec{r}_i^{\,(n)}$), for the 24 symmetry operations of 2D graphite. Such coordinates can be obtained as:

$$\vec{r}_i^{\,(n)} = \mathbf{D}^{(n)} \, \vec{w}_i , \tag{A.4}$$

where $\vec{w}_i$ is the original position of the i^{th} atom, given in equations 2.3 and 2.4 for atoms **1** and **2**, respectively. Then, we can calculate the $\vec{t}_i^{\ (n)}$ vectors for all operations, by evaluating the relation $\vec{t}_i^{(n)} = \vec{w}_i - \vec{r}_i^{(n)}$. Table A.9 shows the $\vec{r}_i$ and $\vec{t}_i$ vectors associated with the 24 symmetry operations of 2D graphite.

Table A.9: $\vec{r}_i$ and $\vec{t}_i$ vectors associated with the 24 symmetry operations of 2D graphite.

Operation	$\vec{r}_1$	$\vec{r}_2$	$\vec{t}_1$	$\vec{t}_2$
E	$\frac{a}{2\sqrt{3}}\hat{x} + \frac{a}{2}\hat{y}$	$-\frac{a}{2\sqrt{3}}\hat{x} + \frac{a}{2}\hat{y}$	0	0
C_3^+	$-\frac{a}{\sqrt{3}}\hat{x}$	$-\frac{a}{2\sqrt{3}}\hat{x} - \frac{a}{2}\hat{y}$	$\frac{3a}{2\sqrt{3}}\hat{x} + \frac{a}{2}\hat{y}$	$a\hat{y}$
C_3^-	$\frac{a}{2\sqrt{3}}\hat{x} - \frac{a}{2}\hat{y}$	$\frac{a}{\sqrt{3}}\hat{x}$	$a\hat{y}$	$-\frac{3a}{2\sqrt{3}}\hat{x} + \frac{a}{2}\hat{y}$
C_2	$-\frac{a}{2\sqrt{3}}\hat{x} - \frac{a}{2}\hat{y}$	$\frac{a}{2\sqrt{3}}\hat{x} - \frac{a}{2}\hat{y}$	$\frac{a}{\sqrt{3}}\hat{x} + a\hat{y}$	$-\frac{a}{\sqrt{3}}\hat{x} + a\hat{y}$
C_6^-	$\frac{a}{\sqrt{3}}\hat{x}$	$\frac{a}{2\sqrt{3}}\hat{x} + \frac{a}{2}\hat{y}$	$-\frac{a}{2\sqrt{3}}\hat{x} + \frac{a}{2}\hat{y}$	$-\frac{a}{\sqrt{3}}\hat{x}$
C_6^+	$-\frac{a}{2\sqrt{3}}\hat{x} + \frac{a}{2}\hat{y}$	$-\frac{a}{\sqrt{3}}\hat{x}$	$\frac{a}{\sqrt{3}}\hat{x}$	$\frac{a}{2\sqrt{3}}\hat{x} + \frac{a}{2}\hat{y}$
$C_2'^A$	$-\frac{a}{2\sqrt{3}}\hat{x} + \frac{a}{2}\hat{y}$	$\frac{a}{2\sqrt{3}}\hat{x} + \frac{a}{2}\hat{y}$	$\frac{a}{\sqrt{3}}\hat{x}$	$-\frac{a}{\sqrt{3}}\hat{x}$
$C_2'^B$	$\frac{a}{\sqrt{3}}\hat{x}$	$\frac{a}{2\sqrt{3}}\hat{x} - \frac{a}{2}\hat{y}$	$-\frac{a}{2\sqrt{3}}\hat{x} + \frac{a}{2}\hat{y}$	$-\frac{a}{\sqrt{3}}\hat{x} + a\hat{y}$
$C_2'^C$	$-\frac{a}{2\sqrt{3}}\hat{x} - \frac{a}{2}\hat{y}$	$-\frac{a}{\sqrt{3}}\hat{x}$	$\frac{a}{\sqrt{3}}\hat{x} + a\hat{y}$	$\frac{a}{\sqrt{3}}\hat{x} + \frac{a}{2}\hat{y}$
$C_2''^A$	$\frac{a}{2\sqrt{3}}\hat{x} - \frac{a}{2}\hat{y}$	$-\frac{a}{2\sqrt{3}}\hat{x} - \frac{a}{2}\hat{y}$	$a\hat{y}$	$a\hat{y}$
$C_2''^B$	$-\frac{a}{\sqrt{3}}\hat{x}$	$-\frac{a}{2\sqrt{3}}\hat{x} + \frac{a}{2}\hat{y}$	$\frac{3a}{2\sqrt{3}}\hat{x} + \frac{a}{2}\hat{y}$	0
$C_2''^C$	$\frac{a}{2\sqrt{3}}\hat{x} + \frac{a}{2}\hat{y}$	$\frac{a}{\sqrt{3}}\hat{x}$	0	$-\frac{3a}{2\sqrt{3}}\hat{x} + \frac{a}{2}\hat{y}$
i	$-\frac{a}{2\sqrt{3}}\hat{x} - \frac{a}{2}\hat{y}$	$\frac{a}{2\sqrt{3}}\hat{x} - \frac{a}{2}\hat{y}$	$\frac{a}{\sqrt{3}}\hat{x} + a\hat{y}$	$-\frac{a}{\sqrt{3}}\hat{x} + a\hat{y}$
S_6^+	$\frac{a}{\sqrt{3}}\hat{x}$	$\frac{a}{2\sqrt{3}}\hat{x} + \frac{a}{2}\hat{y}$	$-\frac{a}{2\sqrt{3}}\hat{x} + \frac{a}{2}\hat{y}$	$-\frac{a}{\sqrt{3}}\hat{x}$
S_6^-	$-\frac{a}{2\sqrt{3}}\hat{x} + \frac{a}{2}\hat{y}$	$-\frac{a}{\sqrt{3}}\hat{x}$	$\frac{a}{\sqrt{3}}\hat{x}$	$\frac{a}{2\sqrt{3}}\hat{x} + \frac{a}{2}\hat{y}$
σ_h	$\frac{a}{2\sqrt{3}}\hat{x} + \frac{a}{2}\hat{y}$	$-\frac{a}{2\sqrt{3}}\hat{x} + \frac{a}{2}\hat{y}$	0	0
S_3^-	$-\frac{a}{\sqrt{3}}\hat{x}$	$-\frac{a}{2\sqrt{3}}\hat{x} - \frac{a}{2}\hat{y}$	$\frac{3a}{2\sqrt{3}}\hat{x} + \frac{a}{2}\hat{y}$	$a\hat{y}$
S_3^+	$\frac{a}{2\sqrt{3}}\hat{x} - \frac{a}{2}\hat{y}$	$\frac{a}{\sqrt{3}}\hat{x}$	$a\hat{y}$	$-\frac{3a}{2\sqrt{3}}\hat{x} + \frac{a}{2}\hat{y}$
σ_d^A	$\frac{a}{2\sqrt{3}}\hat{x} - \frac{a}{2}\hat{y}$	$-\frac{a}{2\sqrt{3}}\hat{x} - \frac{a}{2}\hat{y}$	$a\hat{y}$	$a\hat{y}$
σ_d^B	$-\frac{a}{\sqrt{3}}\hat{x}$	$-\frac{a}{2\sqrt{3}}\hat{x} + \frac{a}{2}\hat{y}$	$\frac{3a}{2\sqrt{3}}\hat{x} + \frac{a}{2}\hat{y}$	0
σ_d^C	$\frac{a}{2\sqrt{3}}\hat{x} + \frac{a}{2}\hat{y}$	$\frac{a}{\sqrt{3}}\hat{x}$	0	$-\frac{3a}{2\sqrt{3}}\hat{x} + \frac{a}{2}\hat{y}$
σ_v^A	$-\frac{a}{2\sqrt{3}}\hat{x} + \frac{a}{2}\hat{y}$	$\frac{a}{2\sqrt{3}}\hat{x} + \frac{a}{2}\hat{y}$	$\frac{a}{\sqrt{3}}\hat{x}$	$-\frac{a}{\sqrt{3}}\hat{x}$
σ_v^B	$\frac{a}{\sqrt{3}}\hat{x}$	$\frac{a}{2\sqrt{3}}\hat{x} - \frac{a}{2}\hat{y}$	$-\frac{a}{2\sqrt{3}}\hat{x} + \frac{a}{2}\hat{y}$	$\frac{a}{\sqrt{3}}\hat{x} + a\hat{y}$
σ_v^C	$-\frac{a}{2\sqrt{3}}\hat{x} - \frac{a}{2}\hat{y}$	$-\frac{a}{\sqrt{3}}\hat{x}$	$\frac{a}{\sqrt{3}}\hat{x} + a\hat{y}$	$\frac{a}{2\sqrt{3}}\hat{x} + \frac{a}{2}\hat{y}$

Tables A.10 and A.11 show the products $\vec{t}_i \cdot \vec{k}$, and the phase factors $e^{\vec{t}_i \cdot \vec{k}}$ for all points inside of the first Brillouin zone of 2D graphite, for all symmetry operations associated with each respective point. The penultimate column of Tables A.10 and A.11 shows the respective characters of the atomic site representations (χ^{as}), obtained from the traces of the atomic site matrices. The last column of Tables A.10 and A.11 shows the characters of the equivalence representations (χ^{eq}), obtained from the traces of the equivalence matrices. Tables A.3 to A.8 show the equivalence representations for all points inside the first Brillouin zone of 2D graphite.

Table A.10: The products $\vec{t}_i \cdot \vec{k}$, and the phase factors $e^{\vec{t}_i \cdot \vec{k}}$, for all points inside of the first Brillouin zone of 2D graphite for all symmetry operations associated with each respective point. The penultimate, and the last columns show the characters of the atomic site representations (χ^{as}), and the characters of the equivalence representations (χ^{eq}), respectively.

Γ	$\vec{t}_1 \cdot \Gamma$	$\vec{t}_2 \cdot \Gamma$	$e^{i(\vec{t}_1 \cdot \Gamma)}$	$e^{i(\vec{t}_2 \cdot \Gamma)}$	χas	χeq
E	0	0	1	1	2	2
C_3^+	0	0	1	1	2	2
C_3^-	0	0	1	1	2	2
C_2	0	0	1	1	0	0
C_6^-	0	0	1	1	0	0
C_6^+	0	0	1	1	0	0
$C_2'^A$	0	0	1	1	0	0
$C_2'^B$	0	0	1	1	0	0
$C_2'^C$	0	0	1	1	0	0
$C_2''^A$	0	0	1	1	2	2
$C_2''^B$	0	0	1	1	2	2
$C_2''^C$	0	0	1	1	2	2
i	0	0	1	1	0	0
S_6^+	0	0	1	1	0	0
S_6^-	0	0	1	1	0	0
σ_h	0	0	1	1	2	2
S_3^-	0	0	1	1	2	2
S_3^+	0	0	1	1	2	2
σ_d^A	0	0	1	1	2	2
σ_d^B	0	0	1	1	2	2
σ_d^C	0	0	1	1	2	2
σ_v^A	0	0	1	1	0	0
σ_v^B	0	0	1	1	0	0
σ_v^C	0	0	1	1	0	0

Table A.11: Table A.10 continuing.

K	$\vec{t}_1 \cdot K$	$\vec{t}_2 \cdot K$	$e^{i(\vec{t}_1 \cdot K)}$	$e^{i(\vec{t}_2 \cdot K)}$	χ^{as}	χ^{eq}
E	0	0	1	1	2	2
C_3^+	$\frac{2\pi}{3}$	$\frac{4\pi}{3}$	$-\frac{1}{2}(1-i\sqrt{3})$	$-\frac{1}{2}(1+i\sqrt{3})$	2	-1
C_3^-	$\frac{4\pi}{3}$	$\frac{2\pi}{3}$	$-\frac{1}{2}(1+i\sqrt{3})$	$-\frac{1}{2}(1-i\sqrt{3})$	2	-1
$C_2'^A$	0	0	1	1	0	0
$C_2'^B$	$\frac{2\pi}{3}$	$\frac{4\pi}{3}$	$-\frac{1}{2}(1-i\sqrt{3})$	$-\frac{1}{2}(1+i\sqrt{3})$	0	0
$C_2'^C$	$\frac{4\pi}{3}$	$\frac{2\pi}{3}$	$-\frac{1}{2}(1+i\sqrt{3})$	$-\frac{1}{2}(1-i\sqrt{3})$	0	0
σ_h	0	0	1	1	2	2
S_3^-	$\frac{2\pi}{3}$	$\frac{4\pi}{3}$	$-\frac{1}{2}(1-i\sqrt{3})$	$-\frac{1}{2}(1+i\sqrt{3})$	2	-1
S_3^+	$\frac{4\pi}{3}$	$\frac{2\pi}{3}$	$-\frac{1}{2}(1+i\sqrt{3})$	$-\frac{1}{2}(1-i\sqrt{3})$	2	-1
σ_v^A	0	0	1	1	0	0
σ_v^B	$\frac{2\pi}{3}$	$\frac{4\pi}{3}$	$-\frac{1}{2}(1-i\sqrt{3})$	$-\frac{1}{2}(1+i\sqrt{3})$	0	0
σ_v^C	$\frac{4\pi}{3}$	$\frac{2\pi}{3}$	$-\frac{1}{2}(1+i\sqrt{3})$	$-\frac{1}{2}(1-i\sqrt{3})$	0	0
M	$\vec{t}_1 \cdot M$	$\vec{t}_2 \cdot M$	$e^{i(\vec{t}_1 \cdot M)}$	$e^{i(\vec{t}_2 \cdot M)}$	χ^{as}	χ^{eq}
E	0	0	1	1	2	2
C_2	$\frac{2\pi}{3}$	$-\frac{2\pi}{3}$	$-\frac{1}{2}(1-i\sqrt{3})$	$-\frac{1}{2}(1+i\sqrt{3})$	0	0
$C_2'^A$	$\frac{2\pi}{3}$	$-\frac{2\pi}{3}$	$-\frac{1}{2}(1-i\sqrt{3})$	$-\frac{1}{2}(1+i\sqrt{3})$	0	0
$C_2''^A$	0	0	1	1	2	2
i	$\frac{2\pi}{3}$	$-\frac{2\pi}{3}$	$-\frac{1}{2}(1-i\sqrt{3})$	$-\frac{1}{2}(1+i\sqrt{3})$	0	0
σ_h	0	0	1	1	2	2
σ_d^A	0	0	1	1	2	2
σ_v^A	$\frac{2\pi}{3}$	$-\frac{2\pi}{3}$	$-\frac{1}{2}(1-i\sqrt{3})$	$-\frac{1}{2}(1+i\sqrt{3})$	0	0
T	$\vec{t}_1 \cdot T$	$\vec{t}_2 \cdot T$	$e^{i(\vec{t}_1 \cdot T)}$	$e^{i(\vec{t}_2 \cdot T)}$	χ^{as}	χ^{eq}
E	0	0	1	1	2	2
$C_2'^A$	0	0	1	1	0	0
σ_h	0	0	1	1	2	2
σ_v^A	0	0	1	1	0	0
Σ	$\vec{t}_1 \cdot \Sigma$	$\vec{t}_2 \cdot \Sigma$	$e^{i(\vec{t}_1 \cdot \Sigma)}$	$e^{i(\vec{t}_2 \cdot \Sigma)}$	χ^{as}	χ^{eq}
E	0	0	1	1	2	2
$C_2''^A$	0	0	1	1	2	2
σ_h	0	0	1	1	2	2
σ_d^A	0	0	1	1	2	2
T$'$	$\vec{t}_1 \cdot T'$	$\vec{t}_2 \cdot T'$	$e^{i(\vec{t}_1 \cdot T')}$	$e^{i(\vec{t}_2 \cdot T')}$	χ^{as}	χ^{eq}
E	0	0	1	1	2	2
$C_2'^A$	$\frac{2\pi}{3}$	$-\frac{2\pi}{3}$	$-\frac{1}{2}(1-i\sqrt{3})$	$-\frac{1}{2}(1+i\sqrt{3})$	0	0
σ_h	0	0	1	1	2	2
σ_v^A	$\frac{2\pi}{3}$	$-\frac{2\pi}{3}$	$-\frac{1}{2}(1-i\sqrt{3})$	$-\frac{1}{2}(1+i\sqrt{3})$	0	0
u	$\vec{t}_1 \cdot u$	$\vec{t}_2 \cdot u$	$e^{i(\vec{t}_1 \cdot u)}$	$e^{i(\vec{t}_2 \cdot u)}$	χ^{as}	χ^{eq}
E	0	0	1	1	2	2
σ_h	0	0	1	1	2	2

A.1.4 Lattice vibrations representations

Since the lattice vibrations are caused by atomic displacements, the lattice vibration representation Γ^{LV} is obtained by the direct product between the representations which transform as the vector coordinates (Γ^{vec}) and the equivalence representation (Γ^{eq}).

$$\Gamma^{LV} = \Gamma^{vec} \otimes \Gamma^{eq} \ . \tag{A.5}$$

We consider the equivalence representation because it carries out the action of the symmetry operations on the atoms inside the unit cell, and also the phase factor associated with the point inside the Brillouin zone to be analyzed.

The vector representation is the sum of those representations which have as basis functions the cartesian coordinates x, y, and z, that is:

$$\Gamma^{vec} = \Gamma^{x} \oplus \Gamma^{y} \oplus \Gamma^{z} \ . \tag{A.6}$$

If the basis functions x and y are partners in a two-dimensional irreducible representation, equation A.6 should be written as:

$$\Gamma^{vec} = \Gamma^{x,y} \oplus \Gamma^{z} \ . \tag{A.7}$$

Tables A.3 to A.8 show the lattice vibration representations for all points inside the first Brillouin zone of 2D graphite.

A.1.5 π electron representation

The p_z orbital of the π electrons is perpendicular to the basal plane of graphite (parallel to the c axes). Therefore, the π electron representation Γ^{π} is obtained by the direct product between the representation which transforms as the cartesian coordinate z and the equivalence representation, that is:

$$\Gamma^{\pi} = \Gamma^{z} \otimes \Gamma^{eq} \ . \tag{A.8}$$

Tables A.3 to A.8 show the π electron representations for all points inside of the first Brillouin zone of 2D graphite.

A.1.6 Determination of the phonon eigenvectors at the Γ point

The eigenvectors of the vibrational normal modes at the Γ point can be evaluated by the projection of each irreducible representation Γ^m in a set of orthogonal vectors, forming a basis for a random displacement $\vec{q}$, applied to one of the two atoms in the unit cell. The displacement is defined here as:

$$\vec{q_{\mathbf{j}}} = \sum_i \hat{u}_{i,\mathbf{j}} \ , \tag{A.9}$$

where the subscript $i = x, y, z$ indices refer to the cartesian coordinates, subscript $\mathbf{j}$ refers to the two atoms in the unit cell ($\mathbf{1}$ and $\mathbf{2}$), and $\hat{u}_{i,\mathbf{j}}$ is an unitary vector along the direction i centered at the atom $\mathbf{j}$. The eigenvector resulting from the projection of the irreducible representations of the random displacement vector associated with one of the two atoms of the unit cell can be evaluated as:

$$\vec{V}_m = \sum_{(n)} \chi_m^{(n)} \left[\mathbf{D}_m^{(n)} \hat{q}_{\mathbf{j}}\right] = \sum_{(n),i} \chi_m^{(n)} \left[\mathbf{D}_m^{(n)} \hat{u}_{i,\mathbf{j}}\right] \ . \tag{A.10}$$

Equation A.10 works well for the eigenvectors associated with one-dimensional irreducible representations. In the case of two-dimensional irreducible representations, we should separate the x and y parts of the eigenvectors in order to understand each part of the doubly degenerate modes. In this case, instead of using the character of the irreducible representations $\chi_m^{(n)}$, we should use the diagonal elements of the representation matrices, defined as $\Gamma_{xx}^m(n)$ and $\Gamma_{yy}^m(n)$ (depicted in Table A.2), that is:

$$\begin{aligned} \vec{V}_m^{\,x} &= \sum_{(n)} \Gamma_{xx}^m(n) \left[\mathbf{D}_m^{(n)} \hat{q}_{\mathbf{j}}\right] \ , \\ \vec{V}_m^{\,y} &= \sum_{(n)} \Gamma_{yy}^m(n) \left[\mathbf{D}_m^{(n)} \hat{q}_{\mathbf{j}}\right] \ . \end{aligned} \tag{A.11}$$

Finally, applying the definitions presented above for all irreducible representations belonging to the lattice vibration representations, we will have the eigenvectors in the form:

$$\begin{aligned} \vec{V}_m \ = \ & v_{\mathbf{11}}\ \hat{u}_{\mathbf{11}} + v_{\mathbf{21}}\ \hat{u}_{\mathbf{21}} + v_{\mathbf{31}}\ \hat{u}_{\mathbf{31}} + \\ & + v_{\mathbf{12}}\ \hat{u}_{\mathbf{12}} + v_{\mathbf{22}}\ \hat{u}_{\mathbf{22}} + v_{\mathbf{32}}\ \hat{u}_{\mathbf{32}} \ , \end{aligned} \tag{A.12}$$

disregarding the orthonormality constants. The results are shown in Table 2.2, giving the coefficients $v_{i\mathbf{j}}$, following the notation:

$$(\ v_{\mathbf{11}}\ ,\ v_{\mathbf{21}}\ ,\ v_{\mathbf{31}}\ )\ (\ v_{\mathbf{12}}\ ,\ v_{\mathbf{22}}\ ,\ v_{\mathbf{32}}\ )\ . \tag{A.13}$$

A.2 3D graphite

A.2.1 Symmetry operations and character tables

As pointed out in Chapter 1, 3D graphite belongs to the space group D_{6h}^4 ($P6_3/mmc$), which is a non-symmorphic space group. The transformation operators associated with the 24 symmetry operations of 3D graphite are defined as:

$$\mathbf{D}^{(n)} = \left\{\mathbf{R}^{(n)}|\tau\right\} \ , \tag{A.14}$$

where $\mathbf{R}^{(n)}$ are the transformation matrices, and τ is the column vector which defines the translation. The superscript (n) indices refer to the 24 symmetry operations of the $P6_3/mmc$ group.

Table A.12 shows the 24 transformation operators for the 3D graphite lattice, in the cartesian system. Notice that the two possible translations are the null vector (that is, no translation), or half of the c lattice parameter along the $\hat{z}$ direction ($\tau = 1/2\, c\hat{z}$). Therefore, we use the notation 0 for operations with no translation, and τ otherwise.

Figure A.2 shows the top view of the unit cell of 3D graphite, with the directions of the horizontal rotation axes (C_2' and C_2'') and the directions of the vertical mirrors (σ_d and σ_v), for reference. The vertical coordinates of the horizontal rotation axes C_2'' are not at $z = 0$, but at $z = \frac{c}{4}$. Another important observation is that the inversion center in operations σ_h, S_3^-, and S_3^+ is not localized at the origin, but displaced by $\frac{c}{4}\,\hat{z}$, that is, it is located at the atomic site **2** in the unit cell (see Figures 2.5 and 2.6, for reference).

The irreducible representations for the Γ point in the first Brillouin zone of 3D graphite are the same as those for the 2D graphite lattice (see Table A.2). Tables A.13, A.14, A.15, A.16, A.17, and A.18 show the character tables for the Γ, **K**, **M**, Σ, **T**(**T**$'$), and **u** points, respectively.

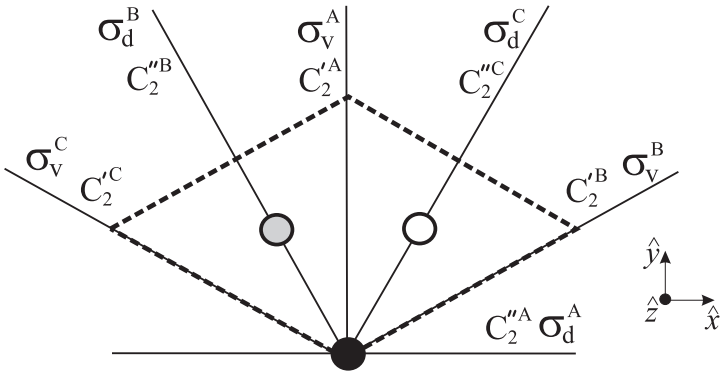

Figure A.2: Top view of the unit cell of the 3D graphite, with the directions of the horizontal rotation axes (C_2' and C_2'') and the directions of the vertical mirrors (σ_d and σ_v).

Table A.12: Transformation operators associated with the 24 symmetry operations in the cartesian system.

$$\{E|0\} = \left[\begin{array}{ccc|c} 1 & 0 & 0 & 0 \\ 0 & 1 & 0 & 0 \\ 0 & 0 & 1 & 0 \end{array}\right] \qquad \left\{C_3^+|0\right\} = \left[\begin{array}{ccc|c} -1/2 & -\sqrt{3}/2 & 0 & 0 \\ \sqrt{3}/2 & -1/2 & 0 & 0 \\ 0 & 0 & 1 & 0 \end{array}\right] \qquad \{C_3^-|0\} = \left[\begin{array}{ccc|c} -1/2 & \sqrt{3}/2 & 0 & 0 \\ -\sqrt{3}/2 & -1/2 & 0 & 0 \\ 0 & 0 & 1 & 0 \end{array}\right]$$

$$\{C_2|\tau\} = \left[\begin{array}{ccc|c} -1 & 0 & 0 & 0 \\ 0 & -1 & 0 & 0 \\ 0 & 0 & 1 & 1/2c \end{array}\right] \qquad \left\{C_6^-|\tau\right\} = \left[\begin{array}{ccc|c} 1/2 & \sqrt{3}/2 & 0 & 0 \\ -\sqrt{3}/2 & 1/2 & 0 & 0 \\ 0 & 0 & 1 & 1/2c \end{array}\right] \qquad \left\{C_6^+|\tau\right\} = \left[\begin{array}{ccc|c} 1/2 & -\sqrt{3}/2 & 0 & 0 \\ \sqrt{3}/2 & 1/2 & 0 & 0 \\ 0 & 0 & 1 & 1/2c \end{array}\right]$$

$$\left\{C_2'^A|0\right\} = \left[\begin{array}{ccc|c} -1 & 0 & 0 & 0 \\ 0 & 1 & 0 & 0 \\ 0 & 0 & -1 & 0 \end{array}\right] \qquad \left\{C_2'^B|0\right\} = \left[\begin{array}{ccc|c} 1/2 & \sqrt{3}/2 & 0 & 0 \\ \sqrt{3}/2 & -1/2 & 0 & 0 \\ 0 & 0 & -1 & 0 \end{array}\right] \qquad \left\{C_2'^C|0\right\} = \left[\begin{array}{ccc|c} 1/2 & -\sqrt{3}/2 & 0 & 0 \\ -\sqrt{3}/2 & -1/2 & 0 & 0 \\ 0 & 0 & -1 & 0 \end{array}\right]$$

$$\left\{C_2''^A|0\right\} = \left[\begin{array}{ccc|c} 1 & 0 & 0 & 0 \\ 0 & -1 & 0 & 0 \\ 0 & 0 & -1 & 0 \end{array}\right] \qquad \left\{C_2''^B|0\right\} = \left[\begin{array}{ccc|c} -1/2 & -\sqrt{3}/2 & 0 & 0 \\ -\sqrt{3}/2 & 1/2 & 0 & 0 \\ 0 & 0 & -1 & 0 \end{array}\right] \qquad \left\{C_2''^C|0\right\} = \left[\begin{array}{ccc|c} -1/2 & \sqrt{3}/2 & 0 & 0 \\ \sqrt{3}/2 & 1/2 & 0 & 0 \\ 0 & 0 & -1 & 0 \end{array}\right]$$

$$\{i|0\} = \left[\begin{array}{ccc|c} -1 & 0 & 0 & 0 \\ 0 & -1 & 0 & 0 \\ 0 & 0 & -1 & 0 \end{array}\right] \qquad \left\{S_6^+|0\right\} = \left[\begin{array}{ccc|c} 1/2 & \sqrt{3}/2 & 0 & 0 \\ -\sqrt{3}/2 & 1/2 & 0 & 0 \\ 0 & 0 & -1 & 0 \end{array}\right] \qquad \left\{S_6^-|0\right\} = \left[\begin{array}{ccc|c} 1/2 & -\sqrt{3}/2 & 0 & 0 \\ \sqrt{3}/2 & 1/2 & 0 & 0 \\ 0 & 0 & -1 & 0 \end{array}\right]$$

$$\{\sigma_h|0\} = \left[\begin{array}{ccc|c} 1 & 0 & 0 & 0 \\ 0 & 1 & 0 & 0 \\ 0 & 0 & -1 & 0 \end{array}\right] \qquad \left\{S_3^-|0\right\} = \left[\begin{array}{ccc|c} -1/2 & -\sqrt{3}/2 & 0 & 0 \\ \sqrt{3}/2 & -1/2 & 0 & 0 \\ 0 & 0 & -1 & 0 \end{array}\right] \qquad \left\{S_3^+|0\right\} = \left[\begin{array}{ccc|c} -1/2 & \sqrt{3}/2 & 0 & 0 \\ -\sqrt{3}/2 & -1/2 & 0 & 0 \\ 0 & 0 & -1 & 0 \end{array}\right]$$

$$\left\{\sigma_d^A|0\right\} = \left[\begin{array}{ccc|c} 1 & 0 & 0 & 0 \\ 0 & -1 & 0 & 0 \\ 0 & 0 & 1 & 0 \end{array}\right] \qquad \left\{\sigma_d^B|0\right\} = \left[\begin{array}{ccc|c} -1/2 & -\sqrt{3}/2 & 0 & 0 \\ -\sqrt{3}/2 & 1/2 & 0 & 0 \\ 0 & 0 & 1 & 0 \end{array}\right] \qquad \left\{\sigma_d^C|0\right\} = \left[\begin{array}{ccc|c} -1/2 & \sqrt{3}/2 & 0 & 0 \\ \sqrt{3}/2 & 1/2 & 0 & 0 \\ 0 & 0 & 1 & 0 \end{array}\right]$$

$$\left\{\sigma_v^A|\tau\right\} = \left[\begin{array}{ccc|c} -1 & 0 & 0 & 0 \\ 0 & 1 & 0 & 0 \\ 0 & 0 & 1 & 1/2c \end{array}\right] \qquad \left\{\sigma_v^B|\tau\right\} = \left[\begin{array}{ccc|c} 1/2 & \sqrt{3}/2 & 0 & 0 \\ \sqrt{3}/2 & -1/2 & 0 & 0 \\ 0 & 0 & 1 & 1/2c \end{array}\right] \qquad \left\{\sigma_v^C|\tau\right\} = \left[\begin{array}{ccc|c} 1/2 & -\sqrt{3}/2 & 0 & 0 \\ -\sqrt{3}/2 & -1/2 & 0 & 0 \\ 0 & 0 & 1 & 1/2c \end{array}\right]$$

Table A.13: Character table for the Γ point (D^4_{6h}, $P6_3/mmc$, No. 194).

	$\{E\|0\}$	$\begin{Bmatrix}C_3^+\|0\}\\C_3^-\|0\}\end{Bmatrix}$	$\{C_2\|\tau\}$	$\begin{Bmatrix}C_6^-\|\tau\}\\C_6^+\|\tau\}\end{Bmatrix}$	$\begin{Bmatrix}C_2'^A\|0\}\\C_2'^B\|0\}\\C_2'^C\|0\}\end{Bmatrix}$	$\begin{Bmatrix}C_2''^A\|0\}\\C_2''^B\|0\}\\C_2''^C\|0\}\end{Bmatrix}$	$\{i\|0\}$	$\begin{Bmatrix}S_6^+\|0\}\\S_6^-\|0\}\end{Bmatrix}$	$\{\sigma_h\|0\}$	$\begin{Bmatrix}S_3^-\|0\}\\S_3^+\|0\}\end{Bmatrix}$	$\begin{Bmatrix}\sigma_d^A\|0\}\\\sigma_d^B\|0\}\\\sigma_d^C\|0\}\end{Bmatrix}$	$\begin{Bmatrix}\sigma_v^A\|\tau\}\\\sigma_v^B\|\tau\}\\\sigma_v^C\|\tau\}\end{Bmatrix}$		
Γ_1^+	1	1	1	1	1	1	1	1	1	1	1	1		$x^2+y^2\ ,\ z^2$
Γ_2^+	1	1	1	1	-1	-1	1	1	1	1	-1	-1		
Γ_3^+	1	1	-1	-1	-1	1	1	1	-1	-1	-1	1		
Γ_4^+	1	1	-1	-1	1	-1	1	1	-1	-1	1	-1		
Γ_5^+	2	-1	-2	1	0	0	2	-1	-2	1	0	0		(xz, yz)
Γ_6^+	2	-1	2	-1	0	0	2	-1	2	-1	0	0		(x^2-y^2, xy)
Γ_1^-	1	1	1	1	1	1	-1	-1	-1	-1	-1	-1		
Γ_2^-	1	1	1	1	-1	-1	-1	-1	-1	-1	1	1	z	
Γ_3^-	1	1	-1	-1	-1	1	-1	-1	1	1	1	-1		
Γ_4^-	1	1	-1	-1	1	-1	-1	-1	1	1	-1	1		
Γ_5^-	2	-1	-2	1	0	0	-2	1	2	-1	0	0	(x, y)	
Γ_6^-	2	-1	2	-1	0	0	-2	1	-2	1	0	0		
χ^{eq}	4	4	0	0	0	4	0	0	4	4	4	0	Γ^{eq}	$2\Gamma_1^+ \oplus 2\Gamma_3^-$
χ^{vec}	3	0	-1	2	-1	-1	-3	0	1	-2	1	1	Γ^{vec}	$\Gamma_2^- \oplus \Gamma_5^-$
χ^{LV}	12	0	0	0	0	-4	0	0	4	-8	4	0	Γ^{LV}	$2\Gamma_4^+ \oplus 2\Gamma_6^+ \oplus 2\Gamma_2^- \oplus 2\Gamma_5^-$
χ^z	1	1	1	1	-1	-1	-1	-1	-1	-1	1	1	Γ^z	Γ_2^-
χ^π	4	4	0	0	0	-4	0	0	-4	-4	4	0	Γ^π	$2\Gamma_4^+ \oplus 2\Gamma_2^-$

Table A.14: Character table for the **K** point (D^4_{3h}, $P\bar{6}2c$, No. 190).

	$\{E\|0\}$	$\{C_3^+\|0\}$ $\{C_3^-\|0\}$	$\begin{Bmatrix}C_2'^A\|0\}\\C_2'^B\|0\}\\C_2'^C\|0\}\end{Bmatrix}$	$\{\sigma_h\|0\}$	$\{S_3^-\|0\}$ $\{S_3^+\|0\}$	$\{\sigma_v^A\|\tau\}$ $\{\sigma_v^B\|\tau\}$ $\{\sigma_v^C\|\tau\}$		
K_1	1	1	1	1	1	1		$x^2+y^2\ ,\ z^2$
K_2	1	1	-1	1	1	-1		
K_3	2	-1	0	2	-1	0	(x, y)	(x^2-y^2, xy)
K_4	1	1	1	-1	-1	-1		
K_5	1	1	-1	-1	-1	1	z	
K_6	2	-1	0	-2	1	0		(xz, yz)
χ^{eq}	4	1	0	4	1	0	Γ^{eq}	$K_1 \oplus K_2 \oplus K_3$
χ^{vec}	3	0	-1	1	-2	0	Γ^{vec}	$K_3 \oplus K_5$
χ^{LV}	12	0	0	4	-2	0	Γ^{LV}	$K_1 \oplus K_2 \oplus 3K_3 \oplus K_4 \oplus K_5 \oplus K_6$
χ^z	1	1	-1	-1	-1	1	Γ^z	K_5
χ^π	4	1	0	-4	-1	0	Γ^π	$K_4 \oplus K_5 \oplus K_6$

Table A.15: Character table for the **M** point (D_{2h}^{17}, $Cmcm$, No. 63).

	$\{E\|0\}$	$\{C_2\|\tau\}$	$\left\{C_2^{'A}\|0\right\}$	$\left\{C_2^{''A}\|0\right\}$	$\{i\|0\}$	$\{\sigma_h\|0\}$	$\{\sigma_d^A\|0\}$	$\{\sigma_v^A\|\tau\}$		
M_1^+	1	1	1	1	1	1	1	1		x^2 , y^2 , z^2
M_2^+	1	1	-1	-1	1	1	-1	-1		xy
M_3^+	1	-1	1	-1	1	-1	1	-1		xz
M_4^+	1	-1	-1	1	1	-1	-1	1		yz
M_1^-	1	1	1	1	-1	-1	-1	-1		
M_2^-	1	1	-1	-1	-1	-1	1	1	z	
M_3^-	1	-1	1	-1	-1	1	-1	1	y	
M_4^-	1	-1	-1	1	-1	1	1	-1	x	
χ^{eq}	4	0	0	4	0	4	4	0	Γ^{eq}	$2M_1^+ \oplus 2M_4^-$
χ^{vec}	3	-1	-1	-1	-3	1	1	1	Γ^{vec}	$M_2^- \oplus M_3^- \oplus M_4^-$
χ^{LV}	12	0	0	-4	0	4	4	0	Γ^{LV}	$2M_1^+ \oplus 2M_2^+ \oplus 2M_3^+ \oplus 2M_2^- \oplus 2M_3^- \oplus 2M_4^-$
χ^z	1	1	-1	-1	-1	-1	1	1	Γ^z	M_2^-
χ^π	4	0	0	-4	0	-4	4	0	Γ^π	$2M_3^+ \oplus 2M_2^-$

Table A.16: Character table for the Σ point (C_s^3, Cm, No. 8).

	$\{E\|0\}$	$\left\{C_2^{''A}\|0\right\}$	$\{\sigma_h\|0\}$	$\{\sigma_d^A\|0\}$		
Σ_1	1	1	1	1	x	x^2 , y^2 , z^2
Σ_2	1	1	-1	-1		zy
Σ_3	1	-1	1	-1	y	xy
Σ_4	1	-1	-1	1	z	zx
χ^{eq}	4	4	4	4	Γ^{eq}	$4\Sigma_1$
χ^{vec}	3	-1	1	1	Γ^{vec}	$\Sigma_1 \oplus \Sigma_3 \oplus \Sigma_4$
χ^{LV}	12	-4	4	4	Γ^{LV}	$4\Sigma_1 \oplus 4\Sigma_3 \oplus 4\Sigma_4$
χ^z	1	-1	-1	1	Γ^z	Σ_4
χ^π	4	-4	-4	4	Γ^π	$4\Sigma_4$

Table A.17: Character table for **T** and **T′** points (C_s^3, Cm, No. 8).

	$\{E\|0\}$	$\left\{C_2'^A\|0\right\}$	$\{\sigma_h\|0\}$	$\{\sigma_v^A\|\tau\}$		
T_1	1	1	1	1	y	x^2 , y^2 , z^2
T_2	1	1	-1	-1		xz
T_3	1	-1	1	-1	x	xy
T_4	1	-1	-1	1	z	yz
χ^{eq}	4	0	4	0	Γ^{eq}	$2T_1 \oplus 2T_3$
χ^{vec}	3	-1	1	1	Γ^{vec}	$T_1 \oplus T_3 \oplus T_4$
χ^{LV}	12	0	4	0	Γ^{LV}	$4T_1 \oplus 2T_2 \oplus 4T_3 \oplus 2T_4$
χ^{z}	1	-1	-1	1	Γ^{z}	T_4
χ^{π}	4	0	-4	0	Γ^{π}	$2T_2 \oplus 2T_4$

Table A.18: Character table for the **u** point (C_s^1, Pm, No. 6).

	$\{E\|0\}$	$\{\sigma_h\|0\}$		
u^+	1	1	x , y	x^2 , y^2 , z^2 , xy
u^-	1	-1	z	zy , zx
χ^{eq}	4	4	Γ^{eq}	$4u^+$
χ^{vec}	3	1	Γ^{vec}	$2u^+ \oplus u^-$
χ^{LV}	12	4	Γ^{LV}	$8u^+ \oplus 4u^-$
χ^{z}	1	-1	Γ^{z}	u^-
χ^{π}	4	-4	Γ^{π}	$4u^-$

A.2.2 The characters of the equivalence representations

Only two cases for the matrices of the atomic sites are possible for the 3D graphite lattice. The first case occurs for those operations in which the four atoms of the unit cell remain in their original (or equivalent) sites. In this case, the atomic site matrix is a 4×4 identity matrix. In the second case, the pairs of atoms (**1** , **2**), and (**3** , **4**), change their respective sites. In this case, the matrix of atomic site is:

$$M_{as} = \begin{pmatrix} 0 & 1 & 0 & 0 \\ 1 & 0 & 0 & 0 \\ 0 & 0 & 0 & 1 \\ 0 & 0 & 1 & 0 \end{pmatrix} . \tag{A.15}$$

The position of the i^{th} atom after application of the n^{th} symmetry operation ($\vec{r}_i^{\,(n)}$) for the 24 symmetry operations of 3D graphite can be obtained as:

$$\vec{r}_i^{\,(n)} = \left\{ \mathbf{R}^{(n)} | \tau \right\} \vec{w}_i = \mathbf{R}^{(n)} \vec{w}_i + \vec{\tau} \ , \tag{A.16}$$

where $\vec{w}_i$ is the original position of the i^{th} atom, given in Equations 2.19, 2.20, 2.21, and 2.22 for atoms **1**, **2**, **3**, and **4** respectively. Table A.19 shows the $\vec{r}_i$ and $\vec{t}_i$ vectors associated with the 24 symmetry operations on 3D graphite.

Table A.19: The $\vec{r}_i$ and $\vec{t}_i$ vectors associated with the 24 symmetry operations on 3D graphite.

Operation	$\vec{r}_1$	$\vec{r}_2$	$\vec{r}_3$	$\vec{r}_4$	$\vec{t}_1$	$\vec{t}_2$	$\vec{t}_3$	$\vec{t}_4$
$\{E\|0\}$	$\frac{3c}{4}\hat{z}$	$\frac{c}{4}\hat{z}$	$\frac{a}{2\sqrt{3}}\hat{x}+\frac{a}{2}\hat{y}+\frac{3c}{4}\hat{z}$	$-\frac{a}{2\sqrt{3}}\hat{x}+\frac{a}{2}\hat{y}+\frac{c}{4}\hat{z}$	0	0	0	0
$\{C_3^+\|0\}$	$\frac{3c}{4}\hat{z}$	$\frac{c}{4}\hat{z}$	$-\frac{a}{\sqrt{3}}\hat{x}+\frac{3c}{4}\hat{z}$	$-\frac{a}{2\sqrt{3}}\hat{x}-\frac{a}{2}\hat{y}+\frac{c}{4}\hat{z}$	0	0	$\frac{3a}{2\sqrt{3}}\hat{x}+\frac{a}{2}\hat{y}$	$a\hat{y}$
$\{C_3^-\|0\}$	$\frac{3c}{4}\hat{z}$	$\frac{c}{4}\hat{z}$	$\frac{a}{2\sqrt{3}}\hat{x}-\frac{a}{2}\hat{y}+\frac{3c}{4}\hat{z}$	$\frac{a}{\sqrt{3}}\hat{x}+\frac{c}{4}\hat{z}$	0	0	$a\hat{y}$	$-\frac{3a}{2\sqrt{3}}\hat{x}+\frac{a}{2}\hat{y}$
$\{C_2\|\tau\}$	$\frac{5c}{4}\hat{z}$	$\frac{3c}{4}\hat{z}$	$-\frac{a}{2\sqrt{3}}\hat{x}-\frac{a}{2}\hat{y}+\frac{5c}{4}\hat{z}$	$\frac{a}{2\sqrt{3}}\hat{x}-\frac{a}{2}\hat{y}+\frac{3c}{4}\hat{z}$	$-\frac{c}{2}\hat{z}$	$-\frac{c}{2}\hat{z}$	$\frac{a}{\sqrt{3}}\hat{x}+a\hat{y}-\frac{c}{2}\hat{z}$	$-\frac{a}{\sqrt{3}}\hat{x}+a\hat{y}-\frac{c}{2}\hat{z}$
$\{C_6^-\|\tau\}$	$\frac{5c}{4}\hat{z}$	$\frac{3c}{4}\hat{z}$	$\frac{a}{\sqrt{3}}\hat{x}+\frac{5c}{4}\hat{z}$	$\frac{a}{2\sqrt{3}}\hat{x}+\frac{a}{2}\hat{y}+\frac{3c}{4}\hat{z}$	$-\frac{c}{2}\hat{z}$	$-\frac{c}{2}\hat{z}$	$-\frac{a}{2\sqrt{3}}\hat{x}+\frac{a}{2}\hat{y}-\frac{c}{2}\hat{z}$	$-\frac{a}{\sqrt{3}}\hat{x}-\frac{c}{2}\hat{z}$
$\{C_6^+\|\tau\}$	$\frac{5c}{4}\hat{z}$	$\frac{3c}{4}\hat{z}$	$-\frac{a}{2\sqrt{3}}\hat{x}+\frac{a}{2}\hat{y}+\frac{5c}{4}\hat{z}$	$-\frac{a}{\sqrt{3}}\hat{x}+\frac{3c}{4}\hat{z}$	$-\frac{c}{2}\hat{z}$	$-\frac{c}{2}\hat{z}$	$\frac{a}{\sqrt{3}}\hat{x}-\frac{c}{2}\hat{z}$	$\frac{a}{2\sqrt{3}}\hat{x}+\frac{a}{2}\hat{y}-\frac{c}{2}\hat{z}$
$\{C_2'^A\|0\}$	$-\frac{3c}{4}\hat{z}$	$-\frac{c}{4}\hat{z}$	$-\frac{a}{2\sqrt{3}}\hat{x}+\frac{a}{2}\hat{y}-\frac{3c}{4}\hat{z}$	$\frac{a}{2\sqrt{3}}\hat{x}+\frac{a}{2}\hat{y}-\frac{c}{4}\hat{z}$	$\frac{3c}{2}\hat{z}$	$\frac{c}{2}\hat{z}$	$\frac{a}{\sqrt{3}}\hat{x}+\frac{3c}{2}\hat{z}$	$-\frac{a}{\sqrt{3}}\hat{x}+\frac{c}{2}\hat{z}$
$\{C_2'^B\|0\}$	$-\frac{3c}{4}\hat{z}$	$-\frac{c}{4}\hat{z}$	$\frac{a}{\sqrt{3}}\hat{x}-\frac{3c}{4}\hat{z}$	$\frac{a}{2\sqrt{3}}\hat{x}-\frac{a}{2}\hat{y}-\frac{c}{4}\hat{z}$	$\frac{3c}{2}\hat{z}$	$\frac{c}{2}\hat{z}$	$-\frac{a}{2\sqrt{3}}\hat{x}+\frac{a}{2}\hat{y}+\frac{3c}{2}\hat{z}$	$-\frac{a}{\sqrt{3}}\hat{x}+a\hat{y}+\frac{c}{2}\hat{z}$
$\{C_2'^C\|0\}$	$-\frac{3c}{4}\hat{z}$	$-\frac{c}{4}\hat{z}$	$-\frac{a}{2\sqrt{3}}\hat{x}-\frac{a}{2}\hat{y}-\frac{3c}{4}\hat{z}$	$-\frac{a}{\sqrt{3}}\hat{x}-\frac{c}{4}\hat{z}$	$\frac{3c}{2}\hat{z}$	$\frac{c}{2}\hat{z}$	$\frac{a}{\sqrt{3}}\hat{x}+a\hat{y}+\frac{3c}{2}\hat{z}$	$\frac{a}{\sqrt{3}}\hat{x}+\frac{a}{2}\hat{y}+\frac{c}{2}\hat{z}$
$\{C_2''^A\|0\}$	$-\frac{c}{4}\hat{z}$	$\frac{c}{4}\hat{z}$	$\frac{a}{2\sqrt{3}}\hat{x}-\frac{a}{2}\hat{y}-\frac{c}{4}\hat{z}$	$-\frac{a}{2\sqrt{3}}\hat{x}-\frac{a}{2}\hat{y}+\frac{c}{4}\hat{z}$	$c\hat{z}$	0	$a\hat{y}+c\hat{z}$	$a\hat{y}$
$\{C_2''^B\|0\}$	$-\frac{c}{4}\hat{z}$	$\frac{c}{4}\hat{z}$	$-\frac{a}{\sqrt{3}}\hat{x}-\frac{c}{4}\hat{z}$	$-\frac{a}{2\sqrt{3}}\hat{x}+\frac{a}{2}\hat{y}+\frac{c}{4}\hat{z}$	$c\hat{z}$	0	$\frac{3a}{2\sqrt{3}}\hat{x}+\frac{a}{2}\hat{y}+c\hat{z}$	0
$\{C_2''^C\|0\}$	$-\frac{c}{4}\hat{z}$	$\frac{c}{4}\hat{z}$	$\frac{a}{2\sqrt{3}}\hat{x}+\frac{a}{2}\hat{y}-\frac{c}{4}\hat{z}$	$\frac{a}{\sqrt{3}}\hat{x}+\frac{c}{4}\hat{z}$	$c\hat{z}$	0	$c\hat{z}$	$-\frac{3a}{2\sqrt{3}}\hat{x}+\frac{a}{2}\hat{y}$
$\{i\|0\}$	$-\frac{3c}{4}\hat{z}$	$-\frac{c}{4}\hat{z}$	$-\frac{a}{2\sqrt{3}}\hat{x}-\frac{a}{2}\hat{y}-\frac{3c}{4}\hat{z}$	$\frac{a}{2\sqrt{3}}\hat{x}-\frac{a}{2}\hat{y}-\frac{c}{4}\hat{z}$	$\frac{3c}{2}\hat{z}$	$\frac{c}{2}\hat{z}$	$\frac{a}{\sqrt{3}}\hat{x}+a\hat{y}+\frac{3c}{2}\hat{z}$	$-\frac{a}{\sqrt{3}}\hat{x}+a\hat{y}+\frac{c}{2}\hat{z}$
$\{S_6^+\|0\}$	$-\frac{3c}{4}\hat{z}$	$-\frac{c}{4}\hat{z}$	$\frac{a}{\sqrt{3}}\hat{x}-\frac{3c}{4}\hat{z}$	$\frac{a}{2\sqrt{3}}\hat{x}+\frac{a}{2}\hat{y}-\frac{c}{4}\hat{z}$	$\frac{3c}{2}\hat{z}$	$\frac{c}{2}\hat{z}$	$-\frac{a}{2\sqrt{3}}\hat{x}+\frac{a}{2}\hat{y}+\frac{3c}{2}\hat{z}$	$-\frac{a}{\sqrt{3}}\hat{x}+\frac{c}{2}\hat{z}$
$\{S_6^-\|0\}$	$-\frac{3c}{4}\hat{z}$	$-\frac{c}{4}\hat{z}$	$-\frac{a}{2\sqrt{3}}\hat{x}+\frac{a}{2}\hat{y}-\frac{3c}{4}\hat{z}$	$-\frac{a}{\sqrt{3}}\hat{x}-\frac{c}{4}\hat{z}$	$\frac{3c}{2}\hat{z}$	$\frac{c}{2}\hat{z}$	$\frac{a}{\sqrt{3}}\hat{x}+\frac{3c}{2}\hat{z}$	$\frac{a}{2\sqrt{3}}\hat{x}+\frac{a}{2}\hat{y}+\frac{c}{2}\hat{z}$
$\{\sigma_h\|0\}$	$-\frac{c}{4}\hat{z}$	$\frac{c}{4}\hat{z}$	$\frac{a}{2\sqrt{3}}\hat{x}+\frac{a}{2}\hat{y}-\frac{c}{4}\hat{z}$	$-\frac{a}{2\sqrt{3}}\hat{x}+\frac{a}{2}\hat{y}+\frac{c}{4}\hat{z}$	$c\hat{z}$	0	$c\hat{z}$	0
$\{S_3^-\|0\}$	$-\frac{c}{4}\hat{z}$	$\frac{c}{4}\hat{z}$	$-\frac{a}{\sqrt{3}}\hat{x}-\frac{c}{4}\hat{z}$	$-\frac{a}{2\sqrt{3}}\hat{x}-\frac{a}{2}\hat{y}+\frac{c}{4}\hat{z}$	$c\hat{z}$	0	$\frac{3a}{2\sqrt{3}}\hat{x}+\frac{a}{2}\hat{y}+c\hat{z}$	$a\hat{y}$
$\{S_3^+\|0\}$	$-\frac{c}{4}\hat{z}$	$\frac{c}{4}\hat{z}$	$\frac{a}{2\sqrt{3}}\hat{x}-\frac{a}{2}\hat{y}-\frac{c}{4}\hat{z}$	$\frac{a}{\sqrt{3}}\hat{x}+\frac{c}{4}\hat{z}$	$c\hat{z}$	0	$a\hat{y}+c\hat{z}$	$-\frac{3a}{2\sqrt{3}}\hat{x}+\frac{a}{2}\hat{y}$
$\{\sigma_d^A\|0\}$	$\frac{3c}{4}\hat{z}$	$\frac{c}{4}\hat{z}$	$\frac{a}{2\sqrt{3}}\hat{x}-\frac{a}{2}\hat{y}+\frac{3c}{4}\hat{z}$	$-\frac{a}{2\sqrt{3}}\hat{x}-\frac{a}{2}\hat{y}+\frac{c}{4}\hat{z}$	0	0	$a\hat{y}$	$a\hat{y}$
$\{\sigma_d^B\|0\}$	$\frac{3c}{4}\hat{z}$	$\frac{c}{4}\hat{z}$	$-\frac{a}{\sqrt{3}}\hat{x}+\frac{3c}{4}\hat{z}$	$-\frac{a}{2\sqrt{3}}\hat{x}+\frac{a}{2}\hat{y}+\frac{c}{4}\hat{z}$	0	0	$\frac{3a}{2\sqrt{3}}\hat{x}+\frac{a}{2}\hat{y}$	0
$\{\sigma_d^C\|0\}$	$\frac{3c}{4}\hat{z}$	$\frac{c}{4}\hat{z}$	$\frac{a}{2\sqrt{3}}\hat{x}+\frac{a}{2}\hat{y}+\frac{3c}{4}\hat{z}$	$\frac{a}{\sqrt{3}}\hat{x}+\frac{c}{4}\hat{z}$	0	0	0	$-\frac{3a}{2\sqrt{3}}\hat{x}+\frac{a}{2}\hat{y}$
$\{\sigma_v^A\|\tau\}$	$\frac{5c}{4}\hat{z}$	$\frac{3c}{4}\hat{z}$	$-\frac{a}{2\sqrt{3}}\hat{x}+\frac{a}{2}\hat{y}+\frac{5c}{4}\hat{z}$	$\frac{a}{2\sqrt{3}}\hat{x}+\frac{a}{2}\hat{y}+\frac{3c}{4}\hat{z}$	$-\frac{c}{2}\hat{z}$	$-\frac{c}{2}\hat{z}$	$\frac{a}{\sqrt{3}}\hat{x}-\frac{c}{2}\hat{z}$	$-\frac{a}{\sqrt{3}}\hat{x}-\frac{c}{2}\hat{z}$
$\{\sigma_v^B\|\tau\}$	$\frac{5c}{4}\hat{z}$	$\frac{3c}{4}\hat{z}$	$\frac{a}{\sqrt{3}}\hat{x}+\frac{5c}{4}\hat{z}$	$\frac{a}{2\sqrt{3}}\hat{x}-\frac{a}{2}\hat{y}+\frac{3c}{4}\hat{z}$	$-\frac{c}{2}\hat{z}$	$-\frac{c}{2}\hat{z}$	$-\frac{a}{2\sqrt{3}}\hat{x}+\frac{a}{2}\hat{y}-\frac{c}{2}\hat{z}$	$\frac{a}{\sqrt{3}}\hat{x}+a\hat{y}-\frac{c}{2}\hat{z}$
$\{\sigma_v^C\|\tau\}$	$\frac{5c}{4}\hat{z}$	$\frac{3c}{4}\hat{z}$	$-\frac{a}{2\sqrt{3}}\hat{x}-\frac{a}{2}\hat{y}+\frac{5c}{4}\hat{z}$	$-\frac{a}{\sqrt{3}}\hat{x}+\frac{3c}{4}\hat{z}$	$-\frac{c}{2}\hat{z}$	$-\frac{c}{2}\hat{z}$	$\frac{a}{\sqrt{3}}\hat{x}+a\hat{y}-\frac{c}{2}\hat{z}$	$\frac{a}{2\sqrt{3}}\hat{x}+\frac{a}{2}\hat{y}-\frac{c}{2}\hat{z}$

Tables A.20 and A.21 show the products $\vec{t}_i \cdot \vec{k}$, and the phase factors $e^{\vec{t}_i \cdot \vec{k}}$, for all points inside the central horizontal plane in the first Brillouin zone of 3D graphite for all symmetry operations associated with each respective point. The penultimate column of Tables A.20 and A.21 show the respective characters of the atomic site representations (χ^{as}) obtained from the traces of the atomic site matrices. The last column of Tables A.20 and A.21 show the characters of the equivalence representations (χ^{eq}) obtained from the traces of the equivalence matrices.

Table A.20: The products $\vec{t}_i \cdot \vec{k}$, and the phase factors $e^{\vec{t}_i \cdot \vec{k}}$, for all points inside of the central plane of the first Brillouin zone of 3D graphite for all symmetry operations associated with each respective point. The penultimate, and the last columns show the characters of the atomic site representations (χ^{as}), and the characters of the equivalence representations (χ^{eq}), respectively.

Γ	$\vec{t}_1 \cdot \Gamma$	$\vec{t}_2 \cdot \Gamma$	$\vec{t}_3 \cdot \Gamma$	$\vec{t}_4 \cdot \Gamma$	$e^{i(\vec{t}_1 \cdot \Gamma)}$	$e^{i(\vec{t}_2 \cdot \Gamma)}$	$e^{i(\vec{t}_3 \cdot \Gamma)}$	$e^{i(\vec{t}_4 \cdot \Gamma)}$	χ^{as}	χ^{eq}
$\{E\|0\}$	0	0	0	0	1	1	1	1	4	4
$\{C_3^+\|0\}$	0	0	0	0	1	1	1	1	4	4
$\{C_3^-\|0\}$	0	0	0	0	1	1	1	1	4	4
$\{C_2\|\tau\}$	0	0	0	0	1	1	1	1	0	0
$\{C_6^-\|\tau\}$	0	0	0	0	1	1	1	1	0	0
$\{C_6^+\|\tau\}$	0	0	0	0	1	1	1	1	0	0
$\{C_2'^A\|0\}$	0	0	0	0	1	1	1	1	0	0
$\{C_2'^B\|0\}$	0	0	0	0	1	1	1	1	0	0
$\{C_2'^C\|0\}$	0	0	0	0	1	1	1	1	0	0
$\{C_2''^A\|0\}$	0	0	0	0	1	1	1	1	4	4
$\{C_2''^B\|0\}$	0	0	0	0	1	1	1	1	4	4
$\{C_2''^C\|0\}$	0	0	0	0	1	1	1	1	4	4
$\{i\|0\}$	0	0	0	0	1	1	1	1	0	0
$\{S_6^+\|0\}$	0	0	0	0	1	1	1	1	0	0
$\{S_6^-\|0\}$	0	0	0	0	1	1	1	1	0	0
$\{\sigma_h\|0\}$	0	0	0	0	1	1	1	1	4	4
$\{S_3^-\|0\}$	0	0	0	0	1	1	1	1	4	4
$\{S_3^+\|0\}$	0	0	0	0	1	1	1	1	4	4
$\{\sigma_d^A\|0\}$	0	0	0	0	1	1	1	1	4	4
$\{\sigma_d^B\|0\}$	0	0	0	0	1	1	1	1	4	4
$\{\sigma_d^C\|0\}$	0	0	0	0	1	1	1	1	4	4
$\{\sigma_v^A\|\tau\}$	0	0	0	0	1	1	1	1	0	0
$\{\sigma_v^B\|\tau\}$	0	0	0	0	1	1	1	1	0	0
$\{\sigma_v^C\|\tau\}$	0	0	0	0	1	1	1	1	0	0

Table A.21: Continuing Table A.20.

K	$\vec{t}_1 \cdot K$	$\vec{t}_2 \cdot K$	$\vec{t}_3 \cdot K$	$\vec{t}_4 \cdot K$	$e^{i(\vec{t}_1 \cdot K)}$	$e^{i(\vec{t}_2 \cdot K)}$	$e^{i(\vec{t}_3 \cdot K)}$	$e^{i(\vec{t}_4 \cdot K)}$	χ^{as}	χ^{eq}
$\{E\|0\}$	0	0	0	0	1	1	1	1	4	4
$\{C_3^+\|0\}$	0	0	$\frac{2\pi}{3}$	$\frac{4\pi}{3}$	1	1	$-\frac{1}{2}(1-i\sqrt{3})$	$-\frac{1}{2}(1+i\sqrt{3})$	4	1
$\{C_3^-\|0\}$	0	0	$\frac{4\pi}{3}$	$\frac{2\pi}{3}$	1	1	$-\frac{1}{2}(1+i\sqrt{3})$	$-\frac{1}{2}(1-i\sqrt{3})$	4	1
$\{C_2'^A\|0\}$	0	0	0	0	1	1	1	1	0	0
$\{C_2'^B\|0\}$	0	0	$\frac{2\pi}{3}$	$\frac{4\pi}{3}$	1	1	$-\frac{1}{2}(1-i\sqrt{3})$	$-\frac{1}{2}(1+i\sqrt{3})$	0	0
$\{C_2'^C\|0\}$	0	0	$\frac{4\pi}{3}$	$\frac{2\pi}{3}$	1	1	$-\frac{1}{2}(1+i\sqrt{3})$	$-\frac{1}{2}(1-i\sqrt{3})$	0	0
$\{\sigma_h\|0\}$	0	0	0	0	1	1	1	1	4	4
$\{S_3^-\|0\}$	0	0	$\frac{2\pi}{3}$	$\frac{4\pi}{3}$	1	1	$-\frac{1}{2}(1-i\sqrt{3})$	$-\frac{1}{2}(1+i\sqrt{3})$	4	1
$\{S_3^+\|0\}$	0	0	$\frac{4\pi}{3}$	$\frac{2\pi}{3}$	1	1	$-\frac{1}{2}(1+i\sqrt{3})$	$-\frac{1}{2}(1-i\sqrt{3})$	4	1
$\{\sigma_v^A\|\tau\}$	0	0	0	0	1	1	1	1	0	0
$\{\sigma_v^B\|\tau\}$	0	0	$\frac{2\pi}{3}$	$\frac{4\pi}{3}$	1	1	$-\frac{1}{2}(1-i\sqrt{3})$	$-\frac{1}{2}(1+i\sqrt{3})$	0	0
$\{\sigma_v^C\|\tau\}$	0	0	$\frac{4\pi}{3}$	$\frac{2\pi}{3}$	1	1	$-\frac{1}{2}(1+i\sqrt{3})$	$-\frac{1}{2}(1-i\sqrt{3})$	0	0
M	$\vec{t}_1 \cdot M$	$\vec{t}_2 \cdot M$	$\vec{t}_3 \cdot M$	$\vec{t}_4 \cdot M$	$e^{i(\vec{t}_1 \cdot M)}$	$e^{i(\vec{t}_2 \cdot M)}$	$e^{i(\vec{t}_3 \cdot M)}$	$e^{i(\vec{t}_4 \cdot M)}$	χ^{as}	χ^{eq}
$\{E\|0\}$	0	0	0	0	1	1	1	1	4	4
$\{C_2\|\tau\}$	0	0	$\frac{2\pi}{3}$	$-\frac{2\pi}{3}$	1	1	$-\frac{1}{2}(1-i\sqrt{3})$	$-\frac{1}{2}(1+i\sqrt{3})$	0	0
$\{C_2'^A\|0\}$	0	0	$\frac{2\pi}{3}$	$-\frac{2\pi}{3}$	1	1	$-\frac{1}{2}(1-i\sqrt{3})$	$-\frac{1}{2}(1+i\sqrt{3})$	0	0
$\{C_2''^A\|0\}$	0	0	0	0	1	1	1	1	4	4
$\{i\|0\}$	0	0	$\frac{2\pi}{3}$	$-\frac{2\pi}{3}$	1	1	$-\frac{1}{2}(1-i\sqrt{3})$	$-\frac{1}{2}(1+i\sqrt{3})$	0	0
$\{\sigma_h\|0\}$	0	0	0	0	1	1	1	1	4	4
$\{\sigma_d^A\|0\}$	0	0	0	0	1	1	1	1	4	4
$\{\sigma_v^A\|\tau\}$	0	0	$\frac{2\pi}{3}$	$-\frac{2\pi}{3}$	1	1	$-\frac{1}{2}(1-i\sqrt{3})$	$-\frac{1}{2}(1+i\sqrt{3})$	0	0
T	$\vec{t}_1 \cdot T$	$\vec{t}_2 \cdot T$	$\vec{t}_3 \cdot T$	$\vec{t}_4 \cdot T$	$e^{i(\vec{t}_1 \cdot T)}$	$e^{i(\vec{t}_2 \cdot T)}$	$e^{i(\vec{t}_3 \cdot T)}$	$e^{i(\vec{t}_4 \cdot T)}$	χ^{as}	χ^{eq}
$\{E\|0\}$	0	0	0	0	1	1	1	1	4	4
$\{C_2'^A\|0\}$	0	0	0	0	1	1	1	1	0	0
$\{\sigma_h\|0\}$	0	0	0	0	1	1	1	1	4	4
$\{\sigma_v^A\|\tau\}$	0	0	0	0	1	1	1	1	0	0
Σ	$\vec{t}_1 \cdot \Sigma$	$\vec{t}_2 \cdot \Sigma$	$\vec{t}_3 \cdot \Sigma$	$\vec{t}_4 \cdot \Sigma$	$e^{i(\vec{t}_1 \cdot \Sigma)}$	$e^{i(\vec{t}_2 \cdot \Sigma)}$	$e^{i(\vec{t}_3 \cdot \Sigma)}$	$e^{i(\vec{t}_4 \cdot \Sigma)}$	χ^{as}	χ^{eq}
$\{E\|0\}$	0	0	0	0	1	1	1	1	4	4
$\{C_2''^A\|0\}$	0	0	0	0	1	1	1	1	4	4
$\{\sigma_h\|0\}$	0	0	0	0	1	1	1	1	4	4
$\{\sigma_d^A\|0\}$	0	0	0	0	1	1	1	1	4	4
T′	$\vec{t}_1 \cdot T'$	$\vec{t}_2 \cdot T'$	$\vec{t}_3 \cdot T'$	$\vec{t}_4 \cdot T'$	$e^{i(\vec{t}_1 \cdot T')}$	$e^{i(\vec{t}_2 \cdot T')}$	$e^{i(\vec{t}_3 \cdot T')}$	$e^{i(\vec{t}_4 \cdot T')}$	χ^{as}	χ^{eq}
$\{E\|0\}$	0	0	0	0	1	1	1	1	4	4
$\{C_2'^A\|0\}$	0	0	$\frac{2\pi}{3}$	$-\frac{2\pi}{3}$	1	1	$-\frac{1}{2}(1-i\sqrt{3})$	$-\frac{1}{2}(1+i\sqrt{3})$	0	0
$\{\sigma_h\|0\}$	0	0	0	0	1	1	1	1	4	4
$\{\sigma_v^A\|\tau\}$	0	0	$\frac{2\pi}{3}$	$-\frac{2\pi}{3}$	1	1	$-\frac{1}{2}(1-i\sqrt{3})$	$-\frac{1}{2}(1+i\sqrt{3})$	0	0
u	$\vec{t}_1 \cdot u$	$\vec{t}_2 \cdot u$	$\vec{t}_3 \cdot u$	$\vec{t}_4 \cdot u$	$e^{i(\vec{t}_1 \cdot u)}$	$e^{i(\vec{t}_2 \cdot u)}$	$e^{i(\vec{t}_3 \cdot u)}$	$e^{i(\vec{t}_4 \cdot u)}$	χ^{as}	χ^{eq}
$\{E\|0\}$	0	0	0	0	1	1	1	1	4	4
$\{\sigma_h\|0\}$	0	0	0	0	1	1	1	1	4	4

Tables A.13 to A.18 show the characters of the equivalence representations for all points inside the central horizontal plane in the first Brillouin zone of 3D graphite.

A.2.3 Calculus of the phonon eigenvectors at the Γ point

We have seen in section A.1.6 that the vector resulting from the projection of the irreducible representations of a random displacement vector associated with one of the four

atoms of the unit cell can be evaluated as:

$$\vec{V}_m = \sum_{(n)} \chi_m^{(n)} \left[\mathbf{D}_m^{(n)} \hat{q}_{\mathbf{j}}\right] = \sum_{(n),i} \chi_m^{(n)} \left[\mathbf{D}_m^{(n)} \hat{u}_{i,\mathbf{j}}\right] \ . \tag{A.17}$$

However, as discussed before, the action of the symmetry operations of 3D graphite can leave atom **1** in atom **2** (vice versa), or atom **3** in atom **4** (vice versa), but never mix these two subsets of atoms. Therefore, we should choose two atoms belonging to each of these subsets (for example atoms **1** and atom **3**), and evaluate Equation A.17 for both:

$$\begin{aligned} \vec{v}_m^{\,A} &= \sum_{(n)} \chi_m^{(n)} \left[\mathbf{D}_m^{(n)} \hat{q}_{\mathbf{1}}\right] \ , \\ \vec{v}_m^{\,B} &= \sum_{(n)} \chi_m^{(n)} \left[\mathbf{D}_m^{(n)} \hat{q}_{\mathbf{3}}\right] \ . \end{aligned} \tag{A.18}$$

As a result, we will have two solutions, and we should take the linear combination of both in order to obtain the two eigenvectors associated with the irreducible representation Γ^m:

$$\begin{aligned} \vec{V}_m^{\,1} &= \vec{v}_m^{\,A} + \vec{v}_m^{\,B} \ , \\ \vec{V}_m^{\,2} &= \vec{v}_m^{\,A} - \vec{v}_m^{\,B} \ . \end{aligned} \tag{A.19}$$

It should be noticed that all of the irreducible representations forming the lattice vibrations representations at the Γ point appear at least twice. This is a direct consequence of the existence of these two subsets of atoms inside of the unit cell which never mix under application of the symmetry operations.

The phonon eigenvectors at the Γ point in the first Brillouin zone of 3D graphite are shown in the Table 2.8, giving the coefficients $v_{i\mathbf{j}}$, following the notation:

$$(v_{\mathbf{11}}, v_{\mathbf{21}}, v_{\mathbf{31}})(v_{\mathbf{12}}, v_{\mathbf{22}}, v_{\mathbf{32}})(v_{\mathbf{13}}, v_{\mathbf{23}}, v_{\mathbf{33}})(v_{1,\mathbf{4}}, v_{\mathbf{24}}, v_{\mathbf{34}}) \ . \tag{A.20}$$

Appendix B

Radiation by the Stokes polarization

This Appendix presents the detailed description of the procedures necessary to calculate the intensity of the radiation by the Stokes polarization (equation 3.23 in Chapter 3). From starting point, we recall the Maxwell's equations for a dielectric, non-magnetic, and electrically neutral medium:

$$\vec{\nabla} \times \vec{E} = -\mu \frac{\partial \vec{H}}{\partial t} \ , \tag{B.1}$$

$$\vec{\nabla} \times \vec{H} = \frac{\partial \vec{D}}{\partial t} \ , \tag{B.2}$$

$$\vec{\nabla} \cdot \vec{D} = 0 \ , \tag{B.3}$$

$$\vec{\nabla} \cdot \vec{H} = 0 \ . \tag{B.4}$$

Grouping equations B.1 and B.2, we have the wave equation for the scattered field inside of the sample:

$$\vec{\nabla} \times \vec{\nabla} \times \vec{E}_S = -\mu \frac{\partial^2 \vec{D}_S}{\partial t^2} \ . \tag{B.5}$$

It should be noticed that the wavevector $\vec{K}_S$ can of the scattered light (whose frequency is necessarily ω_s) can, in principle, take any direction and magnitude for which the wave equation B.5 is satisfied. These possibilities include even the wavevector $\vec{k}_S$ associated with free electromagnetic waves (occurring in the absence of any Stokes polarization) of frequency ω_s, whose magnitude is given as $k_S = \eta_S \omega_S / c$. Therefore, the solution for equation B.5 can be written as the sum of two contributions:

$$\vec{E}_S = \vec{E}_h \, e^{i(\vec{k}_S \cdot \vec{r} - \omega_S t)} + \vec{E}_i \, e^{i(\vec{K}_S \cdot \vec{r} - \omega_S t)}, \tag{B.6}$$

where the subscripts h and i refer to the homogeneous and inhomogeneous parts of the scattered field inside of the sample, respectively. Let us start our analysis from the homogeneous part, for with the vector $\vec{D}$ is written as:

$$\vec{D}_h = \epsilon_0(1+ \overleftrightarrow{\chi}_0)\vec{E}_h\, e^{i(\vec{k}_S\cdot\vec{r}-\omega_S t)} \ , \tag{B.7}$$

and the insertion of the relation $\eta_S^2 = 1+ \overleftrightarrow{\chi}_0$ into equation B.7 gives:

$$\vec{D}_h = \epsilon_0\eta_S^2\vec{E}_h\, e^{i(\vec{k}_S\cdot\vec{r}-\omega_S t)} \ . \tag{B.8}$$

The inhomogeneous part, for which the Stokes polarization acts on the scattered field, has the vector $\vec{D}_i$ on the form:

$$\vec{D}_i = \epsilon_0\left[1+ \overleftrightarrow{\chi}_0 + \overleftrightarrow{\chi}' X^*(\vec{q},\omega_S)\right]\vec{E}_i\, e^{i(\vec{K}_S\cdot\vec{r}-\omega_S t)} \ , \tag{B.9}$$

Now, we write the relation:

$$\vec{D}_S = \vec{D}_h + \vec{D}_i \ , \tag{B.10}$$

and the substitution of equations B.8, B.9, B.10 in the wave equation B.5 gives:

$$\vec{\nabla}\times\vec{\nabla}\times\left[\vec{E}_h\, e^{i(\vec{k}_S\cdot\vec{r}-\omega_S t)} + \vec{E}_i\, e^{i(\vec{K}_S\cdot\vec{r}-\omega_S t)}\right] = \tag{B.11}$$

$$= -\mu\epsilon_0\frac{\partial^2}{\partial t^2}\left\{\eta_S^2\vec{E}_h\, e^{i(\vec{k}_S\cdot\vec{r}-\omega_S t)} + \left[\eta_S^2+ \overleftrightarrow{\chi}' X^*(\vec{q},\omega_S)\right]\vec{E}_i\, e^{i(\vec{K}_S\cdot\vec{r}-\omega_S t)}\right\} \ .$$

The next step is to perform the second order time derivative at the right hand side of equation B.11, and take in account only the spacial dependence of the the amplitude of the electric field, obtainig:

$$\vec{\nabla}\times\vec{\nabla}\times(\vec{E}_h\, e^{i\vec{k}_S\cdot\vec{r}} + \vec{E}_i\, e^{i\vec{K}_S\cdot\vec{r}}) - \frac{\eta_S^2\omega_S^2}{c^2}(\vec{E}_h\, e^{i\vec{k}_S\cdot\vec{r}} + \vec{E}_i\, e^{i\vec{K}_S\cdot\vec{r}}) = \frac{\omega_S^2}{\epsilon_0 c^2}\vec{P}_S(\vec{K}_S,\omega_S)\, e^{i\vec{K}_S\cdot\vec{r}} \ , \tag{B.12}$$

where we have used the relations $\mu_0\epsilon_0 = 1/c^2$, and $\vec{P}_S(\vec{K}_S,\omega_S) = \epsilon_0\ \overleftrightarrow{\chi}'\ X^*(\vec{q},\omega_q)\vec{E}_i$. From here on, we will use the shorthand notation $\vec{P}_S$ for $\vec{P}_S(\vec{K}_S,\omega_s)$.

In order to obtain separately the two contributions for the scattered field, equation B.12 can be uncoupled, giving rise to the following pair of equations:

$$\vec{\nabla}\times\vec{\nabla}\times\left(\vec{E}_h\, e^{i\vec{k}_S\cdot\vec{r}}\right) - \frac{\eta_S^2\omega_S^2}{c^2}\vec{E}_h\, e^{i\vec{k}_S\cdot\vec{r}} = 0 \ , \tag{B.13}$$

and

$$\vec{\nabla}\times\vec{\nabla}\times\vec{E}_i\, e^{i\vec{K}_S\cdot\vec{r}} - \frac{\eta_S^2\omega_S^2}{c^2}\vec{E}_i\, e^{i\vec{K}_S\cdot\vec{r}} = \frac{\omega_S^2}{\epsilon_0 c^2}\vec{P}_S\, e^{i\vec{K}_S\cdot\vec{r}} \ , \tag{B.14}$$

where equations B.13 and B.14 correspond to the homogeneous and inhomogeneous parts of the scattered field, respectively. Now, we can use the relations $\vec{\nabla}\times\vec{\nabla}\times = \vec{\nabla}(\vec{\nabla}\cdot) - \nabla^2$, and $k_S = \eta_S\omega_S/c$, in order to the develop the homogeneous part (equation B.13) as:

$$\begin{aligned}
\vec{\nabla}\left(\vec{\nabla}\cdot\vec{E}_h\, e^{i\vec{k}_S\cdot\vec{r}}\right) - \nabla^2\left(\vec{E}_h\, e^{i\vec{k}_S\cdot\vec{r}}\right) &= \frac{\eta_S^2\omega_S^2}{c^2}\vec{E}_h\, e^{i\vec{k}_S\cdot\vec{r}} \\
\vec{\nabla}\left(\vec{\nabla}\cdot\vec{E}_h\, e^{i\vec{k}_S\cdot\vec{r}}\right) &= 0 \\
\vec{\nabla}\cdot\vec{E}_h\, e^{i\vec{k}_S\cdot\vec{r}} &= 0 \\
\vec{k}_S\cdot\vec{E}_h &= 0\ .
\end{aligned} \tag{B.15}$$

The result $\vec{k}_S\cdot\vec{E}_h = 0$ implies that the homogenous part $\vec{E}_h$ is a transverse wave.

Once again, by using the relations $\vec{\nabla}\times\vec{\nabla}\times = \vec{\nabla}(\vec{\nabla}\cdot) - \nabla^2$, and $k_S = \eta_S\omega_S/c$, we can develop the inhomogeneous part (equation B.14) as:

$$\vec{\nabla}\left(\vec{\nabla}\cdot\vec{E}_i\, e^{i\vec{K}_S\cdot\vec{r}}\right) - \nabla^2\left(\vec{E}_i\, e^{i\vec{K}_S\cdot\vec{r}}\right) = k_S^2\vec{E}_i\, e^{i\vec{K}_S\cdot\vec{r}} + \frac{k_S^2}{\epsilon_0\eta_S^2}\vec{P}_S\, e^{i\vec{K}_S\cdot\vec{r}}$$

$$i\vec{K}_S\left(i\vec{K}_S\cdot\vec{E}_i\, e^{i\vec{K}_S\cdot\vec{r}}\right) + K_S^2\vec{E}_i\, e^{i\vec{K}_S\cdot\vec{r}} = k_S^2\vec{E}_i\, e^{i\vec{K}_S\cdot\vec{r}} + \frac{k_S^2}{\epsilon_0\eta_S^2}\vec{P}_S\, e^{i\vec{K}_S\cdot\vec{r}}$$

$$(K_S^2 - k_S^2)\vec{E}_i\, e^{i\vec{K}_S\cdot\vec{r}} = \frac{k_S^2}{\epsilon_0\eta_S^2}\vec{P}_S\, e^{i\vec{K}_S\cdot\vec{r}} - i\vec{K}_S\left(i\vec{K}_S\cdot\vec{E}_i\, e^{i\vec{K}_S}\right)\ . \tag{B.16}$$

Now, by multiplying both sides of equation B.16 by $\epsilon_0\eta_0^2$, and by summing and subtracting the term $i\vec{K}_S\left(i\vec{K}_S\cdot\vec{P}_S\, e^{i\vec{K}_S}\right)$ on the right-hand side, we obtain:

$$\begin{aligned}
\epsilon_0\eta_0^2(K_S^2 - k_S^2)\vec{E}_i\, e^{i\vec{K}_S\cdot\vec{r}} = k_S^2\vec{P}_S\, e^{i\vec{K}_S\cdot\vec{r}} + i\vec{K}_S\left(i\vec{K}_S\cdot\vec{P}_S\, e^{i\vec{K}_S}\right) - \\
-i\vec{K}_S\left[i\vec{K}_S\cdot\left(\epsilon_0\eta_S^2\vec{E}_i\, e^{i\vec{K}_S\cdot\vec{r}} + \vec{P}_S\, e^{i\vec{K}_S\cdot\vec{r}}\right)\right]\ .
\end{aligned} \tag{B.17}$$

The last term in equation B.17 is null, because $i\vec{K}_S\cdot\left(\epsilon_0\eta_S^2\vec{E}_i\, e^{i\vec{K}_S\cdot\vec{r}} + \vec{P}_S\, e^{i\vec{K}_S\cdot\vec{r}}\right) = \vec{\nabla}\cdot\vec{D}_i = 0$. Finally, we have [19]:

$$\vec{E}_i = \frac{k_S^2\vec{P}_S - \vec{K}_S\left(\vec{K}_S\cdot\vec{P}_S\right)}{\epsilon_0\eta_S^2\left(K_S^2 - k_S^2\right)}\ . \tag{B.18}$$

We should notice that, according to equation B.18, neither $\vec{P}_S$ nor $\vec{E}_i$ are necessarily perpendicular to $\vec{K}_S$, as predicted above in the text.

Figure B.1 shows the geometry of the Raman experiment which will be considered in order to evaluate the intensity of the scattered light. The scattering process takes place in a

region of the sample illuminated by the incident light. We will assume, for simplicity, that this region is a slab of thickness L, with faces perpendicular to the observation direction of the scattered light, taken as the z direction. Although the scattered light is emitted in all directions, we will ignore all contributions except that for which $\vec{K}_S$ is oriented in the positive z direction (backscattering geometry).

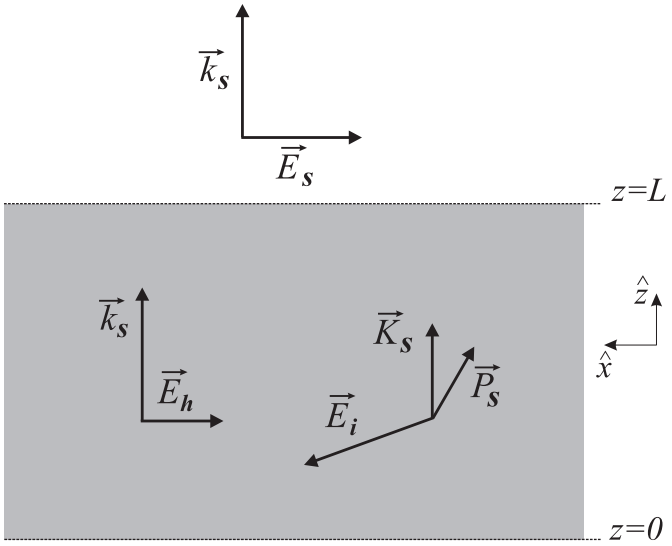

Figure B.1: Region of the sample illuminated by the incident light. We will assume, for simplicity, that this region is a slab of thickness L, with faces perpendicular to the observation direction of the scattered light, taken as the z direction.

The $\hat{x}$ component of the scattered electric field grows from zero intensity in the bottom of the illuminated area ($z=0$), and its generation ceases at the top of the region at $z=L$, where the scattered light passes into the medium in which it will be analyzed. Outside of the slab, the polarization $\vec{P}_S$ is zero, and the electric field has the form $\vec{E}_S e^{i\vec{k}_s\cdot\vec{r}}$, where $\vec{E}_S \cdot \vec{k}_s = 0$.

The shape of the slab forces all the vectors to lie in the plane defined by $\vec{K}_S$ and $\vec{P}_S$, taken as the zx plane. Since the intensity of the scattered light is zero at $z=0$, we have:

$$E_h^x + E_i^x = 0 \ . \tag{B.19}$$

At $z=L$, the boundary conditions require the tangential components of the electric field to be continuous as the boundary is crossed:

$$E_S^x e^{ik_S L} = E_h^x e^{ik_S L} + E_i^x e^{iK_S L} \ . \tag{B.20}$$

Finally, grouping equations B.18, B.19, and B.20, we have the amplitude of the electric

field of the Stokes component of the scattered light [19]:

$$E_S = \frac{k_S^2 \left(\hat{\varepsilon}_S \cdot \vec{P}_S\right)}{\epsilon_0 \eta_S^2 \left(K_S^2 - k_S^2\right)} \left[e^{i(K_S - k_S)L} - 1\right] \ , \tag{B.21}$$

where $\hat{\varepsilon}_S$ is a unit vector parallel to $\vec{E}_S$.

The total cycle-averaged intensity of the scattered field is integrated over its frequency spectrum ω_S, and summed over all $\vec{K}_S$ vectors present in the Stokes polarization:

$$\overline{I}_S = 2\epsilon_0 c \sum_{\vec{K}_S} \int \eta_S E_S^* E_S \, d\omega_S \ . \tag{B.22}$$

Inserting equation B.21 into equation B.22, and taking the average value of the fluctuations in the amplitude of the Stokes polarization, we have:

$$\overline{I}_S = \frac{2c}{\epsilon_0} \sum_{\vec{K}_S} \int \frac{k_S^4 \langle \hat{\varepsilon}_S \cdot \vec{P}_S^*(\vec{K}_S) \ \hat{\varepsilon}_S \cdot \vec{P}_S(\vec{K}_S) \rangle_{\omega_S}}{\eta_S^3 \left(K_S^2 - k_S^2\right)^2} \left| e^{i(K_S - k_S)L} - 1 \right|^2 d\omega_S \ . \tag{B.23}$$

We can now take the product and ratio of the term $\left(K_S - k_S\right)^2$ within the right-hand side of equation B.23, in order to take the limit:

$$\underset{L \to \infty}{Lim} \frac{\left| e^{i(K_S - k_S)L} - 1 \right|^2}{\left(K_S - k_S\right)^2} = 2\pi L \delta\left(K_S - k_S\right) \ , \tag{B.24}$$

and equation B.23 becomes:[1]

$$\overline{I}_S = \frac{4\pi c L}{\epsilon_0} \sum_{\vec{K}_S} \int \frac{k_S^4 \langle \hat{\varepsilon}_S \cdot \vec{P}_S^*(\vec{k}_S) \ \hat{\varepsilon}_S \cdot \vec{P}_S(\vec{k}_S) \rangle_{\omega_S}}{\eta_S^3 \left(K_S^2 - k_S^2\right)^2} \left(K_S - k_S\right)^2 \delta\left(K_S - k_S\right) d\omega_S \ . \tag{B.25}$$

Next, the wavevector summation will be converted to an integration as:

$$\sum_{\vec{K}_S} \rightarrow \frac{V}{(2\pi)^3} \int \int K_S^2 \, dK_S \, d\Omega \ , \tag{B.26}$$

and we can evaluate the integration:

$$\int \frac{K_S^2 \left(K_S - k_S\right)^2}{\left(K_S^2 - k_S^2\right)^2} \, \delta\left(K_S - k_S\right) dK_S = \frac{1}{4} \ . \tag{B.27}$$

Finally, using the relation $k_S = \eta_S \omega_S / c$, the scattered intensity becomes [19]:

$$\overline{I}_S = \frac{L}{8\pi^2 \epsilon_0 c^3} \int \int \eta_S \omega_S^4 \langle \hat{\varepsilon}_S \cdot \vec{P}_S^*(\vec{k}_S) \ \hat{\varepsilon}_S \cdot \vec{P}_S(\vec{k}_S) \rangle_{\omega_S} \, d\omega_S \, d\Omega \ . \tag{B.28}$$

[1] For small crystals, the limit B.24 is not valid, and the delta function is replaced by a broader function, whose value is small unless K_S differs from k_S by an amount less than $2\pi/L$ [19].

Appendix C

The origin of localized states in zigzag edges

In order to understand the origin of the localized states at the zigzag edges, we should evaluate the charge density ρ for lattice points near the edge. Let us consider firstly the atoms belonging to the edge. Figure C.1 shows three A atomic sites belonging to a zigzag edge (white circles), denoted by **1**, **2**, and **3**. The wave function components of the $2_p^{(z)}$ orbital of these edge sites can be written, using the Bloch theorem as follows:

$$|\mathbf{n}\rangle = C_n|\psi_{2p}^{(z)}\rangle \ , \tag{C.1}$$

where the coefficients C_n are the phase factors $e^{i(\vec{k}.\vec{r}_n)}$, being $|\vec{r}_n| = na$ (see Figure C.1). Therefore, considering that the atomic sites **1**, **2**, and **3** in Figure C.1 are in the positions $\vec{r}_{n-1}$, $\vec{r}_n$, and $\vec{r}_{n+1}$, respectively, we can write:

$$|\mathbf{1}\rangle = e^{ika(n-1)}|\psi_{2p}^{(z)}\rangle \ , \tag{C.2}$$

$$|\mathbf{2}\rangle = e^{ika(n)}|\psi_{2p}^{(z)}\rangle \ , \tag{C.3}$$

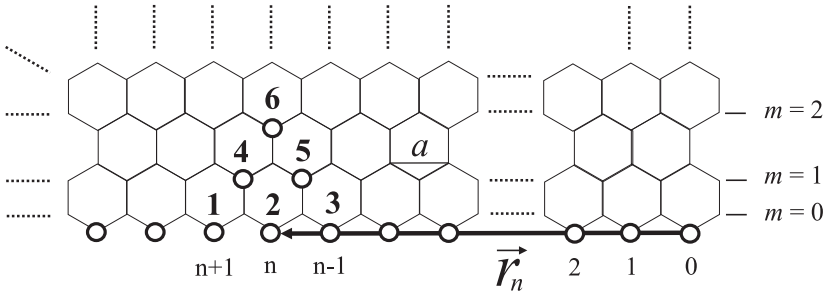

Figure C.1: The atomic sites near a zigzag edge.

$$|\mathbf{3}\rangle = e^{ika(n+1)}|\psi_{2p}^{(z)}\rangle \ . \tag{C.4}$$

The necessary condition for the wave function to be exact for $E = 0$ is that the total sum of the coefficients of the complex wave functions over the neighbor sites should vanish [51, 52]. In this way, for the atomic sites **1**, **2**, **3**, **4**, **5**, and **6** depicted in Figure C.1, we can construct the system of equations:

$$C_1 + C_2 + C_4 = 0 \ , \tag{C.5}$$

$$C_2 + C_3 + C_5 = 0 \ , \tag{C.6}$$

$$C_4 + C_5 + C_6 = 0 \ . \tag{C.7}$$

By solving equations C.5, C.6 and C.7, the wave function components $|\mathbf{4}\rangle$, $|\mathbf{5}\rangle$, and $|\mathbf{6}\rangle$, are found to be:

$$|\mathbf{4}\rangle = -2cos\left(\frac{1}{2}k_y a\right) e^{ika\left(n-\frac{1}{2}\right)}|\psi_{2p}^{(z)}\rangle \ , \tag{C.8}$$

$$|\mathbf{5}\rangle = -2cos\left(\frac{1}{2}k_y a\right) e^{ika\left(n+\frac{1}{2})\right)}|\psi_{2p}^{(z)}\rangle \ , \tag{C.9}$$

$$|\mathbf{6}\rangle = 4cos^2\left(\frac{1}{2}k_y a\right) e^{ika(n)}|\psi_{2p}^{(z)}\rangle \ . \tag{C.10}$$

The charge density ρ related to the edge state in a specific nodal site is proportional to the probability for finding the edge state in that specific site. This probability is obtained by evaluating the square modulus of the Bloch coefficients of the wave function components associated with each specific site, that is:

$$\rho_{\mathbf{1}} \propto \left|e^{ika(n-1)}\right|^2 = 1 \ , \tag{C.11}$$

$$\rho_{\mathbf{2}} \propto \left|e^{ika(n)}\right|^2 = 1 \ , \tag{C.12}$$

$$\rho_{\mathbf{3}} \propto \left|e^{ika(n+1)}\right|^2 = 1 \ , \tag{C.13}$$

$$\rho_{\mathbf{4}} \propto \left|-2cos\left(\frac{1}{2}k_y a\right) e^{ika\left(n-\frac{1}{2}\right)}\right|^2 = 4cos^2\left(\frac{1}{2}k_y a\right) \ , \tag{C.14}$$

$$\rho_{\mathbf{5}} \propto \left|-2cos\left(\frac{1}{2}k_y a\right) e^{ika\left(n+\frac{1}{2}\right)}\right|^2 = 4cos^2\left(\frac{1}{2}k_y a\right) \ , \tag{C.15}$$

$$\rho_{\mathbf{6}} \propto \left|4cos^2\left(\frac{1}{2}k_y a\right) e^{ika(n)}\right|^2 = 16cos^4\left(\frac{1}{2}k_y a\right) \ . \tag{C.16}$$

From relations C.11 to C.16, we conclude that the charge density is proportional to $\left[2cos^2\left(\frac{1}{2}k_y a\right)\right]^{2m}$ at a nodal site belonging to the m-th zigzag chain from the edge (see Figure C.1). Thus, in the range $2\pi/3a \leq k_y \leq \pi/a$, the charge density shows the profile

of an exponential decay. Here, it should be observed that the convergence condition $|-2cos(\frac{1}{2}k_y a)| \leq 1$ is required, otherwise the wave function will diverge in a semi-infinite graphene sheet. This condition defines the region ($2\pi/3a \leq k_y \leq \pi/a$) where the flat band exist.

Table C.1 shows the values of the charge density calculated at k_y=$2\pi/3a$, $7\pi/9a$, $8\pi/9a$, and π/a, for the zigzag lines $m = 0, 1, 2, 3$. We can see from Table C.1 that for $k_y = \pi/a$ the charge density is 1 for $m = 0$, and 0 for all zigzag lines inside of the graphite plane. This confirms the fact that for $k_y = \pi/a$ the edge states are completely localized. On the other hand, it can be seen that for $k_y = 2\pi/3a$ the edge state is completely delocalized. This is reasonable, because in this region the solution of the energy eigenvalues for the edge states should be coupled with the energy eigenvalues of 1D sub-bands obtained by the projection of the dispersion curves of 2D graphite along the cutting lines (see Figure 6.3). Since π electrons are completely delocalized in the 2D graphite lattice, the edge states should also be completely delocalized at $k_y = 2\pi/3a$. For the intermediate region $2\pi/3a < k_y < \pi/a$, the evolution between the two extremes can be clearly observed. Figure C.2 (taken from reference [59]) shows the charge density of the edge state for the k_y values used in Table C.1, where the radius of the circles means the magnitude of the charge density.

Table C.1: Values of the charge density calculated for some k_y values for atoms belonging to the zigzag lines $m = 0, 1, 2, 3$.

k_y	$2\pi/3a$	$7\pi/9a$	$8\pi/9a$	π/a
$m = 0$	1	1	1	1
$m = 1$	1	0.21	0.01	0
$m = 2$	1	0.04	0.001	0
$m = 3$	1	0.002	0.00000003	0

A zigzag graphite edge has peculiar magnetic properties due to the appearance of the edge states, unlike graphene, which is not magnetic [59]. This can be understood as follows: for electrons with wave number $k_y = \pi/a$, the valence and conduction bands touch each other (see Figure 6.3). Considering that the electron spin can assume two values for each band, we have four possible electron states appearing at the Fermi level. Therefore, a local magnetic moment is possible, if we have one electron in the valence band and one electron in the conduction band, both with the same spin [98]. However, such a situation

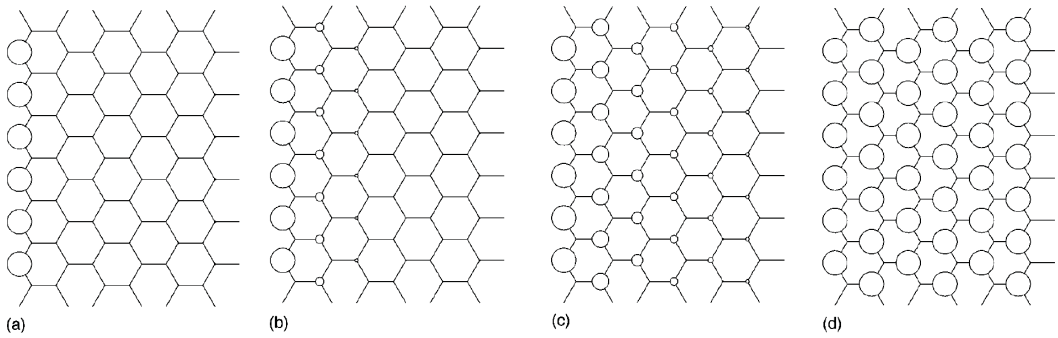

Figure C.2: The charge density of the edge state at (a) $k_y = \pi/a$, (b) $k_y = 8\pi/9a$, (c) $k_y = 7\pi/9a$, and (d) $k_y = 2\pi/3a$, where the radius of the circles corresponds to the magnitude of the charge density (taken from reference [59]).

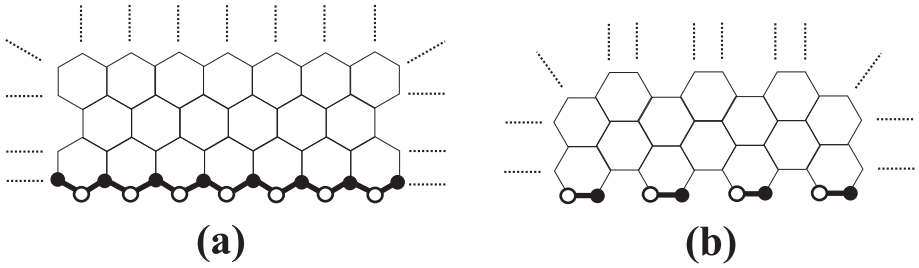

Figure C.3: **(a):** Zigzag edge with $N_A = 7$ and $N_B = 8$ ($S = 1$). **(b):** Armchair edge with $N_A = N_B = 4$ ($S = 0$).

can occur only if the number of spins in the system is odd, that is, the number of total spins is non null. In fact, this is the case of zigzag edges.

According to the Lieb's Theorem [99], for a lattice with two inequivalent atomic sites A and B, the number of total spins is given by the modulus of the difference between the number of atoms of each type, that is, $S = |N_A - N_B|$. Let us consider, for example, the situation depicted in Figure C.3. In part (a), we have a zigzag edge chain where the number of A and B atoms are $N_A = 7$ and $N_B = 8$, respectively. Therefore, $S = 1$, and a resultant magnetic moment is possible in zigzag edges. In the case of part (b), where an armchair edge chain is shown, $N_A = 4$ and $N_B = 4$. Therefore, $S = 0$, and the resultant magnetic moment is zero for armchair edges.

It should be noticed that, although the localized states cause the existence of a magnetic structure in zigzag edges, the total magnetization in a zigzag ribbon is null, since the zigzag edge atoms are inequivalent to each other on opposite sites [98].

Appendix D

The spectrometer intensity calibration

In Chapter 10, we report the measurement of the absolute Raman cross section of nanographites using a micro-Raman Dilor XY system operating in a triple-monochromator mode. The intensity calibration process is a necessary procedure for this type of system since the spectrometer response strongly depends on the wavelength of the scattered light. The calibration process basically consists of the comparison of the power emission spectrum of a standard light source with the spectrum measured by the spectrometer. This procedure requires many practical considerations which will be exposed in this Appendix.

D.1 The standard lamp

The lamp used in the spectrometer calibration process was the LS-1-CAL-INT tungsten halogen Calibrated Light Source, coupled to an Ocean Optics FOIS-1 Fiber Optic Integrating Sphere, provided by the National Institute of Standards and Technology (NIST), and specifically designed for calibrating the absolute spectral response. Figure D.1 shows the LS-1-CAL-INT lamp power spectral density $\rho_l(\lambda)$ (in W/nm units), provided by NIST.

The first step in the intensity calibration process is to convert the lamp power spectral density curve (in W/nm unit) shown in Figure D.1, to a photon spectral curve (in photons/pixel units), suitable for the spectrometer calibration.

The spectrograph is formed by a diffraction grating used to send photons with different

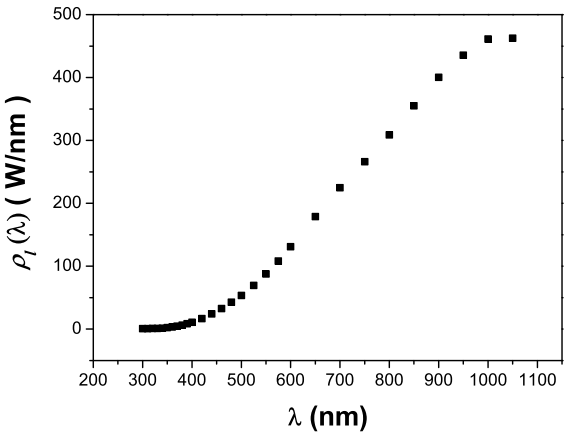

Figure D.1: Lamp's power spectral density $[\rho_l(\lambda)]$. Data provided by the standard lamp's manufactory and certified by NIST.

wavelengths to reach different columns of pixels into the CCD (see Chapter **??** for details). Since each pixel has a finite size ($\sim 26\,\mu$m), each collum of pixels (given rise to each datapoint in the collected spectrum) covers a specific wavelength interval $\Delta\lambda$. Due to the geometry of the diffraction grating, the interval $\Delta\lambda$ depends on lambda.

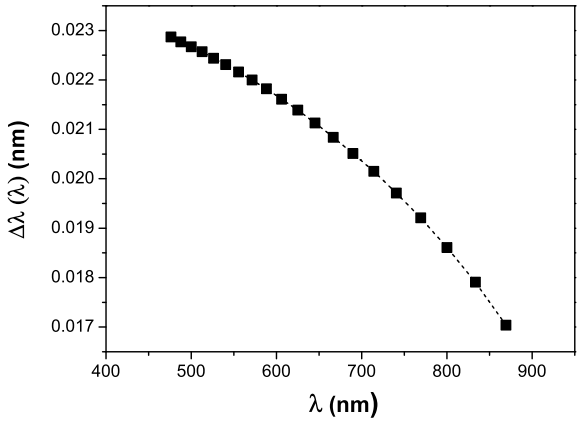

Figure D.2: The measurement of the interval $\Delta\lambda$ covered by the central column of pixels *vs* the absolute wavelength λ.

Figure D.2 shows the measurement of the wavelength range $\Delta\lambda(\lambda)$ covered by the central column of pixels in the CCD system *vs* the absolute wavelength λ. Observe that $\Delta\lambda$ becomes smaller by increasing the absolute wavelength of the light beam reaching the

CCD.

Now, backing to the lamp spectral function, we define the quantity $\Delta P_l(\lambda)$ as the total power emitted by the lamp in the spectral range $\Delta\lambda$:

$$\Delta P_l(\lambda) \simeq \rho_l(\lambda) \cdot \Delta\lambda \ . \tag{D.1}$$

The total energy $\Delta E_l(\lambda)$ emitted by the lamp in the spectral range $\Delta\lambda$ and in a time interval Δt can be obtained as:

$$\Delta E_l(\lambda, \Delta t) \simeq \Delta P_l(\lambda) \cdot \Delta t \simeq \rho_l(\lambda) \cdot \Delta\lambda \cdot \Delta t \ . \tag{D.2}$$

The energy of a photon (in Joules unit) with associated wavelength λ is:

$$E_p(\lambda) = \frac{hc}{\lambda} \ , \tag{D.3}$$

where c = $3{\times}10^{17}$ nm/s is the light speed, and $h = 6.626 \times 10^{-34}$ J·s is the Planck's constant.

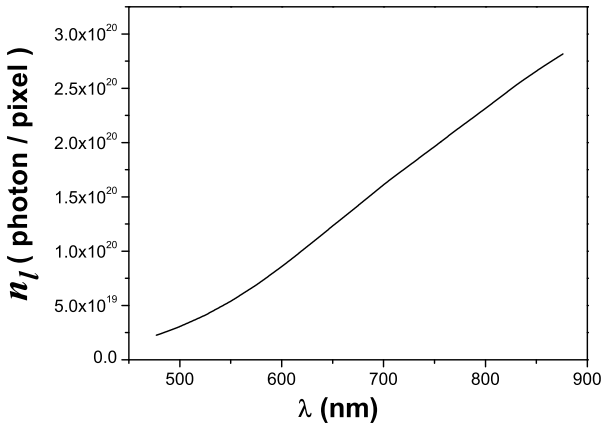

Figure D.3: Curve n_l *vs* the wavelength λ for the standard lamp, obtained from equation D.5, using the power spectral density $\rho_l(\lambda)$ depicted in Figure D.1, and for an integration time $\Delta t = 10$ s.

The number of photons $n_l(\lambda, \Delta t)$ which should reach the specific CCD's column of pixels under consideration, in the time interval Δt, can be obtained as:

$$n_l(\lambda, \Delta t) \simeq \frac{\Delta E_l(\lambda, \Delta t)}{E_p(\lambda)} \ . \tag{D.4}$$

Grouping Equations D.2, D.3, and D.4, we obtain:

$$n_l(\lambda, \Delta t) \simeq \frac{\rho_l(\lambda) \cdot \lambda \cdot \Delta\lambda \cdot \Delta t}{hc} \ . \tag{D.5}$$

Figure D.3 shows the curve n_l *vs* the wavelength λ for the standard lamp, obtained from equation D.5, using the power spectral density $\rho_l(\lambda)$ depicted in Figure D.1, and the curve $\Delta\lambda(\lambda)$ depicted in Figure D.2 for an integration time $\Delta t = 10\,\mathrm{s}$.

D.2 The measured spectrum of the standard lamp

The measurement of the spectrum of the standard lamp was obtained by focusing the end of the fiber optics (coupled to the standard lamp) in the spectrometer microscope objective lens. The integration time was $\Delta t = 10\,\mathrm{s}$. The number of counts were taken in the central pixel for all spectra obtained at different values of absolute wavenumbers ϑ. Figure D.4 shows the lamp spectrum measured curve m_l (in units of count/pixel) *vs* the absolute wavenumbers ϑ.

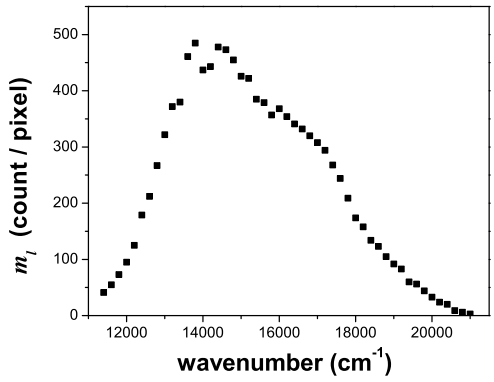

Figure D.4: Lamp spectrum measured curve m_l (in units of count/pixel) *vs* the absolute wavenumber ϑ.

In order to obtain the response curve (next section) we should transform the horizontal scale into wavelength, and multiply the vertical scale by 16 (see equation **??**), so that we obtain the measured curve m_l in units of photon/pixel *vs* the absolute wavelength λ (see Figure D.5). It should be noticed that the m_l curve is not a spectral function, since the horizontal scale is just an index relating the central pixel with the associated wavelength λ or wavenumber ϑ.

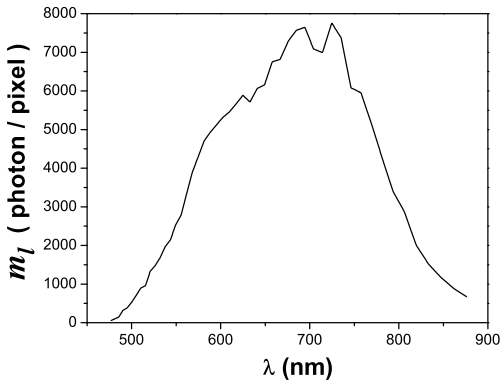

Figure D.5: Measured curve m_l (in units of photon/pixel) *vs* the absolute wavelength λ (in nm units).

D.3 The shape of the spectrometer response curve

The spectrometer response curve $R(\lambda)$ can be obtained by evaluating the ratio between the lamp measured curve $[m_l(\lambda)]$ and the lamp spectral photon emission $[n_l(\lambda)]$, depicted in Figures D.5 and D.3, respectively:

$$R(\lambda) = \frac{m_l(\lambda)}{n_l(\lambda)} \ . \tag{D.6}$$

Figure D.6(a) shows the spectrometer response curve R(λ) *vs* the absolute wavelength λ,

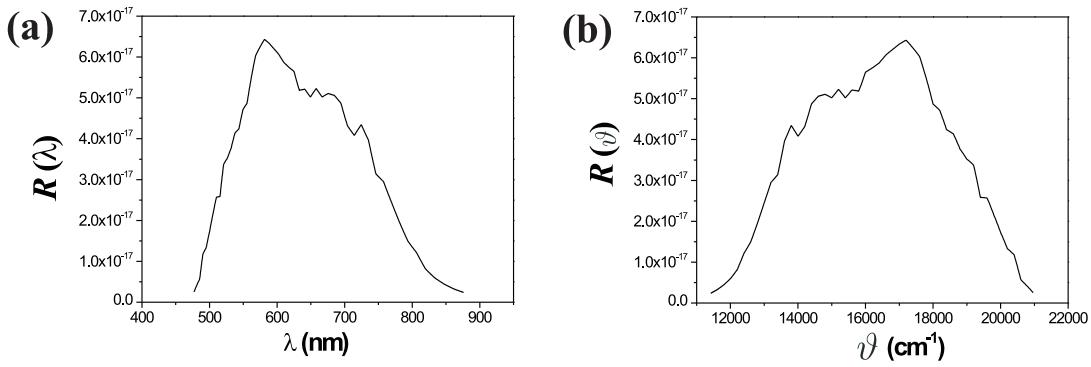

Figure D.6: (a): Spectrometer response curve R(λ) *vs* the absolute wavelength λ. (b): Spectrometer response curve R(ϑ) *vs* the absolute wavenumber ϑ.

obtained by evaluating equation D.6. Since the wavenumber scale is used in most of the

Raman experiments, we have to change the horizontal scale for cm^{-1}, in order to obtain the spectrometer response curve $R(\vartheta)$ *vs* the absolute wavenumber ϑ [see Figure D.6(b)].

The response curve depicted in Figure D.6 is a good correction for the analysis of the relative Raman intensities (integrated areas) of Raman bands centered at different wavenumbers ϑ, or for the relative Raman intensities of the same Raman band obtained using different excitation laser wavelengths. The calibrated intensity $I_c^q(\vartheta)$ of a specific Raman mode q, centered at the absolute wavenumber ϑ, can be obtained from:

$$I_c^q(\vartheta) = \frac{I_m^q(\vartheta)}{R(\vartheta)} \ , \tag{D.7}$$

where $I_m^q(\vartheta)$ is the integrated area of the measured curve and $R(\vartheta)$ is the value of the response curve for the absolute wavenumber ϑ.

D.4 Measuring the absolute differential Raman cross section

In this section, we will calibrate the vertical scale of $R(\vartheta)$, by comparing the corrected integrated area (using Equation D.7) of Raman bands obtained from standard samples with well known values of the differential Raman cross sections taken from the literature.

Our standard sample is the cyclohexane liquid (C_6H_{12}), with 99 % of purity. We will analyze the intensity of the cyclohexane Raman bands centered at 802 cm^{-1} and 2900 cm^{-1}. The 802 cm^{-1} mode is a totally symmetric vibration involving C-C stretching and CH_2 deformation. The 2900 cm^{-1} band is, in fact, a set of 4 strong peaks related to the C-H stretching.[94] We have measured the spectra with a constant incident light intensity of $I_0 = 6.25 \times 10^8$ mW/cm^2, integration time $\Delta t = 60$ s, and using the 80× objective lens ($\Delta\Omega = 2.13$ sr). The spectra were taken using five excitation laser lines, with the following wavelengths: λ_{laser} = 647, 568, 514.5, 488, and 457.9 nm. The integrated areas of the measured bands I_m are depicted in Table D.1, in count units. We start the analysis by calculating the differential integrated area in units of count/s·sr:

$$i_m = \frac{I_m}{\Delta\Omega\Delta t} \ . \tag{D.8}$$

The values obtained for i_m by evaluating Equation D.8 are depicted in Table D.1, and

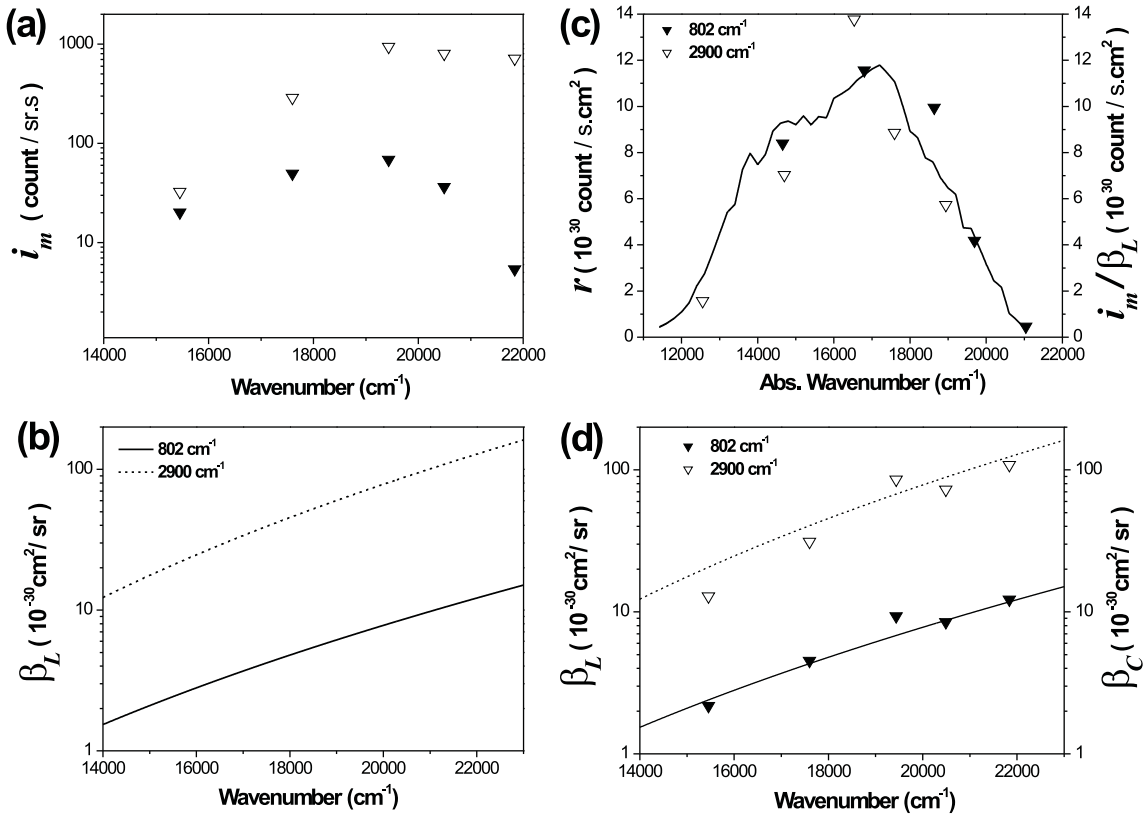

Figure D.7: (a): Values of i_m obtained by evaluating Equation D.8. (b) Fit of the absolute differential cross section β_L of the 802 cm^{-1} and 2900 cm^{-1} Raman bands of the cyclohexane *vs.* the excitation laser wavenumber, obtained from literature data in reference [94]. The horizontal scale is the excitation laser wavenumber used in the Raman experiment (ϑ_{laser}). (c): The dots are the plot of the values of i_m/β_L in function of the absolute wavenumber ϑ of the 802 cm^{-1} (dark triangles) and 2900 cm^{-1} (open triangles) bands, respectively, for the data obtained by using the five excitation laser lines. The solid line is the $r(\vartheta)$ response curve. (d): Plot of the corrected differential cross section values β_C obtained from equation D.11 for the 802 cm^{-1} and 2900 cm^{-1} bands (also depicted in Table D.1), under the absolute differential cross section curve obtained by Trulson and Mathies [94], for reference.

plotted in Figure D.7(a) as a function of the excitation laser wavenumber (ϑ_{laser}) for the 802 cm^{-1} and 2900 cm^{-1} bands.

The absolute differential cross section of the 802 cm^{-1} and 2900 cm^{-1} Raman bands of the cyclohexane were measured by Trulson and Mathies for many excitation laser wavelengths, using an integrator cavity.[94] Figure D.7(b) shows the fit made by the authors in the range of excitation laser wavenumbers which will interest us (from 14000 to 23000 cm^{-1}). The

λ_{laser} (nm)	ϑ (cm^{-1})	I_m (count)	i_m $\left(\frac{count}{sr \cdot s}\right)$	i_m/β_L $\left(10^{30}\frac{count}{s \cdot cm^2}\right)$	β_C $\left(10^{-30}\frac{cm^2}{sr}\right)$
802 cm^{-1}					
647	14654	2574	20	8.4	2.2
568	16799	6355	50	11.6	4.5
514.5	18636	8771	69	9.9	9.3
488	19692	4648	36	4.2	8.5
457.9	21039	686	5	0.5	12.2
2900 cm^{-1}					
647	12554	4158	32.5	1.6	12.9
568	14700	36830	288.2	7	31.2
514.5	16536	120200	940.5	13.8	85.5
488	17592	102231	800	8.9	72.7
457.9	18939	91348	714	5.7	108.3

Table D.1: Values of ϑ, I_m, i_m, i_m/β_L, and β_C for the 802 cm^{-1} and 2900 cm^{-1} cyclohexane Raman peaks, for the five laser lines used in the experiment.

vertical scale gives the differential cross section of the 802 cm^{-1} and 2900 cm^{-1} bands β_L, where the subscript L refers to the literature data obtained from reference [94]. The horizontal scale is the excitation laser wavenumber used in the Raman experiment (ϑ_{laser}).

Now, we can estimate the response factor r, associated with each of our data i_m, in order to obtain the reference value of the differential cross section provided by the literature (β_L). This value can be obtained from:

$$r = \frac{i_m}{\beta_L} \ , \tag{D.9}$$

where r has the units of count/s·cm^2.

The values of the ratio i_m/β_L obtained by evaluating Equation D.9, using the i_m and β_L data associated with all excitation laser lines used in our experiment, are depicted in Table D.7. Figure D.7(c) shows the plot of the values of i_m/β_L as a function of the absolute wavenumber ϑ of the 802 cm^{-1} (dark triangles) and 2900 cm^{-1} (open triangles) bands, respectively, for the data obtained by using the five excitation laser lines (the absolute wavenumber ϑ is depicted in the second column of Table D.7).

There is a curve $r(\vartheta)$ which fits the data points i_m/β_L plotted in Figure D.7(c) (dark and open triangles). This curve has the same profile as the response curve R(ϑ) obtained in the last section (see Figure D.6). Therefore, we can multiply the response curve R(ϑ) by a specific number α, in order to obtain $r(\vartheta)$, that is:

$$r(\vartheta) = \alpha \cdot R(\vartheta) \ . \tag{D.10}$$

The solid line in Figure D.7(c) shows the $r(\vartheta)$ curve obtained from the product between $R(\vartheta)$ depicted in Figure D.6, and the proportionality constant $\alpha = 1.9 \times 10^{17}$. Notice that α is an empirical parameter which transforms $R(\vartheta)$ in $r(\vartheta)$. Now we have the curve $r(\vartheta)$ which can be used to obtain the calibrated value for the absolute differential cross section of the measured data β_C, that is:

$$\beta_C = \frac{i_m}{r(\vartheta)} \ . \tag{D.11}$$

The values of β_C obtained from equation D.11 for the 802 cm^{-1} and 2900 cm^{-1} bands are depicted in Table D.1, and plotted in Figure D.7(d) under the absolute differential cross section curves obtained by Trulson and Mathies [94], for reference. The graphic shows that the response curve $r(\vartheta)$ provides a good absolute intensity calibration, since the data points are in good agreement with the absolute differential cross section values from the literature.

D.5 Final remarks

The response curve $r(\vartheta)$ depicted in Figure D.7(c) is valid only for spectra obtained in the same conditions as the standard spectra, that is, $I_0 = 6.25 \times 10^8$ mW/cm^2. The integration time and the solid angle should also be corrected for 1 s and 1 sr respectively, using Equation D.8. The R(ϑ) curve carries the shape of the spectrometer response and its profile can be always used satisfactorily in order to analyze the relative intensities of Raman bands centered in different absolute wavenumbers ϑ, or for measuring the relative intensity of the same Raman band obtained using different excitation laser wavelengths. This is due to the fact that the profile of the response curve depends basically on fixed parameters, such as the efficiency dependence of mirrors, gratings, or CCD detector on the scattered light wavelength. However, in the case of an absolute Raman intensity analysis, the optical alignment of the spectrometer setup has a strong influence on the results. Unfortunately, the optical alignment is naturally changed in systems where experiments

using different excitation laser lines are performed with daily frequency. Therefore, if one wishes to analyze the absolute Raman cross section, the standard sample spectrum should be performed during each experiment (at least one spectrum for each laser line). In order to obtain the correct $r(\vartheta)$ curve referent to the actual status of the spectrometer's optical alignment, the procedure explained in section D.4 should be performed again, using the data collected during the actual experiment.

Bibliography

[1] M. S. Dresselhaus, G. Dresselhaus, K. Sugihara, I. L. Spain and H. A. Goldberg. *Graphite Fibers and Filaments*, Springer Series in Material Science Vol. 5 (Springer, Berlin, 1988).

[2] R. Saito, G. Dresseulhaus, and M. S. Dresseulhaus, *Physical Properties of Carbon Nanotubes* (Imperial College Press, London, 1998).

[3] M. S. Dresselhaus, G. Dresselhaus, and P. C. Eklund, *Science of Fullerenes and Carbon Nanotubes* (Academic, New York, 1996).

[4] Y. Zhang, Y. W. Tan, H. L. Stormer, and P. Kim, Nature **438**, 201 (2005).

[5] K. S. Novoselov, A. K. Geim, S. V. Morozov, D. Jiang, Y. Zhang, S. V. Dubonos, I. V. Grigorieva, A. A. Firsov, Science **306**, 5296 (2004).

[6] K. S. Novoselov, A. K. Geim, S. M. Morozov, D. Jiang, M. I. Katsnelson, I. V. Grigorieva, S. V. Dubonos, and A. A. Firsov, Nature **438**, 197 (2005).

[7] F. Tuinstra and J. L. Koenig, J. Chem. Phys. **53**, 1126 (1970).

[8] F. Tuinstra and J. L. Koenig, J. Composite Materials **4**, 492 (1970).

[9] P. Lespade, A. Marchand, M. Couzi, and F. Cruege, Carbon **22**, 375 (1984).

[10] H. Wilhelm, M. Lelaurain, McRae, and B. Humbert, Journal of Appl. Physics **84**, 6552 (1998).

[11] A. Hartschuh, E. J. Sanchez, X. S. Xie, and L. Novotny, Phys. Rev. Lett. **90**, 95503 (2003).

[12] International Tables for Crystallography, Volume A: *Space-Group Symmetry* (Institut fr Kristallographie, Technische Hochschule Aachen, D-52056 Aachen, Germany, 2005).

[13] O. Dubay and G. Kresse, Phys. Rev. B **67**, 035401 (2003).

[14] J. C. Charlier, X. Gonze, J. P. Michenaud, Phys. Rev. B **43**, 4579 (1991).

[15] F. Bassani and G. Pastori Parravicini. *Electronic States and Optical Transitions in Solids* (Pergamon Press, Oxford, 1975).

[16] L. Wirtz, and A. Rubio, Solid State Commucations **131**, 141 (2004).

[17] R. A. Jishi and G. Dresselhaus, Phys. Rev. B **26**, 4514 (1982).

[18] L. G. Johnson, and G. Dresseulhaus, Phys. Rev. B **7**, 2275 (1973).

[19] W. Hayes and R. Loudon, *Scattering of Light by Crystals* (John Wiley & Sons, 1978).

[20] H. Poulet and J. P. Mathieu, *Vibration Spectra and Symmetry of Crystals* (Paris: Gordon and Breach, 1976).

[21] R. Loudon, Advances in Physics **50**, 813 (2001).

[22] R. Loudon, *The Quantum Theory of Light*, second edition (Oxford University Press, 1986).

[23] P. Y. Yu, and M. Cardona, *Fundamentals of Semiconductors*, Physiscs and Materials Properties (Springer Berlim Heidelberg New York, 2005).

[24] M. J. Pelletier, *Analytical Applications of Raman Spectroscopy* (Kaiser Optical Systems, Ann Arbor, Michigan, USA, 1990).

[25] M. C. Hutley, *Diffraction Gratings* (Academic Press, London, 1982).

[26] L. G. Cançado, M. A. Pimenta, B. R. A. Neves, M S. S. Dantas, and A. Jorio, Phys. Rev. Letters **93**, 247401 (2004).

[27] M. A. Pimenta, G. Dresselhaus, M. S. Dresselhaus, L. G. Cançado, A. Jorio, and R. Saito, Phys. Chem. Chem. Phys. **9**, 1276 (2007).

[28] A. Hartschuh, E. J. Sánchez, X. S. Xie, and L. Novotny, Phys. Rev. Letters **90**, 095503 (2003).

[29] T. P. Mernagh, R. P. Cooney, and R. A. Johnson, Carbon **22**, 39 (1984).

[30] L.G. Cançado, K. Takai, T. Enoki, M. Endo, Y. A. Kim, H. Mizusaki, A. Jorio, L. N. Coelho, R. Magalhães-Paniago, and M. A.Pimenta, Appl. Phys. Letters **88**, 163106 (2006).

[31] R. Tsu, J. H. Gonzalez, and I. C. Hernandez, Solid State Commun. **27**, 507 (1978).

[32] R. J. Nemanich and S. A. Solim, Solid State Comm. **23**, 417 (1977).

[33] R. J. Nemanich and S. A. Solim, Phys. Rev. B **20**, 392 (1979).

[34] R. P. Vidano, D. B. Fishbach, L. J. Willis, and T. M. Loehr, Solid State Commun. **39**, 341 (1981).

[35] A. V. Baranov, A. N. Bekhterev, Y. S. Bobovich, and V. I. Petrov, Opt. Spectrosc. USSR **62**, 612 (1987).

[36] I. Pócsik, M. Hundhausen, M. Koós, and L. Ley, Journal of non-Crystalline Solids, 1083 (1998).

[37] M. J. Matthews, M. A. Pimenta, G. Dresselhaus, M. S. Dresselhaus, and M. Endo, Phys. Rev. B **59**, R6585 (1999).

[38] C. Thomsen and S. Reich, Phys. Rev. Letters **85**, 5214 (2000).

[39] R. Saito, G. Dresselhaus, and M. S. Dresselhaus, Phys. Rev. B, **61**, 2981 (2000).

[40] R. Saito, A. Jorio, A. G. Souza Filho, G. Dresselhaus, M. S. Dresselhaus, and M. A. Pimenta, Phys. Rev. Letters **88**, 027401 (2002).

[41] L.G. Cançado, M. A. Pimenta, R. Saito, A. Jorio, L. O. Ladeira, A. Gruneis, A. G. Souza-Filho, G. Dresselhaus, and M. S. Dresselhaus, Phys. Rev. B **66**, 035415 (2002).

[42] P. H. Tan, Y. M. Deng, Q. Zhao, Phys. Rev. B, **58**, 5435 (1998).

[43] A. C. Ferrari, and J. Robertson, Phys. Rev. B **61** 14095 (2000).

[44] A. C. Ferrari, and J. Robertson, Phys. Rev. B **64** 075414 (2001).

[45] S. Reich and C. Thomsen, Phil. Trans. R. Soc. Lond. A **362**, 2271 (2004).

[46] J. Kurti, V. Zólyomi, A. Gruneis, H. Kuzmany, Phys. Rev. B **65**, 165433 (2002).

[47] J. Maultzsch, S. Reich, C. Thomsen, H. Requardth, P. Ordejón, Phys. Rev. Lett. **92**, 075501 (2004).

[48] J. Maultzsch, S. Reich, and C. Thomsen, Phys. Rev. B **70**, 155403 (2004).

[49] S. Piscanec, M. Lazzeri, Francesco Mauri, A. C. Ferrari, and J. Robertson, Phys. Rev. Letters **93**, 185503 (2004).

[50] J. J. Maultzsch, *Vibrational properties of carbon nanotubes and graphite*, doctor Thesis (2004).

[51] M. Fujita, K. Wakabayashi, K. Nakada and K. Kusakabe, J. Phys. Soc. Jpn. **65**, 1920 (1996).

[52] K. Nakada, M. Fujita, G. Dresselhaus and M. Dresselhaus, Phys. Rev. B **54**, 17954 (1996).

[53] Mutsuaki Murakami, Sumio Iijima, and Susumu Yoshimura, J. Appl. Phys. **60**, 3856 (1986).

[54] M. Yudasaka, Y. Tasaka, M. Tanaka, H. Kamo, Y. Ohki, S. Usami, and S. Yoshimura, Appl. Phys. Lett. **64**, 3237 (1994).

[55] M. Zhang, D. H. Wu, C. L. Xu, Y. F. Xu, and W. K. Wang, NanoStruct. Mat. **10**, 1145 (1998).

[56] Yubao Li, Sishen Xie, Weiya Zhou, Dongsheng Tang, Xiao-Ping Zou, Zhuqin Liu, and Gang Wang, Carbon **39**, 626 (2000).

[57] K. Wakabayashi, Phys. Rev. B **64**, 125428 (2001).

[58] Ge. G. Samsonidze, R. Saito, A. Jorio, M.A. Pimenta, A.G. Souza Filho, A. Grneis, G. Dresselhaus, and M.S. Dresselhaus, Journal of Nanoscience and Nanotechnology **3**, 431 (2003).

[59] K. Wakabayashi, M. Fujita, H. Ajiki and M. Sigrist, Phys. Rev. B **59**, 8271 (1999).

[60] Y. Miyamoto, K. Nakada and M. Fujita, Phys. Rev. B **59**, 9858 (1999).

[61] F. L. Shyu, M. F. Lin, C. P. Chang, R. B. Chen, J. S. Shyu, Y. C. Wang and C. H. Liao, J. Phys. Soc. Jpn. **70**, 3348 (2001).

[62] A. M. Affoune, B. L. V. Prasad, Hirohiko Sato and Toshiaki Enoki, Langmuir **17**, 547 (2001).

[63] A. M. Affoune, B. L. V. Prasad, Hirohiko Sato, Toshiaki Enoki, Yutaka Kaburagi, Yoshihiro Hishiyama, Chem. Phys. Lett. **348**, 17 (2001).

[64] A. Gruneis, R. Saito, Ge. G. Samsomidze, T. Kimura, M. A. Pimenta, A. Jorio, A. G. Souza Filho, G. Dresselhaus, and M. S. Dresselhaus, Phys. Rev. B **67**, 165402 (2003).

[65] R. Saito, A. Gruneis, Ge. G. Samsomidze, G. Dresselhaus, M. S. Dresselhaus, A. Jorio, L. G. Cançado, M. A. Pimenta, and A. G. Souza Filho, Appl. Phys. A **78**, 1099 (2004).

[66] M. F. Lin and F. L. Shyu, J. Phys. Soc. Jpn. **69**, 3529 (2000).

[67] C. W. Chiu, F. L. Shyu, C. P. Chang, R. B. Chen and M. F. Lin, J. Phys. Soc. Jpn. **72**, 170 (2003).

[68] Ping-Heng Tan, Yuan-Ming Deng, Qian Zhao, and Wen-Chao Cheng, Appl. Phys. Lett. **74**, 1818 (1999).

[69] H. Herchen and M. A. Cappelli, Phys. Rev. B **43**, 11740, (1991).

[70] E. S. Zouboulis and M. Grimsditch, Phys. Rev. B **43**, 12490 (1991).

[71] Hsianpin Chang and Allen J. Bard, Langmuir **7**, 1143 (1991).

[72] I. P. Batra and S. Ciraci, J. Vac. Sci Technol. A **6**, 313 (1988).

[73] G. S. Duesberg *et al.*, Phys. Rev. Letters. **85**, 5436 (2000).

[74] L. G. Cançado, M. A. Pimenta, B. R. A. Neves, G. Medeiros-Ribeiro, T. Enoki, Y. Kobayashi, K. Takai, K. Fukui, M. S. Dresselhaus, R. Saito, and A. Jorio, Phys. Rev Lett. **93**, 047403 (2004).

[75] D. S. Knight and W. White, J. Mater. Res. **4**, 385 (1989).

[76] Kazuyuki Takai, Meigo Oga, Hirohiko Sato, Toshiaki Enoki, Yoshimasa Ohki, Akira Taomoto, Kazutomo Suenaga, Sumio Iijima, Phys. Rev. B, **67**, 214202 (2003).

[77] Mohindar S. Seehra and Arthur S. Pavlovic, Carbon **31**, 557 (1992).

[78] A. C. Ferrari, J. C. Meyer, V. Scardaci, C. Casiraghi, M. Lazzeri, F. Mauri, S. Piscanec, D. Jiang, K. S. Novoselov, S. Roth, and A. K. Geim, Phys. Rev. Lett. **97**, 187401 (2006).

[79] A. Gupta, G. Chen, P. Joshi, S. Tadigadapa, and P.C. Eklund, Nanoletters **6**, 2667 (2006).

[80] D. Graf, F. Molitor, K. Ensslin, C. Stampfer, A. Jungen, C. Hierold, and L. Wirtz, Nanoletters, (2007).

[81] L. G. Cançado, A. Jorio, and M. A. Pimenta, Phys. Rev. B **76**, 064304 (2007).

[82] V. Suresh Babu, and M. S. Seehra, Carbon **34**, 1259 (1996).

[83] E. B. Barros, N. S. Demir, A. G. Souza-Filho, J. Mendes Filho, A. Jorio, G. Dresselhaus, and M. S. Dresselhaus, Phys. Rev. B **71**, 165422 (2005).

[84] Rosalind E. Franklin, Acta Crystal. **4**, 253 (1951).

[85] Y. Wang, D. C. Alsmeyer, and R. L. McCreery, Chem. Mater. **2**, 557 (1990).

[86] A. K. Ganguly, and J. L. Birman, Phys. Rev. **162**, 806 (1967).

[87] José Menendéz, and M. Cardona, Phys. Rev. B **31**, 3696 (1985).

[88] A. Cantarero, C. Trallero-Giner, and M. Cardona, Phys. Rev. B **39**, 8388 (1989).

[89] C. Trallero-Giner, A. Cantarero, and M. Cardona, Phys. Rev. B **40**, 4030 (1989).

[90] C. Trallero-Giner, A. Cantarero, and M. Cardona, Phys. Rev. B **40**, 12290 (1989).

[91] A. Alexandrou, C. Trallero-Giner, A. Cantarero, and M. Cardona, Phys. Rev. B **40**, 1603 (1989).

[92] V. I. Gavrilenko, D. Martínez, A. Cantarero, M. Cardona, and C. Trallero-Giner, Phys. Rev. B **42**, 11718 (1990).

[93] C. Trallero-Giner, A. Cantarero, and M. Cardona, Phys. Rev. B **42**, 6601 (1992).

[94] M. O. Trulson, and R. A. Mathies, J. Chem. Phys. **84**, 2068 (1986).

[95] H. A. Szymanski *Raman Spectroscopy* (Pelenum Press, New York, 1987).

[96] S. Oyama, J. Jiang, L. G. Cançado, M. A. Pimenta, A. Jorio, Ge. G. Samsonidze, G. Dresseulhaus, and M. S. Dresselhaus, Chemical Physics Letters **427**, 117 (2006).

[97] R. M. Martin and L. M. Falicov, Resonant Raman scattering, in *Light Scattering in Solids I: Introductory Concepts*, edited by M. Cardona (Springer, Berlin, 1983), vol. 8 of *Topics in Applied Physics*.

[98] A. Gruneis, *Resonance Raman spectroscopy of single wall carbon nanotubes*, Phd Thesis (Tohoku University, 2004).

[99] E. H. Lieb, Phys. Rev. Letters **62**, 1201 (1989).

———————-